15 October 2010 | $10

Science

AAAS

page 310

page 322

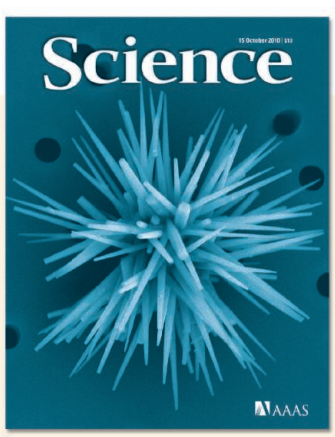

COVER

False-color scanning electron microscopy image of a cluster of L-cystine crystals captured on a porous filtration membrane after growth in the presence of a growth inhibitor. The tapered needles result from binding of the inhibitor at the crystal surface, which reduces the crystal growth rate and the crystal size (the cluster is ~95 μm across). This suggests that inhibitors might be designed to prevent or limit the formation of L-cystine kidney stones. See page 337.

Image: Zhihua An and Timothy G. Bromage/New York University

DEPARTMENTS

Published by AAAS

BREVIA

RESEARCH ARTICLES

REPORTS

CONTENTS continued >>

page 323

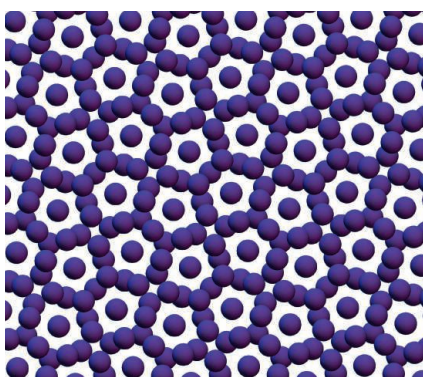

pages 333 & 349

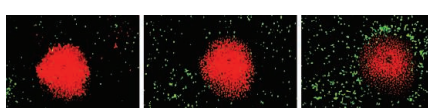

page 362

SCIENCEONLINE

SCIENCEXPRESS
www.sciencexpress.org

Broken-Symmetry States in Doubly Gated Suspended Bilayer Graphene
R. T. Weitz et al.
Ferromagnetic quantum Hall states were observed in suspended bilayer graphene samples in both zero and high magnetic fields.
10.1126/science.1194988

Spin-Light Coherence for Single-Spin Measurement and Control in Diamond
B. B. Buckley et al.
Optical pulses were used to nondestructively probe and manipulate the spin state of nitrogen vacancy defects in diamond.
10.1126/science.1196436

A Low-Magnetic-Field Soft Gamma Repeater
N. Rea et al.
A neutron star lacking a strong magnetic field can still emit short bursts of high-energy radiation.
10.1126/science.1196088

PiggyBac Transposon Mutagenesis: A Tool for Cancer Gene Discovery in Mice
R. Rad et al.
Mutations induced by a transposable element in mice can be used to identify cancer-causing genes.
10.1126/science.1193004

The Role of Discharge Variation in Scaling of Drainage Area and Food Chain Length in Rivers
J. L. Sabo et al.
The lengths of river food chains are indirectly related to drainage area and directly affected by flow and discharge.
10.1126/science.1196005

TECHNICALCOMMENTS

Comment on "Narrow Primary Feather Rachises in *Confuciusornis* and *Archaeopteryx* Suggest Poor Flight Ability"
G. S. Paul
Full text at www.sciencemag.org/cgi/content/full/330/6002/320-b

Comment on "Narrow Primary Feather Rachises in *Confuciusornis* and *Archaeopteryx* Suggest Poor Flight Ability"
X. Zheng et al.
Full text at www.sciencemag.org/cgi/content/full/330/6002/320-c

Response to Comments on "Narrow Primary Feather Rachises in *Confuciusornis* and *Archaeopteryx* Suggest Poor Flight Ability"
R. L. Nudds and G. J. Dyke
Full text at www.sciencemag.org/cgi/content/full/330/6002/320-d

SCIENCENOW
www.sciencenow.org
Highlights From Our Daily News Coverage

Is Your Dog Pessimistic?
Canines with a negative outlook tend to become anxious when their owners leave the house.

At the Smallest Scale, Water Is a Sloppy Liquid
Complex shapes and interactions could explain why H_2O is fundamental to life.

Folklore Confirmed: The Moon's Phase Affects Rainfall
Researchers find link between lunar cycles and precipitation.

SCIENCESIGNALING
www.sciencesignaling.org
The Signal Transduction Knowledge Environment

EDITORIAL GUIDE: Focus Issue—Endocrine Signaling from Clinic to Cell
N. R. Gough
Understanding the molecular details of the response to endocrine hormones should improve treatment options and approaches.

RESEARCH ARTICLE: Sexually Dimorphic Actions of Glucocorticoids Provide a Link to Inflammatory Diseases with Gender Differences in Prevalence
D. Duma et al.

PERSPECTIVE: Stress and Sex Versus Immunity and Inflammation
G. P. Chrousos
Males and females show different responses to stress and to the anti-inflammatory actions of glucocorticoids.

MEETING REPORT: Signal Transduction in Child Health—Closing the Gap Between Clinical and Basic Research
L. Chan et al.
The New Inroads to Child Health Conference focused on plasma membrane receptor-mediated pathways involved in endocrine signaling.

REVIEW: G Protein–Coupled Receptors in Child Development, Growth, and Maturation
A. C. Latronico and Z. Hochberg
Mutations in GPCRs are associated with several disorders that affect the development and maturation of children and adolescents.

PRESENTATION: Hormone Resistance at the Clinical Level
Z. Hochberg
Molecular defects at various steps in hormone production, signaling, or responsiveness can cause disease.

SCIENCECAREERS
www.sciencecareers.org/career_magazine
Free Career Resources for Scientists

Tooling Up: Choosing the Best Fit
D. Jensen
If there isn't good chemistry between you and the company, a job offer can be an offer of entrapment.

In Person: Finding a Path From Oceanography to a Science Communication Career
R. Pidcock
Partway through her Ph.D., Roz Pidcock realized she wanted to talk and write about science, not do it herself.

SCIENCETRANSLATIONAL MEDICINE
www.sciencetranslationalmedicine.org
Integrating Medicine and Science

COMMENTARY: Strategies for Translational Research in the United Kingdom
K. Soderquest and G. M. Lord
Heavy investment in UK translational research has improved infrastructure and advanced clinical medicine.

PERSPECTIVE: Network Dynamics to Evaluate Performance of an Academic Institution
M. E. Hughes et al.
A research collaboration network helps in assessing an institution receiving a translational science award.

RESEARCH ARTICLE: A Defined Tuberculosis Vaccine Candidate Boosts BCG and Protects Against Multidrug-Resistant *Mycobacterium tuberculosis*
S. Bertholet et al.
A fusion peptide vaccine of four *Mycobacterium tuberculosis* proteins boosts an existing vaccine and protects against drug-resistant TB.

RESEARCH ARTICLE: PTEN Deficiency in Endometrioid Endometrial Adenocarcinomas Predicts Sensitivity to PARP Inhibitors
K. J. Dedes et al.
Endometrial cancer cells lacking the PTEN tumor suppressor are sensitive to drugs that block the PARP enzyme.

SCIENCEPODCAST
www.sciencemag.org/multimedia/podcast
Free Weekly Show

Download the 15 October *Science* Podcast to hear about why testing improves memory, advances in nanomedicine, how the body signals neutrophils to respond to injury, and more.

SCIENCEINSIDER
news.sciencemag.org/scienceinsider
Science Policy News and Analysis

SCIENCE (ISSN 0036-8075) is published weekly on Friday, except the last week in December, by the American Association for the Advancement of Science, 1200 New York Avenue, NW, Washington, DC 20005. Periodicals Mail postage (publication No. 484460) paid at Washington, DC, and additional mailing offices. Domestic individual membership and subscription (51 issues): $146 ($74 allocated to subscription). Domestic institutional subscription (51 issues): $910; Foreign postage extra: Mexico, Caribbean (surface mail) $55; other countries (air assist delivery) $85. First class, airmail, student, and emeritus rates on request. Canadian rates with GST available upon request, GST #1254 88122. Publications Mail Agreement Number 1069624. **Printed in the U.S.A.**

Change of address: Allow 4 weeks, giving old and new addresses and 8-digit account number. **Postmaster:** Send change of address to AAAS, P.O. Box 96178, Washington, DC 20090–6178. **Single-copy sales:** $10.00 current issue, $15.00 back issue prepaid includes surface postage; bulk rates on request. The identification code for *Science* is 0036-8075. *Science* is indexed in the *Reader's Guide to Periodical Literature* and in several specialized indexes.

AAAS
ADVANCING SCIENCE, SERVING SOCIETY

Published by AAAS

Annette Schavan is Minister of the Federal Ministry of Education and Research, Germany.

Germany's Energy Research Plan

LAST MONTH, GERMAN CHANCELLOR ANGELA MERKEL APPROVED A LONG-TERM STRATEGY TO PUSH renewable energies as a reliable, economical, and environmentally sound pillar of sustainable economic growth. The "Energiekonzept" (Energy Concept) foresees an end to the country's dependence on fossil fuels and defines key milestones to achieve by 2050, including the reduction of greenhouse gas emissions by 80% (compared to 1990 levels), the modernization and insulation of buildings, and a decrease in electricity consumption by 25%. Innovations must contribute substantially to meet these objectives, and so energy research is an explicit part of the Energiekonzept. By spring 2011, the German government will present a detailed new Energy Research Program that outlines important research tasks to support these new goals.

Renewable energies will play the major role in restructuring Germany's energy supply. These sources already generate about 16% of Germany´s energy, including wind and hydropower, biomass, geothermal, and photovoltaic power. The country's global leadership in Green Tech innovations is based on hefty and continuous investments in research and the dissemination of technologies. In 2010 alone, the German government will spend approximately 1 billion euros on energy and climate research.

The Energy Concept foresees that renewable energies will account for 18% of gross final energy consumption by 2020 (the goal agreed on by the European Union) and 60% by 2050. Renewables will provide 35% of gross electricity consumption in 2020 (80% in 2050). The use of wind power and photovoltaics as electricity sources is a priority that presents a challenge to the existing infrastructure. The considerable fluctuation in the performance of wind and solar systems calls for an overhaul of traditional power grids, which were not designed to cope with dominant shares of green electricity and large numbers of decentralized energy producers. Basic research must lay the foundation for new transmission lines, large-scale storage systems, backup power stations, and information technology–driven networks to balance volatile electricity production.

The German government will provide the finances needed to manage the economic and societal burden of this change. The Federal Ministry of Education and Research will address the challenges and contribute to the new Energy Research Program. But it will take time to complete a cost-efficient transition to a new energy supply system. In the meantime, it is critical that the existing energy supply system remain stable and reliable. Extending the lifetime of nuclear reactors by an average of 12 years is therefore a crucial, but contentious, part of the Energy Concept. Nuclear power accounts for a quarter of Germany's total energy mix. If nuclear power were abandoned today, the German CO_2 output would increase by more than 100 million tons from current levels, which is not permissible. In the Energy Concept, a substantial share of the future profits of nuclear energy suppliers will fund energy research and expand renewable energy sources.

A main goal of the German Federal Ministry of Education and Research is the development of cities that are sustained by "green" services, energy-efficient economic activities, and new consumption models. This is a global challenge as well, and can only be realized through projects based on both national research efforts and an international exchange of experience in this field.

The Energy Concept and the Energy Research Program are vital for Germany's future. They show the country's dedication to the promises made internationally to address climate change, including the commitments made at last year's United Nations Climate Change Conference in Copenhagen. Imponderables will surely arise and may well call for additional measures over the next 40 years. It is therefore important that energy research be defined to include a wide range of technological options, providing policy-makers with the broadest possible options for action. I am confident that the Energiekonzept will galvanize the European Union's commitment to address climate change with long-lasting ambition.

– Annette Schavan

10.1126/science.1198075

Published by AAAS

www.sciencemag.org

Science

1200 New York Avenue, NW
Washington, DC 20005
Editorial: 202-326-6550, FAX 202-289-7562
News: 202-326-6581, FAX 202-371-9227
Bateman House, 82-88 Hills Road
Cambridge, UK CB2 1LQ
+44 (0) 1223 326500, FAX +44 (0) 1223 326501

Subscription Services For change of address, missing issues, new orders and renewals, and payment questions: 866-434-AAAS (2227) or 202-326-6417, FAX 202-842-1065. Mailing addresses: AAAS, P.O. Box 96178, Washington, DC 20090-6178 or AAAS Member Services, 1200 New York Avenue, NW, Washington, DC 20005

Institutional Site Licenses please call 202-326-6755 for any questions or information

Reprints: Author Inquiries 800-635-7181
Commercial Inquiries 803-359-4578

Permissions 202-326-7074, FAX 202-682-0816

Member Benefits AAAS/Barnes&Noble.com bookstore www.aaas.org/bn; AAAS Online Store www.apisource.com/aaas/ code MKB6; AAAS Travels: Betchart Expeditions 800-252-4910; Apple Store www.apple.com/eppstore/aaas; Bank of America MasterCard 1-800-833-6262 priority code FAA3YU; Cold Spring Harbor Laboratory Press Publications www.cshlpress.com/affiliates/aaas.htm; GEICO Auto Insurance www.geico.com/landingpage/go51.htm?logo=17624; Hertz 800-654-2200 CDP#343457; Office Depot https://bsd.officedepot.com/portalLogin.do; Seabury & Smith Life Insurance 800-424-9883; Subaru VIP Program 202-326-6417; VIP Moving Services www.vipmayflower.com/domestic/index.html; Other Benefits: AAAS Member Services 202-326-6417 or www.aaasmember.org.

science_editors@aaas.org	(for general editorial queries)
science_letters@aaas.org	(for queries about letters)
science_reviews@aaas.org	(for returning manuscript reviews)
science_bookrevs@aaas.org	(for book review queries)

Published by the American Association for the Advancement of Science (AAAS), *Science* serves its readers as a forum for the presentation and discussion of important issues related to the advancement of science, including the presentation of minority or conflicting points of view, rather than by publishing only material on which a consensus has been reached. Accordingly, all articles published in *Science*—including editorials, news and comment, and book reviews—are signed and reflect the individual views of the authors and not official points of view adopted by AAAS or the institutions with which the authors are affiliated.

AAAS was founded in 1848 and incorporated in 1874. Its mission is to advance science, engineering, and innovation throughout the world for the benefit of all people. The goals of the association are to: enhance communication among scientists, engineers, and the public; promote and defend the integrity of science and its use; strengthen support for the science and technology enterprise; provide a voice for science on societal issues; promote the responsible use of science in public policy; strengthen and diversify the science and technology workforce; foster education in science and technology for everyone; increase public engagement with science and technology; and advance international cooperation in science.

Information for Authors
See pages 352 and 353 of the 15 January 2010 issue or access www.sciencemag.org/about/authors

EDITOR-IN-CHIEF **Bruce Alberts**
EXECUTIVE EDITOR **Monica M. Bradford**
NEWS EDITOR **Colin Norman**
MANAGING EDITOR, RESEARCH JOURNALS **Katrina L. Kelner**
DEPUTY EDITORS **R. Brooks Hanson, Barbara R. Jasny, Andrew M. Sugden**

Editorial senior editors/commentary Lisa D. Chong, Brad Wible; **senior editors** Gilbert J. Chin, Pamela J. Hines, Paula A. Kiberstis (Boston), Marc S. Lavine (Toronto), Beverly A. Purnell, L. Bryan Ray, Guy Riddihough, H. Jesse Smith, Phillip D. Szuromi (Tennessee), Valda Vinson, Jake S. Yeston; **associate editors** Kristen L. Mueller, Jelena Stajic, Sacha Vignieri, Nicholas S. Wigginton, Laura M. Zahn; **research associate** Alexis Wynne Mogul; **book review editor** Sherman J. Suter; **associate letters editor** Jennifer Sills; **editorial manager** Cara Tate; **senior copy editors** Jeffrey E. Cook, Cynthia Howe, Harry Jach, Lauren Kmec, Barbara P. Ordway, Trista Wagoner; **copy editor** Chris Filiatreau; **editorial coordinators** Carolyn Kyle, Beverly Shields; **publications assistants** Ramatoulaye Diop, Joi S. Granger, Emily Guise, Jeffrey Hearn, Michael Hicks, Lisa Johnson, Scott Miller, Jerry Richardson, Jennifer A. Seibert, Brian White, Anita Wynn; **editorial assistants** Emily C. Horton, Patricia M. Moore, Miriam Weinberg; **executive assistant** Alison Crawford; **administrative support** Maryrose Madrid; **editorial fellow** Melissa R. McCartney

Editorial director, web and new media Stewart Wills; **senior web editor** Tara S. Marathe; **web editor** Robert Frederick; **web development manager** Martyn Green; **web developer** Andrew Whitesell; **intern** Sophia Cai

News deputy news editors Robert Coontz, David Grimm (Online), Eliot Marshall, Jeffrey Mervis, Leslie Roberts; **contributing editors** Elizabeth Culotta, Polly Shulman; **news writers** Yudhijit Bhattacharjee, Adrian Cho, Jennifer Couzin, Jocelyn Kaiser, Richard A. Kerr, Eli Kintisch, Greg Miller, Elizabeth Pennisi, Lauren Schenkman, Robert F. Service (Pacific NW), Erik Stokstad; **web developer** Daniel Berger; **intern** Kristen Minogue; **contributing correspondents** Jon Cohen (San Diego, CA), Daniel Ferber, Ann Gibbons, Sam Kean, Robert Koenig, Andrew Lawler, Mitch Leslie, Charles C. Mann, Virginia Morell, Gary Taubes; **copy editors** Linda B. Felaco, Melvin Gatling, Melissa Raimondi; **administrative support** Scherraine Mack; **bureaus** San Diego, CA: 760-942-3252, FAX 760-942-4979; Pacific Northwest: 503-963-1940

Production senior manager Wendy K. Shank; **assistant manager** Rebecca Doshi; **senior specialists** Steve Forrester, Chris Redwood, Anthony Rosen; **Preflight director** David M. Tompkins; **manager** Marcus Spiegler; **specialist** Jason Hillman

Art director Yael Fitzpatrick; **associate art director** Laura Creveling; **senior illustrators** Chris Bickel, Katharine Sutliff; **illustrator** Yana Hammond; **senior art associates** Holly Bishop, Preston Huey, Nayomi Kevitiyagala; **art associates** Kay Engman, Matthew Twombly; **photo editor** Leslie Blizard

***Science* International**

Europe (science@science-int.co.uk) **editorial: international managing editor** Andrew M. Sugden; **senior editor/commentary** Julia Fahrenkamp-Uppenbrink; **senior editors** Caroline Ash, Stella M. Hurtley, Ian S. Osborne, Peter Stern; **associate editor** Maria Cruz; **locum editor** Helen Pickersgill; **editorial support** Rachel Roberts, Alice Whaley; **administrative support** John Cannell, Janet Clements, Louise Hartwell; **news: europe news editor** John Travis; **deputy news editor** Daniel Clery; **contributing correspondents** Michael Balter (Paris), John Bohannon (Vienna), Martin Enserink (Amsterdam and Paris), Gretchen Vogel (Berlin); **intern** Sarah Reed

Latin America contributing correspondent Antonio Regalado

Asia Japan Office: Asca Corporation, Tomoko Furusawa, Rustic Bldg. 7F, 77 Tenjin-cho, Shinjuku-ku, Tokyo 162-0808, Japan; +81 3 6802 4616, FAX +81 3 6802 4615, inquiry@sciencemag.jp; **asia news editor** Richard Stone (Beijing: rstone@aaas.org); **contributing correspondents** Dennis Normile [Japan: +81 (0) 3 3391 0630, FAX +81 (0) 3 5936 3531; dnormile@gol.com]; Hao Xin [China: cindyhao@gmail.com]; Pallava Bagla [South Asia: +91 (0) 11 2271 2896; pbagla@vsnl.com]

EXECUTIVE PUBLISHER **Alan I. Leshner**
PUBLISHER **Beth Rosner**

Fulfillment Systems and Operations (membership@aaas.org); **director** Waylon Butler; **customer service supervisor** Pat Butler; **specialists** Latoya Casteel, LaVonda Crawford, Vicki Linton, April Marshall; **data entry supervisor** Cynthia Johnson; **specialists** Shirlene Hall, Tarrika Hill, William Jones

Business Operations and Administration director Deborah Rivera-Wienhold; **business systems and financial analysis director** Randy Yi; **manager, business analysis** Eric Knott; **manager, business operations** Jessica Tierney; **financial analysts** Priti Pamnani, Celeste Troxler; **rights and permissions: administrator** Emilie David; **associate** Elizabeth Sandler; **marketing director** Ian King; **marketing managers** Allison Pritchard, Alison Chandler, Julianne Wielga; **marketing associates** Aimee Aponte, Mary Ellen Crowley, Wendy Wise; **senior marketing executive** Jennifer Reeves; **director, site licensing** Tom Ryan; **director, corporate relations** Eileen Bernadette Moran; **publisher relations, eresources specialist** Kiki Forsythe; **senior publisher relations specialist** Catherine Holland; **publisher relations, east coast** Phillip Smith; **publisher relations, west coast** Philip Tsolakidis; **fulfillment supervisor** Iquo Edim; **fulfillment coordinator** Carrie MacDonald; **marketing manager** Christina Schlecht; **marketing associate** Laura Tutino; **electronic media: manager** Lizabeth Harman; **project manager** Trista Snyder; **assistant manager** Lisa Stanford; **senior production specialists** Ryan Atkins, Christopher Coleman, **computer specialist** Walter Jones, Kai Zhang; **production specialists** Angela Forest, Nichele Johnston, Kimberly Oster; **director, web and new media** Will Collins

advertising director, worldwide ad sales Bill Moran
commercial editor Sean Sanders: 202-326-6430
assistant commercial editor Tianna Hicklin 202-326-6463
project director, outreach Brianna Blaser

Product (science_advertising@aaas.org); **midwest** Rick Bongiovanni: 330-405-7080, FAX 330-405-7081; **east coast/e. canada** Laurie Faraday: 508-747-9395, FAX 617-507-8189; **west coast/w. canada** Lynne Stickrod: 415-931-9782, FAX 415-520-6940; **uk/europe/asia** Roger Goncalves: TEL/FAX +41 43 243 1358; **japan** ASCA Corporation, Nanako Ide +81 (0) 3 6802 4616, FAX +81 (0) 3 6802 4615; ads@sciencemag.jp; **senior traffic associate** Deiandra Simms

worldwide associate director of *Science* Careers Tracy Holmes: +44 (0) 1223 326525, FAX +44 (0) 1223 326532

Classified (advertise@sciencecareers.org); **u.s.: midwest/west coast/south central/canada** Tina Burks: 202-326-6577; **east coast/industry** Elizabeth Early: 202-326-6578; **advertising operations manager** Kate Panganiban **sales coordinators** Rohan Edmonson, Shirley Young; **europe/row sales:** Susanne Kharraz, Dan Pennington, Alex Palmer; **sales assistant** Lisa Patterson; **japan** ASCA Corporation, Jie Chin +81 (0) 3 6802 4616, FAX +81 (0) 3 6802 4615; careerads@sciencemag.jp; **advertising support manager** Karen Foote: 202-326-6740; **advertising production operations manager** Deborah Tompkins; **senior production specialist/graphic designer** Amy Hardcastle; **production specialist** Yuse Lajiminmuhip; **senior traffic associate** Christine Hall

China's renewable energy push
305

Retaining minorities in science
306

GULF OIL SPILL

Government Chided for Poor Planning and Communication

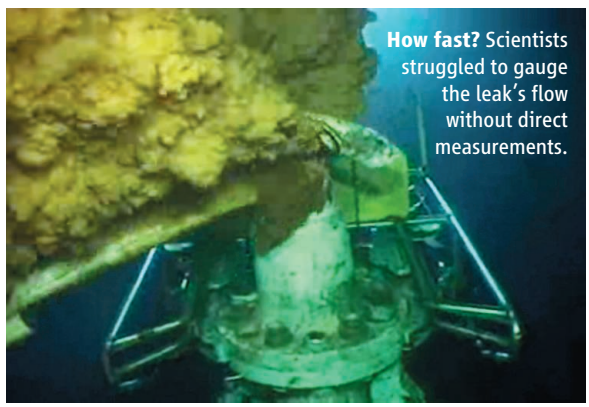

How fast? Scientists struggled to gauge the leak's flow without direct measurements.

It wasn't long after the drilling platform *Deepwater Horizon* sank into the Gulf of Mexico that two contentious scientific issues rose to the surface. Researchers in and out of the government sparred over exactly how much oil was gushing out of the damaged well. And some scientists raised concerns about the wisdom of injecting large volumes of dispersants near the ocean floor to break up the oil gushing from the wellhead, given the potential toxicity of the chemicals and the unprecedented use of dispersants at that depth. Last week, a presidential commission investigating the disaster released two preliminary reports from its staff that fault the government's handling of both issues.

Perhaps most damaging to the government's credibility was its initial, low-ball estimate of how much oil per day was gushing from the well. The commission's report on the fate of the oil reveals for the first time the story behind this controversial first estimate—and the public confusion it sowed.

On 28 April, a week after the *Deepwater Horizon* exploded, government officials released an estimated flow rate of 5000 barrels a day from the Macondo well. Despite immediate skepticism and a flurry of conflicting estimates from outside experts that pegged the flow rate at roughly 10 times as high—estimates that turned out to be in the ball park of the actual figure—the government stood by its figure for a month.

According to the report, the first estimate came from a National Oceanic and Atmospheric Administration (NOAA) scientist who apparently had no particular expertise in the video technique involved. This scientist had cautioned in his e-mail to authorities that his was a "very rough estimate." But neither his warning about the uncertainties in his figure nor any aspects of his methodology made it into the public release. The report found this to be "an overly casual approach."

A month after the spill began, the government set up the interagency Flow Rate Technical Group composed of about 20 members from government, academia, and independent organizations to apply a variety of measurement methodologies. Still, the report laments, the sketchy technical information released by the group discouraged helpful input from the broader scientific community. And the group's official estimates, though growing, continued to come in low, although some group members argued that the flow rate was much higher.

The commission staff says it has no evidence so far that the low estimates slowed the response, but the less-than-transparent estimation process, according to the report, generated "significant controversy, which undermined public confidence in the federal government's response to the spill."

The government could have enhanced confidence, says the report, by being more forthcoming about how bad the spill might have been. From the outset, responders stated that they were scaling their efforts to the "worst-case" spill scenario, not anyone's estimate of the flow rate. But authorities never revealed their worst-case flow rate or how they arrived at it. In late April or early May, NOAA sought to make public some of its worst-case spill models, according to the report, but the White House's Office of Management and Budget (OMB) denied the request. (In a recent statement, OMB claims it delayed release of NOAA's worst-case scenario only for technical reasons, but by the time the report came out, the true flow was known.) The "lack of information may have contributed to public skepticism about whether the government appreciated the size of the *Deepwater Horizon* spill and was truly bringing all of its resources to bear," the report states.

The government also bungled the rollout of a report about the fate of the oil, according to the commission staff. Although the "oil budget" report was technically sound, it was doomed to misinterpretation because of poor presentation, the staff report says. Appearing on news shows on 4 August, the day of the report's release, Carol Browner, the director of the White House Office of Energy and Climate Change Policy, remarked that "the vast majority of the oil is gone" even though the oil budget report in no way supported her take. For months to come, the media would use her comments to characterize the oil budget report as overly optimistic.

A second report focuses on the government decision to use unprecedented volumes of dispersants on the surface and at depth. Neither the Environmental Protection Agency (EPA) nor NOAA had planned for large-scale use of dispersants in a deepwater accident. As a result, according to the

Gulf of Mexico Oil Leak Estimates

Estimated ranges, in barrels per day
(Note: 1 barrel = 42 gallons)

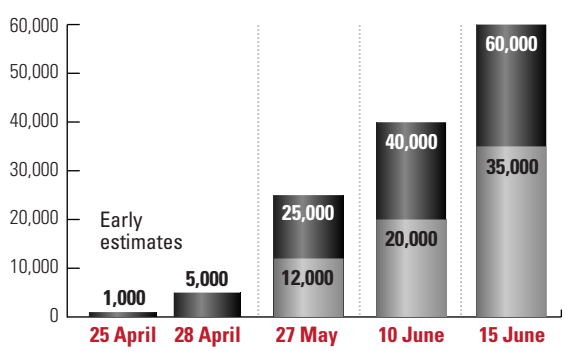

Up and up. Government estimates of the flow from the damaged Gulf of Mexico well grew until early August, when direct measurements put the flow near 60,000 barrels per day.

CREDITS (TOP TO BOTTOM): REUTERS/BP/LANDOV; (GRAPH, SOURCE) DEEPWATER HORIZON INCIDENT JOINT INFORMATION CENTER, REUTERS

Published by AAAS

Can databases feed the census?
310

Asia's mixing bowl for bird flu
313

report, a lack of studies on dispersant toxicity meant that the Coast Guard's Thad Allen, EPA's Lisa Jackson, and NOAA's Jane Lubchenco were "seriously handicapped" when deciding about the use of dispersants. So far, they seem to have made the right call, the staff paper concludes, because dispersants helped protect surface-dwelling wildlife, the wetlands, and cleanup workers.

But the biological impact of the dispersant-oil mixture in the water column remains unknown. "This event clearly shows that ecosystem-based information on dispersants and oil is really inadequate," says Robert Diaz of the Virginia Institute of Marine Science in Gloucester Point, who is not on the panel. "The feds should have seen this [deep-water spill] coming and adjusted their planning," he adds. The report calls for more extensive testing of existing dispersants and development of less-toxic alternatives. EPA and NOAA declined to comment on the dispersant report.

The commission continues to investigate the response to the spill, especially whether the low flow estimates slowed efforts to cap the well. The five-member commission will issue a final report in January.

Meanwhile, says science policy analyst Roger Pielke Jr. of the University of Colorado, Boulder, the government should learn from this crisis "to deal openly and honestly with uncertainties. … The public is smarter than politicians give them credit for. They can handle uncertainties."

–RICHARD A. KERR AND ERIK STOKSTAD

ECONOMICS NOBEL

Three Laureates Explained Why Unemployment Is Inevitable

High unemployment is now plaguing many nations' economies, but even in the best of times, about one out of every 25 workers will be out of a job. This year's winners of the Sveriges Riksbank Prize in Economic Sciences in Memory of Alfred Nobel laid out the theory that explains why full employment is impossible.

Peter Diamond, 70, of the Massachusetts Institute of Technology (MIT) in Cambridge; Dale Mortensen, 71, of Northwestern University in Evanston, Illinois; and Christopher Pissarides, 62, of the London School of Economics will split the $1.5 million prize. Starting in the 1970s, they developed, mostly independently, the theory of markets that suffer "search friction," or costs for consumers and suppliers of a good to find one another. Dubbed the "DMP theory" in the economists' honor, it has become the bedrock for the study of labor markets and explains why people are sure to be out of work even when the number of vacant jobs equals the number of job seekers, so-called equilibrium unemployment.

"It's a wonderful choice," says Michael Elsby, an economist at the University of Michigan, Ann Arbor, of the trio's honor. "If you're going to be thinking about unemployment, you're going to start by playing around with the DMP model."

Classical economics predicts that unemployment should vanish whenever the number of available jobs equals or exceeds the number of workers. In reality, that never happens. For example, even during the economic boom a decade ago, unemployment in the United States dipped only as low as 3.8%.

Diamond, Mortensen, and Pissarides found that they could explain that fact. They began with a dynamical model that considers the flow of workers both into and out of jobs. They imposed costs for an unemployed worker to find a job and for an employer to find a suitable employee, which affected the flows. The economists then showed mathematically that a new equilibrium would arise with at least some unemployment, the amount of which depended on the costs.

In the 1960s, much of economic theory strived to prove that the results from idealized classical economics still held sway as economists made their models more realistic, Diamond said at an MIT press conference after the prize was announced. He preferred to let the improved models lead where they may. "It seemed to me that a better approach was to think about real dynamics and see where they go," he says. "Maybe they go to the [classical] equilibrium solution, and maybe they don't."

Although the DMP theory started out as a mathematical abstraction, it has become a tool for applied economists and policymakers. That's because it provides a framework for studying in detail the effectiveness of a specific intervention in reducing unemployment or ameliorating its effects. "There's a whole literature out there on unemployment insurance that uses the model," says Stephen Woodbury, an economist at Michigan State University in East Lansing.

Given the unemployment crunch afflicting many countries, Pissarides says he favors political action to get people back to work. "What we should really be doing is to ensure that they do not stay unemployed too long," he said at another press conference. "Give them direct work experience—not necessarily advanced training—after a few months so they don't lose touch with the labor market."

–ADRIAN CHO

Published by AAAS

IMMUNOLOGY

Painful Failure of Promising Genital Herpes Vaccine

A vaccine designed to ward off genital herpes has failed in a large clinical trial, abruptly ending the product's seemingly promising future. After 8 years of study in more than 8000 women in the United States and Canada, there was not even a hint of a positive result against the sexually transmitted disease caused by herpes simplex virus-2 (HSV-2). "It's dead negative," says Lawrence Corey, a herpes and vaccine specialist at the Fred Hutchinson Cancer Research Center in Seattle, Washington.

Corey stresses that a vaccine against HSV-2 could have a major public health impact. HSV-2 spreads easily through sexual contact; according to a 2003 estimate from the World Health Organization, more than 300 million women and 200 million men were infected with the virus. The infection often lasts for life and sporadically causes symptoms, including painful blisters that can burst and form ulcers. Pregnant women can spread the virus to their newborns, which sometimes kills them. A person infected with HSV-2 is also much more susceptible to HIV, and a co-infected person may transmit the AIDS virus more readily. "Its biological component to the HIV epidemic has been vastly underestimated," says Corey.

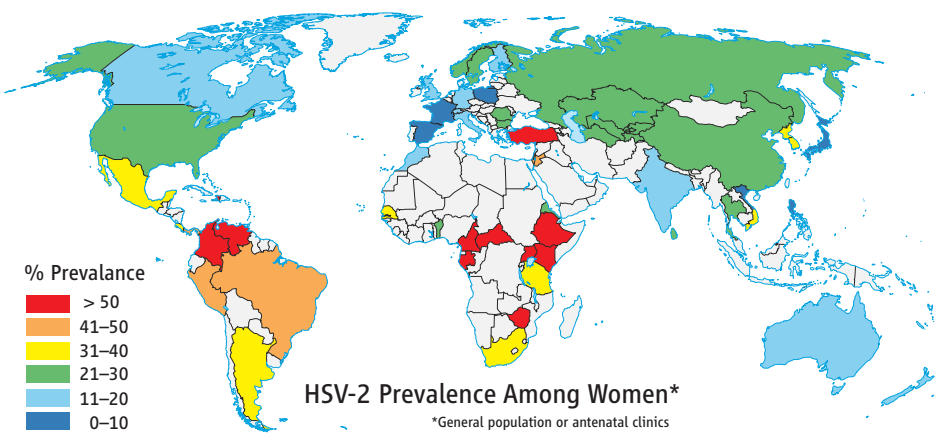

Despite its toll, HSV-2 has generally been seen as a "trivial" disease, says Corey, and vaccines have received scant attention. "It's been the Rodney Dangerfield of the sexually transmitted infection field," he says.

A few large pharmaceutical and biotech companies have shown HSV-2 the respect it deserves, investing heavily in vaccine research over the past few decades. But none of the efforts panned out, leading many to pin high hopes on the vaccine used in the current study. Made by GlaxoSmithKline (GSK) in Rixensart, Belgium, the vaccine contains a protein from HSV-2 mixed with a novel adjuvant, or immune system stimulator, triggering antibodies that researchers hoped could prevent infections. "A lot of the field has been waiting for this result," says Robert Belshe of the St. Louis University School of Medicine in Missouri, who led the study. "It's a great disappointment."

Before the trial, researchers knew the vaccine had serious limitations, but it still offered a toehold for this struggling field. In two earlier studies, the vaccine failed to prevent genital herpes in male and female participants. But when researchers drilled down into the data from those trials, published together in the 21 November 2002 issue of *The New England Journal of Medicine*, they discovered the vaccine may have worked in a subset of women. Specifically, they focused on women who at the trial's start were not infected with HSV-1, a cousin of HSV-2 that causes cold sores in mouths and on lips. Infection with HSV-1 may offer some immune protection against HSV-2. This, in turn, might have masked the impact of the HSV-2 vaccine. The researchers came to this conclusion after noting that in HSV-1–negative women, the vaccine seemed to work more than 70% of the time.

That led the National Institute of Allergy and Infectious Diseases (NIAID) to invest $27.6 million in the massive follow-up study in women who were negative for both HSVs. Researchers recognized that if the vaccine worked, it would have a narrow market: It's designed only for women, and HSV-1 is so widespread in developing countries that the vaccine would be ineffective in much of the world. Still, they hoped to build on the success—a hope that has evaporated with the new negative data. "The inconsistency between the trials is really quite disconcerting," says Corey.

When NIAID and GSK revealed on 30 September the latest vaccine trial's findings, researchers were equally dispirited and confused. "We're really puzzled by the results," says herpes specialist Lawrence Stanberry of Columbia University Medical Center in New York City. Stanberry, who headed the earlier studies of the vaccine and was on the scientific advisory board for the subsequent trial, notes that the follow-up did not recruit the same population of women. In the first trials, women were selected because they were in "discordant" relationships, meaning they had regular sexual partners who were infected with HSV-2. The new study enrolled women who simply perceived themselves as being at risk of infection with the virus. "Discordant couples may by their nature be different biologically or behaviorally than people in a new relationship," says Stanberry. Belshe agrees. "With long-standing relationships, we think there's chronic exposure to herpes antigen, so there might be some immunologic explanation for the different results."

As investigators sort through the wreckage for clues, many worry that the new results will further dampen the little interest industry has shown in an HSV-2 vaccine. GSK has said it will no longer pursue development of this particular vaccine, and no other big pharma company currently has an HSV-2 vaccine in clinical trials. David Knipe, a virologist at Harvard Medical School in Boston who is doing preclinical studies of an HSV-2 vaccine with Sanofi Pasteur that relies on a weakened form of the whole virus, urges NIAID to ramp up its involvement. "As the companies become more cautious about getting into this risky field, the investment is going to have to come from government and nongovernment people."

Corey says the findings underscore how little is known about HSV-2 immunology. He notes that the data make clear that antibodies, which prevent infection, alone are not the answer. Next-generation vaccines, he contends, should also dispatch killer cells to clear cells that HSV-2 manages to infect, as well as less specific innate immune responses. "These results reset the targets," he says. "We've underestimated the kinds of immune responses required to restrain this virus."

–JON COHEN

CREDIT: LAWRENCE COREY/FHCRC

Published by AAAS

CLIMATE CHANGE

Climate Talks Still at Impasse, China Buffs Its Green Reputation

TIANJIN, CHINA—Delegates to a United Nations meeting here last week made scant headway on a global strategy for reining in greenhouse gas emissions. But amid the pessimism and recriminations, one nation won praise from observers for its efforts to boost energy efficiency and invest in green technologies: the host, China.

Negotiators from 177 countries came to this port city near Beijing with low expectations for progress on a deal that could slow global warming, and thick smog that blanketed Tianjin further dampened spirits. Last week's U.N. Framework Convention on Climate Change meeting was a preparatory session for a summit next month in Cancun, Mexico, where countries will resume the Sisyphean task of crafting a successor to the Kyoto Protocol, in which 39 industrialized nations and the European Union committed to reducing greenhouse gas emissions several percent from 1990 levels by 2012. According to the 1997 accord's principle of "common but differentiated responsibilities," developing nations, including China, have pledged to take voluntary steps to rein in carbon emissions.

Talks on a post-Kyoto agreement have floundered, most notably at a sumit in Copenhagen last year (*Science*, 1 January, p. 19). The United States, which endorsed but did not ratify the Kyoto Protocol, and some industrialized nations have balked at the economic cost of deep, legally binding cuts in carbon emissions deemed necessary to avoid catastrophic climate change. Developing nations, the group to which China maintains it still belongs despite its growing economic strength, have vowed to become more energy efficient but as a group have refused to accept binding emissions reductions.

With any progress toward a new accord elusive, the two biggest greenhouse gas emitters—China and the United States—fired broadsides at each other. The lead U.S. negotiator in Tianjin, Jonathan Pershing, criticized China and other major developing nations for refusing to implement a stringent program of monitoring, reporting, and verifying their carbon emissions. "These elements are at the heart of the deal, and the lack of progress on them gives us concern," Pershing told reporters. China, meanwhile, scolded the United States for using the Asian nation as a scapegoat for its own foot-dragging on addressing climate change. The United States "has no measures or actions to show for itself," said Su Wei, director of the powerful National Development and Reform Commission's climate change department, who reiterated China's view that the United States must take "historical responsibility" for rising atmospheric CO_2 levels. In the toxic atmosphere, delegates made only modest progress on issues such as a plan to pay nations to preserve forests.

One silver lining in the smog was China's ramped-up efforts to save energy. The world's biggest greenhouse gas emitter has shuttered thousands of inefficient coal-burning power units in recent months in a frantic bid to reduce its energy intensity—energy consumption per unit of GDP—20% from 2005 levels by the end of this year (*Science*, 4 June, p. 1216). At the Copenhagen summit last December, China upped the ante, vowing to reduce energy intensity by 40% to 45% from 2005 levels by 2020. "China has the will and the way to achieve that," says Barbara Finamore, China program director at the Natural Resources Defense Council (NRDC), a U.S.-based nonprofit. China can meet or exceed its energy-intensity target if, among other things, it eases its reliance on coal from nearly 70% of its energy mix to 62% by 2020, NRDC's David Cohen-Tanugi concluded in an analysis released at the meeting.

A key prong of China's strategy is renewable energy. It aims to raise the non–fossil-fuel share of its primary energy from the current 9% to 15% by 2020. "China is doubling its wind capacity every year" and next year is expected to surpass Germany and the United States as the biggest wind-energy producer, says renewable energy analyst Joanna Lewis of Georgetown University in Washington, D.C. It has also become the world's largest producer of solar cells. And China announced last July that it would spend $738 billion over the next decade on alternative energy.

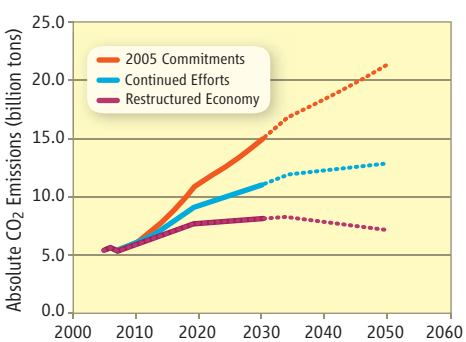

Carbon futures. Three scenarios for China's CO_2 emissions, as envisioned in a new NRDC report.

Scaling up. Solar and wind power are making huge strides in China.

Another element of the nation's energy strategy is to overhaul the electrical grid. Around 80% of China's coal lies in the west and north, and 80% of hydropower generation is in the west, while 75% of energy demand is to the east. To link areas of energy production and demand, China plans to build thousands of kilometers of ultrahigh-voltage transmission lines over the next decade. And starting this year, grid operators must purchase all available renewable energy in their area.

Forecasts indicate that China's greenhouse emissions won't peak for another 10 to 20 years at the earliest. But energy savings from reduced transmission losses, increased renewable energy and electric vehicles, and more-efficient coal burning should allow it to avoid a whopping 1.649 billion tons of CO_2 emissions a year by 2020, according to the State Grid Corporation of China.

All China's initiatives are undergirded by massive investments in clean energy technology, from advanced solar cells to electric vehicles. The International Energy Agency in Paris forecasts a $13 trillion clean energy market over the next 2 decades. According to the Pew Charitable Trusts, in 2009 China invested $34.6 billion in clean energy—an amount second only to the European Union ($41.1 billion) and nearly twice that of the United States ($18.6 billion).

Even though last week's meeting offered little hope for a post-Kyoto compromise, it was clear which greenhouse gas superemitter had made gains in revamping its image. "In the race for a clean energy future, China is already off the starting blocks," says Jake Schmidt, NRDC's international climate policy director. "The U.S. is still taking off its sweatsuit."

–RICHARD STONE

CREDITS (TOP TO BOTTOM): XINHUA/LANDOV; ADAPTED FROM D. COHEN-TANUGI, *PUTTING IT INTO PERSPECTIVE: CHINA'S CARBON INTENSITY TARGET*, NRDC (OCTOBER 2010)

Published by AAAS

UNDERGRADUATE SCIENCE

Better Intro Courses Seen as Key to Reducing Attrition of STEM Majors

Ten years ago, analytical chemist William LaCourse took a hard look at the status of teaching within his department at the University of Maryland, Baltimore County (UMBC). He didn't like what he saw. "We were losing ground," says LaCourse. Students were doing worse on tests, and more were failing or dropping courses. Attendance was spotty, and only the best students were showing up for extra help. The number of chemistry majors was also declining.

A big part of the problem, LaCourse and others decided, was Chemistry 101. It's the gateway course for prospective chemistry majors and a requirement for those in many other fields. "The student newspaper called it a weed-out course," he recalls. "And I thought, 'That doesn't make any sense. Rather than always looking for new customers, why can't we do a better job with the ones we already have?' "

A new report from the National Academies offers advice to universities trying to answer that question. It says that improving introductory courses is one of many steps needed to increase the number of students obtaining degrees in the fields of science, technology, engineering, and mathematics (STEM) and, in particular, the percentage of minorities in the scientific and engineering workforce.

"We are missing what could be called the low-hanging fruit," says Freeman Hrabowski, chair of the National Research Council (NRC) panel that wrote *Expanding Underrepresented Minority Participation: America's Science and Technology Talent at the Crossroads*. "These are students who have gotten into college and are majoring in math and science and who want to be in those disciplines. But more than half of them are not completing degrees in those fields."

Only about 20% of underrepresented minorities who aspire to a STEM degree actually earn one within 5 years, according to a longitudinal study cited in the NRC report by researchers at the University of California, Los Angeles (see graphic). And it's not just minorities who are falling out of the science pipeline. Only 33% of whites and 42% of Asian-Americans complete their STEM degrees in 5 years, the UCLA study finds. "It's really an American issue," says Hrabowski, a mathematician and longtime UMBC president. "It's simply unacceptable for such a large majority of students not to achieve their goal [of a STEM degree]. We must find ways for larger numbers of American students to excel in science."

The new report says that retaining STEM majors will require better academic, social, and financial support for students. Some of those steps are relatively inexpensive, says Hrabowski, although the report does recommend that the government launch a scholarship program to boost the number of needy minority students that could eventually cost $600 million a year.

Under Hrabowski, UMBC has implemented enough of those ideas to become one of the nation's top feeder schools for minorities going on to receive a Ph.D. degree. (Some 22% of UMBC students are underrepresented minorities, and they comprise 20% of all STEM majors.) One especially promising intervention, notes the report, is the university's Meyerhoff Scholars Program, which offers a summer bridge program, scholarships, tutoring and networking, research experiences, and study abroad.

UMBC has also overhauled its introductory courses. The chemistry department, which LaCourse now chairs, has converted Chem 101 and Chem 102 into "Discovery Learning" courses. Students who had once sat passively during a weekly 2-hour recitation section while a graduate student solved problems on the whiteboard are now part of four-person teams responsible for finding the right answer. Teaching assistants act as "Sherpas," says LaCourse, "guiding students up the mountain." Laptops and cell phones have been banned from the sections so that students can focus on the assignment. Attendance is mandatory, and unexcused absences result in lower grades. There are still lectures, but they are delivered by someone "who lives and breathes Chem 101," says LaCourse.

The changes have produced immediate—and dramatic—results. Pass rates for the introductory courses shot up the first year from 70% to 85%—even though the department also raised the minimum score—and have inched up from there. Attendance has improved, and fewer students drop the course. The number of chemistry majors has nearly doubled since 2003, and the outflow from chemistry to other majors has stopped, reversing a chronic leakage of up to a dozen students a year. As a bonus, a once-moribund student chapter of the American Chemical Society is now thriving.

LaCourse freely acknowledges that UMBC's approach draws heavily on a national movement to replace the didactic style of undergraduate teaching with more active, hands-on learning (*Science*, 31 July 2009, p. 527). And although the results are impressive, LaCourse says the transformation is not complete. The person with the primary responsibility for teaching the two intro courses, for example, is not a tenured faculty member. "I'd like that situation to change," he says frankly. "And I think it's only a matter of time before [teaching] becomes a legitimate pathway. But I'm not that powerful."

–JEFFREY MERVIS

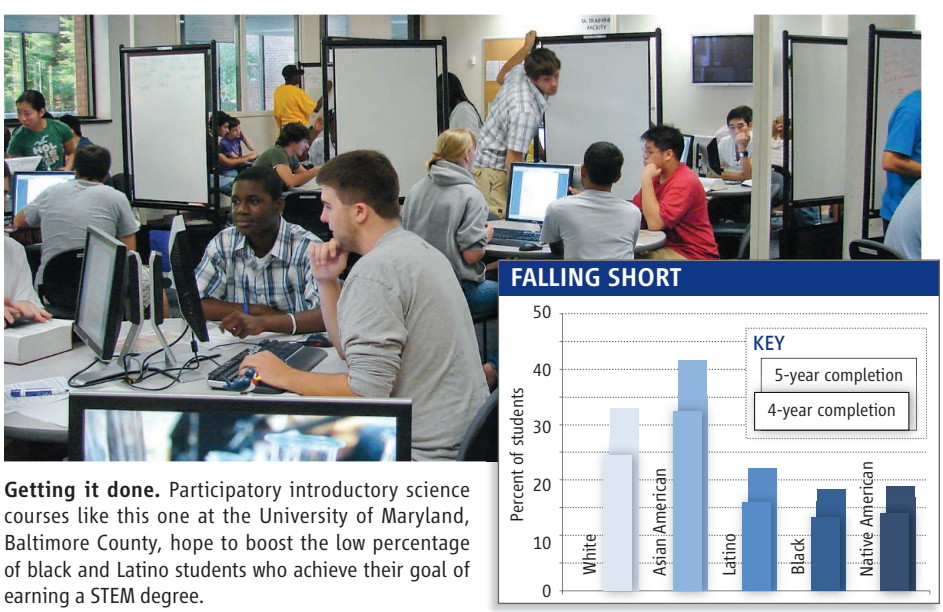

Getting it done. Participatory introductory science courses like this one at the University of Maryland, Baltimore County, hope to boost the low percentage of black and Latino students who achieve their goal of earning a STEM degree.

CREDITS: TIM FORD/UMBC; (INSET, SOURCE) UNIVERSITY OF CALIFORNIA LOS ANGELES, HIGHER EDUCATION RESEARCH INSTITUTE

Published by AAAS

ScienceNOW

From *Science's* Online Daily News Site

Biggest Genome Ever

Now *that's* a genome. A rare Japanese flower named *Paris japonica* sports an astonishing 149 billion base pairs, making its genome 50 times the size of a human genome—and the largest one ever found. Until now, the biggest genome belonged to the marbled lungfish, whose 130 billion base pairs weighed in at an impressive 132.83 picograms. (A picogram is one-trillionth of a gram.) The genome of the new record-holder, revealed in a paper in the *Botanical Journal of the Linnean Society*, would be taller than the Big Ben clock tower if stretched out end to end. The researchers warn, however, that big genomes tend to be a liability: Plants with lots of DNA have more trouble tolerating pollution and extreme climatic extinctions—and they grow more slowly than plants with less DNA because it takes so long to replicate their genomes. http://scim.ag/big-genome

Building Blocks of Life in Titan's Atmosphere?

It's unlikely that the process produced Titanians, but experiments simulating the chemistry of the dense air on Saturn's biggest moon have yielded some of the basic buildings blocks of life. Last week at the American Astronomical Society's Division for Planetary Sciences meeting in Pasadena, California, researchers described how they used radio-frequency radiation—a more convenient substitute for ultraviolet sunlight—to turn methane, nitrogen, and carbon monoxide (the main constituents of Titan's atmosphere) into glycine and alanine, the two smallest amino acids. The experiments also produced cytosine, adenine, thymine, and guanine, the four most basic components of DNA. And they created uracil, a precursor of RNA. The researchers said that because they achieved the reactions without the presence of liquid water, it's possible life could have sprung forth on Earth not in the seas, as commonly assumed, but perhaps in the planet's early atmosphere—a considerably thinner version of the fog enveloping Titan today. http://scim.ag/Titan-life

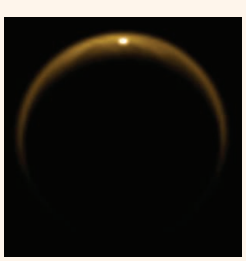

How Volcanoes Feed Plankton

Want to spur plankton growth in the ocean? Hire a volcano.

In August 2008, scientists on a research cruise in the northeastern Pacific Ocean were shocked to witness a sudden, huge spike in the area's plankton population. Within just a few days, the chlorophyll concentration in the water had increased by 150%.

To find out why, the team analyzed air and water chemistry and found that dissolved iron, a nutrient that plankton need to thrive, must have increased dramatically. The source, they deduced, was the 7 to 8 August eruption of the Kasatochi volcano some 2000 kilometers away, chemical oceanographer Roberta Hamme of the University of Victoria in Canada and colleagues report in *Geophysical Research Letters*.

Despite the size of the bloom, however, the plankton's uptake of carbon was relatively modest. Hamme says the team's preliminary analysis suggests that trying to stimulate plankton growth by adding iron to the water—a suggested countermeasure to global warming—would have a minuscule effect on marine CO_2 absorption. http://scim.ag/plankton-bloom

Who's Your Mommy?

Breeders know that sleek, speedy, and spirited thoroughbred horses arose from three Arabian stallions brought to England more than 3 centuries ago. But who were the mares that birthed these noble steeds? A new genetic analysis suggests that thoroughbred foremothers hailed from Ireland and Britain.

Mim Bower, an archaeogeneticist at the University of Cambridge in the United Kingdom, and colleagues analyzed mitochondrial DNA, which is passed down only by the mother, of about 300 thoroughbreds and nearly 2000 other horses of different breeds from across Europe and Asia. Most of the sequences came from a genetic database, but the researchers also contacted horse people, asking for samples of hair pulled from manes. The team then sequenced short stretches of DNA extracted from the tissue attached to the hair.

The thoroughbreds' mitochondrial DNA sequences were closest to those of native Irish and British breeds, like the Connemara (pictured). There was a hint of other ancestries—including Arabian—but thoroughbred moms most likely hailed from the British Isles, the researchers report in *Biology Letters*. And that makes sense—in the early days, breeders thought the important parent was the stallion, says Bower; any old mare would do as a mother. http://scim.ag/find-mom

Read the full postings, comments, and more at **http://news.sciencemag.org/sciencenow**.

CREDITS (TOP TO BOTTOM): ALPSDAKE/WIKIMEDIA; SIMONE/FLICKR/WIKIMEDIA; NASA/JPL/UNIVERSITY OF ARIZONA/DLR

Published by AAAS

COMPUTATIONAL BIOLOGY

Custom-Built Supercomputer Brings Protein Folding Into View

Scientists have long been frustrated in their efforts to use computers to simulate the atomic detail of how proteins fold into their three-dimensional structures. The computing demands for simulating all the motions of a protein's atoms and the surrounding water are so high that scientists have had difficulty tracking the myriad atomic wiggles and gyrations for long enough to see the complete folding process. But now help is on the way. On page 341, computational biologists led by computer scientist and former hedge fund manager David Shaw report that they ran a specially built supercomputer for about 3 weeks to simulate a relatively small protein going through 15 rounds of folding and unfolding over 200 microseconds. They also tracked the folding gyrations of a similarly sized protein for more than a millisecond.

"This is a landmark paper," says David Baker, a protein-folding expert at the University of Washington, Seattle. Klaus Schulten, a molecular simulations expert at the University of Illinois, Urbana-Champaign, who has been Shaw's friendly rival, agrees, calling the paper "very important."

Baker notes that the simulations from Shaw and his colleagues revealed that the folding protein followed more or less the same general pattern of movements each time it folded rather than each folding having a distinct progression. That was something of a surprise because it wasn't clear from previous modeling and experimental work this would be the case. Others note that simulating individual proteins for long periods isn't the only way to investigate protein folding: networks of computers can also cobble together large numbers of shorter simulations to explore some key events. Still, the new work sets the stage for extended simulations of dozens, if not hundreds, of other proteins that are less well understood, which could reveal whether all proteins follow a similar set of rules as they fold. "Now one can approach these questions in a quantitative manner," Baker says.

That's been Shaw's dream since he left the world of high finance 9 years ago to start an outfit called D. E. Shaw Research in New York City. Shaw, who now also has an affiliation with Columbia University, originally trained as a computer scientist and specialized in designing parallel supercomputers. After a brief stint on the faculty of Columbia in the 1980s, he moved to Wall Street, where he designed powerful algorithms for stock trading. He later moved on to run his own hedge fund, winding up on the Forbes list of 400 richest Americans in the process. (He also recently served as the treasurer of AAAS, *Science*'s publisher.) But Shaw missed the intellectual challenge of science. "I found myself at night solving math problems for fun," he says.

After conversations with friends in computational biology, Shaw chose the challenge of simulating the motion of proteins for his reentry into science. Drawing on his early career, he decided to design and build a customized supercomputer to push the boundaries of the field. Two years ago Shaw revealed the result, Anton, a supercomputer containing 512 specially designed computer chips hard-wired to speed the

CHEMISTRY

Carbon-Linking Catalysts Get Nobel Nod

Credit the matchmaker for this one. This year's Nobel Prize in chemistry went to three chemists—Ei-ichi Negishi, Akira Suzuki, and Richard Heck—for discovering catalysts used to tie the knot between carbon atoms on separate molecules. The ability to tailor such molecular unions has spawned whole sectors of advanced technology, making possible the synthesis of everything from anticancer drugs and agricultural pesticides to advanced displays and electronic chips in computers.

At the heart of these applications are organic molecules made from chains and rings of carbon atoms. Carbon is the key to organic chemistry—and life—thanks to its ability to link with its neighbors to form molecular chains and rings of an enormous variety of shapes, much as lumber can be nailed together to build houses of almost any design. To build synthetic molecules, chemists continually look for new ways to join together carbon atoms on separate molecules. The trouble is that in most organic molecules, the carbon atoms are happy with where they are and thus unlikely to react with their neighbors. In the early 1900s, German chemists came up with ways to link metal atoms to carbons, making them more reactive and willing to bond with neighbors. But the reactions weren't specific. Instead of producing just the desired molecule, the more-reactive carbons would bond willy-nilly with any carbon around, producing all sorts of junk that had to be tossed out.

CHEMISTRY
NOBEL PRIZE
2010


RICHARD HECK

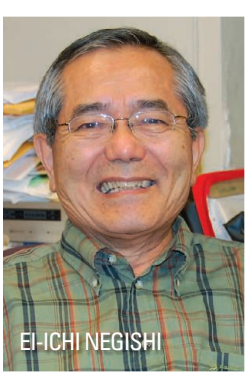
EI-ICHI NEGISHI


AKIRA SUZUKI

In the late 1960s, Heck, then with chemical manufacturing company Hercules Corp. in Wilmington, Delaware, and later at the University of Delaware, Newark, found that he could tailor just which carbons he wanted to link together. In one early example, Heck first linked a bromine atom to one of the six carbon atoms in a molecule of benzene. This slightly modified the electronic structure of the carbon and tagged it as the one that would react. He then added small, two-carbon molecules called olefins to the solution, as well as palladium. The palladium temporarily binds with both the carbon on the bro-

CREDITS (FROM LEFT): © THE NOBEL FOUNDATION; D. PERRY/UNIVERSITY OF DELAWARE; PURDUE UNIVERSITY; HOKKAIDO UNIVERSITY

Published by AAAS

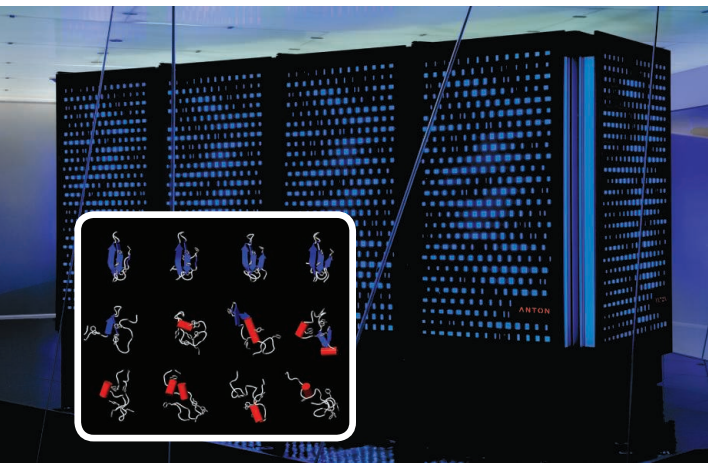

Custom job. By speeding calculations, this Anton supercomputer can run all-atom simulations (*inset*) 100 times longer than can general purpose supercomputers.

relatively simple calculations involved in determining how neighboring atoms in a protein interact. By speeding computations, Shaw says, Anton has run all-atom simulations 100 times longer than general purpose supercomputers can. In the current study, for example, Shaw and his colleagues were able to track 13,564 atoms, comprising a relatively small protein and surrounding water molecules, long enough to see the protein fold and unfold repeatedly.

Like all supercomputers, the Anton used in the current study still has its limits and can't run such lengthy simulations of very large proteins. But Shaw says he and his colleagues are already making progress on that. In addition to building 11 supercomputers incorporating 512 custom-designed computer chip cores, or nodes—Shaw donated one to the National Resource for Biomedical Supercomputing in Pittsburgh, Pennsylvania—Shaw's team has built a 1024-node machine and one with 2048 nodes. The larger machines, he notes, are more efficient tracking the motions of larger proteins. Moreover, Shaw says his team is already building successors to Anton, using the next generation of chip technology to burn through calculations significantly faster. And Shaw says he's happy to be back in the thick of a knotty intellectual challenge: "I love this. It's just the most fun I've ever had. It's very satisfying."

–ROBERT F. SERVICE

mine-tagged benzene as well as one from the olefin, bringing them close enough to pair up. When they do so, they form styrene, the building block of polystyrene plastics. The reacting molecules kick the bromine out into solution and send the palladium on its way to orchestrate another hookup. In the late 1970s, Japanese-born Negishi, who spent the bulk of his career at Purdue University in West Lafayette, Indiana, and Suzuki, of Hokkaido University in Sapporo, Japan, modified the approach, adding different tagging atoms as well as metals to tailor the reaction to make other organic compounds.

Today, the three approaches are collectively known in chemistry parlance as "palladium-catalyzed cross-coupling reactions," and they continue to grow more popular. "Of all methodologies developed over the past 50 years, it is safe to say that palladium-catalyzed cross-coupling methodologies have had the biggest impact on how organic compounds are made," says Eric Jacobsen, an organic chemist at Harvard University. "Cross-coupling methods are now used in all facets of organic synthesis, but nowhere more so than in the pharmaceutical industry, where they are used on a daily basis by nearly every practicing medicinal chemist."

As a result, Jacobsen and other chemists say they were not surprised by the award. "It was just a matter of time for this chemistry to be recognized," says Joseph Francisco, a chemist at Purdue University and the president of the American Chemical Society. Jacobsen says the Nobel Committee could have also chosen any of a few other cross-coupling pioneers, such as Barry Trost of Stanford University. But Nobel rules limit the committee to picking no more than three recipients. "I think they got it right," says Jeremy Berg, who heads the National Institute of General Medical Sciences in Bethesda, Maryland.

For Negishi in particular, the prize is a dream come true. After immigrating to the United States from Japan, Negishi says he had the opportunity to interact with several Nobel Laureates while studying at the University of Pennsylvania. "I began dreaming about this prize half a century ago," Negishi says. At a press conference televised in Japan, Suzuki said he hopes his work will have a similar effect on the next generation. "Japan has no natural resources. Knowledge is all we've got," Suzuki says.

–ROBERT F. SERVICE

With reporting by Dennis Normile in Tokyo.

CREDITS: COURTESY OF MATTHEW MONTEITH; (INSET) COURTESY OF D. E. SHAW RESEARCH

ScienceInsider

From the *Science* Policy Blog

A National Academies' report on how U.S. universities have **managed intellectual property** in the wake of the 1980 Bayh-Dole Act has concluded that things are pretty much hunky-dory but that schools may be trying too hard to cash in on discoveries. Universities instead should aim to disseminate technology for the public good, which may mean passing up a more lucrative licensing deal. http://bit.ly/bayh-dole-update

The U.S. Food and Drug Administration is pressing for a $25 million funding boost for research that can help it **evaluate new treatments** better and faster. Commissioner Margaret Hamburg says such "regulatory science" would allow the agency to help turn the nation's sizable investment in basic biomedical research "into vital products for those who need them." http://bit.ly/fda-research

Israel's minister of education, Gideon Sa'ar, has **fired his chief scientist** for comments that questioned the tenets of evolution and global warming. Gavriel Avital's trial appointment last December had been controversial from the start. http://bit.ly/sacked-adviser

The National Ignition Facility, the highest energy laser in the world, has fired its first shot in what officials at Lawrence Livermore National Laboratory hope will be a successful **campaign to achieve ignition**—a self-sustaining fusion burn that produces more energy than was pumped in to make it happen. http://bit.ly/first-blast

The National Institutes of Health has launched a $60 million program that will allow a few talented **young scientists to become independent investigators** shortly after earning their Ph.D.—provided they can get jobs with institutions willing to nominate them for the award. http://bit.ly/early-independence

The European Union has unveiled a new plan to foster innovation. Officials hope its emphasis on making it easier for companies to actually **use the fruits of science** will bridge a valley of death that slows commercialization. http://bit.ly/innovation-union

For more science policy news, visit **http://news.sciencemag.org/scienceinsider**.

Published by AAAS

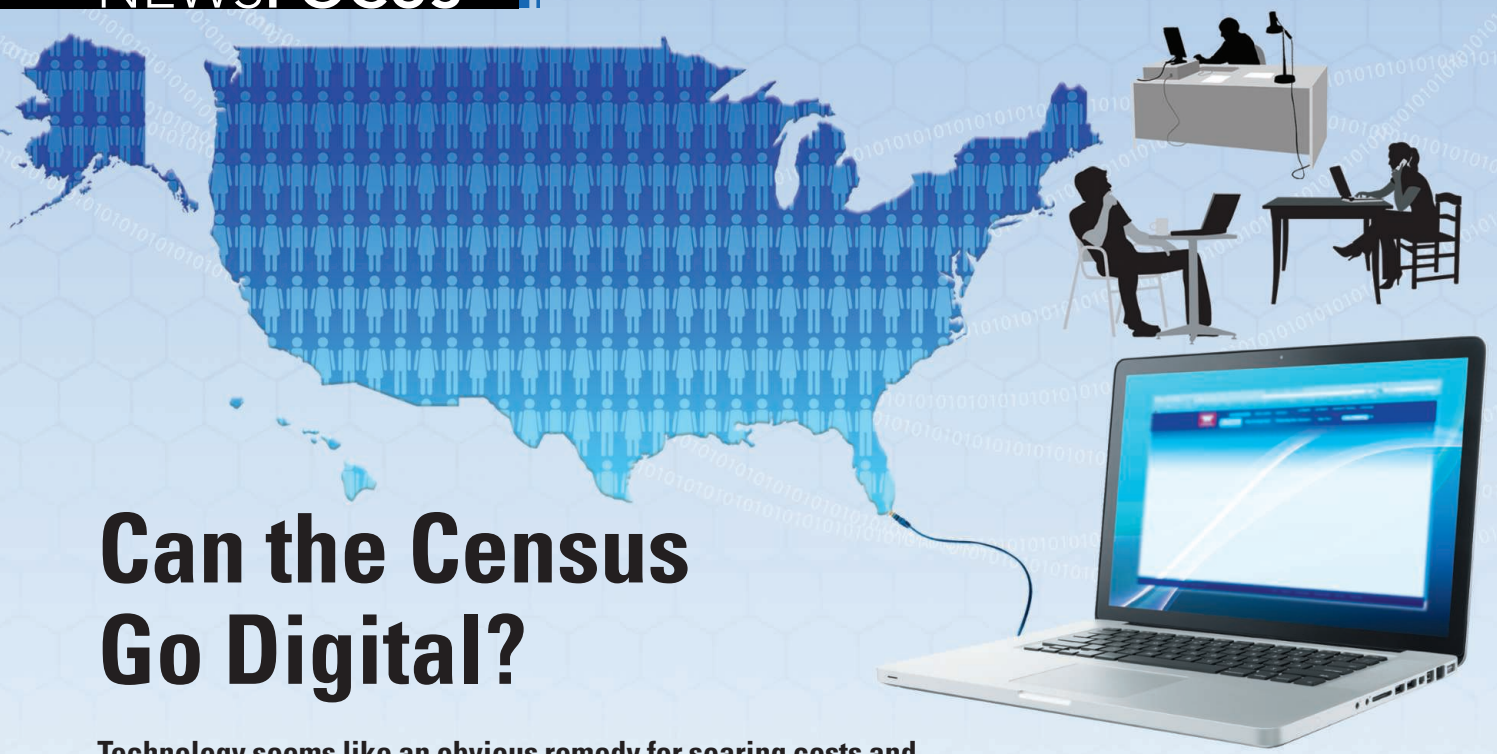

Can the Census Go Digital?

Technology seems like an obvious remedy for soaring costs and privacy concerns. But demographers say the cure to what ails the U.S. census isn't nearly that simple

AFTER KENNETH PREWITT WAS DISMISSED this summer from jury duty, the former director of the U.S. Census Bureau assumed that he wouldn't have to perform this particular civic responsibility again for another 4 years. But the jury foreman had a surprise: New York uses various government databases to form its pool of potential jurors, and Prewitt's name was listed four separate times. For legal reasons, those public agencies can share only small amounts of personal data, making it impossible to determine how many Kenneth Prewitts actually lived in the city.

For Prewitt, a professor of public affairs and vice-president for Global Centers at Columbia University, the ambiguity meant that he could be called again for jury duty any day. But it also highlights a bigger problem for the agency he once headed as it struggles to meet its constitutional mandate to conduct a decennial nose count of the nation. The 2010 census that's winding down will cost U.S. taxpayers $13 billion, a figure that has roughly doubled each of the past two censuses. That staggering sum—it's the most expensive census in the world—has prompted policymakers to ask if there are cheaper and better ways for the Census Bureau to do its job. For instance, why not tap into the vast amount of digital data on U.S. residents already being collected by various state and federal agencies and sitting in computers?

Cold hard data. Director Robert Groves greets local officials in Noorvik, Alaska, to kick off the 2010 census.

But Prewitt's experience shows that using digital data is not as straightforward as it would appear. It also suggests that the Census Bureau must be very careful if it decides to rely on it in the future. For starters, a census can't err on the side of counting someone four times. Data from government agencies also contain more mistakes about individual characteristics—age, race, sex, and so on—than a census can tolerate. In addition, few databases come close to delivering the universal coverage the decennial census demands.

What's more, there are no obvious technical fixes to these problems. Part of the reason is the dearth of research on the topic. Few demographers have access to these databases to examine these questions. And when they do, the research is very expensive because they must sort through enormous volumes of complicated data.

U.S. demographers aren't alone in feeling pressure to come up with a better census. In July, the newly elected coalition government in the United Kingdom announced that it might scrap the 2021 census to save money. (The upcoming 2011 census will cost £480 million.) A few weeks before, Canadian Prime Minister Stephen Harper decreed that the long form to be used in the 2011 census would be voluntary rather than mandatory. Harper never consulted his statistics bureau, Statistics Canada, before making the announcement, which he said was being done in response to privacy concerns. Canada's chief statistician resigned in protest, noting that a voluntary questionnaire would generate results incompatible with those of previous censuses even if the response rate is the same, because the volunteers won't be representative of the entire country. "Censuses around the world are

Published by AAAS

having a hell of a time figuring out a design that will guarantee high levels of data quality but keep costs low," Prewitt observes.

U.S. Census Director Robert Groves has ordered the bureau to determine how a 2010 digital census might compare to the real one. Although results won't be available for at least 2 years, Groves already knows one thing: "I could not guarantee that, if we wanted a 2011 census and we assembled the information from administrative records, that we could do as good a job."

Digital divide

The future of the census isn't simply a concern for government bureaucrats. Its fate affects researchers across many fields. Census results are used by public health officials to study the quality of medical care, by economists to study the economy, and by epidemiologists to determine how common diseases are. As Nancy Krieger, a social epidemiologist at Harvard School of Public Health in Boston who uses census data in her research, says, even "to determine if heart disease mortality is going up or down, or breast cancer rates are going up or down, without census [population] data you have a problem."

While it's not clear that the United States can run a wholly digital census, here's what one might look like. A few months beforehand, the Census Bureau would send workers out with hand-held electronics to update its master address file of all domiciles in the country. These devices would have built-in GPS maps to avoid the need for expensive printed ones, and their ability to record information digitally right away would help avoid problems that arise when blackened bubbles don't (for whatever capricious reason) upload into computers correctly.

The census itself would likely follow one of two tracks. Under one scheme, people would be directed to Web sites to enter details like name, age, and race. That online process would be far more efficient than having the bureau scan mailed-in questionnaires. Respondents could instantly request a form in another language, too, a feature likely to improve the response rate for recent immigrants, a difficult group to tally. Electronic programs would also prompt people to change nonsensical answers—*can someone born in 2003 really be married?*—and correct any arithmetic mistakes.

At this point, the census would have gathered information on most people. Instead of sending workers out to knock on doors to fill in the gaps, the census would mine government databases to fill in gaps and check a respondent's answer if it didn't make sense. This would be especially helpful in places like Alaska, where such follow-up activities can be extremely expensive because of the need to fly around the state. The bureau might still deploy workers with hand-held devices, but far fewer than before. And the hand-helds could be updated in real time, for example, to cancel a visit to someone whose form arrived after the tardy list was compiled.

As a second option, the bureau could decide to use administrative records as the census itself. Alan Zaslavsky, a health statistician at Harvard Medical School in Boston who has advised the Census Bureau, estimates that digital records could gather up to 90% of the data needed without asking anyone any questions. In this case, the Internet form and personal follow-ups would only clear up records with flaws or ambiguities. (The bureau already uses administrative data for between-census updates, but these updates use official census data as a baseline and merely adjust figures up or down.)

However, each step in a digital census would have to overcome serious technical, statistical, or political obstacles. For instance, the planned transition to hand-held electronics for the 2010 U.S. census turned into a costly mess. Forced to buy equipment years in advance because of the extensive preparation time needed, the bureau was stuck with somewhat outdated technology that was slow to upload data and froze frequently. The problems were exacerbated when officials tried to add new features to the devices, like one critical "dashboard" interface, *after* conducting a full-scale dress rehearsal in 2007.

The census finally abandoned the devices for most 2010 fieldwork and reverted to pencils and paper. As for how much the botched effort cost, the bureau says it spent an extra $1.4 billion it received to pay for the transition back to paper and other increased costs.

Prewitt also questions how much money would actually be saved by converting to online response forms. For example, tying someone to an address—so that Jane Q. Public in Hawaii can't get online and claim she lives in Maine—the Census Bureau would have to mail postcards with unique ID numbers to all addresses in the U.S. anyway.

There's a more fundamental problem facing the census that online forms prob-

Soap or Census?

While response rates to population surveys like the census have been sledding downhill for decades, the average person seems less guarded than ever about airing personal details. As Alan Zaslavsky, a health statistician at Harvard Medical School in Boston, puts it, "People provide vast amounts of information about themselves online. They'll fill out a form for a coupon for a $2 box of soap and [provide] about as much as the Census Bureau asks for."

Is Zaslavsky just engaging in hyperbole, or will people really out themselves for nominal discounts on lavatory cleansers? The answer seems to be yes.

The census short form asks for a person's name, date of birth, gender, housing status (own or rent), phone number, address, and race—plus details about those who live with him or her. An online form from Proctor and Gamble promising $1 off Dawn dish soap asked pretty much the same things: name, date of birth, gender, phone number, and address. Scoring an Oil of Olay coupon requires dishing up those details, too.

Neither of those soaps ask for racial data. But an online survey for Tide laundry soap—after pages of interrogating your laundry habits and exact level of awareness of Tide products—does indeed ask for race. And really, there's no reason to pick on soaps. Getting a deal on toiletries or anything else online probably requires trading demographic data. (And at least the census doesn't require e-mail addresses on top of everything else, with invitations to join special census discount clubs.)

This survey of consumer data-gathering was of course unscientific. But in a way, that's the point: Even a cursory look around cyberspace suggests that Zaslavsky is more right than wrong. When it comes to soap or the census, the people choose soap. **–S.K.**

CREDIT: ISTOCKPHOTO.COM

Published by AAAS

Living proof. Census workers began using GPS devices in March 2009 to update the bureau's address list.

CREDIT: U.S. CENSUS BUREAU, PUBLIC INFORMATION OFFICE

ably wouldn't address: decreasing response rates. As with most censuses, there are two parts to the U.S. tally. The short form, which goes out every 10 years to every household, asks about age, race, and other basic demographic characteristics. A longer version, which seeks details about housing, transportation, and other issues, is sent to a much smaller population. In the United States, the American Community Survey is conducted monthly and reaches 3 million households a year (*Science*, 9 April 2010, p. 158).

There's only so much the Census Bureau can do to encourage participation. Despite spending $370 million to publicize this year's census—and despite the fact that failure to participate is illegal and subject to a fine of up to $100—only 72% of the 2010 census forms were returned. The rate dipped below 20% in a few rural U.S. counties. Zaslavsky suspects that people are so bombarded with information nowadays that it is simply easier than in the past to blow off the census, no matter the medium. Paradoxically, people seem generally less guarded about providing information than ever before (see sidebar, p. 311).

Using administrative records would sidestep the low response rates, to be sure. But whacking this mole only causes others to pop up. The Internal Revenue Service (IRS), which has the most promising database because of its wide coverage, often takes a year to process data. That's a nonstarter for the census, which must report to the president by December of each census year. (Using 2019 IRS data for the 2020 census is not an option, either, as it would miss anyone who moved in the intervening year.)

Demographers worry even more about the accuracy of administrative data. The IRS might not know if it had someone's address or age wrong, for instance. Gathering accurate racial data would be even trickier, says John Czajka, a statistician at the think tank Mathematica Policy Research Institute, who has done research on incorporating government data into the census. Federal law requires the census to collect race statistics to monitor (non)compliance with the Voting Rights Act and Civil Rights Act. But few other agencies do. The other major one that does, Czajka notes, is the Social Security Administration, which began collecting it in the pre–Civil Rights era, when racial classifications were cruder.

Another problem is that the census would need to supplement federal data with information collected by local agencies, like those that issue food stamps or birth certificates. These systems are generally not comparable across all 50 states, Czajka says. For instance, he has found strong evidence in his research that local offices in different areas that perform the same function will tabulate race in different ways. So there is often no consistent methodology for gathering such data, making it useless for a census.

Even if data from other agencies are trustworthy, demographers worry that it may be patchy. The IRS, for example, would have little data about people who pay no taxes (e.g., many students and the very poor), and agencies for education or housing would have similar blind spots.

Those blind spots come on top of the existing shortcomings of most censuses. Many undercount immigrants and minorities, especially the urban poor. (Demographers learned this by borrowing a trick from ecologists, called capture-tag-recapture, in which they interview people in urban neighborhoods, then return to see how many of the same people they meet again.) But demographers have studied these shortcomings for decades and can at least correct the biases. With administrative data, no one yet knows how to quantify the biases.

The nation's denominator

Some European countries, including Sweden, the Netherlands, and Denmark, have met these challenges by forming a strong central registry that collates data from other agencies and keeps a master file on each person. Demographers salivate over these registries—not only because they make population counts much easier, but because they offer enhanced research opportunities.

"I'm jealous as can be of what the Nordic countries do with their data," says Michael Marmot, an epidemiologist at University College London who has worked on population data with the World Health Organization. He'd like to see the United Kingdom build a registry and then compare it to the results of a traditional 2021 census. If the registry looks accurate, he says he would feel comfortable letting the census die.

Setting up such a registry would be politically unpopular in many Western nations, however. Requiring residents to notify the government every time they move or change jobs "might be regarded as extreme," says Ivan Fellegi, the longtime head of Statistics Canada who retired in 2008. In fact, those privacy concerns led the U.K. government recently to scrap its plans for a national ID system, a necessary precursor to a registry. Echoing those concerns, in August the Republican National Committee passed a resolution comparing the census to "a scam artist … asking very personal questions and using fear of penalties to manipulate the respondent to answer."

While political leaders debate the future of the census, scientists who rely on its data sit and wait, hoping that budget cuts or changes in methodology won't unravel their research. Even simple measures of public health become fraught to calculate when census error bars expand. Says Krieger, "Whenever you have a rate of disease or mortality, it's always a numerator divided by a denominator. And in the U.S. the denominator for mortality rates and many disease rates comes from the census."

–SAM KEAN

Published by AAAS

ZOONOSES

In China's Backcountry, Tracking Lethal Bird Flu

Five years after flu devastated wild birds in China, researchers have confirmed one likely transmission route

QINGHAI LAKE, CHINA—The lake glitters like a sapphire under a blue sky as birds circle near the shore. On the rocky beach, two researchers are tying a GPS transmitter to the back of a small gray duck. They will track its migration by satellite, part of a series of investigations that began after highly pathogenic avian influenza (H5N1 subtype) first swept the region in 2005.

The studies aim to pinpoint the viral reservoir and the role that wild birds play in transmission. "The lake has attracted the whole world's researchers to keep a close eye on it," says He Yubang, vice director of Administration of Qinghai Lake Chinese National Nature Reserve. No reservoir has yet been found, but transmission routes have come into clearer focus.

The emergence of H5N1 was a disaster for wildlife and humans alike. Since 2003, H5N1 has killed 300 people, including 18 so far this year, according to the World Health Organization. More than 250 million infected domestic poultry have been culled, and thousands of wild birds have been felled. In 2005 alone, more than 6000 wild birds at Qinghai Lake died, "the single largest H5N1 wild bird mortality event that has ever occurred," says Scott Newman, an animal health officer for the UN Food and Agriculture Organization (FAO) in Rome.

H5N1 was first isolated in 1996 from a domestic goose in China's Guangdong Province. The next year, the virus spread to people in Hong Kong. After laying low, H5N1 flared in 2004 in several Asian nations. It kills about 60% those infected but does not spread easily from person to person. The virus has been held in check by poultry vaccination and better husbandry, but 16 countries, including China and Romania, have reported H5N1 outbreaks in poultry so far this year. A constant worry is that the virus will mutate into a more transmissible form among humans.

Because Qinghai Lake sits within the eastern portion of the Central Asian Flyway—which reaches from India and Bangladesh to Russia—some experts suspect it is a focal point of viral transmission. Others question whether wild birds play a major role in H5N1 dispersal, suggesting that the virus spreads primarily among poultry (*Science*, 21 October 2005, p. 426). To date, all human cases but one have been associated with exposure to poultry or found on farms. Researchers now believe that wild waterfowl on the eastern portion of the Central Asian Flyway help spread H5N1 into Mongolia each spring as they move across the Qinghai-Tibetan plateau to the north and east, says Newman. The role of wild waterfowl on the other major flyway is less certain.

Poultry production is on the rise in Asia, as are farming, trade, and the mixing of wild and domestic birds. "All of them are increasing the opportunities for viral transmission and persistence," says Xiao Xiangming, a landscape ecologist and remote sensing expert at the University of Oklahoma, Norman.

Every summer, more than 100,000 migratory birds descend on Qinghai Lake, China's largest inland body of salt water. Half the birds that died here in 2005 were bar-headed geese (*Anser indicus*), says Lei Fu-Min, an ornithologist at the Institute of Zoology of the Chinese Academy of Sciences. Yan Baoping, chief engineer at the Computer Network Information Center in Beijing, led an academy team that set up a monitoring network after the die-off. The next year international scientists joined the effort. To date, the team led by FAO and the U.S. Geological Survey has tracked more than 525 waterfowl from 24 species in 11 countries.

In the past 5 years, the involvement of wild birds has become clearer, Lei says. "The H5N1 strains from wild birds that subsequently arrived in Asia and Eastern Europe were most like the H5N1 strains of Qinghai Lake," far from large poultry farms, he says. GPS data on migration paths are now being used for the first time to explore the relationships between different groups of birds and their interactions with domestic fowl, says Diann Prosser, a biologist at USGS's Patuxent Wildlife Research Center in Beltsville, Maryland. This year, she says, researchers learned that the majority of bar-headed geese tagged at Qinghai spend their winters in the Lhasa region of Tibet, south of the lake. These wintering grounds have domestic poultry and captive bar-headed goose farms—and H5N1 outbreaks have been reported there, suggesting a path for the virus to move from captive to wild birds.

Southeast of Lhasa, the ruddy shelduck may help explain the virus's spread, says John Takekawa, an ecologist at USGS's Western Ecological Research Center. In autumn and winter the ducks gather at Poyang Lake in the lower reaches of the Yangtze River within the East Asia Flyway (*Science*, 23 October 2009, p. 508). Qinghai strains can be traced to one early strain from Poyang based on the genomic analysis, Lei said. But recent work suggests that the viral reservoir may lie farther to the north, in Siberia—an area shared by both major Asian flyways—or that another as-yet-unstudied migratory bird may be carrying the virus from lake to lake. Since 2006, Xiao has led an international team to develop an early-warning system for H5N1 in Asia, focusing on agricultural and ecological risk factors.

Researchers need a better understanding of wild bird distribution, habitat use, and daily movements, Newman says. And the human role—including population growth and urbanization—must be better accounted for, says Takekawa. Why some people exposed to the virus become infected and others do not "is still an unsolved question," says Shu Yuelong, director of the National Influenza Center of the Chinese Center for Disease Control and Prevention. China has launched a nationwide monitoring network to check poultry markets for H5N1. That's a good start, but what's needed is a global network, says Shu. It must get started now, he says, "without delay."

–LI JIAO

Li Jiao is a writer in Beijing.

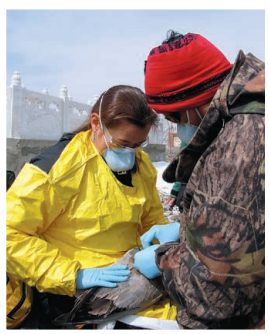

Mixing bowl. Scientists track birds entering and leaving Qinghai Lake with GPS transmitters.

CREDITS (TOP TO BOTTOM): HOU YUANSHENG; YANG TAO/COMPUTER NETWORK INFORMATION CENTER

Published by AAAS

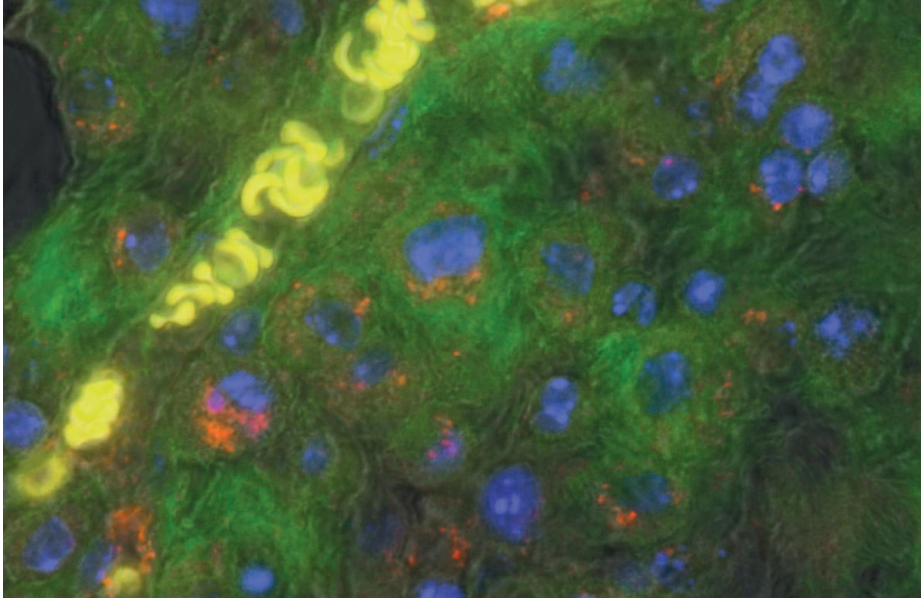

On target. Red blood cells (yellow) ferry nanoparticles (red) containing a chemotherapy drug to tumor tissue (green) in a mouse. Nanoparticles shield normal cells from chemotherapy toxins and deliver higher doses to tumors.

CREDIT: COURTESY OF CERULEAN PHARMA INC.

NANOTECHNOLOGY

Nanoparticle Trojan Horses Gallop From the Lab Into the Clinic

Experimental cancer treatments aim to deliver toxic medicines to cells inside packages that protect normal tissues and evade the body's immune system

In the early 1990s, Mark Davis's career was thriving. As a chemical engineer at the California Institute of Technology (Caltech) in Pasadena, Davis pioneered work on catalysts called zeolites. Then in 1995, his wife, Mary, was diagnosed with breast cancer and his research interests took a sharp turn.

After a mastectomy, Mary's oncologist recommended chemotherapy with a medicine nicknamed the Red Death because its toxic side effects are so debilitating. The surgery and medication worked: Mary's cancer is in remission. During a treatment, she made an offhand comment to Mark that there had to be a better way to design chemotherapy drugs so others wouldn't have to endure what she had to go through. He took the comment to heart and in 1996 turned part of his lab over to engineering nanoparticles to ferry toxins into tumor cells before they release their cargo. Now, 14 years later, one of Davis's compounds has been picked up by a Cambridge, Massachusetts–based company called Cerulean Pharma that is now in the middle of a midstage clinical trial to measure its safety and establish doses for combating various cancers.

Davis's novel nanoparticle-based medicine is not the only one under development. After many years of studies with cell cultures and animals, nearly a dozen nanoparticle-based drugs are in clinical trials, most of which aim at treating or diagnosing cancer. Many other compounds are progressing through preclinical studies and are nearing human trials. "There is a continuous pipeline" with numerous nanomedicine compounds at each stage of development, says Piotr Grodzinski, who directs the National Cancer Institute's Alliance for Nanotechnology in Cancer in Bethesda, Maryland. Grodzinski, Davis, and others underscore that it will require several more years of testing to determine whether the compounds are safe and effective. However, Davis says, "I'm very optimistic. I think the potential is very high to have some good results."

That would be welcome news in the fight against cancer. Despite a decades-long "war" on the disease, the number of people diagnosed remains stubbornly high. In the United States alone, more than 1.3 million people this year will be diagnosed with cancer, and more than 550,000 will die from it. Overall, the rate of death among those who contract cancer has barely changed since 1950. There has been progress, Grodzinski acknowledges. Researchers know far more about the myriad different tumor types and about molecular hallmarks of some forms of the disease, and few novel treatments have earned widespread attention. Still, today most cancers are treated with the same blunt instruments of surgery, radiation, and harsh chemotherapy that oncologists have wielded for decades. And of the chemotherapies available to patients, many are as toxic to normal cells as they are to cancer cells.

Nanomedicines have the potential to change that, Grodzinski says, because unlike traditional medicines they can be engineered to optimize several different functions. To treat cancer, a medicine must not only kill tumor cells but also be soluble in water in order to travel through the bloodstream; it must evade immune cell sentries and avoid being cleared out by the liver or kidneys; and it must find its targets. Traditional medicines have to build all these functions into single molecules. Nanomedicines, by contrast, can divide them among different components. Particle surfaces can be tailored for solubility, friendliness to immune cells, and target-seeking ability, while the particles' cargoes can be tailored to kill tumor cells.

That was the hope, anyway, more than a decade ago when Davis and other researchers first looked into nanoparticle-based medicines. The field received widespread hype early on, and a handful of compounds made it all the way to market. In 2005, for example, the U.S. Food and Drug Administration approved Abraxane for treating metastatic breast cancer. The compound is simply a conventional anticancer compound called paclitaxel—better known by its trademarked name, Taxol—linked to a common blood protein called albumin. The albumin shields the paclitaxel, increasing its solubility and circulation time and giving it a greater chance of winding up in tumor cells. In addition to proving effective in fighting metastatic breast cancer, Abraxane is now in a phase III clinical trial for treating advanced lung cancer and in phase II trials against pancreatic cancer and melanoma. A handful of other compounds, packaged in lipid vessels called liposomes or combined with biofriendly polymers, have also made it to market. Those successes have the field booming. Grodzinski says more than 50 companies are developing nanoparticle-based medicines as diagnostics and treatments for cancer alone; 34 of them formed in the past 4 years.

Most early successes have been very simple drug carriers; many next-generation nanoparticles are more complex. In December, for example, Bind Biosciences in Cambridge, Massachusetts, expects to launch a phase I clinical trial of nanoparticle carriers made from a trio of biodegradable polymers abbreviated PLA, PLGA, and PEG. PLA and PLGA are the polymers currently

Published by AAAS

Some Nano-Oncology Drugs in Clinical Trials

COMPANY	AGENT	INDICATION	STATUS
Cerulean Pharma	Cyclodextrin NPs/Camptothecin	Various cancers	Phase 2
Calando Pharmaceuticals	Cyclodextrin NPs/siRNA	Solid tumors	Phase 1
Alnylam Pharmaceuticals	Lipid NP/siRNA	Liver cancer	Phase 1
BIND Biosciences	PLGA/PLA NPs/Docetaxel	Prostate cancer and others	Phase 1, Dec. 2010
Memgen	Adenovirus NPs/Tumor necrosis Factor (TNF)	Chronic lymphocytic leukemia	Phase 1
CytImmune Sciences	Gold NP/TNF	Solid tumors	Phase 1
Nanospectra Biosciences	Gold-coated silica NPs	Head and neck cancer	Phase 1

On trial. Several first-generation nanomedicines have already made it to market. Now, more than 50 companies are working to bring second-generation nanomedicines to market. A dozen such nanoparticles (NPs) are in clinical trials, most for treating, imaging, and diagnosing cancer.

used to make biodegradable sutures; PEG helps shield the particles from being recognized and cleared by immune cells. The combination was originally developed by Robert Langer, a chemical and biomedical engineer at the Massachusetts Institute of Technology, and colleagues. In recent work, Langer's team incorporated the anticancer compound docetaxel into the PLGA polymer matrix and added a targeting molecule that seeks out prostate-specific membrane antigen, a protein expressed on the surface of prostate cancer cells and other types of solid tumor cells. According to Bind's CEO Scott Minick, animal trials showed that the combination of the targeting compound and slow release of the docetaxel by degrading nanoparticles increases the tumor cell concentration of the anticancer drug 20-fold over docetaxel packaged in conventional liposomes. Moreover, Langer notes that the byproducts of the polymer are lactic acid and glycolic acid, naturally occurring substances safe to the body.

Other groups are working on variations on the strategy. Davis's and Cerulean's particles, for example, are engineered to degrade over time while leaving their building blocks intact. The shell of the particles, Davis explains, is made from sugars called cyclodextrins coated with PEG. These sugars contain hydroxyl groups that bind readily with water, making them—and the particles—highly soluble. But once they are inside tumor cells, the acidic environment there breaks the cyclodextrin particles and PEG apart, releasing an anticancer compound called camptothecin. The remaining fragments of the cyclodextrin are small enough to be cleared by the cells and the kidney. In August, at the American Chemical Society meeting in Boston, Cerulean researchers reported that initial results from a phase I trial showed that patients tolerated the compound well, and in several patients with advanced, progressive cancer, the disease stabilized for more than 6 months. Those results are encouraging, says Cerulean's senior vice president for research and business operations, Alexandra Glucksmann, because previous trials showed that giving patients camptothecin alone was too toxic. "This gives us the opportunity to rescue drugs that have failed before," Glucksmann says.

Nanoparticles are also being harnessed for less-traditional therapies. Numerous teams are using them to package tiny snippets of specific RNA molecules, in the hope that they can enter tumor cells and kill them by binding to the cells' own RNA molecules required for building essential proteins. This strategy, known as antisense, became a white-hot field in the early 2000s, when numerous teams developed antisense RNAs to block proteins critical to a variety of diseases. Numerous clinical trials using this strategy to kill cancer cells failed, however, primarily because researchers injected antisense RNA directly into patients' bloodstreams, where it was quickly chopped up by enzymes and cleared. "For RNA, nanoparticles are enabling, because delivery is such a key issue," Langer says.

An early clinical trial underscores this hope. In the 15 April issue of *Nature*, Davis and researchers at Calando Pharmaceuticals in Pasadena, California, and several other institutions reported the first results from an initial human clinical trial with nanoparticles packed with RNA designed to target melanoma tumor cells and interfere with critical protein production. The RNA-packed nanoparticles readily penetrated tumor cells, where they blocked the RNA target for a gene called *RRM2* that cancer cells need to multiply. The trial wasn't intended to gauge the particles' efficacy, but Davis says the early results look promising.

A very different approach to making nanoparticles may also soon revolutionize the way common vaccines are made and delivered. The work builds on progress by Joseph DeSimone and colleagues at the University of North Carolina, Chapel Hill, in using computer chip manufacturing techniques to make nanoparticle medicines. DeSimone's group came up with a sort of nano–cookie cutter approach to mold virtually any organic compound into nanoparticles of whatever size, shape, and stiffness they want. Along the way they found that making such changes yielded big results. Stiff nanoparticles injected into animals, for example, are cleared within as little as 2 hours. But soft, flexible ones circulate for 93 hours. Similarly, cylindrical particles have a knack for getting inside cells far more readily than spheres do. In animal studies, DeSimone says, as many as 15% of the particles they inject can find their way inside tumor cells, compared with about 5% for conventional spherical liposomes.

DeSimone recently launched a company called Liquidia to commercialize the technology. Liquidia is working to deliver particles packed with anticancer drugs and RNA. But in an initial clinical trial, likely to begin later this year, the company intends to deliver particles shaped like pathogenic bacteria to carry influenza proteins already used in vaccines. Animals injected with pathogen-shaped particles produce antibody titers as much as 10 times as high as animals dosed with conventional vaccines, DeSimone says. Working with flu proteins that are already part of conventional vaccines could also help Liquidia get its initial vaccines to market more quickly. "We think it's just a beachhead" and that many other products will soon follow, DeSimone says. **–ROBERT F. SERVICE**

Online
sciencemag.org
Podcast interview with author Robert Service.

Published by AAAS

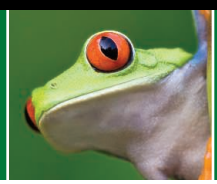

LETTERS

edited by Jennifer Sills

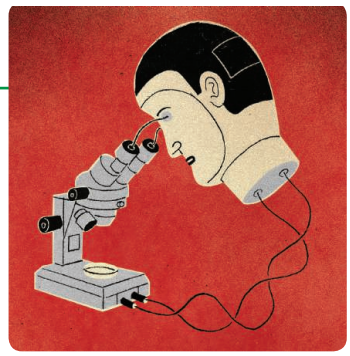

Machine Science: The Human Side

J. EVANS AND A. RZHETSKY ("MACHINE SCIENCE," PERSPECTIVES, 23 July, p. 399) misrepresent the crucial role played by humans in using computational tools for automated hypothesis generation. There is no doubt, as they argue, that text mining software and networks of concepts such as those captured by bio-ontologies greatly increase researchers' ability to mine huge masses of data, compare concepts used across scientific fields, and, ultimately, generate new hypotheses (*1*, *2*). However, both the development and the effective use of these tools are strongly dependent on researchers' understanding of their scientific fields and the data being mined.

For instance, building bio-ontologies that adequately represent the concepts and relations used within specific communities requires huge efforts of curation (*3*, *4*). In turn, for researchers to use such ontologies for the purposes of discovery, they must understand how the ontologies were constructed and the choices curators have made in selecting the relevant structures and concepts (*5*). Without such understanding, researchers are likely to misclassify or misinterpret results. It is thus misleading and unhelpful to equate the effective use of computational tools with the ideal of full automation, as Evans and Rzhetsky have done. Rather, researchers using computational tools should be as aware as possible of the human interventions and assumptions built into those systems, so as to be able to interpret the biological significance of results obtained through these tools and, when needed, to challenge and/or update the assumptions that they incorporate.

SABINA LEONELLI

ESRC Centre for Genomics in Society, University of Exeter, EX4 4PJ Exeter, UK. E-mail: s.leonelli@exeter.ac.uk

References

1. L. D. Stein, *Nat. Rev. Genet.* **9**, 678 (2008).
2. T. Hey, S. Tansley, K. Tolle, Eds., *The Fourth Paradigm: Data-Intensive Scientific Discovery* (Microsoft Research, Redmond, WA, 2009); http://research.microsoft.com/en-us/collaboration/fourthparadigm.
3. D. Howe, S. Y. Rhee, *Nature* **455**, 47 (2008).
4. S. Leonelli, *Biol. Theory* **3**, 8 (2008).
5. S. Leonelli, in *How Well Do Facts Travel? The Dissemination of Reliable Knowledge*, P. Howlett, M. S. Morgan, Eds. (Cambridge Univ. Press, Cambridge, 2010).

Machine Science: Truly Machine-Aided Science

THE PERSPECTIVE BY J. EVANS AND A. Rzhetsky ("Machine science," 23 July, p. 399) implies that the next Einstein could be a computer. During the past centuries, the epistemological debates on the scientific trends and revolutionary aspects in the scientific breakthroughs of every century showed the centrality of the investigators and their impressive capabilities (and sometimes their luck). The use of computer-aided simulations and analysis has been an important part of modern science; technological developments have led to shorter computational times and the opportunity for scientists to develop an increased number of simulations, mathematical models, and scientific calculi.

However, despite the effectiveness of computer tools, the centrality of the researchers has not changed in science. Scientists define the computation of models, the analysis of data, and the validation of scientific hypotheses, as well as the guidelines for ad hoc software and large-scale computations. Technology is a useful tool for the scientists, but it cannot solve open problems such as the Riemann Conjecture.

"Machine science" could more accurately be considered "machine-aided science." Science will not fundamentally change until a machine can produce results or solve open problems without human direction. The Perspective describes our current scientific methodology, not the beginning of a new scientific era.

FRANCESCO GIANFELICI

Department of Health Science and Technology, Faculty of Engineering, Science, and Medicine, Aalborg University, Fredrik Bajers Vej 7E-4, DK-9220 Aalborg E, Denmark. E-mail: frgianf@hst.aau.dk

Machine Science: What's Missing

MUCH IS MISSING IN J. EVANS AND A. Rzhetsky's Perspective "Machine science" (23 July, p. 399), which needs to be placed within a broader understanding of scientific practice. Recent discussions of data-driven science are misrepresented. Far from "conjectur[ing] that hypotheses are obsolete," Golub writes that "hypothesis-driven, experimental research should remain central" (*1*), and we write that "hypothesis generation and testing are important to science at many points in a wider topography of inquiry" (*2*). Leroy Hood, a proponent of

Letters to the Editor

Letters (~300 words) discuss material published in *Science* in the previous 3 months or issues of general interest. They can be submitted through the Web (www.submit2science.org) or by regular mail (1200 New York Ave., NW, Washington, DC 20005, USA). Letters are not acknowledged upon receipt, nor are authors generally consulted before publication. Whether published in full or in part, letters are subject to editing for clarity and space.

Published by AAAS

discovery science, also acknowledges the role of "high-quality hypothesis-driven biology" (*3*). These sources and many others emphasize iterative feedback between hypothesis testing and a broader process of data-driven, technology-oriented, question-forming and generally "exploratory" inquiry, which provides the very context for ongoing hypothesis formulation and testing (*2*).

By focusing on the computational generation and selection of simplified lego-like hypotheses, Evans and Rzhetsky rip scientific practice out of this context. Even the simplest hypotheses are generated within a complex system of not only discovery-oriented activities, but also human actors with intuition and expertise, disciplinary traditions, social norms, funding structures, and anticipation of future research directions. The specific modes of research that are most appropriate, and the iterative relationships between those modes, will vary according to these contextual factors. Automated analysis can indeed be useful, but many of the most interesting scientific questions involve determining the circumstances under which such analysis works best and how discovery-oriented research modes intersect with other modes, including hypothesis testing. Machine science misrepresents and misleads when removed from this multidimensional understanding of practice.

CHRIS HAUFE,[1]* KEVIN C. ELLIOTT,[2] RICHARD M. BURIAN,[3] MAUREEN A. O'MALLEY[4]

[1]Department of Philosophy, University of Chicago, Chicago, IL 60637, USA. [2]Department of Philosophy, University of South Carolina, Columbia, SC 29208, USA. [3]Department of Philosophy, Virginia Tech, Blacksburg, VA 24061, USA. [4]Egenis, Byrne House, University of Exeter, Exeter, UK.

*To whom correspondence should be addressed. E-mail: haufe@uchicago.edu

References

1. T. Golub, *Nature* **464**, 679 (2010).
2. M. A. O'Malley *et al.*, *Cell* **138**, 611 (2009).
3. C. Auffray, Z. Chen, L. Hood, *Genome Med.* **1**, 2 (2009).

Response

LEONELLI AND GIANFELICI MISINTERPRET OUR Perspective as a call for the "full automation" of science. The approach we describe advocates a symbiotic partnership between scientists and machines (*1*) to make scientists and science much more productive. Our title "Machine science" emphasizes that computation is expanding beyond data analysis and entering hypothesis generation, becoming part of the scientific creative process, not unlike computer-aided design (CAD) tools used in present-day engineering. As computational approaches to the synthesis of hypotheses mature, a new generation of scientists will be trained to develop and operate them and to screen for those most novel

and fruitful. As it seems improbable to claim that CAD simulations and design suggestions have left architecture and integrated-circuit design unchanged, we disagree that nothing will change in science with the rise of intellectual "design tools." But how will the activity of human scientists change?

Leonelli argues that computational tools through which scientists develop new hypotheses involve human assumptions, decision-making, and error. We agree, and suggest that human assumptions and biases are the very phenomenon that should be measured, modeled, and used as instruments to generate entire new classes of fruitful hypotheses. In our Perspective, we described exploiting knowledge about the social and linguistic disconnect between scientific communities. We and others have also explored patterns by which scientists prematurely converge to consensus (*2*, *3*), and the implicit rules by which scientists select new topics and journals publish new research (*4*, *5*). We argue that computation can help researchers systematically identify fruitful paths not taken.

Gianfelici argues that the "next Einstein" will not be a computer. Our question is: What problems will the next Einstein pose and solve with computational support (*6*, *7*) that he or she could not consider or unravel without it? In 1997, IBM's Deep Blue defeated grand master Garry Kasparov in a chess competition. We can conceive of future scientists as Deep Blue–enhanced Kasparovs solving seemingly impenetrable chess puzzles from nature (*8*, *9*). We argue that with the advancement of computational approaches to hypothesis generation, the most effective scientists will not only craft specific empirical conjectures, but will generalize the logic of those conjectures into novel algorithms that can generate entire new classes of hypotheses. In short, rather than assuming that scientists become irrelevant in a world of computational hypothesis generation—the Luddite fallacy (*10*)—we argue that computation will free them to become more productive and more central to a growing enterprise.

Haufe argues that we misrepresent the vision of high-throughput data science, which reserves a hallowed place for focused, hypothesis-driven investigations. We acknowledge that we could not do justice to the diversity and complexity of data-driven perspectives in our brief essay. Perhaps the strongest disagreement within this community is not whether hypotheses are useful, but whether they should be invoked before or after the data are collected (or both) (*11*). One view is represented by a "nearly hypothesis-neutral" approach, such as genome-wide association (GWA) studies that group patients by phenotype and then compare genomic variation to identify genetic loci putatively associated with the disease. Because these studies involve numerous statistical tests, there is often not enough statistical power to identify many loci, including those with known association with the phenotype. In the case of GWA, computationally generated hypotheses would constrain the search space, alleviating the multiple-test problem. We argue that by using computation to generate hypotheses, the scientific community could focus the scope of their investigations, learn much more, and advance faster with the same high-throughput experimental resources available today.

JAMES A. EVANS[1,2]* AND ANDREY RZHETSKY[2,3]

[1]Department of Sociology, University of Chicago, Chicago, IL 60637, USA. [2]Computation Institute, University of Chicago, Chicago, IL 60637, USA. [3]Department of Medicine, University of Chicago, Chicago, IL 60637, USA.

*To whom correspondence should be addressed. E-mail: jevans@uchicago.edu

References

1. J. C. R. Licklider, *IRE Trans. Human Factors Electron.* **1**, 4 (1960).
2. A. Rzhetsky, I. Iossifov, J. M. Loh, K. P. White, *Proc. Natl. Acad. Sci. U.S.A.* **103**, 4940 (2006).
3. S. A. Greenberg, *Br. Med. J.* **339**, b2680 (2009).
4. M. Cokol, R. Rodriguez-Esteban, A. Rzhetsky, *Genome Biol.* **8**, 406 (2007).
5. J. A. Evans, *Am. J. Soc.* **116**, 389 (2010).
6. M. Schmidt, H. Lipson, *Science* **324**, 81 (2009).
7. J. Bongard, H. Lipson, *Proc. Natl. Acad. Sci. U.S.A.* **104**, 9943 (2007).
8. D. Rasskin-Gutman, *Chess Metaphors: Artificial Intelligence and the Human Mind* (MIT Press, Cambridge, MA, 2009).
9. G. Kasparov, *The Chess Master and the Computer* (New York Review of Books, New York, 2010).
10. W. Easterly, The Elusive Quest for Growth: Economists' Adventures and Misadventures in the Tropics (MIT Press, Cambridge, MA, 2001).
11. T. Hey, S. Tansley, K. Tolle, Eds., *The Fourth Paradigm: Data-Intensive Scientific Discovery* (Microsoft Research, Redmond, WA, 2009).

CORRECTIONS AND CLARIFICATIONS

Perspectives: "Feasting on minerals" by D. K. Newman (12 February, p. 793). The second figure reproduced errors found in the *BMC Genomics* figure from which it was adapted. In the corrected version (shown here), the direction of the arrow through the aa3 membrane protein has been reversed and ATPase has been changed to ATPsyn. The corrected caption is "Electron transfer in *Acidithiobacillus ferrooxidans*. Fe(II) is oxidized to Fe(III) by proteins on the cell surface. These proteins transfer electrons from Fe(II) to other parts of the respiratory chain, leading to the generation of an energized membrane in the cell. This energy is used to generate metabolites necessary for growth and other cellular functions. ATP, adenosine 5′-triphosphate; ADP, adenosine 5′-diphosphate; Pi, inorganic phosphate; NAD^+ and NADH, oxidized and reduced forms of nicotinamide adenine dinucleotide; NDH1, NADH:ubiquinone oxidoreductase; bc1 complex, ubiquinol:cytochrome c oxidoreductase; aa3, cytochrome oxidase; CtaTAB, likely involved in heme sythesis and export to cytochrome oxidase; ATPsyn, ATP synthase catalyzes ATP synthesis. [Adapted from figure 1 in (*10*)]"

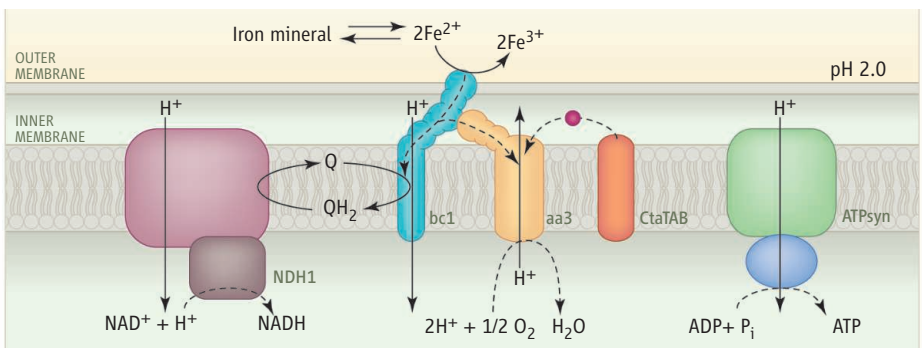

TECHNICAL COMMENT ABSTRACTS

Comment on "Narrow Primary Feather Rachises in *Confuciusornis* and *Archaeopteryx* Suggest Poor Flight Ability"

Gregory S. Paul

Nudds and Dyke (Reports, 14 May 2010, p. 887) reported that the primary features of the early birds *Archaeopteryx* and *Confuciusornis* were too weak to power flight. This conclusion is not supported because the authors overestimated the mass of the subjects and understated the strength of the primary shafts in at least one example. The total biology of the birds indicates that they could achieve flapping flight.

Full text at www.sciencemag.org/cgi/content/full/330/6002/320-b

Comment on "Narrow Primary Feather Rachises in *Confuciusornis* and *Archaeopteryx* Suggest Poor Flight Ability"

Xiaoting Zheng, Xing Xu, Zhonghe Zhou, Desui Miao, Fucheng Zhang

Nudds and Dyke (Reports, 14 May 2010, p. 887) compared the rachis diameters of the primary feathers of *Archaeopteryx* and *Confuciusornis* to those of modern birds and found that the primary feathers of these two basal birds were too weak to support sustained flight. Our measurements of *Confuciusornis* specimens suggest that their conclusions need to be further evaluated.

Full text at www.sciencemag.org/cgi/content/full/330/6002/320-c

Response to Comments on "Narrow Primary Feather Rachises in *Confuciusornis* and *Archaeopteryx* Suggest Poor Flight Ability"

Robert L. Nudds and Gareth J. Dyke

Paul and Zheng *et al.* challenge our conclusions regarding the flight of *Confuciusornis* and *Archaeopteryx*, which derive from our method of assessing flight ability from estimated feather strength. They suggest that our mass and rachis data for these fossil birds are incorrect. Neither comment, however, invalidates our method nor alters conclusions of poor flight ability based upon our original data. We encourage researchers to use our method before critiquing our conclusions regarding early bird flight.

Full text at www.sciencemag.org/cgi/content/full/330/6002/320-d

Comment on "Narrow Primary Feather Rachises in *Confuciusornis* and *Archaeopteryx* Suggest Poor Flight Ability"

Gregory S. Paul

Nudds and Dyke (Reports, 14 May 2010, p. 887) reported that the primary features of the early birds *Archaeopteryx* and *Confuciusornis* were too weak to power flight. This conclusion is not supported because the authors overestimated the mass of the subjects and understated the strength of the primary shafts in at least one example. The total biology of the birds indicates that they could achieve flapping flight.

In their attempt to estimate the aerial performance of the early birds *Archaeopteryx* and *Confuciusornis* based on the strength of their primary feathers, Nudds and Dyke (*1*) correctly observe that accurate body mass estimates are crucial to their calculations that flight feathers were not strong enough for powered flight. However, they used excessive mass values that underestimated the flight potential of the ancient fliers. They also did not test their methods by estimating the mass and feather strength of derived fossil avians with more highly developed flight adaptations.

A number of problems prevent restoring the flight of *Archaeopteryx* using feather shaft dimensions. The absence of feathers adorning the largest skeleton, the Solnhofen specimen weighing a little over half a kilogram with a 68-mm-long femur, bars assessing the fully mature aerial abilities of the adults. Other specimens are juveniles whose mass varies by a factor of more than 7 (*2*, *3*). With a 46-mm-long femur, the Munich specimen examined by Nudds and Dyke (*1*) is a small juvenile of just ~140 g (*2*, *4*). A same-scale comparison confirms that it is not possible for it to have weighed as much as a pigeon (Fig. 1, A and C) as assumed by Nudds and Dyke, who incorrectly applied the quarter kilogram that a number of researchers agree was the mass of the much larger-bodied Berlin specimen (*1*–*6*) to the little juvenile. The primary feathers of the Munich specimen are poorly preserved. Nudds and Dyke did not provide high-resolution images showing that the shaft base diameter of the longest primary is only 0.75 mm, and I cannot confirm such a low value using large-format, high-resolution photographs of the Munich slabs. Somewhat more medial primary shafts measuring 1.25 to 1.4 mm across at shaft mid-length are clearly present (Fig. 2), and those rachises were probably even more robust at their bases. The rachises of the Berlin specimen's well-preserved primaries do not show evidence of becoming more slender progressing laterally toward the outer wing, and the maximal diameter of the proximal shafts is obscured by other feathers (*7*). The buckling resistance of the longest outer primaries therefore cannot be estimated in any *Archaeopteryx*, but the thickness of some of the primary rachises of the Munich juvenile combined with its low mass indicate that its immature wings were strong enough for flapping flight, and the flight capacity of adults may have been much better.

Lacking high-resolution images of the well-preserved, unobscured proximal shafts of the longest primaries of *Confuciusornis,* the 1.2-mm average diameter reported by Nudds and Dyke is not sufficiently documented. The mass of the specimen in figure 1A in (*1*) could not have been close to the authors' estimate of 0.5 kg, which equals the weight of some teals and ducks (*8*–*10*). Instead, at ~180 g, the shallow-bodied basal bird was intermediate in mass to the Munich *Archaeopteryx* and the deep-bodied pigeon, so the feathers were a number of times stronger than calculated by Nudds and Dyke (Fig. 1, A to C).

Because focusing on one narrow aspect of a fossil organism increases the risk of error, the whole biology should be considered. The gross degree of powered flight in animals with well-developed brachial airfoils is primarily determined by the muscle power of the arms (*2*, *3*). Because gliding does not require the arms to have more strength than is needed to hold the animal off the ground, major adaptations for increasing the arm musculature above normal levels are not present in nonflapping gliders, and increasing adaptations for expanded forelimb muscles is indicative of increasing powered flight performance. The wings of *Archaeopteryx* and *Confuciusornis* were large enough for powered flight (*1*–*3*, *5*, *6*, *10*). In *Archaeopteryx*, the large furcula and greatly expanded pectoral crest indicate an expanded musculature beyond the tetrapod norm and are indicative of some level of flapping flight beyond simple gliding, albeit well below that typical of most birds (*2*, *3*, *11*). The presence of a large sternal plate anchored by ossified sternal ribs, an even larger pectoral crest, and the flattening of the hand and fingers to better anchor the primaries shows that *Confuciusornis* was markedly better adapted for powered flight than was *Archaeopteryx*, and was approaching derived fliers in performance (*2*).

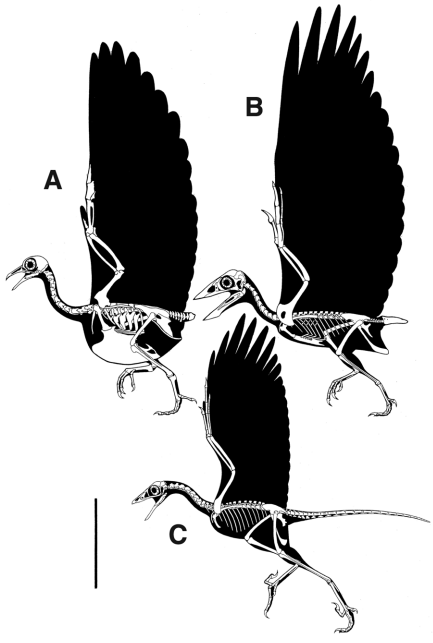

Fig. 1. Same-scale comparison of the skeletons with muscle profiles and wing feathers of (**A**) rock pigeon, 250 g, 43 mm femur; (**B**) *Confuciusornis* of the size of the specimen in figure 1A in (*1*), 47 mm femur; (**C**) Munich juvenile *Archaeopteryx*. Scale bar, 100 mm.

Fig. 2. Detail of primary feathers of the Munich specimen counterslab, including some rachises at mid-shaft. Lateral is to the left; finger elements are near the top. Scale bar, 10 mm.

3109 N. Calvert Street, Baltimore, MD 21218, USA. E-mail: GSP1954@aol.com

Because *Confuciusornis* is preserved as enormous numbers of complete specimens that lack evidence of substantial hydrodynamic transport in lake bottom deposits, with volcanic aerial pollutants probably being the killing mechanism (*12*), it appears that the birds formed large flocks able to fly out over large bodies of water (*13*). Flocking and over-water flights are common attributes of capable powered fliers, not of gliders that live singly or in small groups and must avoid flying over large stretches of water. The less-developed flight abilities of *Archaeopteryx* are compatible with its scarcity in the Solnhofen lagoonal deposits.

The thesis that large-winged basal avians with primary feathers large and asymmetrical enough to produce lift and thrust had shafts that would buckle under the load is a priori illogical, and it can be presumed to be correct only if it is conclusively shown that the adults were sufficiently massive to overstress the flight feathers. Because the hypothesis that basal avians were not powered fliers due to weak feathers is entirely dependent on mass estimates that are controversially high, implausible for the specimens examined, and impossible to verify; is contradicted by the anatomy and lifestyle of the early birds; and in one case is based on a small juvenile specimen, the hypothesis cannot be sustained. It follows that powered flight was probably further improved, not initiated, in more derived birds.

References and Notes

1. R. L. Nudds, G. J. Dyke, *Science* **328**, 887 (2010).
2. G. S. Paul, *Dinosaurs of the Air* (Johns Hopkins Univ. Press, Baltimore, 2010).
3. G. S. Paul, *Predatory Dinosaurs of the World* (Simon and Schuster, New York, 1988).
4. That the volumetric mass estimates in (*2*) and (*3*) incorporate high specific gravities of 0.85, large flight muscles, and feathers reduces the possibility that they are too low. Using the method of Christiansen and Farina (*14*), the mass estimate for the Munich specimen is a similar 135 g.
5. D. W. Yalden, *Zool. J. Linn. Soc.* **82**, 177 (1984).
6. A. Elzanowski, in *Mesozoic Birds: Above the Heads of Dinosaurs*, L. M. Chiappe, L. M. Witmer, Eds. (University of California Press, Berkeley, 2002), pp. 129–159.
7. The visible rachises of the Berlin specimen primaries are up to 1.3 mm in diameter, but they taper strongly proximally, so their maximum widths are probably much higher.
8. Mass estimates based on extrapolations from skeletal dimensions as used by Nudds and Dyke regarding *Confuciusornis* are less reliable than volumetric estimates because of very large variations in mass/dimension ratios in different animals (*2*, *3*, *9*, *10*). The mass estimate in (*2*) for *Confuciusornis* is too high for specimens of the size examined herein.
9. G. S. Paul, *Dinofest International*, D. L. Wolberg, E. Stump, G. D. Rosenberg, Eds. (The Academy of Natural Sciences, Philadelphia, 1997), pp. 129–154.
10. The wings of *Confuciusornis* are exceptionally large relative to mass (Fig. 1), perhaps an adaptation for achieving sustained flight with its grade of flight adaptations (*2*).
11. S. L. Olson, A. Feduccia, *Nature* **278**, 247 (1979).
12. M. Chang, *The Jehol Biota* (Shanghai Scientific and Technical Publishers, Shanghai, 2003).
13. Preservation of large numbers of nonaquatic, nonflocking flying vertebrates over large areas of lake bottoms is rare at best, while this taphonomic event is fully compatible with power flying in groups.
14. P. Christiansen, R. A. Farina, *Hist. Biol.* **16**, 85 (2004).

28 May 2010; accepted 20 September 2010
10.1126/science.1192963

Comment on "Narrow Primary Feather Rachises in *Confuciusornis* and *Archaeopteryx* Suggest Poor Flight Ability"

Xiaoting Zheng,[1,2] Xing Xu,[3]* Zhonghe Zhou,[3] Desui Miao,[4] Fucheng Zhang[3]

Nudds and Dyke (Reports, 14 May 2010, p. 887) compared the rachis diameters of the primary feathers of *Archaeopteryx* and *Confuciusornis* to those of modern birds and found that the primary feathers of these two basal birds were too weak to support sustained flight. Our measurements of *Confuciusornis* specimens suggest that their conclusions need to be further evaluated.

Nudds and Dyke reported their latest analysis on the flight capability of two famous basal birds, *Archaeopteryx* and *Confuciusornis* (*1*). By comparing the rachis (central shaft) diameters of the primary feathers of these two basal birds to those of modern birds, the authors found that the primary feathers of these birds were too weak to support sustained flight and thus concluded that flapping flight might have originated relatively late in avian evolution (*1*).

Nudds and Dyke's innovative analysis offers important new insights into early avian evolution. However, we noticed a substantial discrepancy between their presented data based on specimens with dubious origins and our recently collected data on confuciusornithids and believe that their conclusions need to be further evaluated. Our measurements show that the primary feathers of confuciusornithids have considerably thicker rachises than Nudds and Dyke suggest (*1*).

Measuring the rachis diameter in modern birds appears to be straightforward and easy, but this might not be true for fossil feathers—even for those of confuciusornithids, which are the best documented Mesozoic fossil birds and have some exquisitely preserved feathers (*2*). The Shandong Tianyu Museum of Nature has 536 specimens of confuciusornithids, but only four specimens preserve clear impressions of the rachis of the primary feathers (Fig. 1A). Many specimens exhibit relatively thick parallel lines throughout the wing, but they are preservational artifacts between remiges (flight feathers of a bird's wing) rather than rachises. Several other possibilities leading to smaller measured values include mistaking a covert rachis as a primary feather rachis (Fig. 1B), mistaking the longitudinal ventral furrow of the rachis of primary feathers as the whole rachis, or measuring rachis diameter of primary feathers on the dorsal side rather than ventral side (the diameter is considerably larger on the ventral side) (Fig. 1C).

Fig. 1. (**A**) Well-preserved primary feathers of a *Confuciusornis* specimen (STM13-62, housed at Shandong Tianyu Museum of Nature). (**B**) Right wing of a pigeon in dorsal view. Note rachises of coverts. (**C**) Close-up of a primary feather of a pigeon in ventral (top) and dorsal (bottom) views. Note the considerably wider rachis in ventral view than in dorsal view.

The rachises of primary feathers of confuciusornithids measure 2.1 to 2.3 mm in diameter on four Tianyu specimens, about twice as large as the measurements reported by Nudds and Dyke (*1*). Because the specimen we measured is similar in size to those studied by Nudds and Dyke, it is unlikely that the difference is caused by different body sizes. Nudds and Dyke's study thus underestimates the thickness and strength of the rachises of confuciusornithid primary feathers. Their resulting inference that confuciusornithids were not able gliders and could only parachute thus needs to be further evaluated based on newly collected, more accurate data.

However, even our measurements are considerably smaller than the predicted rachis diameter of primary feathers with similar feather length in similarly sized extant birds. This lends support to Nudds and Dyke's conclusion that basal birds have narrow rachises of primary feathers and thus had poorer flight capability than extant birds (*1*), which is consistent with previous studies (*3*). Furthermore, rachis diameter of the primary feathers is only one of several useful indicators of flight capability, and other features such as the curvature of flight feathers, asymmetry of vanes, and the right angle between the scapula and coracoid in both *Archaeopteryx* and *Confuciusornis* also should be considered. Although Nudds and Dyke's inference about flight capability of basal birds needs more data to be verified, their study outlines one of the future directions on early avian flight. Further investigations on strength of flight feathers of other basal birds, including enantiornithines and basal ornithuromorphans, promise to shed new light on this interesting evolutionary issue.

[1]Shandong Tianyu Museum of Nature, Pingyi, Shandong 273300, China. [2]Linyi Normal College, Linyi, Shandong 276000, China. [3]Key Laboratory of Evolutionary Systematics of Vertebrates, Institute of Vertebrate Paleontology and Paleoanthropology, Chinese Academy of Sciences, 142 Xiwai Street, Beijing 100044, China. [4]Biodiversity Institute, University of Kansas, Lawrence, KS 66045–7561, USA.

*To whom correspondence should be addressed. Email: xingxu@vip.sina.com

References and Notes

1. R. L. Nudds, G. J. Dyke, *Science* **328**, 887 (2010).
2. L. M. Chiappe, S.-A. Ji, Q. Ji, M. A. Norell, *Bull. Am. Museum Nat. Hist.* **242**, 1 (1999).
3. Z. Zhou, J. A. Farlow, in *New Perspectives on the Origin and Early Evolution of Birds*, J. A. Gauthier, L. F. Gall, Eds. (The Peabody Museum of Natural History, Yale University, New Haven, 2001), pp. 237–254.
4. Support for this research was provided by the Shandong Tianyu Museum of Nature, Major Basic Research Projects of the Ministry of Science and Technology, China, the National Natural Sciences Foundation of China, and the Chinese Academy of Sciences.

3 June 2010; accepted 20 September 2010
10.1126/science.1193223

Response to Comments on "Narrow Primary Feather Rachises in *Confuciusornis* and *Archaeopteryx* Suggest Poor Flight Ability"

Robert L. Nudds[1]* and Gareth J. Dyke[2]

Paul and Zheng *et al*. challenge our conclusions regarding the flight of *Confuciusornis* and *Archaeopteryx*, which derive from our method of assessing flight ability from estimated feather strength. They suggest that our mass and rachis data for these fossil birds are incorrect. Neither comment, however, invalidates our method nor alters conclusions of poor flight ability based upon our original data. We encourage researchers to use our method before critiquing our conclusions regarding early bird flight.

We recently published a method for estimating the strength of primary feather rachises and extrapolating this to the maximum lift forces sustainable by a bird, thereby providing a quantitative, and novel way of estimating the flight abilities of fossil birds (*1*). Our model is, of course, dependent on the data fed into it. Here, we respond to the comments of Paul (*2*) and Zheng *et al*. (*3*) challenging our conclusion that *Confuciusornis* and *Archaeopteryx* were not capable of powered flight. Paul suggests that our mass estimates for these fossil birds and our methodology are unsound, whereas Zheng *et al*. present new data that highlight potential errors associated with feather taphonomy or open the possibility that the Confusciusornithidae may be composed of more than one species—neither of which confounds our original conclusion of poor flight ability based on data from our original specimens.

Zheng *et al*. (*3*) present measurements that add a new twist to the debate over the flight capabilities of Mesozoic birds based on feather morphology. However, we cannot fully assess the importance of their alternative rachis diameters because measurements of primary feather length relative to overall wing length for individual specimens are also required to repeat our calculations. Nonetheless, if we use a rachis diameter of 2.15 mm and assume everything else is equal to the data in our initial study (*1*), the primary feather safety factor for the specimens reported by Zheng *et al*. (assuming hollow feathers) is 3.2, implying that their specimens of *Confuciusornis* were capable of flapping. We do not agree with the statement of Zheng *et al*. that confuciusornithids have considerably thicker rachises than we measured, because what they have shown is only that some confuciusornithids may have thicker rachises, which is a potentially interesting development. Other work has indicated that the known specimens of this taxon show a bimodal size distribution (*4*, *5*). This would either suggest that *Confuciusornis* was sexually dimorphic or that this bird, currently represented by one predominant species, needs to be further split. Differences in feather morphology may also indicate different flight abilities, which could most parsimoniously be explained by the data being extracted from separate species, based on what we know about extant birds.

It is also worth balancing the debate about preservation influencing the dimensions of the rachis diameters by considering what could lead to overestimates, for example, flattening of the rachises or measuring the calamus, which is embedded and supported by soft tissue. Of course, we are also assuming that the feather rachises are cylindrical in cross section and that the dorsal or ventral orientation of the feathers that is measured from the fossils is representative of the lateral dimension. Feather and rachis preservation remains an interesting area for future work, as it is also possible that rachis apparent diameters are increased during fossilization.

As Zheng *et al*. (*3*) acknowledge, a rachis diameter of 2.1 to 2.3 mm is still very thin compared to an extant bird with a similar wingspan, and this alone certainly implies relatively poorer flight abilities. We hope that as more specimens are found with preserved feathers, the methodology we described (*1*) will prove important and useful in assessing the flight capabilities of fossil birds—not least because it provides a direct quantitative assessment, as opposed to often qualitative and subjective conclusions drawn from morphological shape and palaeoecology data.

In a second comment on our study (*1*), Paul (*2*) states that our conclusion of poor flight ability in *Confuciusornis* and *Archaeopteryx* is incorrect because both our mass estimates for these fossil birds and our methodology were unsound. Paul, however, did not present any new primary feather safety factors based on his body mass estimates, so exactly how his contradictory conclusion was reached is puzzling. In our paper (*1*) we were explicit about our model, its assumptions, and the measurements used to feed it. Researchers (including Paul) can use our method to input alternative measurements from fossil birds and calculate primary feather safety factors.

In response to Paul's criticisms, consider first his suggestion that unless we test our methods against other fossil avians the method we use is flawed. This logic is problematic: You cannot test predictions from a model against an organism in which flight ability is unknown. This is why we used extant birds with known and observable flight abilities to test our predictions of primary feather safety factors.

Paul (*2*) argues that we have overestimated the size of both *Confuciusornis* and *Archaeopteryx* and suggests that his estimates for the body masses for these extinct avians are more valid. If, however, we use Paul's (*2*) lower mass estimates in our model, then the safety factor for a hollow primary-feathered *Archaeopteryx* with a 140-g body mass is 1.1, which is still not sufficient for flapping flight and barely enough for gliding under static forces. Similarly, if we use 180 g for the body mass of *Confuciusornis*, then the calculated safety factor is 1.4—again, barely enough to sustain a glide and certainly nowhere near sufficient to allow flapping or any flight maneuvers, which involve sudden high dynamic forces.

Paul's third criticism is that the rachis measurements we present for *Archaeopteryx* (*1*) are inaccurate. A rachis diameter of 1.4 mm, suggested by Paul based on a photograph, would yield a safety factor of 3.6, below that of modern birds (almost always >4.8), but probably enough to sustain some level of flapping. The suggestion that heavier adult *Archaeopteryx* were likely better at flapping than juveniles (*2*) implies that adult feathers are thicker than those of juveniles, which is unlikely and has not yet been shown for fossil or modern birds.

The final four paragraphs of Paul's comment (*2*) outline other lines of evidence as to why our conclusion of poor flight ability in the two Mesozoic birds may be incorrect. As we have already argued, the one clear advantage of our method is that it is quantitative as opposed to being qualitative or subjective, as are many discussions about the lifestyles of fossil taxa based on anatomy and palaeoecology. Such arguments may be extraneous anyway: If the feathers of early birds were too weak to withstand the forces of flight, then we know (thanks to the laws of physics) that they could not fly regardless of any other morphological features they might, or might not, have possessed.

[1]Faculty of Life Sciences, University of Manchester, Manchester, M13 9PT, UK. [2]School of Biology and Environmental Science, University College Dublin, Belfield 4, Dublin, Ireland.

*To whom correspondence should be addressed. E-mail: Robert.Nudds@manchester.ac.uk

References

1. R. L. Nudds, G. J. Dyke, *Science* **328**, 887 (2010).
2. G. S. Paul, *Science* **330**, 320 (2010); www.sciencemag.org/cgi/content/full/330/6002/320-b.
3. X. Zheng, X. Xu, Z. Zhou, D. Miao, F. Zhang, *Science* **330**, 320 (2010); www.sciencemag.org/cgi/content/full/330/6002/320-c.
4. L. M. Chiappe, S. Ji, Q. Ji, M. A. Norell, *Bull. Am. Mus. Nat. Hist.* **242**, 1 (1999).
5. L. M. Chiappe, J. Marugán-Lobón, S. Ji, Z. Zhou, *Biol. Lett.* **4**, 719 (2008).

23 June 2010; accepted 20 September 2010
10.1126/science.1193474

PSYCHOLOGY

Our Evolving View of Childhood

Alison Gopnik

Melvin Konner's *The Evolution of Childhood* is the sort of book that is often described as "magisterial": It is very long, nearly a thousand pages; it is obviously the product of extensive and painstaking research; and it contains an enormous amount of extremely varied and often interesting material. It is clearly intended as a grand synthesis. As a developmental psychologist with a deep interest in evolution, I had looked forward to learning from it. And yet the result is curiously unsatisfying. For Konner's principal conclusions from all this research are that human childhood is the result of evolution and that genetics and culture interact—conclusions that are both surely obvious to everyone but creationists in the first place.

The Evolution of Childhood
Relationships, Emotion, Mind
by Melvin Konner
Harvard University Press, Cambridge, MA, 2010. 959 pp. $39.95, £29.95, €36.
ISBN 9780674045668.

This unsatisfying quality is common to much evolutionary psychology. Either the researchers make the empty general claim that behavior evolved or they draw substantive conclusions from this claim that simply don't follow. To say that a human behavior is adaptive or is the result of evolution tells us nothing about whether that behavior is innate or learned, universally triggered or culturally transmitted. This is because our particularly powerful ability to adapt through learning and culture, is, arguably, the most important human evolutionary advantage. For human beings, culture is our nature, and the drive to learn is our most important and fundamental instinct.

Of course, sometimes evolutionary evidence really can lead to interesting and specific insights. For example, Sarah Hrdy has made a substantive and intriguing argument that human "alloparenting"—having many adults besides mothers take care of babies—is the result of a particular evolutionary history (*1*). Her argument is not simply based on the claim that alloparenting would be good for humans but on quite exact comparisons among primates living in different niches. The great apes (our closest evolutionary relatives) don't alloparent as much as we do. But langurs, who (like us, but unlike the great apes) have to haul babies for long distances, have evolved the equivalent of teen-aged baby-sitters. Unfortunately, one searches in vain through the many pages of this book for similarly interesting arguments.

Konner's book is also unsatisfying because of a striking lacuna: the nearly complete absence of cognition. It's understandable that Konner (an anthropologist at Emory University) might not be up to date on all the varied research he tries to integrate, but this omission is still surprising. For 40 years, progress in psychology (and particularly developmental psychology) has hinged on the insight that what we know about the world and our fellow creatures shapes our behavior. Most importantly, it shapes our social behavior. Perceiving, representing, and learning about the environment are central biological functions. For an intensely social species like ours, learning how our fellow humans work is a fundamental biological imperative. To understand relationships, emotions, and minds (as the book's subtitle suggests), one has to understand what children perceive, know, and learn.

The absence of cognition is particularly odd in a book explicitly concerned with how genetic and environmental factors might work together. Konner offers long discussions of epigenesis and the Baldwin effect (the genetic assimilation of acquired characters). But, for complex organisms, cognition is one key—arguably, the key—mechanism that allows genes and the environment to interact. Genetically determined processes of perception and learning permit organisms to directly represent their specific, immediate environment in their own lifetime and to adapt to that environment quickly and directly.

Without thinking about cognition, the evolutionary results that Konner describes are a jumble. Clearly evolution often selects for innovations in developmental programs, and Konner includes long lists of variations in developmental patterns among different species. But as he describes them, there is little rhyme or reason behind those variations. In part, this reflects a basic fact that is intrinsically problematic for all evolutionary psychology: Evolution is contingent. Closely related species may develop different developmental patterns because of the complex interaction of many factors and because of the fine details of their environmental niches and evolutionary history. Moreover, similar behaviors may have different developmental origins in different species.

Nevertheless, there is a robust, though certainly not universal, generalization that a long period of immaturity—childhood—is correlated with sophisticated and flexible cognitive abilities, across many different species in many different environments. The best explanation for this relationship centers on learning. A long protected period of immaturity allows young animals to learn about their specific physical and social environment. Once they have figured out how the world around them works, they can act on that world effectively and safely. So capacities for complex cognition and childhood itself are closely related, and it is no coincidence that we humans remain helpless children for so long.

I suspect that Konner neglects cognition because he holds the common but outdated view that cognition and childhood are antithetical—that children are somehow less cognitively adept than adults and that infants and young children in particular have very limited cognitive abilities. He consistently writes, for example, as if mothers' behaviors simply trigger or shape social behavior in infants and as if infants' responses are simple and reflexive. He perpetuates the idea that capacities for logic and reason only emerge in middle childhood.

But, actually, given the correlation between childhood and cognition, an evolutionary perspective should predict that human children would be equipped with powerful mechanisms for understanding and learning

The reviewer is at the Department of Psychology, University of California, Berkeley, CA 94720–1690, USA. E-mail: gopnik@berkeley.edu

about the world and other people. And this has turned out to be true. One of the most important, and by now uncontroversial, findings from the past 30 years of research is that infants and preschoolers are far more cognitively sophisticated than we once thought. Similarly, developmentalists have discovered that there are complex interactions among caregivers and infants and young children that include interpretations on all sides.

In the same way, although Konner describes both innately triggered behavior and learning, his versions of both the innate and the learned are extremely simple—his catalog of learning mechanisms could have come out of a 1950s textbook—and lack the abstractness and complexity we actually see even in infancy. Developmental psychologists now believe that children have complex and abstract representations of the world in place very early and that those representations are then revised, modified, and reshaped by experience. Konner's old-fashioned view of children leads to what are simply mistakes. For example, he says repeatedly that "theory of mind" (our ability to understand the mental states of others) emerges only in middle childhood, after basic social relationships have already been formed. That was the standard view in Piaget's day, but 20 years of research have made it clear that even infants learn about the minds of others and that such learning is at its peak between ages two and five. Konner's mistake is important because the early emergence of theory of mind tells us that, from the very beginning, children are actively interpreting and understanding the people around them.

Human beings—even, indeed especially, the youngest—perpetually change what they think and what they do in the light of experience. This allows us to invent a greater variety of physical and social environments than does any other species and to pass information about those environments on to the next generation. The challenge is to show, in detail, how these capacities evolved. Exactly how do our minds differ from those of our closest relatives? What happened to bring about the change from our ancestors? Our unprecedentedly long human childhood is likely to play a key role in resolving those questions. We can hope that a magisterial survey of the next 20 years of research into the evolution of childhood will provide more satisfying answers.

References

1. S. B. Hrdy, *Mothers and Others: The Evolutionary Origins of Mutual Understanding* (Harvard Univ. Press, Cambridge, MA, 2009); reviewed in (*2*).
2. G. R. Brown, *Science* **324**, 1646 (2009).

10.1126/science.1191553

EXHIBITION

Descended from Refuse

Thomas Junier[1] and Pilar Junier[2]

Imagine that it is 3010 and a group of paleontologists are excavating a site in what is currently the small Swiss city of Neuchâtel. The researchers will be surprised with what they might find: biological forms that evolved skeletons made out of cardboard and plastic and whose remains (including some nicely preserved complete life cycles) are clustered within boxes with transparent lids. What geological process could have led to the preservation of this peculiar trove of fossils? The answer probably lies somewhere in the imagination of the artist François Riou, whose works are highlighted in the exhibition *Espèces en voie d'apparition*, currently at Neuchâtel's Museum of Natural History.

Espèces en voie d'apparition [Species About to Evolve]
Œuvres de François Riou

Muséum d'Histoire Naturelle Neuchâtel, Neuchâtel, Switzerland. Through 9 January 2011. www.museum-neuchatel.ch/new/navigation.php?cat=5

The forms and color patterns of living things have long been a source of inspiration for artists. The particularity of Riou is that his creatures have all evolved from everyday human implements. Scouring such wild jungles as supermarkets, the artist is constantly on the lookout for whatever beasts and bugs lurk not behind but under the guise of food, clothing, and other items. Recycling mundane implements—such as beer caps and used mobile phone keyboards that seem to sprout jointed legs and colorful elytra—he brings sudden life to what otherwise would quickly have turned into pieces of refuse. As is fitting for creative temperaments, the myriad of Riou's fauna evidences an inordinate fondness for insects.

Riou's mortal hand framed the fearful symmetry of living things, which he reveals in objects that we normally disregard. This symmetry is what makes his creatures seem familiar and recognizable. And in turn, that familiarity causes an actual beetle hidden among the other pieces of the exhibition to remain unnoticed by unwary visitors.

Shapes and colors are not the only simulacra of animals displayed in the exhibition. The collection arrayed about the room also includes shadows, tracks, and skeletons. Again our brains fill in the missing information, and all of a sudden we see a mop flying through the room or a predator lurching on a wall. While other exhibits and activities at the museum invite visitors to learn about the biodiversity of Neuchâtel, *Espèces en voie d'apparition* offers an intriguing perspective on how we perceive organic forms.

10.1126/science.1198342

The reviewers are at [1]Computational Evolutionary Genomics Group, University of Geneva, CH-1211 Geneva, Switzerland, and [2]Laboratory of Microbiology, Institute of Biology, University of Neuchâtel, CH-2009 Neuchâtel, Switzerland. E-mail: pilar.junier@unine.ch

An inordinate fondness for insects. (Left) François Riou's *Muséum mutation* (detail); (right) *Escalator* (detail).

CREDITS: © MUSEUM-PHOTOS ALAIN GERMOND/COURTESY MUSEUM D'HISTOIRE NATURELLE NEUCHÂTEL

CONSERVATION

Ecosystem Services for 2020

The Convention on Biological Diversity's 2020 targets are an improvement over the 2010 target, but they could be strengthened.

C. Perrings,[1]* S. Naeem,[2] F. Ahrestani,[2] D. E. Bunker,[3] P. Burkill,[4] G. Canziani,[5] T. Elmqvist,[6] R. Ferrati,[5] J. Fuhrman,[7] F. Jaksic,[8] Z. Kawabata,[9] A. Kinzig,[1] G. M. Mace,[10] F. Milano,[5] H. Mooney,[11] A.-H. Prieur-Richard,[12] J. Tschirhart,[13] W. Weisser[14]

The vast majority of nations have fallen far short of the Convention on Biological Diversity's (CBD's) 2010 target: to reduce the rate of loss of biodiversity (*1*, *2*). This prompted the CBD to develop a new plan of action, supported by 20 "SMART" (specific, measurable, ambitious, realistic, and time-bound) targets for 2020 (*3*, *4*). As the 10th Conference of the Parties (COP) of the CBD meets in Nagoya, Japan, to negotiate both plan and targets, it is critical that targets also be grounded in the real interests that people have in benefits provided by biodiversity. To evaluate targets on this basis, we use the ecosystem services framework developed by the Millennium Ecosystem Assessment (MA) (*5*). This framework balances resource conservation and use according to how societies value consumptive (e.g., food and fuel) and nonconsumptive (e.g., health and aesthetics) services provided by ecosystems.

The ecosystem services framework has four main consequences for target setting. First, what and how much biodiversity should be targeted for conservation depends on what services are important to maintain and with what reliability. Second, the temporal and spatial scale of targets should be based on the changing temporal and spatial distribution, and risk profiles, of ecosystem services. Third, target development and implementation should include all agencies involved with management of biodiversity and the ecosystem services they support. Fourth, interdependence among ecosystem services, the benefits they provide, and the value placed on those benefits implies that targets must be conditional. Implementation of one target may be affected by implementation of another.

The CBD 2020 Targets

The 2020 targets, color-coded according to (*6*), are highlighted in the figure. Red refers to imminent biosecurity threats due either to collapse of ecosystems or populations or to the rapid increase of pests or pathogens. Green addresses society's conservation goals. Blue addresses longer-term scientific, socioeconomic, and institutional conditions required to meet and sustain red and green targets. Red targets are typically "short term" (2 to 5 years). Green and blue targets are typically "longer term" (10+ years). Although none of the targets are presented as short term, we red-coded three because they address imminent threats.

Several 2020 targets refer to ecosystem services, including carbon sequestration and resilience (target 15), foods, fuels, and fibers (targets 6, 7, and 13). Target 14 addresses "ecosystems that provide essential services." But aside from capture fisheries (target 6), there is no clear correspondence between ecosystem services referred to in the targets and services identified as at risk in the MA (*5*) and subsequent studies (*1*). This is especially marked for marine systems, in part because targets tend to be biased toward terrestrial systems.

All targets have, in principle, the same time horizon—2020—and apply everywhere. The spatial and temporal distribution of services and variation in rates of change in the processes involved are not considered. Targets addressing imminent threats (e.g., 6, 8, and 9) should be sensitive to the time available to act and more closely related to the threat to human well-being. Similarly, some targets (e.g., 1, 2, and 3) may only be met over time scales longer than 10 years, but their implementation requires action now.

There is limited attention to coordination of targets across agreements and agencies. Some targets can be achieved solely through the sum of individual country efforts (e.g., 5 and 8), others only by collaboration across international agreements and agencies (e.g., 4, 9, and 13). For example, target 9 requires action on trade and alien invasive species. Although port inspection is within the competence of member states, trade interventions are not. The World Trade Organization and the parties to the General Agreement on Tariffs and Trade would have to be willing partners to reach this target.

The conditionality of targets is partly recognized in the identification of blue targets for enabling conditions that have to be met for green and red targets to be reached. But interdependence among green and red targets is largely ignored.

What Is Missing?

Although some 2020 targets are congruent with an ecosystem-services approach, four main things are missing:

1) *Functional diversity*. Ecosystem services derive from ecosystem functions and the species that perform those functions. In some cases, individual species play a disproportionately large role in the provision of services, but in most cases, targets should focus on conserving critical functional diversity. What matters for most ecosystem services is the diversity of traits species possess (e.g., nitrogen fixers, pollinators, and nutrient recyclers) (*7*–*10*). However, only target 13, on crop and livestock genetic diversity, references functional diversity.

2) *Environmental uncertainty and target adjustment.* How much diversity it is critical to maintain depends on the range of environmental conditions expected. The greater the expected variation in environmental conditions, the greater the required diversity within groups providing particular functions. Ecological functioning may change as environmental conditions change (*11*, *12*). Targets for diversity within functional groups of species should adjust with changes in expectations about the state of the environment.

3) *Interactions between targets*. Target 3 explicitly recognizes harmful environmental

[1]Arizona State University, Tempe, AZ 85287, USA [2]Columbia University, New York, NY 10027, USA. [3]New Jersey Institute of Technology, Newark, NJ 07102, USA. [4]Sir Alister Hardy Foundation for Ocean Science, Plymouth, PL12PB, UK. [5]Universidad Nacional del Centro, Buenos Aires, Argentina. [6]Stockholm University, SE-106 91 Stockholm, Sweden. [7]University of Southern California, Los Angeles, CA 90089, USA. [8]Pontificia Universidad Católica de Chile, Santiago, Chile. [9]Research Institute for Humanity and Nature, Kyoto, 603-8047, Japan. [10]Imperial College London, Ascot, SL5 7PY, UK. [11]Stanford University, Stanford, CA 94305, USA. [12]Muséum National d'Histoire Naturelle, 75231 Paris 05, France. [13]University of Wyoming, Laramie, WY 82071, USA. [14]Friedrich-Schiller-Universität, Jena 07743, Germany.

*Author for correspondence. E-mail: Charles.Perrings@asu.edu

Published by AAAS

Strategic Goals	Targets: By 2020…
Address underlying causes of biodiversity loss by mainstreaming biodiversity across government and society.	1. All people are aware of the values of biodiversity and the steps they can take to conserve and use it sustainably. 2. The values of biodiversity are integrated into [national accounts], national and local development, and poverty reduction strategies.... 3. Incentives [including subsidies] harmful to biodiversity are eliminated, phased out, or reformed in order to minimize negative impacts.... 4. Governments, business, and stakeholders ... have taken steps to achieve or have implemented plans for sustainable production ...
Reduce direct pressures on biodiversity and promote sustainable use.	5. The rate of loss and degradation, and fragmentation, of natural habitats [including forests] is [at least halved] [brought close to zero]. 6. [Overfishing is ended, destructive fishing practices are eliminated, and all fisheries are managed sustainably.].... 7. Areas under agriculture, aquaculture, and forestry are managed sustainably, ensuring conservation of biodiversity. 8. Pollution, including from excess nutrients, has been brought to levels that are not detrimental to ecosystem function and biodiversity. 9. Invasive alien species are identified, prioritized, and controlled or eradicated, and measures are in place to control pathways.... 10. To have minimized the multiple pressures on coral reefs and other vulnerable ecosystems affected by climate change....
Improve status of biodiversity by safeguarding ecosystems, species, and genetic diversity.	11. At least [15%][20%] of terrestrial, inland-water, and [*X*%] of coastal and marine areas are conserved.... 12. The extinction and decline of known threatened species has been prevented.... 13. The loss of genetic diversity of cultivated plants and domestic farm animals in agricultural ecosystems and of wild relatives is halted....
Enhance benefits to all from biodiversity and ecosystem services.	14. Ecosystems that provide essential services and contribute to health, livelihoods, and well-being, are safeguarded.... 15. Ecosystem resilience and the contribution of biodiversity to carbon stocks has been enhanced, through conservation and restoration....
Enhance implementation through participatory planning, knowledge management, and capacity building.	16. Access to genetic resources is [promoted] [facilitated] [enhanced], and benefits are shared.... 17. Each party has developed, adopted, ... and implemented, an effective, participatory, and updated national biodiversity strategy and action plan. 18. [[Have [sui generis legal] systems in place to protect] traditional knowledge, innovations, and practices relevant to biodiversity ...].... 19. Knowledge, the science base and technologies relating to biodiversity, its values, functioning, status, and trends, are improved. 20. Capacity (human resources and financing) for implementing the convention has increased [10-fold].

2020 targets to be considered at CBD COP10. Authors compiled headline text to be discussed by COP delegates on each of the targets [from (*21*)], and color-coded according to (*6*) (see text for explanation of code). Bracketed terms have not been agreed upon and are to be debated. For expanded text on each target, see Supporting Online Material.

effects of agricultural subsidies. But potential interactions between most other targets are ignored. Targets 7 and 13 would be expected to have well-understood effects on the supply of ancillary ecosystem services and on species not directly exploited in the production of crops or livestock (*13*–*15*). Also, target 6 addresses threats to fish production. Its implementation would affect and be affected by implementation of targets for other ecosystem services, including regulation of climate (*16*, *17*).

4) *Trade-offs between targets*. Different services require different diversity. How much diversity is critical depends on the set of services we need. But species that support a service such as climate regulation are different from species that support a service such as food production (*18*, *19*), and there may be trade-offs between them. That is the core message of the MA (*5*). Targets need to be set in recognition of these trade-offs. It may not be possible to meet all of the 2020 targets.

Options for the Future

The 2020 targets are a significant improvement over the 2010 target and its indicators (*2*), but they could be strengthened. If there have to be 20 targets, they should address the 20 highest-priority threats to critical ecosystem services and should not include omnibus targets (e.g., targets 14 and 15) that necessarily fail the SMART test. Setting such priorities is a political process that reflects national perceptions of both the relative importance of different services and their relative vulnerability. For example, the importance of preserving genetic information in rare and endangered species is fairly well recognized. But the importance of maintaining species needed to protect many other services during a period of rapid environmental change is not as widely appreciated. Identifying what we collectively lose from failing to meet different targets is an important step toward target prioritization.

Collective action to identify and implement biodiversity targets is needed most where people have the weakest incentive to take the biodiversity impacts of their actions into account. Open-access common pool resources—like the high seas—are especially vulnerable. But collective action is also needed where services at risk are of high social value.

Toward these ends, efforts to establish an Intergovernmental Science-Policy Platform on Biodiversity and Ecosystem Services (IPBES) are in their closing stages (*20*). IPBES would create capacity to evaluate both progress toward biodiversity targets and the costs of falling short. Such resources could provide an opportunity to put in place a more structured sequence of objectives for the collective management of biosphere change.

References and Notes

1. S. H. M. Butchart *et al.*, *Science* **328**, 1164 (2010).
2. Convention on Biological Diversity Secretariat, *Global Biodiversity Outlook 3* (CBD, Montreal, 2010).
3. H. Mooney, G. Mace, *Science* **325**, 1474 (2009).
4. G. M. Mace, J. E. M. Baillie, *Conserv. Biol.* **21**, 1406 (2007).
5. Millennium Ecosystem Assessment, *Ecosystems and Human Well-Being: General Synthesis* (Island Press, Washington, DC, 2005).
6. G. M. Mace *et al.*, *Curr. Opin. Environ. Sustain.* **2**, 3 (2010).
7. P. B. McIntyre, L. E. Jones, A. S. Flecker, M. J. Vanni, *Proc. Natl. Acad. Sci. U.S.A.* **104**, 4461 (2007).
8. D. E. Bunker *et al.*, *Science* **310**, 1029 (2005).
9. M. E. Bracken, S. E. Friberg, C. A. Gonzalez-Dorantes, S. L. Williams, *Proc. Natl. Acad. Sci. U.S.A.* **105**, 924 (2008).
10. M. Solan *et al.*, *Science* **306**, 1177 (2004).
11. M. T. Bulling *et al.*, *Philos. Trans. R. Soc. Lond. B Biol. Sci.* **365**, 2107 (2010).
12. J. A. Godbold, M. Solan, *Mar. Ecol. Prog. Ser.* **396**, 273 (2009).
13. P. A. Matson, W. J. Parton, A. G. Power, M. J. Swift, *Science* **277**, 504 (1997).
14. J. Pretty, *Philos. Trans. R. Soc. Lond. B Biol. Sci.* **363**, 447 (2008).
15. M. R. W. Rands *et al.*, *Science* **329**, 1298 (2010).
16. J. B. C. Jackson *et al.*, *Science* **293**, 629 (2001).
17. B. Worm *et al.*, *Science* **314**, 787 (2006).
18. D. Tilman, K. G. Cassman, P. A. Matson, R. Naylor, S. Polasky, *Nature* **418**, 671 (2002).
19. Y. Malhi *et al.*, *Science* **319**, 169 (2008).
20. A. Larigauderie, H. Mooney, *Curr. Opin. Environ. Sustain.* **2**, 9 (2010).
21. CBD, *Revised and Updated Strategic Plan: Technical Rationale and Suggested Milestones and Indicators* (CBD, Montreal, 2010); www.cbd.int/doc/meetings/cop/cop-10/official/cop-10-09-en.pdf.

22. The authors are associated with the ecoSERVICES and bioSUSTAINABILITY projects of DIVERSITAS.

Supporting Online Material

www.sciencemag.org/cgi/content/full/330/6002/323/DC1

10.1126/science.1196431

Published by AAAS

MEDICINE

Stopping the Stones

Compounds that prevent the crystallization of an amino acid may represent a new class of therapeutic agent for kidney stones.

Fredric L. Coe[1] and John R. Asplin[2]

An imbalance in the fluid and mineral content of urine can cause debilitating kidney stones to form. Most of the time, the stones are composed of calcium oxalate crystals. Much less common are stones that develop from crystals of the amino acid L-cystine. The latter only occurs in patients with cystinuria, a condition with great morbidity due to the early age of onset, high frequency of stone recurrence, and increased risk of chronic kidney damage (*1*). The rarity of the disease—it occurs in about 1 in 15,000 in the United States—has deprived the field of clinical trials to assess treatment options. Treatment has not changed in over 20 years and remains unsatisfactory for many patients. On page 337 in this issue, Rimer *et al*. (*2*) report a potential new therapy for cystinuria, using compounds to retard cystine crystal growth.

Cystinuria is an inherited disorder in which intestinal and renal transport of cystine is abnormal (*3*). As a result, excretion of cystine into the urine increases, and its poor solubility leads to the formation of kidney stones (see the figure). Mutations in either of the *SLC3A1* or *SLC7A9* genes, which encode protein subunits of an amino acid transporter, account for almost all cases of cystinuria (*4*, *5*).

Current treatments for cystinuria involve reducing the saturation of urine with cystine by lowering its excretion, increasing the volume of urine, or increasing cystine's solubility in urine. Unfortunately, not all patients can maintain either the necessary high urine flow over time or the low-sodium, low-protein diets needed to reduce excretion of cystine (*6*, *7*). Cystine solubility increases appreciably when urinary pH is raised, but only at values approaching 8.0, the maximum that kidneys will attain. This requires amounts of alkaline compounds that often exceed the dose that patients can tolerate (*8*). Thiol-containing compounds that undergo a disulfide bond exchange reaction can convert cystine to a soluble cysteine-drug complex. Although these agents lower cystine saturation (decrease the amount of cystine in solution relative to its solubility), such drugs have adverse side effects and have not been studied in rigorous clinical trials to prove that they reduce kidney stone formation (*9*, *10*). Clearly, this is a disease that could greatly benefit from new therapies.

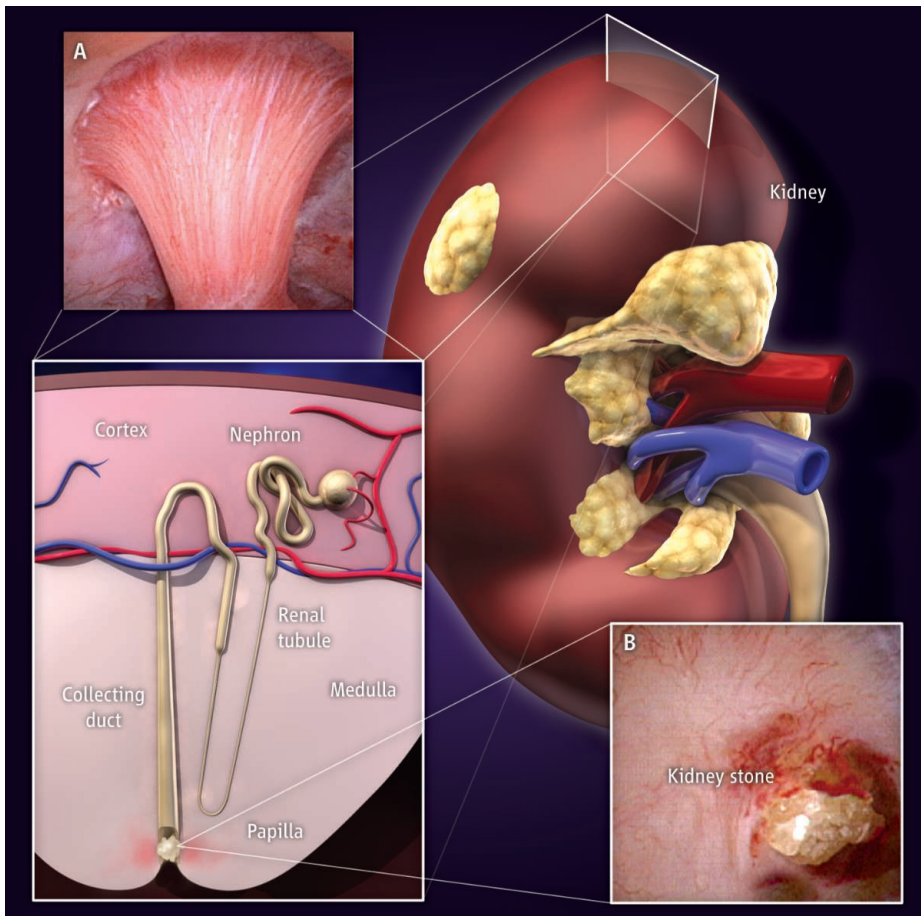

Cystinuria. In the human kidney, cystine can form crystals in the urine, leading to debilitating kidney stones. A normal renal papilla (**A**) and one from a patient with cystinuria (**B**) are shown. In the latter case, there is a dilated collecting duct with a protruding cystine stone. [The photos are reprinted from (*1*) with permission from the publisher, *Nature* Publishing Group]

Although human urine contains many highly anionic proteins and glycosaminoglycans that inhibit calcium crystal growth and aggregation, none of these components have given rise to effective treatments for calcium stones. For example, synthetic polymers of aspartic acid can inhibit calcium crystal growth but when taken orally, can be digested to small peptides. Even if they remain intact, the polymers usually cannot be absorbed by the body. Citrate also inhibits calcium crystallization, and the concentration of this anion in urine can be boosted by ingesting an alkali (such as potassium bicarbonate), which changes ion transport in renal cells. However, citrate also forms complexes with calcium, so it is unclear to what extent citrate directly blocks calcium crystal growth.

Clinicians have no therapeutic agents for any type of kidney stone that act strictly to inhibit crystal formation. Now, Rimer *et al*. have identified two compounds that directly bind to preferred crystal growth sites on cystine, thereby retarding crystal growth in vitro. The most effective molecule was L-cystine dimethylester (CDME). Even when present in solution at a small fraction of the cystine concentration, CDME reduced crystal growth and changed crystal shape and size as determined by atomic force microscopy and bulk phase crystallization experiments.

The finding of Rimer *et al*. is encouraging, but the path to clinical practice is very long. Whether CDME will act in urine as it does in synthetic solutions remains to be seen; per-

[1]University of Chicago, Chicago, IL 60637, USA. [2]Litholink Corporation, Chicago, IL 60612, USA. E-mail: f-coe@uchicago.edu; jasplin@litholink.com

haps urinary proteins and other macromolecules will influence the binding of CDME to the surface of the cystine crystal. It's also not clear whether CDME will interact with thiol drugs in a synergistic or antagonistic manner. The fate of CDME when administered orally also must be determined. For instance, will it be absorbed from the gut, and if so, will it be hydrolyzed to cystine? Will it even reach the urine at all? Fortunately, mice that have been engineered to lack the *SLC7A9* gene develop cystinuria and provide a model for studying whole-animal safety, CDME metabolism, and the drug's effectiveness in preventing stone formation (*11*). Rimer *et al*. suggest that the dose of CDME required to prevent cystine crystallization must reach 5 to 10 mg per liter of urine in humans—is that safe? Interestingly, CDME can actually cause the accumulation of cystine within lysosomes of cultured cells and in animal models (*12*). Such accumulation can cause crystals to form and thus damage cells. These issues should be addressed through rigorous clinical trials.

Even if CDME is not a safe and effective therapy, the molecular modeling method outlined by Rimer *et al*. could identify other compounds that inhibit cystine crystallization. Likewise, at least in principle, it could provide candidate drug prototypes for the far more common calcium oxalate, calcium phosphate, and uric acid stones. Even though clinical trials support calcium stone prevention with inexpensive drugs, selective inhibitors might be more efficient and better tolerated.

References and Notes

1. A. P. Evan *et al*., *Kidney Int.* **69**, 2227 (2006).
2. J. D. Rimer *et al*., *Science* **330**, 337 (2010).
3. J. Chillarón *et al*., *Nat. Rev. Nephrol.* **6**, 424 (2010).
4. E. Pras *et al*., *Nat. Genet.* **6**, 415 (1994).
5. L. Feliubadaló *et al.*, International Cystinuria Consortium, *Nat. Genet.* **23**, 52 (1999).
6. J. S. Rodman *et al*., *Clin. Nephrol.* **22**, 273 (1984).
7. A. Lindell, T. Denneberg, E. Edholm, J. O. Jeppsson, *Nephron* **71**, 407 (1995).
8. Y. Nakagawa, J. R. Asplin, D. S. Goldfarb, J. H. Parks, F. L. Coe, *J. Urol.* **164**, 1481 (2000).
9. D. J. Dolin, J. R. Asplin, L. Flagel, M. Grasso, D. S. Goldfarb, *J. Endourol.* **19**, 429 (2005).
10. C. Y. Pak, C. Fuller, K. Sakhaee, J. E. Zerwekh, B. V. Adams, *J. Urol.* **136**, 1003 (1986).
11. M. Font-Llitjós *et al*., *Am. J. Physiol. Renal Physiol.* **293**, F732 (2007).
12. M. J. Wilmer *et al*., *Pediatr. Res.* **62**, 151 (2007).
13. J.R.A. is a partner in the Ravine group, a company that focuses on developing treatments for calcium kidney stones.

10.1126/science.1197207

EVOLUTION

Variation Catches a Ride

Genetic hitchhiking appears to shape variability in quantitative traits

Brian Charlesworth

Evolutionary change often involves what geneticists call quantitative traits—traits such as height, weight, or skin color that are determined by more than one gene and vary "continuously" or "semicontinuously" within a population (when graphed, the variation in the trait often resembles a bell-shaped curve). Quantitative traits are involved in many human diseases and in breeding economically important plants and animals; as a result, researchers are interested in understanding the underlying causes of their variation. Geneticists are getting ever closer to pinpointing the locations of the genetic variants that cause variability in quantitative traits, thanks to increasingly detailed studies of genomes that identify naturally occurring variants at individual chromosomal sites, especially differences at single-nucleotide sites in the DNA sequence (single-nucleotide polymorphisms, or SNPs) (*1*). There has been every reason to suppose that quantitative trait variation is subject to the same evolutionary forces that affect other types of DNA sequence variability, primarily by effects on the genes concerned through selection on a specific trait. On page 372 of this issue, Rockman *et al*. (*2*) test this idea and find that evolutionary mechanisms that target larger regions of the genome are more prominent than expected.

For their study, the researchers created a set of inbred strains of the nematode worm *Caenorhabditis elegans* by crossing two existing stocks: the N2 strain, which researchers used to produce the standard genome sequence, and a strain first identified in Hawaii. Then, in the young adult stages of the resulting progeny, which each contained a different mixture of variants from each parent, they identified more than 2300 quantitative trait loci (QTL), stretches of chromosomal DNA that are closely linked to the expression of known genes.

They saw a striking pattern. QTL density was much lower in the central parts of the chromosomes than on the adjacent arms. They also found that the arms contributed

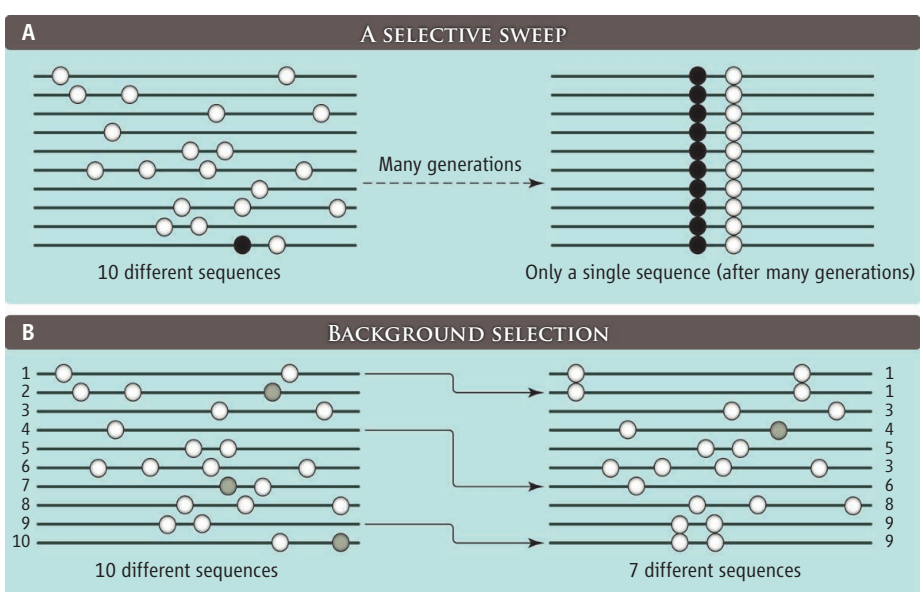

Evolving variation. Hitchhiking effects when there is no genetic recombination. (**A**) A selective sweep. A selectively neutral genetic variant (white circle) spreads though a population because it is linked to an advantageous mutation (black circle). (**B**) With background selection, variation in traits linked to deleterious mutations (gray circles) is reduced as selection eliminates the deleterious mutants from the population. (The gray circle in 4 on the right represents a newly arisen deleterious mutation.)

Institute of Evolutionary Biology, University of Edinburgh, Edinburgh EH9 3JT, UK. E-mail: brian.charlesworth@ed.ac.uk

more to the genetic variation between the two strains than the centers. At first glance, this result is paradoxical, because the centers have much higher gene densities than the arms; where there are more genes, one would expect to detect many more variant loci that regulate gene expression. This paradox, however, can be explained by another difference between the two regions: The arms also have much higher rates of genetic recombination (exchange of genetic material between the maternal and paternal genomes of an individual) than the centers. Investigators have found a similar pattern in other organisms, including *Drosophila*; in these organisms, genome regions with higher levels of genetic recombination also have greater DNA sequence variability (*3*).

The process producing this pattern is likely to be genetic hitchhiking, in which changes in allele frequencies at sites that are under selection affect the frequencies of variants at nearby sites on the chromosome. In other words, a variant present at one place in the genome can spread through a gene pool because it "catches a ride" with a closely linked DNA sequence variant that is under selection. Two forms of hitchhiking may be important: "selective sweeps" caused by the spread of variants favored by selection (*4*); and "background selection" (*5*), which involves the elimination of rare deleterious mutations from the population (see the figure). Other things being equal, genome regions with low levels of recombination are the most likely to experience hitchhiking effects, resulting in a reduction of variation within regions close to the sites under selection. Because of this effect of hitchhiking, the effective population size (N_e) in these regions (a measure of the number of individuals in the population that contribute to the next generation) is reduced. Thus, the combination of linkage and low recombination reduces both the variability of the region and its potential for adaptation, because levels of variability within a population and the efficacy of selection are both proportional to N_e (*6*).

Rockman *et al*. investigated whether background selection could explain the variation in levels of gene expression between the chromosome centers and arms. They used information on genomic parameters such as gene densities and recombination rates across the *C. elegans* genome and also estimated the values for two unknown variables: the intensity of selection against deleterious mutations and the level of inbreeding in the population (*7*). The inbreeding parameter is important for *C. elegans* because it is a hermaphrodite with a high frequency of reproduction by self-fertilization. The resulting lack of genetic differences between the paternal and maternal genomes of an individual greatly reduces the effectiveness of recombination.

The results are consistent with a major role for background selection, but contributions from selective sweeps cannot be ruled out. A limitation of the study is that it is based on examining differences between only two strains, one of which has been in laboratory culture for many years.

Nonetheless, the analysis convincingly shows that hitchhiking effects are the most likely cause of the observed patterns of variation and provides the first evidence that hitchhiking can shape quantitative variability. It will be interesting to see whether similar patterns are observed in more representative samples from the population and for DNA sequence variants as well as quantitative variability. It is also important to seek for similar patterns with respect to quantitative trait variation in other systems, such as human populations.

References

1. J. Flint, T. F. C. Mackay, *Genome Res.* **19**, 723 (2009).
2. M. V. Rockman, S. S. Skrovanek, L. Kruglyak, *Science* **330**, 372 (2010).
3. W. Stephan, *Phil. Trans. R. Soc. B.* **365**, 1245 (2010).
4. J. M. Smith, J. Haigh, *Genet. Res.* **23**, 23 (1974).
5. B. Charlesworth, M. T. Morgan, D. Charlesworth, *Genetics* **134**, 1289 (1993).
6. M. Kimura, *The Neutral Theory of Molecular Evolution* (Cambridge Univ. Press, Cambridge, 1983).
7. R. R. Hudson, N. L. Kaplan, *Genetics* **141**, 1605 (1995).

10.1126/science.1197700

APPLIED PHYSICS

Filling the Light Pipe

David J. Richardson

As data transmission rates continue to increase, optoelectronic engineers are developing techniques to deal with the approaching "capacity crunch."

It has been a landmark year for the field of optical telecommunications, with the award of the 2009 Nobel Prize to Charles Kao for his insight in the mid-1960s that the future of communications lay in single-mode silica-based optical fibers (*1*) as well as the 50th anniversary of the first demonstration of the laser—both key technologies responsible for the development of the global-scale communications networks of today (*2*). Recently, however, a growing realization has emerged within the telecommunications industry that the end of the phenomenal growth in optical fiber communication capacity is within sight. At this year's Optical Fiber Communication Conference (OFC 2010), several groups reported results within a factor of ~2 of the ultimate capacity limits of existing optical fiber technology. Without radical innovation in our physical network infrastructure—that is, improvements in the key physical properties of transmission fibers and the optical amplifiers that we rely on to transmit data over long distances—we face what has been widely referred to as a "capacity crunch" that could severely constrain future Internet growth, as well as having social and political ramifications.

Most of the information we exchange over the Internet is carried through optical fibers encoded on a beam of laser light. Data traffic on the world's networks is growing at around 40% year-on-year (*3*). This growth is driven primarily by social networking, cloud computing, and bandwidth-hungry video services such as YouTube. Video is responsible for most of the increased demand, and with high definition firmly established in the marketplace and both 3D and ultrahigh-definition formats emerging, this trend is set to continue.

The data-carrying capacity of a single optical fiber is determined by the spectral bandwidth over which suitably low-loss signal transmission can be achieved and our technical ability to exploit this bandwidth through suitable data coding and decoding schemes. The bandwidth of current fiber systems is limited to around 11 THz by the optical amplifiers used to boost the power of flagging signals attenuated by fiber transmission loss. Until relatively recently this bandwidth was considered to be effectively infinite, and the primary issue was one of developing cost-effective means to keep pace with the increasing traffic demands. Key to this has been the development of a technique referred to as

Optoelectronics Research Centre, University of Southampton, Southampton SO17 1BJ, UK. E-mail: djr@orc.soton.ac.uk

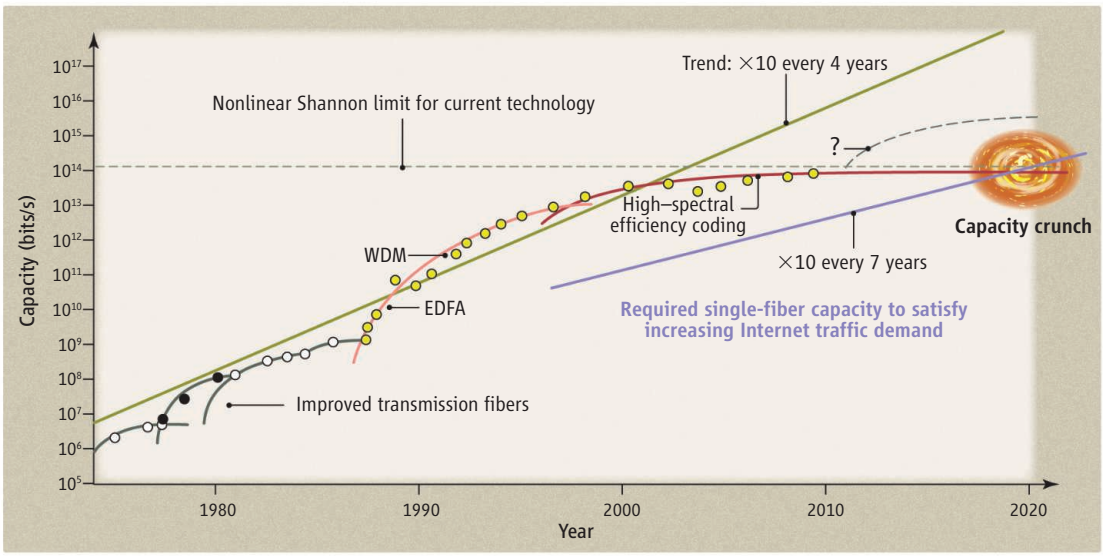

And on the data flows. The figure shows both the record data transmission capacity of fiber transmission systems (numerical values scaled to be representative for a ~1000-km system) as a function of year along with an estimate of the single-fiber capacity required to meet the 40% per annum in Internet traffic. The nonlinear Shannon limit for the existing fiber technology is rapidly being approached and a "capacity crunch" looms ahead without major innovation in the basic fiber infrastructure used within our networks, as illustrated by the question mark labeling the idealized future growth curve. Progress toward the capacity limit of current fiber technology has resulted from several key breakthroughs over the years, which include the development of low-loss, single-mode transmission fiber, the invention of the erbium-doped fiber amplifier (EDFA), the development of wavelength division multiplexing (WDM), and most recently the development of DSP-based coherent detection, which allows for high-SE signaling. Although a capacity crunch has been marked around 2020, this should not be taken too literally, as there is considerable uncertainty in this date given differing estimates of traffic growth for different countries and different future fiber deployment scenarios.

wavelength division multiplexing (WDM) in which the bandwidth is occupied by multiple, independent and spectrally distinct wavelength channels each carrying encoded data.

The maximum amount of information that can be transported per unit bandwidth for each WDM channel is quantified by a number referred to as the spectral efficiency (SE) as measured in terms of numbers of bits per second per Hz (b/s/Hz). An upper bound on the SE was established by Claude Shannon in 1948 on the basis of fundamental information theory principles and is given by $SE = \log_2(1 + SNR)$ where SNR is the signal-to-noise ratio (*4*). It was later shown that optical nonlinearity, which restricts the signal powers that can be usefully sent through the fiber for a given transmission distance, limits the SE values that can be achieved in practice (*5*). The current consensus is that the maximum practical value is likely to be ~10 b/s/Hz. Such values of SE should be possible using advanced coding schemes borrowed from radio communications that exploit the phase, amplitude, and polarization of the optical field (*6*).

Until recently, binary amplitude coding (turning the laser on and off to define "1" and "0" bits, respectively) was the preferred and only practical coding option—providing for SEs of less than 1 b/s/Hz and considerably much less in most practical implementations. However, as a result of steady technological improvements, most notably in the speed and power of electronic digital signal processing (DSP), the use of (coherent) phase encoding has now become possible. Moreover, at the same time, through advances in laser and filtering technologies, the individual WDM wavelength channels can now be packed more closely together without intolerable interference, providing a further boost to overall bandwidth utilization. These developments have culminated in the flurry of impressive results at OFC 2010, which included demonstrations of a record 69.1 terabit/s data transmission over 240 km of fiber at a SE of 6.4 b/s/Hz (*7*), 64 terabit/s transmission over 320 km at a SE of 8.0 b/s/Hz (*8*), and finally, extending the distance, transmission of quadrature phase shift–keyed signals at 3 b/s/Hz over >10,600 km (*9*). These are staggering results and are within a factor of ~2 of the nonlinear Shannon limit for the current fiber technology, and it is therefore hard to envisage substantial further improvements. Although it will take much effort to transfer these high-SE results over to commercial systems, it will provide welcome headroom for several years to come. However, in terms of capacity scaling of existing fiber systems, the end is within sight. Once the capacity of conventional single-mode fiber-based systems is exhausted, the only option will be to add additional parallel systems, an option that is highly undesirable from a cost and, ultimately, a power sustainability perspective.

Further innovation and breakthroughs in the basic fiber infrastructure are urgently required. Potential ways forward include the use of spatial division multiplexing, where N optical cores rather than one are incorporated within the fiber to provide a factor of N increase in the data-carrying capacity; the development of broader-bandwidth amplifiers; reduction of fiber attenuation; and the mitigation of optical nonlinearity (either by reducing the nonlinearity of the transmission fiber itself, or by introducing active electronic or optical means to compensate it). However, it should be stressed that while many ideas exist, improving upon the current technology will be extremely challenging and network operators will also need to look increasingly at ways of reducing traffic—for example, by caching data locally throughout the network, because storing large amounts of data is far easier and cheaper than transmitting it over long distances. Perhaps adopting different charging models for Internet use could also substantially affect traffic demands, and we may all increasingly need to get used to the idea that bandwidth (just like water and energy) is a valuable commodity to be used wisely.

References

1. K. C. Kao, G. A. Hockham, *Proc. IEEE* **113**, 1151 (1966).
2. T. H. Maiman, *Nature* **187**, 493 (1960).
3. Cisco Visual Networking Index: Forecast and Methodology, 2009–2014 (www.ciscosecure.net/en/US/solutions/collateral/ns341/ns525/ns537/ns705/ns827/white_paper_c11-481360_ns827_Networking_Solutions_White_Paper.html).
4. C. E. Shannon, *Bell System J.* **27**, 379 (1948).
5. P. P. Mitra, J. B. Stark, *Nature* **411**, 1027 (2001).
6. R.-J. Essiambre, G. J. Foschini, G. Kramer, P. J. Winzer, *Phys. Rev. Lett.* **101**, 163901 (2008).
7. A. Sano *et al.*, in *Proceedings of the 2010 Optical Fiber Communication Conference* (Optical Society of America, Washington, DC, 2010), PDPB7.
8. X. Zhou *et al.*, in *Proceedings of the 2010 Optical Fiber Communication Conference* (Optical Society of America, Washington, DC, 2010), PDPB9.
9. J. X. Cai *et al.*, in *Proceedings of the 2010 Optical Fiber Communication Conference* (Optical Society of America, Washington, DC, 2010), PDPB10.

10.1126/science.1191708

CIRCADIAN RHYTHMS

Temperatures to Communicate By

Temperature changes synchronize circadian clocks in organs that can't sense light-dark cycles.

Isaac Edery

If a large orchestra were suddenly without a conductor, the individual players could continue to play music, but the overall harmony of the symphony likely would be lost. This relationship is analogous to the circadian timing system in mammals, which governs the wake-sleep cycle and synchronizes biological processes and behaviors to roughly 24-hour time periods. In the mammalian brain, a "master clock" located in the suprachiasmatic nucleus (SCN) of the hypothalamus keeps in sync the many independent clocks located in tissues and organs throughout the body (*1*). The coherence of these peripheral clocks is achieved presumably through a two-tiered system in which the master clock follows the daily light-dark cycles, informed by ocular pathways that detect light. Somehow this temporal information is converted to nonphotic cues that permeate the rest of the body, coordinating the oscillation of peripheral clocks (*2*). On page 379 of this issue, Buhr *et al*. show fascinating differences in the properties of the mouse SCN and peripheral clocks that provide a simple yet elegant model for how peripheral clocks "see" the light initially perceived by the SCN (*3*).

Buhr *et al*. found that although the SCN can be entrained (synchronized) by daily light-dark cycles, it is resistant to fluctuations in body temperature. Just the opposite is true for peripheral clocks. In animals, core body temperature undergoes daily rhythms, fluctuating between 2° and 4°C. Buhr *et al*. show that this oscillation is sufficient to synchronize clocks in a wide variety of tissues. Thus, the SCN's ability to drive core body temperature rhythms, while remaining resistant to temperature cycles itself, enables it to function as a master clock that uses the universal language of temperature to communicate temporal information to subsidiary cellular clocks (see the figure).

The findings of Buhr *et al.* also shift the debate on the relative importance of thermal signals in the circadian systems of organisms. The body temperature of ectoderms depends on the surrounding environment and is controlled through external means

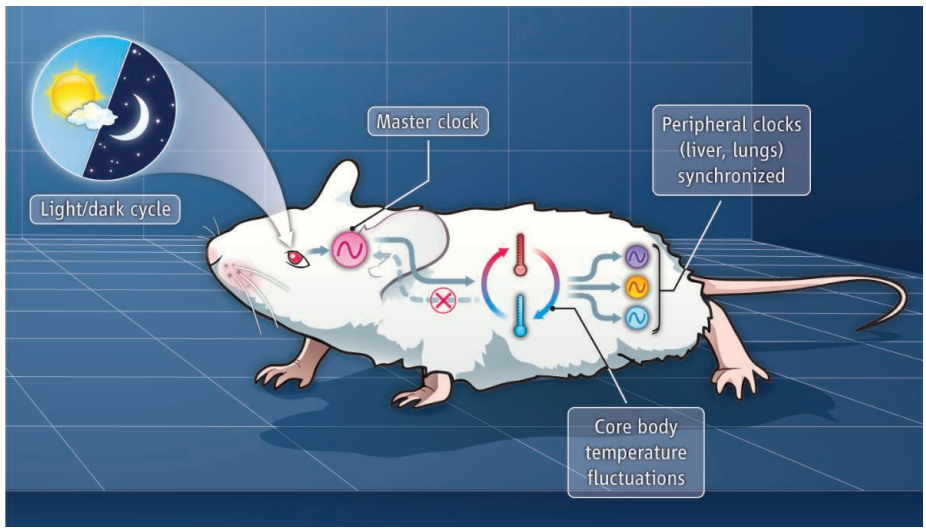

Keeping clocks in sync. The mammalian master clock in the brain's suprachiasmatic nucleus (SCN) controls fluctuations in core body temperature in response to daily light-dark cycles. These cyclical temperature changes synchronize the oscillation of circadian clocks in peripheral tissues. The SCN is resistant to temperature change.

(such as exposure to the heat of the Sun). By contrast, endotherms maintain a certain body temperature despite large variations in the surrounding environmental temperature. Although temperature entrainment is widely observed in ectothermic organisms (such as insects and reptiles), very few examples have been reported for endotherms (*4*). The obvious rationale is that the homeostatic mechanisms operating in thermoregulatory endothermic organisms would also render their clocks largely insensitive to the small daily changes in body temperature. However, recent work has raised the possibility of temperature as an entraining agent of mammalian peripheral clocks. For example, circadian gene expression in rat fibroblasts cultured in vitro and in livers of intact mice can be entrained by "square-wave" temperature rhythms (alternating regularly between two temperatures), but these changes in ambient temperature have no effect on the phase of the independent cellular clocks in the SCN (*5*). Buhr *et al*. expand on these findings by using genetically altered mice that express a bioluminescence protein (a reporter) to reflect circadian gene expression in real time. They show that explants of many tissues, such as lung and pituitary, have circadian clocks that can be synchronized not only to square-wave temperature cycles but also to "natural" conditions that reproduce the endogenous core body rhythms of mice.

Why is the master clock in the SCN resistant to temperature cycles? After all, the core molecular mechanisms underlying this and the peripheral clocks are very similar, if not identical (*6*). Even though individual SCN neurons can exhibit cell-autonomous circadian oscillators, neuronal network properties are integral to their synchronization and thus to the normal function of the master clock. The SCN is a bilaterally paired structure of about 10,000 neurons each, with distinct anatomic subdivisions and functional properties (*1*). The findings of Buhr *et al*. indicate that resistance of the SCN clock to temperature entrainment is a higher-order network property. For example, SCN explants acquire sensitivity to perturbation by temperature pulses when treated with drugs that block communication among neurons.

Clocks in isolated brains of the model fly *Drosophila melanogaster* can be entrained by photic cues but not by temperature cycles (*7*). Moreover, altering the neuronal circuitry of the central clock in the *Drosophila* brain decreases its resistance to entrainment by temperature cycles (*8*). Perhaps the master clock in the brains of animals, which directly governs the all-encompassing wake-

Department of Molecular Biology and Biochemistry, Center for Advanced Biotechnology and Medicine, Rutgers University, Piscataway, NJ 08854, USA. E-mail: edery@cabm.rutgers.edu

CREDIT: Y. HAMMOND/*SCIENCE*

Published by AAAS

sleep cycle, evolved complex network structures to ensure that its ticking is firmly synchronized with the daily light-dark cycle—a very reliable and predictable measure of external time.

Buhr *et al*. also make inroads into the molecular pathways involved in temperature entrainment by building on an old idea that the heat shock response plays a role in circadian systems (*9*). In animals, a sudden temperature jump can induce the oligomerization of heat shock transcription factor 1 (HSF1), leading to the production of a diverse group of heat shock proteins (Hsps) (*10*) whose function includes stabilizing proteins under stressful conditions. Intriguingly, the expression level of Hsp70 exhibits a diurnal rhythm in humans, which suggests that the heat shock response can track slight variations in core body temperature (*11*). Buhr *et al*. show that compounds that specifically inhibit HSF1 function also block the ability of heat pulses to shift the phases of peripheral clocks. Ultimately, to evoke such a shift requires changes in the oscillations of central clock genes in peripheral clocks. Several clock proteins exhibit a binding site for HSF1 (*12*). Roles for temperature and HSF1 in the circadian systems of mammals are part of an emerging realization of the deep interconnections between metabolism and peripheral clock function (*13*).

Thus, despite the homeostatic regulation of temperature in endotherms, seemingly slight fluctuations in core body temperature—if occurring at regular intervals—appear to be a major modality used to track the cyclical changes imposed by Earth's rotation on its axis. It will be important to understand the extent to which ambient temperature modulates core body temperature rhythms in endotherms, possibly helping peripheral clocks to undergo seasonal adjustments.

References

1. D. K. Welsh *et al*., *Annu. Rev. Physiol.* **72**, 551 (2010).
2. C. Dibner *et al*., *Annu. Rev. Physiol.* **72**, 517 (2010).
3. E. D. Buhr *et al*., *Science* **330**, 379 (2010).
4. L. Rensing, P. Ruoff, *Chronobiol. Int.* **19**, 807 (2002).
5. S. A. Brown, G. Zumbrunn, F. Fleury-Olela, N. Preitner, U. Schibler, *Curr. Biol.* **12**, 1574 (2002).
6. H. Dardente, N. Cermakian, *Chronobiol. Int.* **24**, 195 (2007).
7. H. Sehadova *et al*., *Neuron* **64**, 251 (2009).
8. A. Busza *et al*., *J. Neurosci.* **27**, 10722 (2007).
9. L. Rensing *et al*., *Chronobiol. Int.* **4**, 543 (1987).
10. R. Voellmy, *Cell Stress Chaperones* **9**, 122 (2004).
11. M. E. Sandström *et al*., *Amino Acids* **37**, 279 (2009).
12. H. Reinke *et al*., *Genes Dev.* **22**, 331 (2008).
13. M. Stratmann, U. Schibler, *J. Biol. Rhythms* **21**, 494 (2006).

10.1126/science.1197747

EVOLUTION

RNA GPS

Detailed "fitness landscapes" could reveal the paths for evolution of function.

Christien Kluwe and Andrew D. Ellington

For most of recorded human history, maps had a local focus and were used to navigate from landmark to landmark. This changed with the invention of the sextant, which for the first time allowed us to place ourselves relative to an external standard such as the Sun, Moon, or a distant star. Maps quickly became global, although navigation was still largely local. Then we decided to build our own star-equivalents, satellites, and it became possible to have a Global Positioning System (GPS) that could determine our location to within meters.

On page 376 of this issue, Pitt and Ferré-D'Amaré (*1*) offer what is, in essence, a GPS for RNA. They use "next-generation" (NextGen) sequencing methods, computer analysis, and a selection experiment to show that a molecular sequence's abundance is correlated with peak fitness for a particular function and to produce detailed "fitness landscapes." The method offers insights into how molecules evolve and could help researchers more quickly map the best routes to optimal functional sequences for developing new vaccines or drugs.

In their experiment, the authors evaluated the catalytic abilities of large pools of ribozymes that rejoin strands of RNA. The ribozymes were allowed to react with beads coated with an RNA substrate. Then, at various times, they removed the molecules that became bound to the beads, thus "selecting" the most "successful" (or fittest) variants, and sequenced them. Tapping the relative ease, speed, and power of NextGen sequencing methods, the researchers were able to analyze the ribozymes captured via ligation in depth, and create a classic fitness landscape (see the figure) with extraordinarily high resolution, comprising ~10^7 unique RNA genotypes.

In general, the fittest genotypes for a particular function are found at the peaks in such landscapes, and less fit sequences are down in the valleys. The landscape can help researchers see potential paths to acquiring new or desired functions through mutation. As a result of Pitt and Ferré-D'Amaré's work, it is now possible to provide a comprehensive picture of the fitness landscape surrounding a ribozyme, without making painstaking serial measurements of the fitness of this army of mutant "neighbors." In addition, the information content of individual sequences can be readily determined in a single experiment, and mutual information (covariation) helps to reveal secondary structures [such as a transfer RNA (tRNA) cloverleaf].

Each successive generation of DNA technologies brings about a deeper understanding of evolution, and this work can be seen as a logical extension of using microarray technology to recapitulate fitness landscapes. For example, researchers generated an array containing single through triple point mutants of the anti-IgE (immunoglobulin E) DNA aptamer and measured the IgE-binding abilities of 44,000 individual mutants in parallel (*2*). The vast majority of mutations handicapped binding, suggesting that even minor changes in sequence greatly reduced fitness.

Prior to this work, fitness landscapes for functional RNAs were charted using more of a sextant. Investigators used multiple rounds of directed evolution to cull fit from unfit sequences, and they frequently assumed that the relative representation of "active" binding or catalytic species was a measure of relative function (more common species were more active). However, fitness during evolution can mean many things other than just catalytic efficiency. For instance, the original selection process that yielded the class II Bartel ligase used by Pitt and Ferré-D'Amaré also produced a wealth of different ligases; the more highly represented species, however, were not necessarily the fastest-acting. Less functional species may have predominated either because they contained shorter motifs or because they were more highly replicable. Indeed, one seminal study suggested that simpler structures were less fit, but became preferentially ampli-

Department of Chemistry and Biochemistry, University of Texas at Austin, Austin, TX 78712 USA. E-mail: andy.ellington@mail.utexas.edu

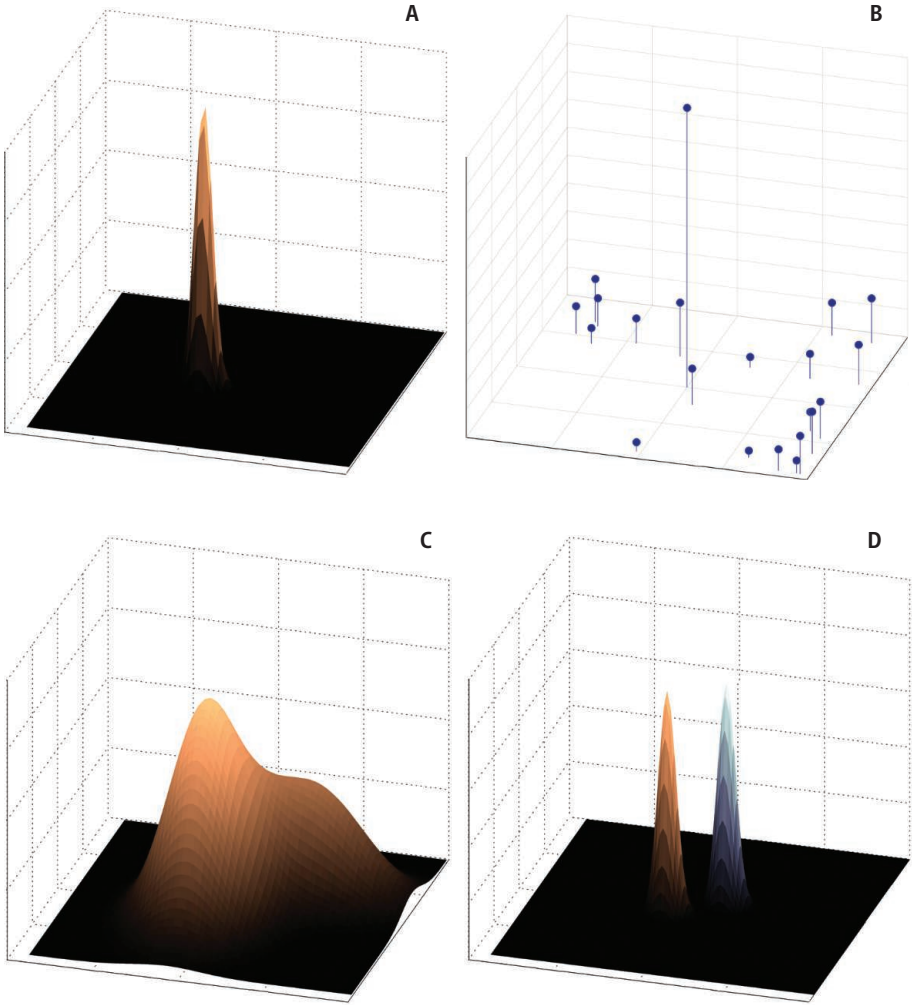

Experimental fitness landscapes. A high-resolution landscape developed with NextGen sequencing methods (**A**) provides extensive data for high-density mapping, compared to the pointillated landscapes constructed previously (**B**). Although the landscapes in (A) and (B) seem to suggest that unnatural catalysts extracted from large libraries can reach peak fitness, a naturally evolved ribozyme species may have more available paths for evolution to new fitness peaks (**C**). The peak fitness of a functional nucleic acid (orange) may be farther from sequences with similar functions than from a new functional phenotype (blue) (**D**).

fied, even though more complex sequences were much more functional (*3*).

The question of whether we need a GPS for RNA is in part dependent upon the nature of the fitness landscapes discovered. If sequence changes are highly correlated with changes in function, then even a small number of points may describe the landscape. If sequence and function are not closely correlated, then successfully navigating the landscape will require more detailed knowledge of the many abrupt peaks and drop-offs. In the case of Pitt and Ferré-D'Amaré, the landscape proved to be relatively steep and narrow; most individual mutations greatly decreased functionality and there was not a large neutral plateau where sequence changes did not strongly affect function. This conclusion is consonant with results from previous studies (*4*).

The steep peaks observed in the current and previous studies seemingly stand in contrast to other work from Lehman and co-workers (*5*). The *Tetrahymena* Group I self-splicing intron was set the task of using calcium rather than magnesium, and the sequences of evolving variants were determined (albeit not at the resolution available today). Rather than just falling quickly off of its peak, there appeared to be multiple paths by which new function could be acquired. It is tempting to hypothesize that unnatural, functional RNA molecules, originally borne of a large random population, have very different fitness landscapes than natural, functional RNA molecules, which have spent billions of years descending from a single ancestor via short mutational moves (see the figure). Although this hypothesis has not yet been tested, recent work has suggested that both natural and unnatural functional nucleic acids have similar compositions (*6*).

If the landscapes for unnatural and natural nucleic acids are truly different, then it may be difficult for unnatural nucleic acids to acquire new function. So far, however, this has not proven to be the case. For instance, flavin adenine dinucleotide (FAD)–binding aptamers could acquire guanosine monophosphate (GMP)–binding function via a relatively small number (five) of mutations (*7*), while the class III Bartel ligase could become a ribozyme cleavase via a similar number of mutational steps (four) (*8*). It is odd that sequences that cannot reacquire their own function after undergoing a small number of mutational steps (as shown in depth by Pitt and Ferré-D'Amaré) can suddenly acquire new functions in just a few additional mutational steps. What gives?

One solution to this conundrum is that the overall function space (the area holding possible functions) is more densely packed than we might have imagined, with many new functions being close to old ones (see the figure). Theoretical work by Schuster and Fontana (*9*), who simulated in silico the evolution of a random population of RNAs to a tRNA-like shape, bolsters this hypothesis. Their work showed that large changes in fitness occurred primarily by discontinuous transitions. Sequences would percolate along, accumulating neutral or bifunctional mutations, before jumping to a new shape and/or function. Such jumps would not necessarily recapitulate old function, but might very well allow the acquisition of new function. If this turns out to be true, then the early evolution of the RNA world might have been easier than previously imagined, because each new catalyst would have been able to duplicate and quickly jump to a new function.

References

1. J. N. Pitt, A. R. Ferré-D'Amaré, *Science* **330**, 376 (2010).
2. E. Katilius, C. Flores, N. W. Woodbury, *Nucleic Acids Res.* **35**, 7626 (2007).
3. J. M. Carothers, S. C. Oestreich, J. H. Davis, J. W. Szostak, *J. Am. Chem. Soc.* **126**, 5130 (2004).
4. M. Levy, K. E. Griswold, A. D. Ellington, *RNA* **11**, 1555 (2005).
5. N. Lehman, M. D. Donne, M. West, T. G. Dewey, *J. Mol. Evol.* **50**, 481 (2000).
6. R. Kennedy *et al.*, *RNA* **16**, 280 (2010).
7. D. M. Held, S. T. Greathouse, A. Agrawal, D. H. Burke, *J. Mol. Evol.* **57**, 299 (2003).
8. E. A. Schultes, D. P. Bartel, *Science* **289**, 448 (2000).
9. W. Fontana, P. Schuster, *Science* **280**, 1451 (1998).

10.1126/science.1197667

SOCIAL SCIENCE

The Benefits of Multilingualism

Bilingual rearing of children, instead of confusing them, may bring lifelong advantages.

Jared Diamond

Multilingualism—the ability to understand and speak several languages—is exceptional in the United States but common elsewhere, especially in small-scale traditional societies. For instance, once while I was camped with some New Guinea Highlanders conversing simultaneously in several local languages, I asked each man to name each language in which he could converse. It turned out that everyone present spoke at least 5 languages, and the champion was a man who spoke 15. What are the cognitive effects of such multilingualism? Recent studies (*1*–*5*) show that children raised bilingually develop a specific type of cognitive benefit during infancy, and that bilingualism offers some protection against symptoms of Alzheimer's dementia in old people.

Competing inputs. A typical moment in the life of a typical *Science* reader, who is simultaneously processing various sensory inputs with his eyes, ears, nose (the smell of the food), skin touch receptors (the friend's handshake, the briefcase being held), and proprioreceptors (the cramp in his leg), and having competing thoughts. Depending on the circumstances, any one of those stimuli or thoughts may warrant full attention. Recent studies suggest that multilingual people may have an advantage over monolinguals in sifting and managing these distracting stimuli.

Bilingual education is politically controversial in the United States. Even immigrants whose native language is not English often believe that their children should learn only English and will be confused by learning two languages simultaneously. Until the 1960s, research appeared to show that bilingual children acquired language more slowly than monolingual children and achieved smaller vocabularies. But other variables correlated with bilingualism in those early studies, such as schooling and parental socioeconomic status, confounded their interpretation. More recent studies, comparing subjects matched for those other variables, have found bilinguals and monolinguals to be largely similar in cognition and language processing (*6*–*8*).

The clearest difference identified by these studies involves an advantage that bilinguals have over monolinguals, rather than a disadvantage. Our minds are assaulted by varied sights, sounds, and other external sensory inputs, plus thoughts and proprioceptive sensations (which make us aware of the relative positions of our own body parts) (see the figure). To succeed in doing anything at all, we must temporarily inhibit 99% of those inputs and attend to just 1% of them, and the appropriate choice varies with the circumstances. That selective attention involves a set of processes, termed executive function, that reside in the prefrontal cortex and develop especially over the first 5 years of life (*9*).

Multilingual people have a special challenge involving executive function. Monolinguals hearing a word need only compare it with their single stock of arbitrary phoneme (sound) and meaning rules, and when uttering a word they draw it from that single stock. But multilinguals must keep several stocks separate. For instance, on hearing the phonemes b-u-rr-o, a Spanish/Italian bilingual instantly interprets them to mean either "donkey," if the context is Spanish, or "butter," if the context is Italian. Multilinguals participating in a multilingual conversation, like my New Guinea Highland friends or shop assistants in Scandinavian department stores, switch frequently and unpredictably between their stocks of phoneme/meaning rules. As a result, multilinguals have constant unconscious practice in using the executive function system.

Recent studies assess this ability by assigning to subjects game-like tasks designed to be confusing, either because the task rules change unpredictably, or because the task presents misleading cues that must be ignored (*1*–*3*, *7*, *8*). For instance, children are shown cards depicting either a rabbit or a boat, colored either red or blue, with or without a star. If the card has a star, the children must sort cards by color; if a star is absent, they must instead sort cards by the object depicted. It turns out that monolingual and bilingual subjects are equally successful if the rule remains the same from trial to trial (e.g., "sort by color"), but monolinguals have more difficulty than bilinguals at accommodating to a switch in rules. Although success at these games won't by itself make one rich or happy, our lives are full of other misleading information and rule changes. If bilinguals' advantage over monolinguals in these games also applies to real-life situations, that could be useful for bilinguals.

While this superior executive function has been reported for bilinguals of all ages, results for the youngest and the oldest subjects are of particular interest. Kovács and Mehler (*4*, *5*) tested confusing game tasks on "monolingual" infants and "crib bilingual" infants—i.e., infants reared from birth to hear and eventually to speak two languages, because mother and father speak to the infant in different languages. It might seem meaningless to describe infants who cannot speak as monolingual or bilingual. Actually, infants learn to discriminate the sounds of the language or languages heard around them and to ignore sound distinctions not heard around them. For instance, Japanese infants lose, and English infants retain, the ability to discriminate the liquid consonants l and r, which the Japanese language does not distinguish.

How can one test responses to speech by those preverbal infants? Kovács and Mehler (*4*, *5*) devised a clever protocol in which infants looked for pictures of a puppet appearing on

Geography Department, University of California Los Angeles, Los Angeles, CA 90095–1524, USA. E-mail: jdiamond@geog.ucla.edu

Published by AAAS

the left side of a computer screen. The infants were conditioned to anticipate the puppet by first hearing a nonsense trisyllable (e.g., "lo-lo-vu"). Within nine trials, both monolingual and bilingual infants learned to look toward the screen's left side when they heard that trisyllable. But when Kovács and Mehler changed the rules and made the puppet appear on the screen's right side after broadcasting a different trisyllable, the "bilingual" infants unlearned their previous lesson and learned the new response within six more trials. In contrast, the "monolingual" infants couldn't learn the new response even after nine trials. Evidently, shifting frequently and unpredictably between hearing two parental languages made "bilingual" infants better able to cope with other unpredictable rule changes.

Do these findings suggest that bilinguals have an advantage over monolinguals in negotiating our confusing world of changing rules, and not merely in the task of discriminating lo-lo-vu from lo-vu-lo? You readers may demand evidence of more tangible benefits before you commit yourselves to babbling in two different languages to your infant children. Hence, you may be more impressed by recent results suggesting a protective effect of lifelong bilingualism against symptoms of Alzheimer's disease (*10*). Among hundreds of elderly Canadian patients with a probable Alzheimer's diagnosis, bilingual patients showed their first symptoms at an age 5 years older than did monolingual patients matched in other respects. Canadian life expectancy is 79, hence a 5-year delay for people in their 70's translates into a 47% decreased probability that they will develop Alzheimer's symptoms at all before they die.

How might this be? A short answer is the aphorism, "Use it or lose it." Exercising body systems improves their function; not exercising them lets their function deteriorate. That's why athletes and musicians practice. It's also why Alzheimer's patients are encouraged to play brain-challenging games like bridge or to solve Sudoku puzzles. But bilingualism is arguably the most constant practice possible for the brain. Whereas even a Sudoku fanatic can spend only a fraction of a day on Sudoku puzzles, bilinguals impose extra exercise on their brain every minute of their waking hours. Consciously or unconsciously, the bilingual brain constantly has to decide: Shall I think, speak, or interpret sounds spoken to me according to the arbitrary rules of language A or language B?

There are other unanswered questions. If one extra language offers some protection, do two extra languages offer more protection? If so, is the relationship between protection and number of extra languages linear, sublinear, or supralinear? For example, if bilinguals get 5 years of protection from their one extra language, do Scandinavian shop assistants speaking five languages also get just 5 years of protection, or do they get $5 \times 4 = 20$ years of protection? If you, alas, were not raised as a crib bilingual, will learning a second language in school let you catch up? Do bilinguals' advantages in coping with rule changes and confusing cues extend beyond trivial game tasks to real-life situations, such as school success and understanding other peoples' mental states? What neural mechanisms underlie bilingualism's reported protection against Alzheimer's symptoms? These questions will be of theoretical interest to linguists, and of practical interest to parents wondering how best to raise their children.

References

1. E. Bialystok, *Dev. Psychol.* **46**, 93 (2010).
2. E. Bialystok, X. Feng, *Brain Lang.* **109**, 93 (2009).
3. E. Bialystok, M. Viswanathan, *Cognition* **112**, 494 (2009).
4. A. M. Kovács, J. Mehler, *Science* **325**, 611 (2009).
5. A. M. Kovács, J. Mehler, *Proc. Natl. Acad. Sci. U.S.A.* **106**, 6556 (2009).
6. E. Bialystok, *Bilingualism and Development* (Cambridge Univ. Press, New York, 2001).
7. S. M. Carlson, A. N. Meltzoff, *Dev. Sci.* **11**, 282 (2008).
8. A. Costa, M. Hernández, N. Sebastián-Gallés, *Cognition* **106**, 59 (2008).
9. T. Shallice, *From Neuropsychology to Mental Structure* (Cambridge Univ. Press, Cambridge, 1988)
10. E. Bialystok, F. I. Craik, M. Freedman, *Neuropsychologia* **45**, 459 (2007).

10.1126/science.1195067

MATERIALS SCIENCE

Recasting Metal Alloy Phases with Block Copolymers

Highly complex metal alloy phases have been replicated at a larger scale with spherical aggregates formed from polymers.

Mihai Peterca and Virgil Percec*

Crystalline order develops through a balance between short-range attractive and repulsive interactions (*1*) that not only operate on atoms but work at the nanoscale on supramolecular structures (*2*). Spherical particles often pack together into simple, high-symmetry arrangements, but more complex topologically close-packed structures, such as the Frank-Kasper σ phase (*3*, *4*) first seen in metal alloys, have also been observed (see the figure, panel A). Spherical supramolecular aggregates formed from polymers and monodisperse branched macromolecules (*5*–*7*) can be used to mimic atoms and explore how these phases arise. On page 349 of this issue, Lee *et al*. (*8*) show that linear block copolymers that form spherical aggregates through microphase separation can crystallize into a Frank-Kasper σ phase. Relative to metal alloys, the volume of its crystalline repeating unit, the unit cell, is six orders of magnitude greater (see the figure, panel C). The scaling up of atomic lattices by using spherical supramolecular aggregates is also of practical interest because such structures could be used as photonic materials (*9*), nanoreactors (*5*), or drug delivery vehicles (*10*).

Understanding how spherical supramolecular aggregates organize into crystals remains a challenging task. In the ideal case of incompressible "hard" spheres—which are a good model for metal atoms—the most stable structures correspond to the hexagonal close-packed (hcp) and face-centered cubic (fcc) periodic close-packing configurations shown in panel A of the figure. These structures maximize the packing of atoms and fill 74% of their unit cell volume (versus 68% for the body-centered cubic, or bcc, packing). The stability of the packing derives from large numbers of nearest neighbors interactions that decrease free energy.

Spherical aggregates formed by soft macromolecules, including block copolymers, should follow the same principle and pre-

Roy and Diana Vagelos Laboratories, Department of Chemistry, University of Pennsylvania, Philadelphia, PA 19104–6323, USA. *To whom correspondence should be addressed. E-mail: percec@sas.upenn.edu

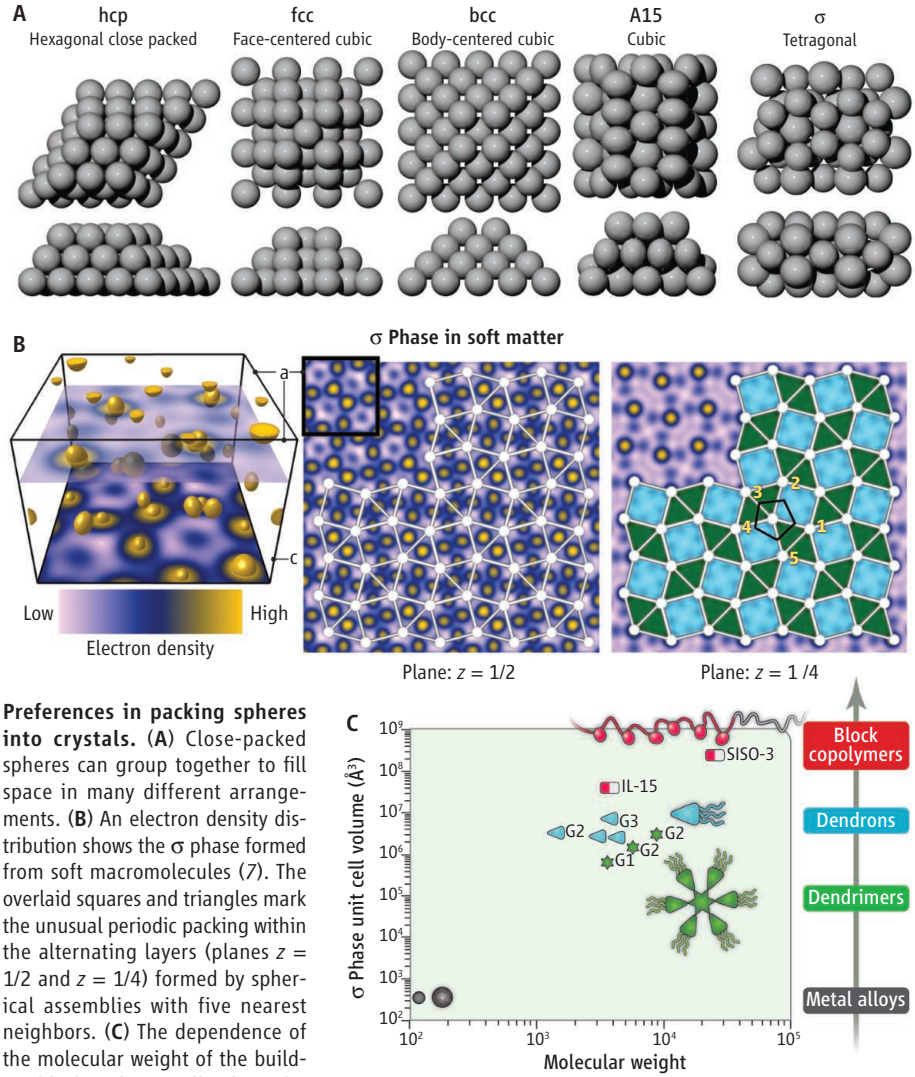

Preferences in packing spheres into crystals. (**A**) Close-packed spheres can group together to fill space in many different arrangements. (**B**) An electron density distribution shows the σ phase formed from soft macromolecules (*7*). The overlaid squares and triangles mark the unusual periodic packing within the alternating layers (planes z = 1/2 and z = 1/4) formed by spherical assemblies with five nearest neighbors. (**C**) The dependence of the molecular weight of the building block and unit cell volume for the σ phase illustrating the scaling-up principle in soft matter. The large unit cells seen by Lee *et al*. result from the large spherical aggregates formed by hundreds of individual polymers. Data were calculated for metal alloys from (*4*), for self-assembling dendrons and dendrimers from (*13*, *16*–*19*), and for block copolymers from (*8*).

dominantly self-organize into hcp, fcc, and bcc structures (*6*). However, compared to atoms, such aggregates are more compressible—they have intrinsic "softness"—which can be expected to create slight deviations from spherical symmetry that can favor other complex three-dimensional organizations. Such deviations are driven not only by minimization of the free energy of the overall crystal structure but also by changes within the aggregate (*11*) that are neglected in the simplistic "hard sphere" model.

One notable example in soft materials is the ubiquitous A15 cubic phase (see the figure, panel A) that self-organizes from spherical and oblate spherical (*12*) or polyhedral (*11*) supramolecular dendrimers, which are formed by monodisperse branched macromolecules resembling covalent or non-covalent bonded fractal structures. This cubic packing seems to replace (*13*) the fcc and bcc structures because of the peculiar internal structure of the supramolecular dendrimers that form it. They consist of a "hard" aromatic core surrounded by a "soft" aliphatic shell. This combination was shown theoretically to favor the A15 cubic packing that minimizes the surface free energy better than fcc and bcc structures (*14*) and to increase the filling of the unit cell volume to higher fractions, in the range of 76 to 83% (*12*). Remarkably, a few soft spherical aggregates self-assembled from dendrons (partial wedges of dendrimers), and dendrimers occasionally form unexpected quasiperiodic structures that have rotational symmetry but no translation symmetry (*15*–*17*) and σ phases (*16*–*19*). The rare occurrence of the σ phase in soft macromolecules is correlated with the formation of alternating layers populated by spherical assemblies exhibiting the atypical five first nearest neighbors within the layer (see the figure, panel B).

The study of first-order phase transitions driven by heating or cooling can also provide insight into the structural parameters that control the formation of these phases. Such control is essential to the next step of the scaling-up of structure seen in atomic and small-molecule crystals in soft matter. For example, the σ phase was consistently observed to form before the bcc phase upon heating (*8*, *19*). In this first example of the σ phase formed by block copolymers, Lee *et al*. attribute this order to the slightly lower surface area per unit volume in the σ phase compared to the bcc phase, which can account for a lower enthalpy (*8*). However, the similarity of the A15 and σ phases eluded a definitive assessment of their thermal order. Nevertheless, self-assembling dendrons and dendrimers exhibiting these two close-packing of spheres consistently reverse their thermal sequence from σ to A15, to A15 to σ, respectively, illustrating that the macromolecular topology (*7*) also plays an important role in selecting the type of close packing in soft matter.

The discovery of a new equilibrium phase in block copolymers, which have been studied for more than half a century, is truly rare. Their remarkable finding of the thermodynamically stable σ phase hints that block copolymers might also form quasiperiodic phases (*8*, *15*–*17*) and opens the door to the fabrication of other complex supramolecular organizations from soft nanomaterials.

References

1. J. M. Lehn, *Science* **295**, 2400 (2002).
2. G. M. Whitesides, B. Grzybowski, *Science* **295**, 2418 (2002).
3. F. C. Frank, J. S. Kasper, *Acta Crystallogr.* **12**, 483 (1959).
4. D. P. Shoemaker, C. B. Shoemaker, *Commun.* **42**, 3 (1986).
5. V. Percec *et al*., *Science* **328**, 1009 (2010).
6. F. S. Bates, G. H. Fredrickson, *Phys. Today* **52**, 32 (1999).
7. B. M. Rosen *et al*., *Chem. Rev.* **109**, 6275 (2009).
8. S. Lee, M. J. Bluemle, F. S. Bates, *Science* **330**, 349 (2010).
9. J. D. Joannopoulos, P. R. Villeneuve, S. H. Fan, *Nature* **386**, 143 (1997).
10. A. D. Dinsmore *et al*., *Science* **298**, 1006 (2002).
11. M. Peterca *et al*., *J. Am. Chem. Soc.* **132**, 11288 (2010).
12. V. Percec *et al*., *J. Am. Chem. Soc.* **130**, 13079 (2008).
13. B. M. Rosen *et al*., *J. Am. Chem. Soc.* **131**, 17500 (2009).
14. P. Ziherl, R. D. Kamien, *Phys. Rev. Lett.* **85**, 3528 (2000).
15. X. B. Zeng *et al*., *Nature* **428**, 157 (2004).
16. V. Percec *et al*., *J. Am. Chem. Soc.* **128**, 3324 (2006).
17. V. Percec *et al*., *J. Am. Chem. Soc.* **131**, 7662 (2009).
18. V. Percec, M. R. Imam, M. Peterca, D. A. Wilson, P. A. Heiney, *J. Am. Chem. Soc.* **131**, 1294 (2009).
19. G. Ungar, Y. S. Liu, X. B. Zeng, V. Percec, W. D. Cho, *Science* **299**, 1208 (2003).

10.1126/science.1196698

Published by AAAS

Why Testing Improves Memory: Mediator Effectiveness Hypothesis

Mary A. Pyc* and Katherine A. Rawson

An intuitive but incorrect assumption is that learning only occurs during study and that testing is useful only for evaluating the state of memory (*1*). However, testing improves memory, as demonstrated with a wide variety of materials and learners (*2*). Given the wealth of research establishing the empirical benefits of testing, it is surprising that the mechanisms underlying testing effects are not well understood.

We propose the mediator effectiveness hypothesis, stating that testing improves memory by supporting the use of more-effective mediators during encoding (a mediator is a word, phrase, or concept that links a cue to a target). What makes a mediator effective? Two key factors are mediator retrieval (i.e., mediator is recallable when prompted with the cue) and mediator decoding (i.e., mediator elicits the target from memory) (*3*). The mediator effectiveness hypothesis assumes that mediators generated during testing (versus restudy only) are more likely to be subsequently retrieved and decoded, increasing recall of target responses.

To test this hypothesis, we presented 118 participants with 48 Swahili-English translation pairs (e.g., wingu-cloud) for an initial study trial and then three blocks of practice trials. In the test-restudy group, each practice trial for an item involved a cued recall test followed immediately by restudy. In the restudy group, each trial involved only restudy. On the initial study trial and each restudy trial, all participants generated and reported keyword mediators (keywords are mediators that look or sound similar to the foreign language cue and are semantically related to the English target) (*4*). On the final test 1 week later, participants received only the cue (cue only, C group, as in prior research), the cue with their own mediator from practice (cue plus mediator, CM group), or the cue with a prompt to recall their own mediator before recalling the target (cue plus mediator recall, CMR group).

The mediator effectiveness hypothesis makes two key predictions. Concerning mediator retrieval, retrieval of mediators at the final test in the CMR group will be greater after test-restudy versus restudy practice. Concerning mediator decoding, retrieval of targets at final test in the CM group will be greater after test-restudy versus restudy practice.

Replicating the robust testing effects from prior research, test-restudy practice produced almost a threefold increase in final test performance in the C group (Fig. 1A). According to the mediator effectiveness hypothesis, this benefit is due to differential effectiveness of mediators, with testing improving mediator retrieval and decoding.

Confirming the prediction of increased mediator retrieval, recall of mediators at final test in the CMR group was greater after test-restudy versus restudy practice (51% versus 34%). For converging evidence, consider final test performance in the C and CM groups. Providing mediators at final test significantly improved recall after restudy practice but not after test-restudy practice, suggesting that explicitly providing mediators was largely redundant with participants' spontaneous retrieval of mediators in the test-restudy group.

Confirming the prediction of increased mediator decoding, final test performance in the CM group was significantly greater after test-restudy versus restudy practice. Even when differences in mediator retrieval were circumvented by providing participants with their mediators, mediators were more likely to elicit recall of targets after test-restudy versus restudy practice. As converging evidence, the same pattern is apparent when examining recall as a function of mediator retrieval in the CMR group (Fig. 1B). Although mediator retrieval benefited recall in both groups, the benefit was greater after test-restudy versus restudy practice. Furthermore, in trials in which mediators were retrieved, recall was greater after test-restudy versus restudy practice.

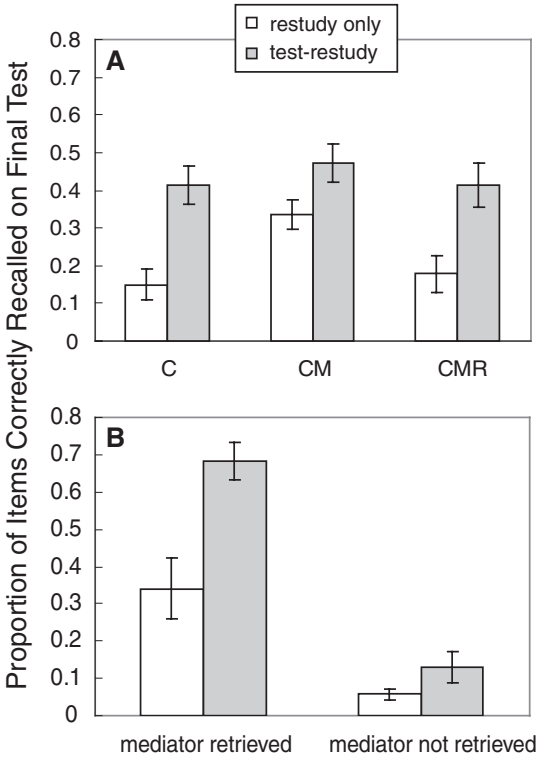

Fig. 1. (**A**) Final recall by group. (**B**) Final recall in CMR group as a function of whether mediators were retrieved before attempting target recall. Error bars represent standard errors.

Results support the mediator effectiveness hypothesis and offer one theoretical explanation for why testing is beneficial for memory: Mediators generated during encoding are more effective (i.e., more likely to be retrieved and decoded) with test-restudy versus restudy practice. We are not claiming that mediator effectiveness is the only mechanism underlying testing effects. However, mediator effectiveness may be an important contributor.

Why did testing yield more-effective mediators? Successfully retrieving mediators during practice may enhance their memory strength. Additionally, retrieval failures during encoding may promote shifting from less- to more-effective mediators (*5*), and retrieval failure occurs during testing but not restudy. Consistent with this idea, shifting to new keywords was more likely during test-restudy versus restudy practice (25% versus 19% of trials). Importantly, the mediator effectiveness hypothesis defines two components of mediator effectiveness (i.e., mediator retrieval and decoding), and results provide evidence for a contribution of each of these factors to the testing effect.

References and Notes

1. J. D. Karpicke, H. L. Roediger 3rd, *Science* **319**, 966 (2008).
2. H. L. Roediger, J. D. Karpicke, *Perspect. Psychol. Sci.* **1**, 181 (2006).
3. J. Dunlosky, C. Hertzog, A. Powell-Moman, *Dev. Psychol.* **41**, 389 (2005).
4. Materials, methods, and keyword example are available as supporting material on *Science* Online.
5. H. P. Bahrick, L. K. Hall, *J. Mem. Lang.* **52**, 566 (2005).
6. Research supported by a Collaborative Award from the James S. McDonnell Foundation 21st Century Science Initiative in Bridging Brain, Mind and Behavior.

Supporting Online Material

www.sciencemag.org/cgi/content/full/330/6002/335/DC1
Materials and Methods
References

26 April 2010; accepted 6 August 2010
10.1126/science.1191465

Department of Psychology, Kent State University, Kent, OH 44242, USA.

*To whom correspondence should be addressed. E-mail: mpyc@kent.edu

IDH2 Mutations in Patients with D-2-Hydroxyglutaric Aciduria

Martijn Kranendijk,[1]* Eduard A. Struys,[1] Emile van Schaftingen,[2] K. Michael Gibson,[3] Warsha A. Kanhai,[1] Marjo S. van der Knaap,[4] Jeanne Amiel,[5] Neil R. Buist,[6] Anibh M. Das,[7] Johannis B. de Klerk,[8] Annette S. Feigenbaum,[9] Dorothy K. Grange,[10] Floris C. Hofstede,[11] Elisabeth Holme,[12] Edwin P. Kirk,[13] Stanley H. Korman,[14] Eva Morava,[15] Andrew Morris,[16] Jan Smeitink,[17] Rám N. Sukhai,[18] Hilary Vallance,[19] Cornelis Jakobs,[1]† Gajja S. Salomons[1]

Recent studies in human cancer genetics have led to a resurgence of interest in a group of metabolic enzymes called isocitrate dehydrogenases. A recurrent heterozygous somatic mutation in the gene encoding cytosolic isocitrate dehydrogenase-1 (IDH1) is present in glioblastoma multiforme and alters residue Arg^{132} (R132) in the enzyme's active site (*1*). This mutation disables the enzyme's normal ability to convert isocitrate to 2-ketoglutarate (2-KG) and confers on it a new function: the ability to convert 2-KG to D-2-hydroxyglutarate (D-2-HG) (*2*). Heterozygous mutations that alter residues R140 and R172 of mitochondrial isocitrate dehydrogenase-2 (IDH2), the latter corresponding to R132 of IDH1, have been detected in other tumor types, acute myeloid leukemia and gliomas. These mutations also lead to abnormal production of D-2-HG (*3*, *4*).

This unusual pathophysiological mechanism prompted us to explore whether mutations in *IDH1* or *IDH2* are associated with D-2-hydroxyglutaric aciduria (D-2-HGA) (Mendelian Inheritance in Man no. 600721). D-2-HGA is a rare inherited neurometabolic disorder with a wide clinical spectrum. Although some children with D-2-HGA are asymptomatic, others exhibit characteristics that can include developmental delay, epilepsy, hypotonia, cardiomyopathy, and dysmorphic features. All affected individuals have consistently increased D-2-HG levels in urine, plasma, and cerebrospinal fluid (*5*). About 50% of patients with this disorder, denoted D-2-HGA type I, have autosomal recessive mutations in the gene *D2HGDH* encoding D-2-hydroxyglutarate dehydrogenase (*6*), but the genetic basis of the disease in the remaining patients is unknown (*5*).

We sequenced the open reading frames of *IDH1* and *IDH2* in 17 unrelated idiopathic D-2-HGA patients (i.e., normal D-2-HGDH enzyme activity or no mutations in *D2HGDH* and consistently increased D-2-HG levels in body fluids). No mutations were detected in *IDH1*. In 15 patients, germline mutations were detected in *IDH2*: the known heterozygous G-to-A substitution at position 419 (c.419G>A), resulting in the replacement of Arg^{140} with Gln^{140} (p.R140Q) (*4*), and a novel heterozygous C-to-G substitution at position 418 (c.418C>G), Arg^{140}→Gly^{140} (p.R140G) (Fig. 1 and table S1). Although the D-2-HGDH enzyme functions normally in these patients, the active protein appears to lack the catalytic capacity to oxidize all D-2-HG formed by IDH2 containing the R140 mutation; we thus denote the disorder in these patients as D-2-HGA type II. The higher urinary excretion of D-2-HG in the type II patients compared with that of type I patients (Fig. 1) is best explained by hyperproduction of this metabolite. The involvement of mitochondrial IDH2 is also consistent with the finding that D-2-HG is derived from mitochondrial 2-KG (*7*).

In eight of nine sets of parents, the mutation could not be detected, indicating that the heterozygous mutation arose de novo and that D-2-HGA type II is an autosomal dominant trait. In one family, however, three subsequent affected pregnancies were diagnosed by increased D-2-HG levels in amniotic fluid, suggesting germline mosaicism in the mother who herself had normal urinary D-2-HG levels and showed somatic mosaicism in her blood (Fig. 1).

	D-2-HGA type I	D-2-HGA type II
Number of participants	24	15
Urinary D-2-HG (mmol mol creat.$^{-1}$) [normal amount in controls < 17.0]	Mean = 969 (n = 20)	Mean = 2153 (n = 14)
Gene and accession no.	*D2HGDH* NM_152783.3	*IDH2* NM_002168.2
Type of mutations	Heterogeneous (*5*, *6*)	c.419G>A, R140Q (n = 14) c.418C>G, R140G (n = 1)
Trait	Autosomal recessive	Autosomal dominant
Probability of affected fetus	25%	>0%–50%

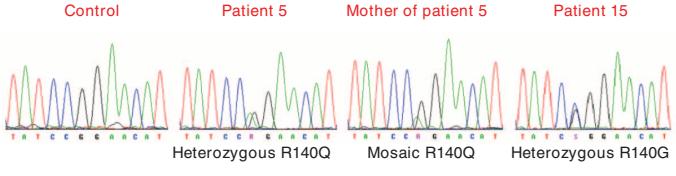

Fig. 1. Characteristics of patients with D-2-HGA types I and II. The living D-2-HGA type II patients (n = 6) range in age from 3 to 22 years. The age of death of the remaining patients (n = 9) ranged from a few months up to 14 years. To date, none of the patients has been diagnosed with cancer. Shown below the table are sequence chromatograms from patients 5 and 15 (table S1), who have heterozygous *IDH2* mutations. Somatic mosaicism for the R140Q mutation was detected in DNA of the mother of patient 5, unlike the other sets of parents in whom the mutation was not detected.

The pathophysiological consequences of increased D-2-HG in both cancer and D-2-HGA remain to be determined. Dang *et al*. have hypothesized that D-2-HG is an "onco-metabolite" that contributes to the formation of gliomas (*2*). However, patients with malignant gliomas and anaplastic astrocytomas that harbor *IDH1* or *IDH2* mutations show improved survival in comparison to patients whose tumors lack these mutations (*1*, *4*). The absence of cancer diagnoses in our D-2-HGA patient population (>85 patients) is also not consistent with the proposed role of D-2-HG as an onco-metabolite, although the 15 D-2-HGA type II patients are young, which may preclude firm conclusions about cancer susceptibility (Fig. 1 and table S1).

An increased incidence of brain tumors has been noted among patients with L-2-hydroxyglutaric aciduria (L-2-HGA) (*8*). L-2-hydroxyglutarate (L-2-HG) is the stereoisomer of D-2-HG, but L-2-HGA is a distinct neurometabolic disease. In contrast to D-2-HGA, L-2-HGA is a leukodystrophy. L-2-HGA manifests in early childhood with slowly progressive neurological symptoms, including psychomotor retardation, cerebellar ataxia, variable macrocephaly, and epilepsy (*9*). The biochemical defect in L-2-HGA is caused by mutations in the *L2HGDH* gene, which encodes an enzyme that specifically degrades the L enantiomer of 2-HG (*9*).

Now that disease-associated mechanisms have been described for nearly all D-2-HGA patients, genetic counseling is expected to be enhanced. Our findings provide additional impetus for investigating the role of D-2-HG in the pathophysiology of inborn errors of metabolism and neoplastic disorders.

References

1. D. W. Parsons *et al*., *Science* **321**, 1807 (2008); published online 4 September 2008 (10.1126/science.1164382).
2. L. Dang *et al*., *Nature* **462**, 739 (2009).
3. P. S. Ward *et al*., *Cancer Cell* **17**, 225 (2010).
4. H. Yan *et al*., *N. Engl. J. Med.* **360**, 765 (2009).
5. M. Kranendijk *et al*., *Hum. Mutat.* **31**, 279 (2010).
6. E. A. Struys *et al*., *Am. J. Hum. Genet.* **76**, 358 (2005).
7. E. A. Struys, N. M. Verhoeven, H. Brunengraber, C. Jakobs, *FEBS Lett.* **557**, 115 (2004).
8. M. Aghili, F. Zahedi, E. Rafiee, *J. Neurooncol.* **91**, 233 (2009).
9. M. E. Steenweg *et al*., *Hum. Mutat.* **31**, 380 (2010).

Supporting Online Material

www.sciencemag.org/cgi/content/full/science.1192632/DC1
Materials and Methods
Tables S1 and S2
References

21 May 2010; accepted 11 August 2010
Published online 16 September 2010;
10.1126/science.1192632
Include this information when citing this paper.

[1]Metabolic Unit, Department of Clinical Chemistry, VU University Medical Center, 1081 HV Amsterdam, Netherlands.

*The list of all affiliations is available in the supporting online material.

†To whom correspondence should be addressed. E-mail: c.jakobs@vumc.nl

Crystal Growth Inhibitors for the Prevention of L-Cystine Kidney Stones Through Molecular Design

Jeffrey D. Rimer,[1]*† Zhihua An,[1]* Zina Zhu,[1]* Michael H. Lee,[1] David S. Goldfarb,[2] Jeffrey A. Wesson,[3] Michael D. Ward[1]‡

Crystallization of L-cystine is a critical step in the pathogenesis of cystine kidney stones. Treatments for this disease are somewhat effective but often lead to adverse side effects. Real-time in situ atomic force microscopy (AFM) reveals that L-cystine dimethylester (L-CDME) and L-cystine methylester (L-CME) dramatically reduce the growth velocity of the six symmetry-equivalent {100} steps because of specific binding at the crystal surface, which frustrates the attachment of L-cystine molecules. L-CDME and L-CME produce L-cystine crystals with different habits that reveal distinct binding modes at the crystal surfaces. The AFM observations are mirrored by reduced crystal yield and crystal size in the presence of L-CDME and L-CME, collectively suggesting a new pathway to the prevention of L-cystine stones by rational design of crystal growth inhibitors.

Kidney stones comprising L-cystine (Fig. 1) affect at least 20,000 individuals in the United States. Although this number is substantially smaller than the number of individuals afflicted by calcium oxalate monohydrate (COM) stones (approximately 10% of the U.S. population), L-cystine stones are larger, recur more frequently, and are more likely to cause chronic kidney disease (*1*). The formation of L-cystine stones is a consequence of excessive levels of L-cystine in the urine because of defective reabsorption of filtered cystine (*2*). This condition is the result of an autosomal recessive disorder caused by mutations in one of the two genes, either *SLC3A1* on chromosome 2 (type A cystinuria) or *SLC7A9* on chromosome 19 (type B cystinuria), which code for components of the major proximal renal tubule cystine and dibasic amino acid transporter (*3*). This condition is exacerbated by the low solubility of L-cystine (*4*), which favors facile formation of crystals that aggregate into stones, often with centimeter dimensions (Fig. 2A).

Current treatments for L-cystine stone prevention, including dilution through high fluid intake (*5*) and increasing urine pH through ingestion of alkalinizing potassium or sodium salts (*5*, *6*), can suppress but may not completely prevent stone formation. Severely afflicted individuals often rely on additional treatment with L-cystine–binding thiol drugs such as D-penicillamine [$HSC(CH_3)_2CH(NH_2)COOH$] and α-mercaptopropionylglycine [$HSCH(CH_3)C(O)NHCH_2COOH$], which react with L-cystine to generate more soluble asymmetric disulfides (*2*). These drugs, however, have an unpleasant odor and can cause adverse side effects, such as nausea, fever, fatigue, skin allergies, and hypersensitivity (*5*). For patients with very high L-cystine concentrations, L-cystine–binding thiol drugs may not reduce L-cystine levels sufficiently at dosages (up to 2000 mg per day) regarded as below the threshold for toxicity, and patient adherance to these prescribed medications and high fluid intake can be problematic (*5*). We report an alternative approach to the prevention of L-cystine kidney stones that is based on crystal growth inhibition achieved through the binding of tailored growth inhibitors—L-cystine dimethylester (L-CDME) and L-cystine methylester (L-CME)—to specific crystal surfaces, as revealed by in situ real-time atomic force microscopy (AFM) (*7*, *8*) and parallel bulk crystallization studies (*9*).

L-cystine stones are aggregates of individual crystals with hexagonal habits (Fig. 2). L-cystine can be crystallized in vitro at physiological pH ($6 \leq pH \leq 8$) by means of slow evaporation (*10*), acidification of basic L-cystine solutions to neutral pH (*11*), or gradual cooling of solutions supersaturated with L-cystine (*12*). Under these conditions, L-cystine crystallizes as hexagonal plates (Fig. 2B) with large (001) basal surfaces that can achieve widths of 400 μm and are bounded by six equivalent {100} faces. The typical thickness of these crystals ranges from 10 to 30 μm. The crystal structure (hexagonal $P6_122$ space group, $a = b = 0.5422$ nm, $c = 5.6275$ nm) reveals L-cystine molecules organized as a helix about the 6_1 screw axis so that six cystine molecules span the ~5.6-nm unit cell length of the c axis (*13*). The L-cystine molecules exhibit intermolecular $NH_3^+ \cdots {}^-O(C{=}O)$ hydrogen bonding along the 6_1 screw axis (Fig. 2C, I), intermolecular S…S interactions between the helices at intervals of $c/2$ along each of the six equivalent {100} directions (Fig. 2C, II), and $NH_3^+ \cdots {}^-O(C{=}O)$ hydrogen bonding (Fig. 2D, III and IV) between adjacent helices in the (001) plane. The hexagonal plate habit reflects the multiple strong intermolecular interactions in the (001) plane. The basal surfaces of L-cystine grown at neutral pH are decorated with {100} steps that are observable through either optical (Fig. 2B) or scanning electron microscopy (SEM) (fig. S2).

Crystal growth near equilibrium is commonly described by the terrace-ledge-kink model (*14*), in which steps created by dislocations advance across crystal terraces by the addition of solute molecules to kink sites along the ledge (a ledge is the intersection of a step and terrace). Steps originating from screw dislocations typically exhibit a spiral growth pattern, with the

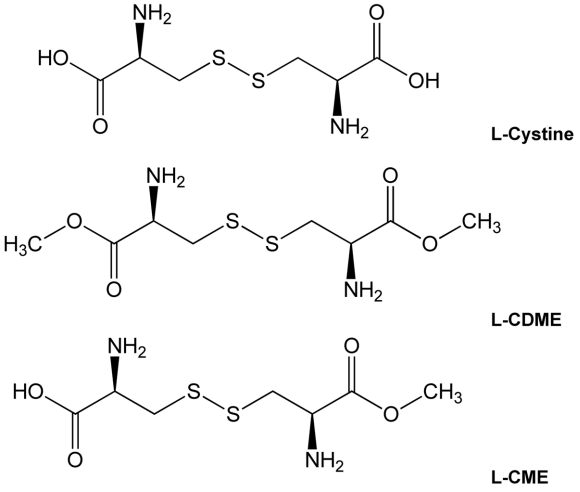

Fig. 1. Molecular structures of L-cystine and the inhibitors L-CDME and L-CME.

[1]Department of Chemistry and the Molecular Design Institute, New York University (NYU), 100 Washington Square East, New York, NY 10003–6688, USA. [2]Nephrology Section, New York Harbor Veterans Affairs Medical Center, and School of Medicine, NYU, New York, NY 10010, USA. [3]Nephrology Division, Department of Veterans Affairs Medical Center and the Medical College of Wisconsin, 5000 West National Avenue, Milwaukee, WI 53295, USA.

*These authors contributed equally to this work.
†Present address: Department of Chemical and Biomolecular Engineering, University of Houston, S222 Engineering Building, 4800 Calhoun Avenue, Houston, TX 77204–4004, USA.
‡To whom correspondence should be addressed. E-mail: mdw3@nyu.edu

first turn occurring once every step has reached its critical length (*15*). Real-time in situ AFM of the L-cystine (001) face during growth in aqueous solutions containing L-cystine revealed steps emanating from screw dislocations, generating hexagonal hillocks in a spiral growth pattern. Occasionally, multiple dislocations were observed (Fig. 3, A and B, and movie S1), merging to generate a range of step heights from 1 nm to 60 nm, with the larger steps observed distant from the dislocation cores, where step bunching would be expected (fig. S3). In contrast, hillocks generated by single isolated dislocations were bounded by six well-defined major {100} steps, each with a ~6-nm height corresponding to the unit cell length along *c*, separating (001) terraces. Each hillock terrace was decorated with six minor {100} steps at 60° intervals, each with a ~1-nm height corresponding to a single L-cystine molecule, creating the appearance of a pinwheel. These minor steps most likely reflect a splitting of the dislocation into six equivalent dislocations described by a Burgers vector having a magnitude of *c*/6. Consecutive images during crystal growth revealed a clockwise rotation of the pinwheel at the dislocation core (a left-handed screw) accompanied by continuous generation of new hillocks. Attachment of L-cystine molecules to both the minor and major steps on the surrounding terraces results in outward advancement of the steps with respect to the dislocation core (Fig. 3C and movie S2). The spiral growth pattern also is observed for D-cystine, the unnatural enantiomer, but with counterclockwise (a right-handed screw) rotation of the pinwheel (Fig. 3D and movie S3). A preference for screw dislocations of opposite handedness for enantiomeric crystals has been predicted (*16*).

Quantitative determination of crystal growth rates at the near-molecular level were obtained by using AFM to measure the {100} step velocity (Fig. 4, A and B, and fig. S4). In order to achieve growth rates within a reasonable measurement timeframe, the L-cystine concentration was adjusted to 480 mg/liter (2 mM), which is five times larger than L-cystine solubility at room temperature (*17*). The {100} step velocity (V_o), determined through measurement of the step advance in successive images, was 11 nm/s, which is equivalent to 50 molecules/nm^2 s. The step velocity was equivalent along all six directions, as expected for the hexagonal symmetry.

Crystallization outcomes such as habit, chirality, and polymorphism can be influenced by tailored growth inhibitors that reduce crystallization rates through binding at specific step sites (*18*, *19*). These inhibitors, which have been described as "imposters," (*15*) consist of a binder moiety that emulates a critical structural element of the solute that attaches to a specific crystal site and a perturber moiety that obstructs the approach of additional solute molecules to neighboring sites, pinning step motion. Growth inhibitors may be monomers that closely resemble the solute, as demonstrated for amino acid and adipic acid crystals (*20*–*22*). The effect of molecular inhibitors on the crystal growth of β-hematin—a synthetic malaria pigment—and their potential role as antimalarial drugs has been reported (*23*, *24*). Polyvalent macromolecules capable of binding to multiple crystal sites, such as peptides and proteins, also can influence ice crystallization (*25*) and the formation of biominerals, including calcium carbonate (*26*, *27*) and calcium oxalates (*28*–*30*).

AFM revealed that addition of L-CDME, a structural mimic of L-cystine in which the carboxylate groups are replaced by methylester groups, resulted in roughening of the otherwise highly linear {100} step edges and rounding of the hillock corners, which is consistent with step pinning through adsorption of L-CDME at the {100} steps (Fig. 3, E and F). This effect was reversible because the steps once again become linear after addition of aqueous solutions containing only L-cystine (fig. S5). The step velocity decreased monotonically with increasing L-CDME concentration, becoming negligible above 30 mg/liter (Fig. 4, A and C). Similarly to the step roughening, the inhibitor effect was reversible, with the rates returning to the original value once the growth medium was replaced with aqueous solutions containing only L-cystine. The reduction of the step velocity was equivalent along all six directions in the (001) plane, as expected for the hexagonal symmetry of the crystal. These observations are consistent with attachment of L-CDME to the {100} step planes through a

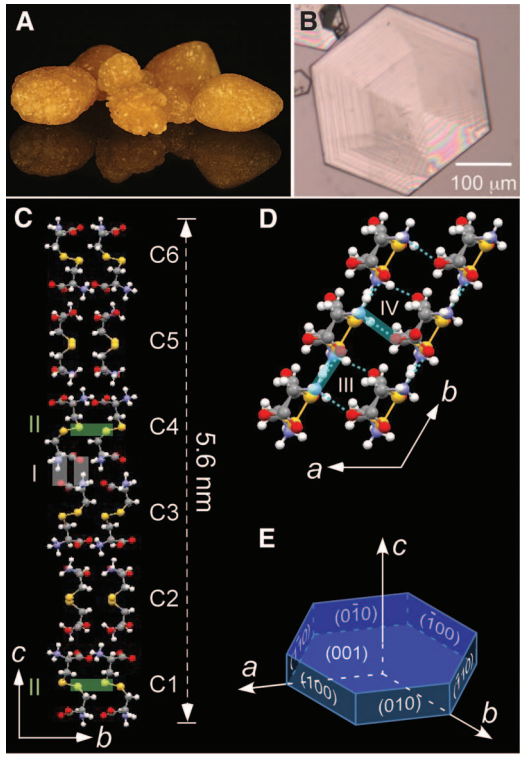

Fig. 2. (**A**) Human stones with millimeter-scale dimensions [courtesy of M. Lewis, International Cystinuria Foundation]. (**B**) A hexagonal L-cystine crystal prepared in vitro. The faint lines on the top surface of the crystal, parallel to the edges, are the {100} steps. (**C**) Two adjacent helices of L-cystine molecules, viewed on the (100) plane, each winding about a 6_1 screw axis that coincides with the *c* axis. Six L-cystine molecules, denoted C1 to C6, span the 5.6-nm *c* axis. Key intermolecular interactions include amine-carboxylate hydrogen bonds along the helix (I, $d_{N\cdots O}$ = 2.87 Å) and S…S interactions (II, $d_{S\cdots S}$ = 3.47 Å) between helices at intervals of *c*/2, depicted here for C1 and C4 along the [010] direction (identical S…S interactions occur at symmetry-related sites along the other five equivalent directions). (**D**) Intermolecular amine-carboxylate hydrogen bonds in the (001) plane (III, $d_{N\cdots O}$ = 2.79 Å and IV, $d_{N\cdots O}$ = 2.81 Å). Atom color code is gray, carbon; red, oxygen; blue, nitrogen; yellow, sulfur; and white, hydrogen. (**E**) Schematic illustration of a hexagonal L-cystine crystal, with Miller indices. The six planes flanking (001) belong to the {100} family.

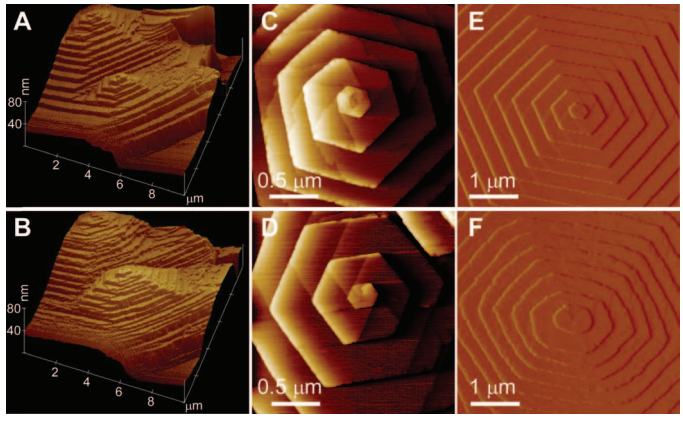

Fig. 3. (**A** and **B**) Real-time in situ AFM images of a L-cystine crystal, acquired 12 min apart. A pair of hexagonal hillocks generated by two closely spaced dislocations serve as landmarks. (**C** and **D**) AFM images of a single dislocation center of (C) L-cystine and (D) D-cystine crystal during growth. (**E** and **F**) AFM image of a hexagonal growth hillock on the (001) face of L-cystine (E) before and (F) after addition of L-CDME (5 mg/liter; 0.02 mM), revealing roughening of the {100} steps due to step pinning. Images were acquired in aqueous solutions containing 2 mM L-cystine.

combination of intermolecular (cystine)S…S(L-CDME), (cystine)C(=O)O$^-$…$^+$H$_3$N(L-CDME), and (cystine)N-H…O=C(L-CDME) interactions in a manner that mimics the attachment of L-cystine solute molecules at the {100} steps, with the ester methyl groups of bound L-CDME molecules blocking the attachment of L-cystine solute molecules at neighboring crystal sites. The steric bulk of the ester methyl group is not sufficient to prevent binding of L-CDME to the {100} steps.

The AFM measurements demonstrate that L-CDME slows growth along the naturally fast growth directions within the (001) plane. This microscopic behavior was mirrored in bulk crystallization by a gradual change in the crystal habit from (001) plates to small hexagonal needles oriented along the [001] direction as the L-CDME concentration was increased (Fig. 5A and fig. S6). At L-CDME concentrations as low as 5 mg/liter (0.02 mM; equivalent to 1% of the L-cystine concentration), the area of the (001) face was reduced by a factor of 1000, whereas the length of the needles was comparable with the thickness of the hexagonal plates grown in the absence of L-CDME (~30 μm), resulting in crystals that were 1000 times smaller. Moreover, the total crystallization yields decreased with increasing L-CDME concentration, approaching complete inhibition above 2 mg/liter (Fig. 4D), which is consistent with the AFM observations. The dramatic change in crystal habit in the presence of L-CDME and L-CME may influence the aggregation of crystals and their attachment to renal cells, which are also critical steps in stone formation (*31*). L-CDME also promoted the formation of small amounts of minute crystals of tetragonal L-cystine (Fig. 5B). The formation of the tetragonal polymorph, which ordinarily crystallizes only under more basic conditions (pH > 8) (*32*), can be attributed to the suppressed growth of the hexagonal form by L-CDME.

The unsymmetrical L-CME, a cystine mimic with only one ester methyl group, also inhibited L-cystine crystallization. AFM measurements revealed that the {100} step velocity declined with increasing L-CME concentration, but to a lesser extent than L-CDME (Fig. 4, B and C). L-CME also reduced the size of L-cystine crystals substantially, and it reduced the crystal yield, but to a lesser extent than did L-CDME (Fig. 4D). Step roughening was observed in the presence of L-CME, but at higher concentrations as compared with that of L-CDME (fig. S5). These observations are consistent with weaker inhibition of L-CME as compared with that of L-CDME. The L-cystine crystals grown in the presence of L-CME exhibited a tapered hexagonal habit, with six faces intersecting the basal (001) plane at an angle of 85°, which is attributable to the emergence of six equivalent {101} surfaces (Fig. 5, C and D, and fig. S7). The different crystal habits generated by L-CDME and L-CME provide interesting insight into the binding modes of these inhibitors at the L-cystine crystal surface.

The P6$_1$22 space group symmetry generates inequivalent projections of the L-cystine molecules on each flank of a hexagonal hillock. Each projection winds around the hillock by translations of ±*c*/6 on adjacent faces. In the 5.6-nm span of the hillock, diad axes create two distinct pairs of symmetry-related projections in which the L-cystine molecules are oriented in opposite directions along *c*—for example, C1/C3 and C4/C6 on the (010) face (Fig. 6). The two remaining sites, located on the diad special positions, create two additional distinct projections along directions containing the aforementioned intermolecular S…S contacts. Molecular models reveal that binding of L-CDME at (001)∩{100} ledge sites [illustrated in Fig. 6 by the intersection of (001) and (010) planes] is precluded by the steric obstruction introduced by one of the ester methyl groups (Fig. 6). Consequently, attachment of L-CDME must occur at L-cystine sites above the ledge sites. It is reasonable to suggest that L-CDME would bind preferentially at the diad sites because of the additional S…S interactions—for example, the C2 and C5 sites on the (010) face. Binding of L-CDME would

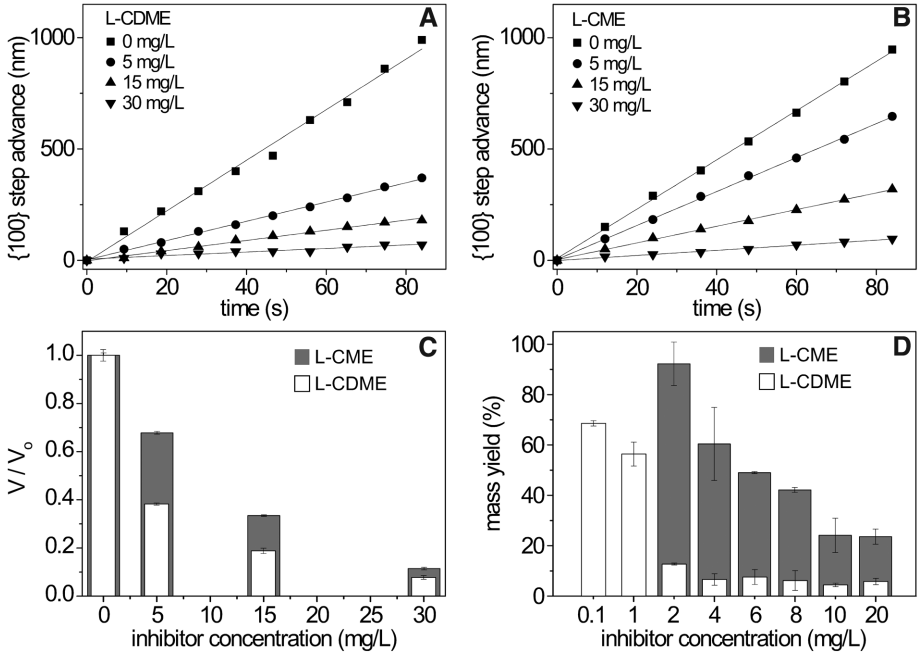

Fig. 4. (**A** and **B**) The position of the 5.6-nm-high {100} steps, as measured from the center of the spiral dislocations during growth in aqueous solutions containing 2 mM L-cystine with various concentrations of L-CDME or L-CME. The step velocities in the absence of inhibitor, determined from the slopes of the lines, are V_o = 11.4 ± 0.3 and 11.3 ± 0.1 nm/s, respectively. The SD is based on the average of the velocities determined for three independent steps. (**C**) Comparison of the effectiveness of L-CDME and L-CME on the inhibition of the {100} step velocity, expressed as V/V_o. (**D**) The mass yield of L-cystine crystals obtained after crystallization for 72 hours in the presence of various concentrations of L-CDME or L-CME. The error bars represent 1 SD based on three measurements for each inhibitor concentration.

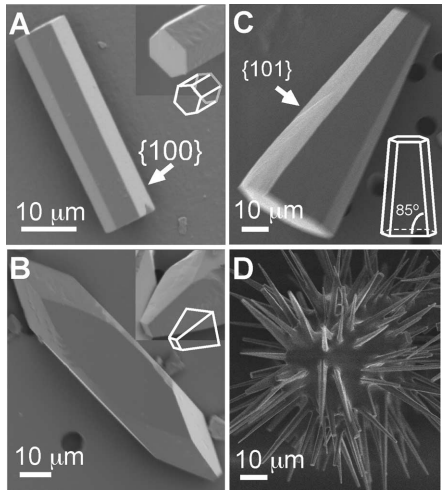

Fig. 5. (**A**) Minute L-cystine crystals grown in the presence of L-CDME (5 mg/liter; 0.02 mM) exhibit a hexagonal needle-like habit with prominent {100} faces and high *c*/*a* aspect ratios, approaching 30 for many crystals. (**B**) Small quantities of the tetragonal $P4_1$ polymorph are formed in the presence of L-CDME (5 mg/liter). (**C**) L-CME (10 mg/liter; 0.04 mM) produces tapered hexagonal needles with six {101} faces. Some crystals exhibit the tapered habit at both ends of the crystal, as expected for the crystal symmetry (fig. S7). The observation of only one half of the tapered crystal suggests that growth often begins on a surface. (**D**) The tapered needles formed in the presence of 10 mg/liter L-CME occasionally grow from a nidus that may be an amorphous L-cystine particle or a microscopic unidentified foreign object. Crystal growth was performed in aqueous solutions containing 3 mM L-cystine (700 mg/liter).

prevent steps from advancing further above the inhibitor site, leading to step bunching that would terminate in {100} planes and producing hexagonal needles with small cross sections. L-CDME binding to other sites cannot be excluded; the projections of L-cystine molecules at each site of a diad-related pair (blue-blue or green-green on each hillock face in Fig. 6) differ only with respect to their "up" or "down" orientation (denoted by the white arrows). The C_2 symmetry of L-CDME would result in equivalent binding to either site of a diad pair.

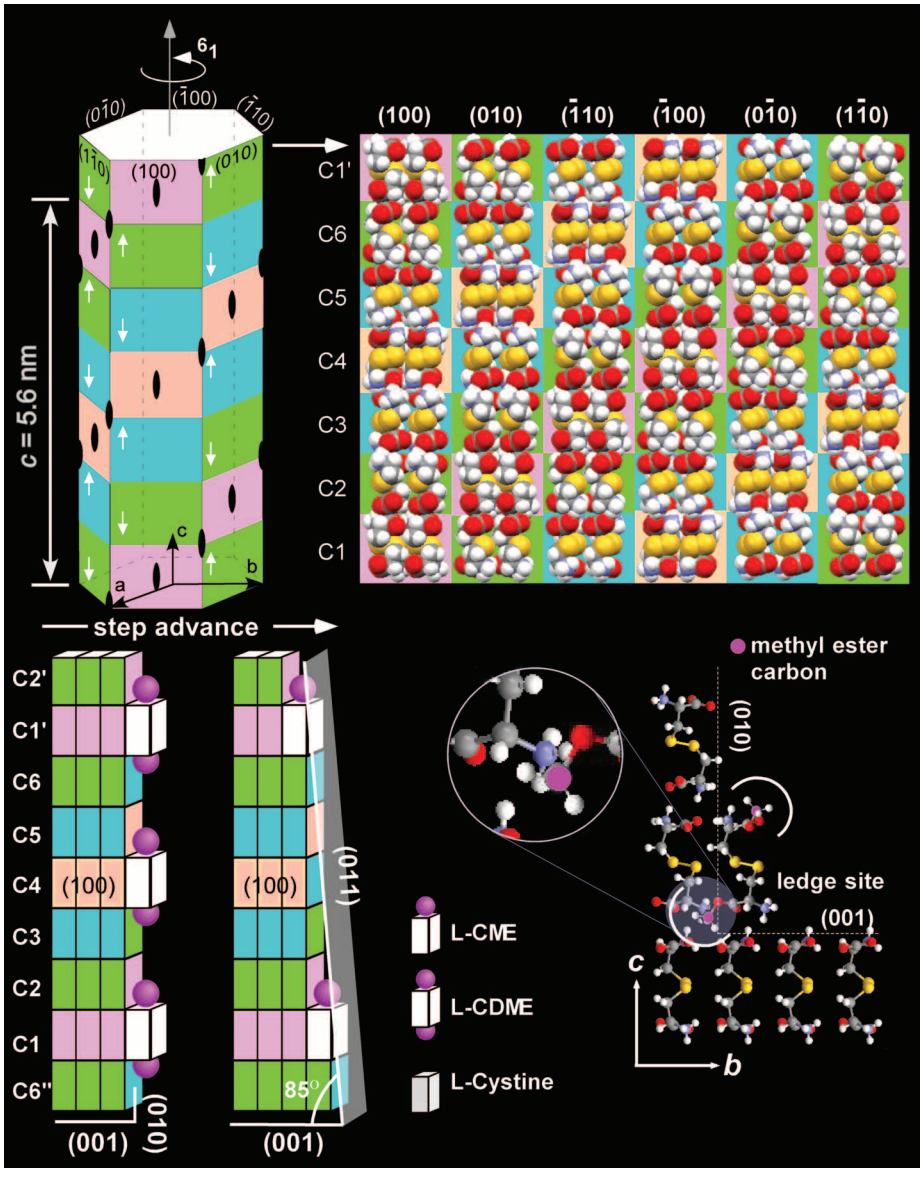

Fig. 6. (**Top left**) Schematic representation of an L-cystine hillock, color-coded to denote the distinct projections of L-cystine along each flank of the 5.6-nm-high hillock. The six flanks are depicted in the unraveled version of the hillock on the right. Equivalent projections on adjoining flanks are related by the 6_1 screw axis. Diad axes, denoted by black ovals, generate two identical projections that differ only with respect to their up or down orientation (denoted by white arrows). (**Bottom right**) L-CDME binding at a (001)∩{010} ledge site is frustrated by one of the ester methyl group, emphasized here by the white arc. (**Bottom left**) L-CDME binding to the (010) step: The ester methyl groups of L-CDME, depicted by purple spheres, block attachment of L-cystine to adjacent sites. Binding to the C1 and C4 sites on the {010} step allows S…S and hydrogen-bonding interactions between L-cystine molecules projecting from the step surface and L-CDME. In contrast, in the up orientation the carboxylic acid terminus of L-CME can bind to the ledge sites in a manner like L-cystine, through hydrogen-bonding interaction I, at the (001) terrace, as well as S…S interactions and hydrogen bonding at the (010) step. Crystallographically equivalent (001)∩(010) ledge sites, depicted here for the C6″-C1 and C6-C1′ combinations, are spaced at intervals of *c*, generating a vicinal surface equivalent to a (011) plane. This plane intersects the (001) plane at an angle of 85°, which is consistent with the tapered faces observed in the presence of L-CME.

In contrast, L-CME can bind at (001)∩{100} ledge sites in its up orientation because the carboxylic acid terminus is indistinguishable from the ends of L-cystine (the ester methyl group would prevent binding at the ledge in the down orientation). The terrace of the ledge site effectively breaks the twofold up-down symmetry of the diad-related pairs. Consequently, each flank of the hexagonal hillock contains six crystallographically, and therefore chemically, inequivalent (001)∩{100} ledge sites along the 5.6-nm span of the *c* axis (fig. S8). The tapered crystals grown in the presence of L-CME can be explained only by highly selective binding of L-CME at one of these sites. Crystal step motion would then be pinned at these sites, repeating at an interval of *c*, creating a vicinal face with a tangent plane intersecting the (001) plane at an angle of 85°, which is identical to the angle of the tapered faces on the macroscopic crystals and assignable to {101} planes. The different mode of binding in the presence of L-CDME and L-CME, particularly the discrimination of L-CME for one of the six possible ledge sites, is a remarkable illustration of molecular recognition between tailored inhibitors and crystal surface sites. Moreover, the step velocity measurements, step roughening, crystal habit effects, and crystal yields represent a rare example of a correspondence between inhibitor effects at the microscopic level and macroscopic crystallization behavior.

L-CDME is extraordinarily effective compared with inhibitors examined for other kidney stone–forming materials. Molecular additives have been found to be substantially less effective as crystal growth inhibitors of COM as compared with that of their polymeric forms; for example, aspartic acid is more than 1000 times less active for COM inhibition than poly(aspartic acid), in which the carboxylate side chains are thought to bind to calcium sites on the crystal surfaces. The effective inhibition observed for polymers can be attributed to the entropic benefit associated with binding of multiple carboxylate groups on a single chain. Surprisingly, the concentrations at which L-CDME becomes effective for L-cystine inhibition (~2 mg/liter) is comparable with those observed for poly(amino acid) inhibitors of COM crystallization (*28*). The importance of molecular recognition between L-CDME and the L-cystine step planes is underscored by our observations that other additives with proximal carboxylate and amine groups, such as those in L-cystine, had a negligible influence on L-cystine growth. For example, L-cysteine, the thiol relative of L-cystine, reduced the size of L-cystine crystals somewhat (at 10 mg/liter), but its effect on crystallization yield was negligible (fig. S9). Urinary proteins such as osteopontin, human serum albumin, and Tamm-Horsfall protein afforded only modest reductions in crystallization yield at concentrations comparable with physiological values (2 mg/liter), suggesting a neg-

ligible role for these substances in the regulation of cystine stone formation.

Collectively, the AFM and bulk crystallization behavior for L-cystine suggest that L-CDME is a viable therapeutic agent for the prevention of L-cystine kidney stones. This approach to stone prevention uses a potentially benign crystal growth inhibitor at low concentrations rather than drugs that rely on a chemical reaction with L-cystine (L-cystine–binding thiol drugs), increases in urine alkalinity (which are often accompanied by undesirable side effects), or dramatic increases in urine volume (which can be unreliable owing to patient nonadherance). The reduction in mass yield in the presence of inhibitors is a kinetic effect that maintains a metastable supersaturated L-cystine concentration, but from a pathological perspective this is a sufficient condition for preventing stone formation. L-cystine stone formers typically have urinary L-cystine concentrations ranging from 250 to 1000 mg/liter (equivalent to 1 to 4 mM), which is comparable with the concentrations we used for the AFM and bulk crystallization studies. Therefore, L-CDME concentrations near 2 mg/liter (<0.01 mM), at which inhibition of L-cystine growth was highly effective, may be adequate for therapeutic effect. Cell culture data, acquired for the purpose of evaluating cystine exodus from lysosomes, show loss of cell viability at approximately 1 mM L-CDME, and studies in rats, performed to measure oxidative stress in the brain cortex, demonstrated adverse effects at dosages of approximately 500 mg/kg (mass of rat) per day (*33*–*35*). Although the pharmacokinetics of L-CDME are not well known, on the basis of typical daily urine volumes a L-CDME dose of 10 to 50 mg per day—far below toxic levels but greater than the amount needed for crystal growth inhibition in vitro—may prove sufficient to achieve adequate L-CDME concentrations in urine for crystal growth inhibition in vivo.

References and Notes

1. K. Ahmed, P. Dasgupta, M. S. Khan, *Postgrad. Med. J.* **82**, 799 (2006).
2. D. J. Dolin, J. R. Asplin, L. Flagel, M. Grasso, D. S. Goldfarb, *J. Endourol.* **19**, 429 (2005).
3. A. Mattoo, D. S. Goldfarb, *Semin. Nephrol.* **28**, 181 (2008).
4. O. W. Moe, *Lancet* **367**, 333 (2006).
5. G. Becker, *Nephrology* **12** (suppl. 1), S4 (2007).
6. Y. Nakagawa, J. R. Asplin, D. S. Goldfarb, J. H. Parks, F. L. Coe, *J. Urol.* **164**, 1481 (2000).
7. A. C. Hillier, M. D. Ward, *Science* **263**, 1261 (1994).
8. M. D. Ward, *Chem. Rev.* **101**, 1697 (2001).
9. Materials and methods are available as supporting material on *Science* Online.
10. S. Dahaoui, V. Pichon-Pesme, J. A. K. Howard, C. Lecomte, *J. Phys. Chem. A* **103**, 6240 (1999).
11. E. K. Girija, S. N. Kalkura, P. Ramasamy, *J. Mater. Sci.* **6**, 617 (1995).
12. Y. Fujiki, N. Tokunaga, S. Shinkai, K. Sada, *Angew. Chem. Int. Ed.* **45**, 4764 (2006).
13. B. M. Oughton, P. M. Harrison, *Acta Crystallogr.* **12**, 396 (1959).
14. W. A. Tiller, *The Science of Crystallization: Microscopic Phenomena and Defect Generation* (Cambridge Univ. Press, Ithaca, NY, 1991).
15. J. P. Sizemore, M. F. Doherty, *Cryst. Growth Des.* **9**, 2637 (2009).
16. L. S. Levitt, *J. Phys.* **49**, 696 (1975).
17. R. Carta, G. Tola, *J. Chem. Eng. Data* **41**, 414 (1996).
18. I. Weissbuch, L. Addadi, L. Leiserowitz, L. Leiserowitz, *Science* **253**, 637 (1991).
19. G. Clydesdale, R. B. Hammond, K. J. Roberts, *J. Phys. Chem. B* **107**, 4826 (2003).
20. I. Weissbuch, M. Lahav, L. Leiserowitz, *Cryst. Growth Des.* **3**, 125 (2003).
21. R. J. Davey *et al.*, *J. Chem. Soc. Faraday Trans.* **88**, 3461 (1992).
22. A. S. Michaels, F. W. Tausch Jr., *J. Phys. Chem.* **65**, 1730 (1961).
23. R. Buller, M. L. Peterson, Ö. Almarsson, L. Leiserowitz, *Cryst. Growth Des.* **2**, 553 (2002).
24. I. Solomonov *et al.*, *J. Am. Chem. Soc.* **129**, 2615 (2007).
25. Y. C. Liou, A. Tocilj, P. L. Davies, Z. Z. Jia, *Nature* **406**, 322 (2000).
26. C. A. Orme *et al.*, *Nature* **411**, 775 (2001).
27. A. E. Stephenson *et al.*, *Science* **322**, 724 (2008).
28. S. W. Guo, M. D. Ward, J. A. Wesson, *Langmuir* **18**, 4284 (2002).
29. T. Jung *et al.*, *Langmuir* **20**, 8587 (2004).
30. B. Grohe *et al.*, *J. Am. Chem. Soc.* **129**, 14946 (2007).
31. X. Sheng, T. Jung, J. A. Wesson, M. D. Ward, *Proc. Natl. Acad. Sci. U.S.A.* **102**, 267 (2005).
32. M. O. Chaney, L. K. Steinrauf, *Acta Crystallogr. B* **30**, 711 (1974).
33. A. Kessler *et al.*, *Neurochem. Res.* **33**, 737 (2008).
34. M. J. Wilmer *et al.*, *Pediatr. Res.* **62**, 151 (2007).
35. J. W. Foreman, M. A. Bowring, J. Lee, B. States, S. Segal, *Metabolism* **36**, 1185 (1987).

36. This work was supported primarily by NIH (NIDDK R01-DK068551) and the NYU Molecular Design Institute. The authors also acknowledge support from the Office of Rare Disease Research (1U54DK083908-01) and the Advanced Photon Source, ChemMatCARS Sector 15, which is principally supported by NSF/U.S. Department of Energy (DOE) (NSF/DOE; CHE-0535644). The authors thank C. Hu, M. Li, Y.-S. Chen, and G. Kowach for technical assistance and B. Kahr for helpful discussions.

Supporting Online Material

www.sciencemag.org/cgi/content/full/330/6002/337/DC1
Materials and Methods
Figs. S1 to S10
Table S1
References
Movies S1 to S3

7 May 2010; accepted 13 August 2010
10.1126/science.1191968

Atomic-Level Characterization of the Structural Dynamics of Proteins

David E. Shaw,[1,2]* Paul Maragakis,[1]† Kresten Lindorff-Larsen,[1]† Stefano Piana,[1]† Ron O. Dror,[1] Michael P. Eastwood,[1] Joseph A. Bank,[1] John M. Jumper,[1] John K. Salmon,[1] Yibing Shan,[1] Willy Wriggers[1]

Molecular dynamics (MD) simulations are widely used to study protein motions at an atomic level of detail, but they have been limited to time scales shorter than those of many biologically critical conformational changes. We examined two fundamental processes in protein dynamics—protein folding and conformational change within the folded state—by means of extremely long all-atom MD simulations conducted on a special-purpose machine. Equilibrium simulations of a WW protein domain captured multiple folding and unfolding events that consistently follow a well-defined folding pathway; separate simulations of the protein's constituent substructures shed light on possible determinants of this pathway. A 1-millisecond simulation of the folded protein BPTI reveals a small number of structurally distinct conformational states whose reversible interconversion is slower than local relaxations within those states by a factor of more than 1000.

Many biological processes involve functionally important changes in the three-dimensional structures of proteins. Conformational changes associated with protein folding (*1*), signal transduction (*2*), the catalytic cycles of enzymes (*3*), and the operation of molecular machines and motor proteins (*4*) often involve transitions among two or more structurally distinct states. These states are often characterized as "basins" separated by barriers on an "energy landscape" (*5*).

Substantial progress has been made, using both experimental (*1*, *6*) and computational (*7*, *8*) techniques, in characterizing conformational basins and the ways that proteins move within and among them. It has proven difficult, however, to structurally characterize sparsely populated or disordered states and to elucidate the "basin-hopping" mechanisms involved in the interconversion of various states.

All-atom molecular dynamics (MD) simulations are designed to provide a high-resolution view of the motions of biological macromolecules (*9*), producing continuous trajectories with the potential to connect static structural snapshots generated from experimental data. Computational constraints, however, have limited such

[1]D. E. Shaw Research, 120 West 45th Street, New York, NY 10036, USA. [2]Center for Computational Biology and Bioinformatics, Columbia University, New York, NY 10032, USA.

*To whom correspondence should be addressed. E-mail: David.Shaw@DEShawResearch.com
†These authors contributed equally to this work.

simulations to ~1 μs of simulated biological time. [The longest previously published all-atom MD simulation of a protein, at 10 μs, required more than 3 months of supercomputer time (*10*).] This has limited the usefulness of MD, as many biological processes involve conformational changes that take place on time scales between 10 μs and 1 ms.

To access such time scales, we designed and constructed a special-purpose machine, called Anton (*11*), that greatly accelerates the execution of such simulations, producing continuous trajectories as much as 1 ms in length. This has allowed new insight into two fundamental processes in protein dynamics: protein folding and the interconversion among distinct structural states of a folded protein.

Specifically, we have been able to formulate a detailed description of the folding of a WW domain (*12*) as well as the folded-state dynamics of bovine pancreatic trypsin inhibitor (BPTI), a workhorse in the study of protein dynamics [and the subject of the first protein MD simulation (*13*) and of pioneering computational studies of protein folding (*14*)]. Our choice of biological systems was motivated in part by the fact that a considerable amount of experimental data is available for both of these proteins, providing us with various ways to test the reliability of our simulations.

Folding of a WW domain. WW domains are small, independently folding protein domains that bind to proline-rich sequences. The topology of WW domains is characterized by two β hairpins, which form a three-stranded β sheet (*15*). Mutational analyses of the folding of WW domains show that the rate-limiting step in the folding reaction involves the formation of the first hairpin (*16*–*18*). This information facilitated the original design of the fastest-folding WW domain reported to date, FiP35 (*12*), which folds in 14 μs.

FiP35 has several features that make it attractive as a model system for use in computational studies of protein folding. A great deal of experimental data is available for this system (*12*, *16*, *17*), and previous attempts to characterize its folding mechanism through explicit-solvent simulations have been largely unsuccessful (*10*, *19*). It has been suggested that WW domains such as FiP35 fold through multiple distinct routes that differ in the order of formation of the individual hairpins (*20*–*22*), but this has not been conclusively demonstrated. It has also been speculated that the mutations involved in the design of FiP35 may have shifted the rate-limiting step relative to that of the Pin1 WW domain, which formed the basis for its design. Finally, it has been suggested (*12*) that the fast folding of FiP35 may be close to the downhill regime, with only a small ($<3k_BT$) free-energy barrier. Many of the unresolved questions surrounding the folding of FiP35 raise issues central to the process of protein folding more generally, and we believed they might be amenable to investigation using very long atomistic simulations.

Folding FiP35 and villin to experimental resolution using the same force field. We first ran a simulation at 337 K, a temperature at which FiP35 should be predominantly folded. The protein was initially configured in a fully extended state and was observed to fold to a stable conformation with a backbone root-mean-squared deviation (RMSD) of ~1 Å from the crystal structure (*15*) (Fig. 1B). A previous attempt to fold FiP35 computationally, using a 10-μs explicit solvent simulation (*10*), did not converge to the native state, and subsequent work (*19*) provided evidence that this was attributable to deficiencies in the force field. Our successful folding simulation was based on a modified version of the Amber ff99SB force field (*23*).

One potential concern in simulating the folding of an all-β protein is the possibility that the force field used might tend to overstabilize β sheets, thus "assisting" the folding process in a nonphysical manner. The force field we used, however, also folded a variant of the villin headpiece C-terminal fragment, a small all-α protein (*24*), to within an RMSD of ~1 Å from the crystal structure. (These results cannot be taken as evidence that the same force field would necessarily succeed in folding other proteins.)

Reversible folding and unfolding in an equilibrium simulation of FiP35. In the hope of observing a number of folding and unfolding events under equilibrium conditions, we then ran two independent 100-μs MD simulations of FiP35 at a temperature (395 K) approximating the protein's in silico melting temperature. [The in silico melting temperature was estimated using a replica exchange metadynamics simulation (*25*) and is ~40 K higher than the experimental melting temperature.] In each of the two equilibrium simulations, FiP35 underwent multiple folding and unfolding transitions, for a total of 15 events in the two simulations (Fig. 2A). We found the folding time, as calculated from the average waiting time in the unfolded state, to be 10 ± 3 μs, in relatively close agreement with the experimental folding time [14 μs (*12*)]. The population of the folded state in the simulations was 60%.

In our simulations, a well-defined sequence of events leads from the disordered, unfolded state to the native state: In all folding transitions, formation of the tip of the first hairpin is followed by formation of the entire first hairpin, then by formation of the second hairpin, and finally by consolidation of the hydrophobic core (Fig. 2B, top). Unfolding transitions follow the reverse pattern. Thus, the folding mechanism of FiP35 appears to be dominated by a single pathway, with any flux through alternative pathways being small. This is in contrast with recent studies of WW domains (*20*–*22*)—using simulations shorter than the folding time—which found structurally heterogeneous dynamics with multiple parallel pathways connecting folded and unfolded states.

To explain why FiP35 folds along a single, dominant route, we performed reversible folding simulations of peptides corresponding to the two hairpins of FiP35. Both the first and second hairpin, in isolation, fold to the structure found in the full WW domain, with similar time constants (1.2 ± 0.1 μs and 0.86 ± 0.06 μs for hairpins 1 and 2, respectively). The two hairpins, however, differ substantially in their stabilities, with the population of the folded state being 25% and 4% for the first and second hairpins, respectively. Thus, the order in which the individual hairpins form during folding of the full WW domain mirrors their intrinsic thermodynamic stabilities, with the slower but more stable hairpin 1 forming first. We suspect that the alternative pathway in which the second hairpin forms first may not be substantially utilized because of the relatively large difference in stability between the two hairpins (~1.5 kcal mol^{-1}). Indeed, experiments have shown that variations in substructure stabilities can cause substantial shifts in folding pathways (*26*, *27*), as have computational studies in the context of the diffusion-collision model for protein folding (*28*).

Our simulations show that both hairpins also form with similar rate constants in the context of the full WW domain. The first hairpin forms with a time constant of 5 ± 1 μs, slower than in isolation by a factor of 4; such a slowdown is greater than expected for a simple hydrodynamic drag. To determine its origin, we performed simulations in which we systematically added residues

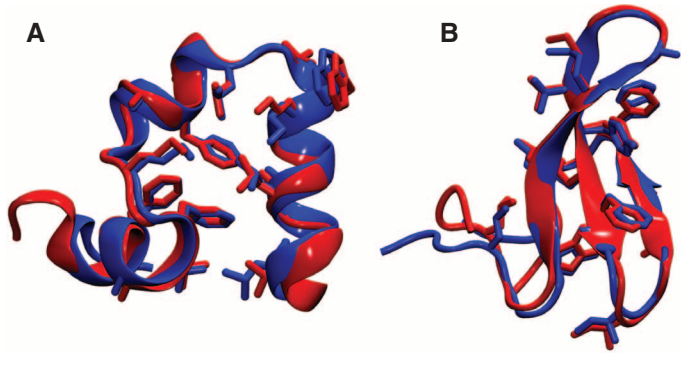

Fig. 1. Folding proteins at x-ray resolution, showing comparison of x-ray structures (blue) (*15*, *24*) and last frame of MD simulation (red): (**A**) simulation of villin at 300 K, (**B**) simulation of FiP35 at 337 K. Simulations were initiated from completely extended structures. Villin and FiP35 folded to their native states after 68 μs and 38 μs, respectively, and simulations were continued for an additional 20 μs after the folding event to verify the stability of the native fold.

in silico, three at a time, to the two ends of the hairpin (*25*). Adding 12 C-terminal residues resulted in a slowdown by a factor of 2. There was no change in the folding rate upon adding the first three N-terminal residues (residues 1 to 3), but the addition of residues 4 to 6 slowed hairpin formation by a factor of 2. Thus, approximately half of the observed slowdown is determined by the addition of just a few residues.

Characterizing the transition state for folding. MD simulations can in principle provide detailed insight into all steps of the protein-folding pathway. Experiments, however, are generally limited to the characterization of stable states and rate-limiting transition states. To facilitate comparison with experiment, we determined the transition state in our simulations. We used a previously described variational approach (*29*) to find an optimized reaction coordinate that separates the transition state from the stable folded and unfolded basins (*25*). To validate the resulting transition-state ensemble (TSE, Fig. 2C), we calculated the commitment probability (P_{fold}), the probability that simulations initiated from a given structure will fold before unfolding. For each of 101 structures sampled at random from the TSE, we ran four simulations until either the folded or unfolded state was reached, requiring in total an additional 151 μs of simulation.

The distribution of P_{fold} obtained with this approach peaked at 0.5, closely resembling the binomial distribution expected for an ideal TSE (Fig. 2D), thus validating the reaction coordinate and the TSE. The average commitment time observed in the simulations initiated from the transition-state region is relatively long (0.36 μs and 0.40 μs for folding and unfolding, respectively), suggestive of a diffusional process over a flat free-energy barrier. Inspection of the TSE shows that formation of the first hairpin, but not the second, is part of the rate-limiting step. We note also that the time constant of formation of the first hairpin determined above (5 ± 1 μs) is half of that for folding (10 ± 3 μs), consistent with our finding that formation of this hairpin is rate-limiting in folding. (The factor of 2 difference in time constants arises from the 50% probability of folding from the TSE.)

The most important experimental strategy for inferring the structural properties of the TSE is the protein engineering method, in which folding

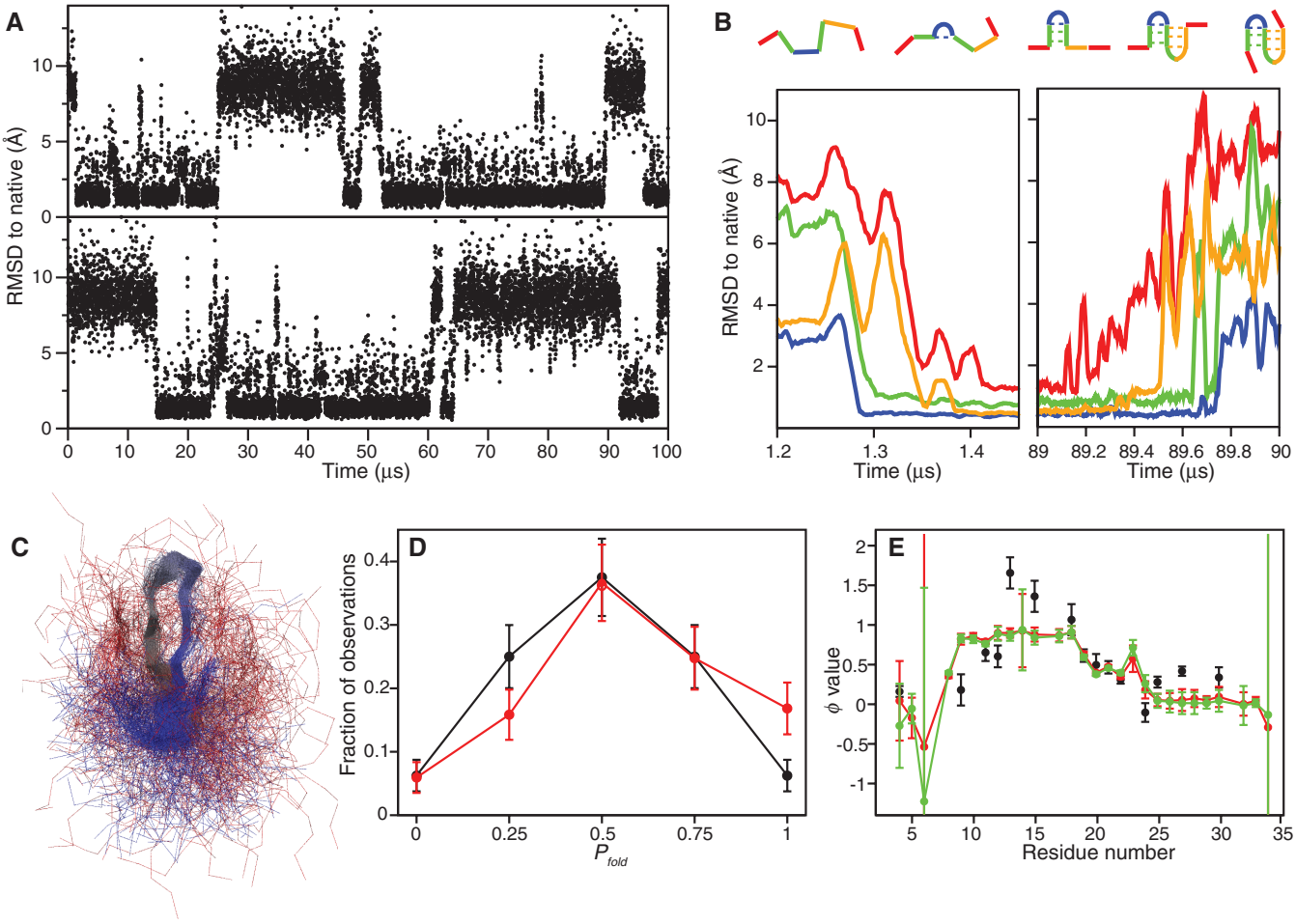

Fig. 2. Reversible folding simulation of FiP35. (**A**) RMSD time series of two independent 100-μs simulations of FiP35 initiated from an extended state. RMSD with respect to the x-ray structure (*15*) was calculated for the C_α atoms of residues 4 to 32. A total of eight folding and seven unfolding events can be observed within the two simulations. (**B**) Representative sequence of events leading to folding (left) and unfolding (right). RMSD to the x-ray structure was calculated for different regions of the protein, namely the tip of hairpin 1 (residues 12 to 18, blue), the entire hairpin 1 (residues 8 to 22, green), hairpin 2 (residues 19 to 30, orange), and the full protein (residues 2 to 33, red). Analyses of the individual transitions reveal a consistent sequence of events leading to folding (upper panel): The tip of hairpin 1 forms first, followed by hairpin 1, followed by hairpin 2, followed by the rest of the protein. The reverse sequence of events is observed in unfolding transitions. (**C**) Representative members of the transition-state ensemble reveal that the first, but not second, hairpin is structured in the TSE for folding. The transition-state ensemble was identified from equilibrium simulations using a previously described procedure (*29*), and representative structures were superimposed using Theseus software. (**D**) Commitment probability (P_{fold}) distribution of the TSE as calculated from 101 structures, using four simulations for each structure. The observed distribution of P_{fold} (red) is compared with the binomial distribution expected for a true TSE (black). (**E**) Comparison of experimental and calculated φ values. Two sets of φ values (red and green) were calculated independently from the two simulations and are compared to the experimental values (black) obtained for wild-type Pin1 WW domain (*17*). Error bars in (D) and (E) correspond to ±1 SEM.

and unfolding rates are measured for a series of mutants. The results are typically presented as ϕ values (*30*). A ϕ value of ~1 suggests that the interactions formed by a residue in the native state are also present in the TSE, whereas a value close to zero indicates that the native-state interactions are not present in the TSE. Commonly, ϕ values are calculated from simulation by approximating the mutational free-energy changes from the fraction of native side-chain contacts lost upon mutation (*31*). We used this approach to calculate ϕ values for side chains and a free-energy perturbation approach (*25*) for the backbone, and compared the results to experimental measurements in a related WW domain (Fig. 2E) (*17*). The values obtained confirm the observation that the first hairpin is essentially fully formed in the TSE, whereas the second hairpin only makes a fraction of the contacts found in the native state.

Although the agreement between simulation and experiment (Fig. 2E) is encouraging, it may also be somewhat fortuitous, as the number of atomic contacts is only a rough approximation for the free energy (*32*). We thus also calculated ϕ values directly from the folding and unfolding rates obtained from reversible folding simulations of mutant proteins (*33*, *34*) and compared these results to ϕ values calculated by applying the contact approximation to the TSE for FiP35.

We chose to study the effects of six mutations that we expected to have different effects on the folding and unfolding rates (Fig. 2E). Ser^{13} → Ala, located in the tip of the first hairpin, and Arg^{11} → Ala, located in the central β strand, are expected to have high ϕ values; Tyr^{19} → Leu and Phe^{21} → Leu, both located in the central β strand, are expected to have intermediate ϕ values; and Leu^{4} → Ala and Trp^{8} → Phe, located in the hydrophobic core, are expected to have low ϕ values.

All six mutants folded reversibly to the native state, albeit with different rates and stabilities (Table 1). For most mutants, the changes in stability upon mutation were in good agreement with experimental data. Most of the ϕ values calculated from the folding and unfolding rates were in reasonable agreement with the magnitude calculated from the TSE of FiP35 (Table 1), although our results support the notion that individual ϕ values are best interpreted qualitatively (*35*, *36*).

A notable exception is the Arg^{11} → Ala mutation, whose low ϕ value calculated from the folding kinetics (0.2) is substantially smaller than the high value expected from the contact approximation (0.8). Although the reasons for this discrepancy remain unclear, our results overall support the use of experimentally derived ϕ values to infer the structural properties of the TSE, with the caveat that the contact approximation may fail in individual cases (*35*); all the experimental ϕ values should thus be considered simultaneously when inferring the overall structural properties for a TSE (*31*). Finally, we note that all mutant proteins fold via the same overall pathway as FiP35, although some of the mutations appear to cause a noticeable Hammond-like shift in the structure of the TSE (fig. S4).

It is perhaps worth noting that these simulations may also provide a computational gold standard for future studies exploring the accuracy and efficiency of methods for the prediction of mutational free-energy differences and folding rates.

FiP35 folds across a small free-energy barrier. We determined the free-energy profile and position-dependent diffusion constant along the optimized reaction coordinate (*25*). We found that the free-energy barrier for folding is small (1.6 kcal mol^{-1} or ~$2k_BT$), consistent with the suggestion that FiP35 is an incipient downhill folder (*12*). The transition-state region is broad and flat (Fig. 3A), helping to explain the long commitment time observed in the P_{fold} analysis. Langevin simulations on the free-energy profile (Fig. 3B) approximate well the folding dynamics observed in the MD simulations, and we are thus able to use this kinetic model to simulate a temperature-jump experiment (*25*). In addition to the slow phase associated with folding, we observed a fast "molecular" phase whose amplitude and time constant depend on both the size of the temperature jump and the spectroscopic probe used (*25*). Such features are spectroscopic indications of protein folding across a low free-energy barrier, and they support the notion that experimental studies of fast-folding proteins might be used to probe directly the spectroscopic properties of the TSE (*37*).

It has been argued that the fast molecular phase provides an estimate of the time scale for transition paths in folding of FiP35 (*37*). The value obtained in these experiments (≤0.7 μs) is in agreement with theoretical estimates (0.3 μs) as well as with the upper bound (200 μs) obtained directly through single-molecule experiments (*6*). These values also agree with the average transition path time observed in our equilibrium simulations (0.4 ± 0.1 μs). Thus, a range of different techniques (simulation, theory, ensemble, and single-molecule experiments) provide independent evidence for transition path times for protein folding on the order of 1 μs.

Native-state dynamics of BPTI. Dynamic changes in protein structure typically occur not only during but also after the folding process. The 58-residue protein BPTI was the subject of the first nuclear magnetic resonance (NMR) experiments of the internal motions of proteins (*38*). NMR studies showed that on time scales ranging from nanoseconds to milliseconds, several internal water molecules exchange with the bulk (*39*, *40*), a number of aromatic rings rotate (*38*, *41*), and a disulfide bridge isomerizes (*42*, *43*). We used a 1-ms MD simulation at a temperature of 300 K to reproduce and interpret the kinetics of folded BPTI.

Table 1. Computational ϕ-value analysis of FiP35. In columns 2 and 3, the ϕ values for six selected mutants, calculated from the folding and unfolding rates obtained from reversible folding simulations, are compared with the values estimated from a contact approximation. In columns 4 and 5, the calculated free-energy changes upon mutation are compared to the values measured experimentally at the melting temperature of the hPin1 WW domain (*49*).

Mutation	ϕ Value		$\Delta\Delta G_{mut}$ (kcal mol^{-1})	
	MD	Contact approx.	MD (±SEM)	Experiment
Leu^{4} → Ala	−0.6	−0.1	0.5 (0.4)	1.5
Trp^{8} → Phe	−0.1	0.4	1.6 (0.4)	1.8
Arg^{11} → Ala	0.2	0.8	1.8 (0.5)	1.7
Ser^{13} → Ala	1.1	0.9	0.4 (0.5)	n/a
Tyr^{19} → Leu	0.3	0.7	1.1 (0.4)	1.1
Phe^{21} → Leu	0.4	0.5	2.4 (0.5)	1.4

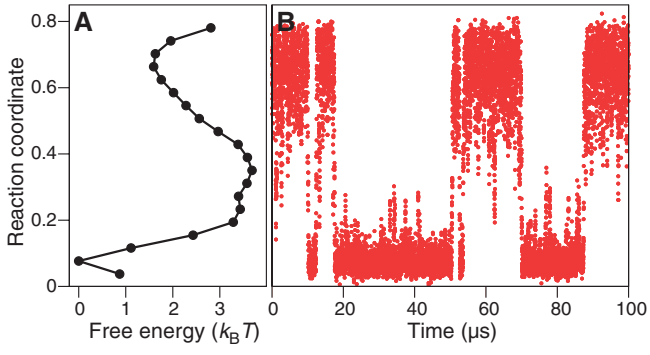

Fig. 3. Folding kinetics across a low energy barrier. (**A**) Free-energy profile along an optimized reaction coordinate. The profile exhibits two minima, centered at 0.1 and 0.7, corresponding to the folded and unfolded basins, respectively. The folding and unfolding free-energy barriers are $2k_BT$ and $3.5k_BT$, respectively. (**B**) Langevin simulation of WW folding in a one-dimensional model. The simulation was based on the one-dimensional free-energy profile in (A) and a position-dependent diffusion coefficient, both derived from the MD simulation data.

Our simulation of BPTI transitioned reversibly among a small number of structurally distinct long-lived states (Fig. 4A) of lifetimes ranging from 6 to 26 μs. The two most populated states in the simulation, which together accounted for 82% of the trajectory, are supported by experimental data. The average structure of the "crystallographic" state, which was occupied 27% of the time in our simulation, had an RMSD (between nonsymmetric heavy atoms of residues 4 to 54) of only 0.8 Å from the crystal structure (*44*). The most populated state (occupied 56% of the time) exhibits a left-handed conformation of the disulfide bridge between Cys^{14} and Cys^{38}, which has been previously suggested by NMR experiments (*42*, *43*). The imbalance in populations between simulation and experiment represents an error in the conformational free-energy difference of just a few times the thermal energy, which falls within the expected accuracy range of the force field representation.

In addition to the two states anticipated by previous experiments, the systematic analysis of the dynamics provides evidence for the existence of at least three additional states. In some, the exposed surface area of BPTI was large, as the conformation displayed an additional water-filled cavity or even a pore; in others, the small N-terminal helix unfolded.

Separation of time scales in protein dynamics. As part of our analysis of the native-state dynamics of BPTI, we performed dynamical content calculations, derived from the autocorrelation of bond orientations over a very wide (and previously inaccessible) range of time lags, to quantify the structural relaxation occurring on different time scales and the persistence of various structural features (*25*). These analyses revealed a distinct separation of time scales: Hopping among conformational basins occurs on time scales on the order of 10 μs, whereas motions within the individual basins occur on a time scale that is faster by several orders of magnitude. Substantially less dynamical content is measured within the wide gap that lies between these two time scales (Fig. 4B).

This separation of time scales, a hallmark of barrier-crossing dynamics (*5*), allowed us to partition the trajectory into distinct long-lived states (color-coded in Fig. 4A) using a new kinetic clustering scheme, which was designed to retain important aspects of the long–time scale behavior observed in the MD simulation (*25*).

We found that the fast relaxations, which extend up to the 10-ns time scale, originate primarily from side-chain motions, whereas the slow relaxations—corresponding to hops between well-separated basins—originate almost exclusively from backbone motions (Fig. 4B). Apart from low-amplitude vibrations with frequencies several orders of magnitude higher than those of conformational state transitions, bond orientations within the backbone exhibit little variation within a given state; motion is "frozen out" not only at the level of the protein's global structure, but at a local level within the polypeptide chain. Side chains, on the other hand, experience large fluctuations on the nanosecond time scale; these fluctuations, however, are nearly identical in all conformational states, leading to the absence of a long–time scale signature in the side-chain dynamical content. These findings provide a unifying model, encompassing an extremely wide range of time scales, that integrates the previously established picture of "liquid-like" side chains attached to a "solid backbone" (*45*, *46*) with the common observation of distinct conformational states (*2*, *3*).

The transition path time for conformational transitions was generally at least several hundred nanoseconds (*25*). This time—which might, if anything, tend to increase with protein size—serves as a lower bound for the lifetime of indi-

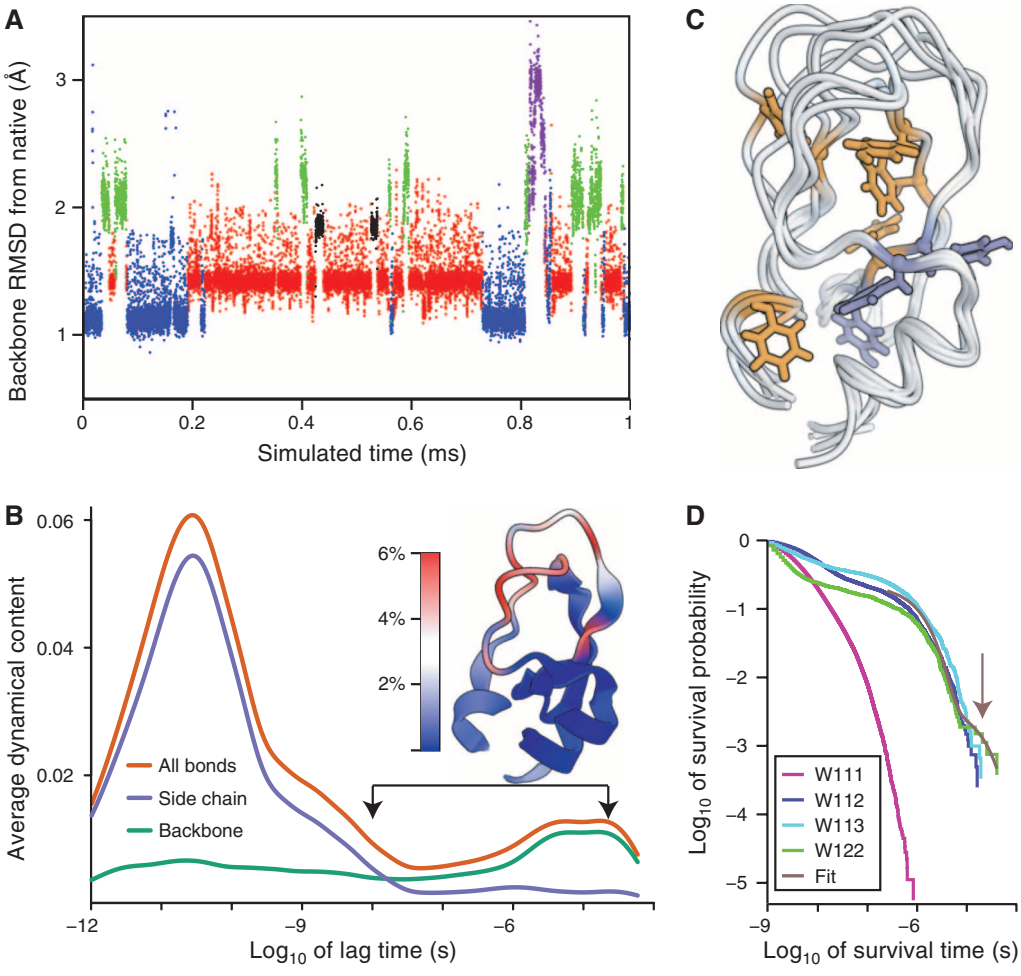

Fig. 4. Native-state dynamics of BPTI. (**A**) All-residue backbone RMSD from the crystal structure with PDB ID 5PTI (*44*). Each point shows the median value in a window of 50 ns. The color of the data points denotes cluster membership. [See (*25*) for PDB files representative of each of the five most-visited states in the 1-ms simulation of BPTI, together with a more detailed analysis of the local structural features that best discriminate each state from the others.] (**B**) Dynamical content of the P_2 internal correlation functions (*25*) and its decomposition into side-chain and backbone contributions. The peak near 28 ps results from the relaxation of the side chains within a conformation, whereas the peak around 10 μs results from the relaxation of the backbone during jumps between states. The cartoon shows the fractional contribution of each residue to the decay of the average internal correlation function between lag times of 10 ns and 20 μs. (**C**) Crystal structure of BPTI, highlighting the aromatics that rotate slowly in purple and those that rotate quickly in orange, with representative structures from each of the four additional conformations observed in the simulation. (**D**) Survival probability distributions for each of the four internal water molecules of BPTI. The arrow at 14 μs marks the lifetime of the slowest waters, as determined from a double-exponential fit of the tail of the W122 survival times.

vidual conformational states. Even for a protein as small as BPTI, this lower bound is more than an order of magnitude larger than the time scale of intrabasin side-chain motions. This observation suggests that a distinct separation of time scales, with a region of reduced dynamical activity in the interval between those time regimes, is likely to be a common feature of the dynamics of folded proteins.

Local probes that report on large-scale conformational change. Seven of the eight aromatic rings of BPTI rotated in the simulation (*25*) with rates that generally agree with experiment (*38*, *41*). We found that the rings that rotated slowly in the simulation were all located in the portion of the protein that did not change during hops between basins (purple side chains in Fig. 4C). In contrast, the rings that rotated quickly in the simulation were located in the portion of the protein that changed in the different conformational states (orange side chains in Fig. 4C) (*25*).

In agreement with experiment (*40*), the simulation displayed three distinct behaviors for the four internal water molecules (Fig. 4D), with W111 exchanging very rapidly with the solvent, W112 and W113 exchanging on a slower time scale, and W122 exchanging even more slowly. The tail of the survival probability of W122 displays single-exponential decay with a lifetime of 14 μs, suggesting that the longest-lived waters have a single escape mechanism. The binding events of the eight longest-lived instances of W122 (each bound for more than 9 μs) all occurred while the simulation was in the "crystallographic" state. Accordingly, the lifetime of this state in the simulation (25 μs) is longer than the lifetime of W122 (14 μs). The lifetime of the longest-lived waters may thus provide an experimentally measurable lower bound on the lifetime of the protein conformation that most tightly binds to that water.

The water escape path lasted only a few picoseconds. Before the escape, a small pocket opened on the protein surface that allowed a single water molecule to form a hydrogen bond with W122; W122 took the place of that hydrogen-bonded water, and a transient empty cavity was created inside the protein. The wide contrast between the lifetime of W122 and the duration of its exit and entry pathways suggests that ligand entry and escape can proceed without the need for long-lived intermediate conformations; thus, binding and escape events can be considerably faster than the lifetime of the ligand.

Transition path times for conformational changes. Conformational changes such as those described here for FiP35 and BPTI differ from simpler chemical reactions in that the former occur on a rough free-energy landscape characterized by many local minima. The roughness of the landscape manifests itself in a substantial slowdown of conformational changes and in a kinetic preexponential factor, k_0, that is many orders of magnitude larger than the value expected for elementary reactions in small molecules. Using the folding rate and barrier height we obtained for FiP35, we estimate the preexponential factor to be ~1 μs^{-1}. A related quantity is the average transition-path time $\langle t_{TP} \rangle$ (i.e., the time required for the actual conformational change to occur). This value is also expected to be sensitive to the landscape roughness. We obtained a $\langle t_{TP} \rangle$ value of 0.4 μs for the folding reaction of FiP35 and 0.3 μs for the conformational changes observed in BPTI.

Indirect estimates for k_0 and $\langle t_{TP} \rangle$ have previously been proposed on the basis of theory and experiment (*6*, *12*, *24*, *37*, *47*, *48*), but these fundamental quantities have proven difficult to measure. The microsecond time scales associated with these constants are not only in general agreement with previous estimates, but also close to the observed time scales for conformational changes in FiP35 and BPTI, thus strengthening the notion that landscape roughness is a major determinant of the rates for conformational transitions in biological macromolecules.

Conclusions. The specialized machine we developed has allowed us to perform continuous, all-atom molecular dynamics simulations of proteins in an explicitly represented solvent environment over periods as much as 100 times longer than was previously feasible. Comparison of the results of these simulations with experimental measurements provides evidence for the non-obvious finding that existing force fields are capable of realistically describing of the structure and dynamics of proteins over even these extended time scales. More generally, our findings suggest that very long molecular dynamics simulations can serve as a powerful tool for elucidating the atomic-level behavior of proteins on a biologically critical but previously inaccessible time scale.

References and Notes

1. A. Mittermaier, L. E. Kay, *Science* **312**, 224 (2006).
2. A. K. Gardino *et al.*, *Cell* **139**, 1109 (2009).
3. J. P. Abrahams, A. G. W. Leslie, R. Lutter, J. E. Walker, *Nature* **370**, 621 (1994).
4. H. Noji, R. Yasuda, M. Yoshida, K. Kinosita Jr., *Nature* **386**, 299 (1997).
5. H. Frauenfelder, S. G. Sligar, P. G. Wolynes, *Science* **254**, 1598 (1991).
6. H. S. Chung, J. M. Louis, W. A. Eaton, *Proc. Natl. Acad. Sci. U.S.A.* **106**, 11837 (2009).
7. H. Lei, Y. Duan, *Curr. Opin. Struct. Biol.* **17**, 187 (2007).
8. C. D. Snow, H. Nguyen, V. S. Pande, M. Gruebele, *Nature* **420**, 102 (2002).
9. J. L. Klepeis, K. Lindorff-Larsen, R. O. Dror, D. E. Shaw, *Curr. Opin. Struct. Biol.* **19**, 120 (2009).
10. P. L. Freddolino, F. Liu, M. Gruebele, K. Schulten, *Biophys. J.* **94**, L75 (2008).
11. D. E. Shaw *et al.*, Millisecond-scale molecular dynamics simulations on Anton. In *Proceedings of the ACM/IEEE Conference on Supercomputing (SC09)* (ACM Press, New York, 2009).
12. F. Liu *et al.*, *Proc. Natl. Acad. Sci. U.S.A.* **105**, 2369 (2008).
13. J. A. McCammon, B. R. Gelin, M. Karplus, *Nature* **267**, 585 (1977).
14. M. Levitt, A. Warshel, *Nature* **253**, 694 (1975).
15. M. Jäger *et al.*, *Proc. Natl. Acad. Sci. U.S.A.* **103**, 10648 (2006).
16. S. Deechongkit *et al.*, *Nature* **430**, 101 (2004).
17. M. Jäger, H. Nguyen, J. C. Crane, J. W. Kelly, M. Gruebele, *J. Mol. Biol.* **311**, 373 (2001).
18. M. Petrovich, A. L. Jonsson, N. Ferguson, V. Daggett, A. R. Fersht, *J. Mol. Biol.* **360**, 865 (2006).
19. P. L. Freddolino, S. Park, B. Roux, K. Schulten, *Biophys. J.* **96**, 3772 (2009).
20. F. Noé, C. Schütte, E. Vanden-Eijnden, L. Reich, T. R. Weikl, *Proc. Natl. Acad. Sci. U.S.A.* **106**, 19011 (2009).
21. D. L. Ensign, V. S. Pande, *Biophys. J.* **96**, L53 (2009).
22. J. Juraszek, P. G. Bolhuis, *Biophys. J.* **98**, 646 (2010).
23. K. Lindorff-Larsen *et al.*, *Proteins Struct. Funct. Bioinform.* **78**, 1950 (2010).
24. J. Kubelka, T. K. Chiu, D. R. Davies, W. A. Eaton, J. Hofrichter, *J. Mol. Biol.* **359**, 546 (2006).
25. See supporting material on *Science* Online.
26. S. Gianni *et al.*, *Proc. Natl. Acad. Sci. U.S.A.* **100**, 13286 (2003).
27. E. L. McCallister, E. Alm, D. Baker, *Nat. Struct. Biol.* **7**, 669 (2000).
28. M. Karplus, D. L. Weaver, *Protein Sci.* **3**, 650 (1994).
29. R. B. Best, G. Hummer, *Proc. Natl. Acad. Sci. U.S.A.* **102**, 6732 (2005).
30. A. Matouschek, J. T. Kellis Jr., L. Serrano, A. R. Fersht, *Nature* **340**, 122 (1989).
31. M. Vendruscolo, E. Paci, C. M. Dobson, M. Karplus, *Nature* **409**, 641 (2001).
32. E. Cota, S. J. Hamill, S. B. Fowler, J. Clarke, *J. Mol. Biol.* **302**, 713 (2000).
33. H. Nymeyer, N. D. Socci, J. N. Onuchic, *Proc. Natl. Acad. Sci. U.S.A.* **97**, 634 (2000).
34. G. Settanni, F. Rao, A. Caflisch, *Proc. Natl. Acad. Sci. U.S.A.* **102**, 628 (2005).
35. C. D. Geierhaas, X. Salvatella, J. Clarke, M. Vendruscolo, *Protein Eng. Des. Sel.* **21**, 215 (2008).
36. A. R. Fersht, S. Sato, *Proc. Natl. Acad. Sci. U.S.A.* **101**, 7976 (2004).
37. F. Liu, M. Nakaema, M. Gruebele, *J. Chem. Phys.* **131**, 195101 (2009).
38. K. Wüthrich, G. Wagner, *FEBS Lett.* **50**, 265 (1975).
39. G. Otting, E. Liepinsh, K. Wüthrich, *Science* **254**, 974 (1991).
40. E. Persson, B. Halle, *J. Am. Chem. Soc.* **130**, 1774 (2008).
41. G. Wagner, D. Brühwiler, K. Wüthrich, *J. Mol. Biol.* **196**, 227 (1987).
42. G. Otting, E. Liepinsh, K. Wüthrich, *Biochemistry* **32**, 3571 (1993).
43. M. J. Grey, C. Wang, A. G. Palmer 3rd, *J. Am. Chem. Soc.* **125**, 14324 (2003).
44. A. Wlodawer, J. Walter, R. Huber, L. Sjölin, *J. Mol. Biol.* **180**, 301 (1984).
45. Y. Zhou, D. Vitkup, M. Karplus, *J. Mol. Biol.* **285**, 1371 (1999).
46. K. Lindorff-Larsen, R. B. Best, M. A. DePristo, C. M. Dobson, M. Vendruscolo, *Nature* **433**, 128 (2005).
47. S. Chakrapani, A. Auerbach, *Proc. Natl. Acad. Sci. U.S.A.* **102**, 87 (2005).
48. J. Kubelka, J. Hofrichter, W. A. Eaton, *Curr. Opin. Struct. Biol.* **14**, 76 (2004).
49. M. Jäger, M. Dendle, J. W. Kelly, *Protein Sci.* **18**, 1806 (2009).

50. We are very grateful to all members of the Anton hardware and software teams, without whom this work would not have been possible. We thank G. Hummer for providing us with the software to calculate position-dependent diffusion constants, A. Pan for helpful suggestions, T. Tu for assisting with trajectory analysis, A. Philippsen for helping with the BPTI renderings, K. Mackenzie for monitoring and supporting the BPTI simulation, and R. Kastleman and J. McGrady for editorial assistance.

Supporting Online Material

www.sciencemag.org/cgi/content/full/330/6002/341/DC1
Materials and Methods
Figs. S1 to S14
Tables S1 to S3
PDB files S1 to S5

22 January 2010; accepted 31 August 2010
10.1126/science.1187409

Particle Acceleration on Megaparsec Scales in a Merging Galaxy Cluster

Reinout J. van Weeren,[1]* Huub J. A. Röttgering,[1] Marcus Brüggen,[2] Matthias Hoeft[3]

Galaxy clusters form through a sequence of mergers of smaller galaxy clusters and groups. Models of diffusive shock acceleration suggest that in shocks that occur during cluster mergers, particles are accelerated to relativistic energies, similar to conditions within supernova remnants. In the presence of magnetic fields, these particles emit synchrotron radiation and may form so-called radio relics. We detected a radio relic that displays highly aligned magnetic fields, a strong spectral index gradient, and a narrow relic width, giving a measure of the magnetic field in an unexplored site of the universe. Our observations show that diffusive shock acceleration also operates on scales much larger than in supernova remnants and that shocks in galaxy clusters are capable of producing extremely energetic cosmic rays.

In the universe, structure forms hierarchically, with smaller structures merging to form bigger ones. On the largest scales, clusters of galaxies merge, releasing energies on the order of 10^{64} ergs on time scales of 1 billion to 2 billion years (*1*, *2*). During such merger events, large-scale shock waves with moderate Mach numbers of 1 to 5 should be created. In such shocks, diffusive shock acceleration is expected to accelerate electrons to high energies; in the presence of a magnetic field, these particles are expected to form large regions emitting synchrotron radiation at radio wavelengths (*2*–*4*). The accelerated particles at the shock front have a power-law energy distribution, which directly translates into an integrated power-law radio spectrum (flux $\propto \nu^{\alpha}$, where α is the spectral index and ν is frequency). The slope of the particle distribution s in the linear test particle regime, and thus the radio spectral index [$\alpha = (1 - s)/2$], depends only on the compression ratio r of the shock (*5*, *6*), with $s = (r + 2)/(r - 1)$. At the shock front, the intracluster medium (ICM) is compressed such that magnetic fields align parallel to the shock front (*7*). These ordered and aligned magnetic fields cause the radio emission to be highly polarized. Synchrotron and inverse Compton losses cool the radio plasma behind the shock, creating a strong spectral index gradient in the direction toward the cluster center. It has been suggested that such synchrotron-emitting regions from shocks can be identified with radio relics (*3*, *7*). These are elongated radio sources located mostly in the outskirts of massive merging galaxy clusters (*8*–*14*).

We detected a 2-Mpc radio relic (Figs. 1 and 2) located in the northern outskirts of the galaxy cluster CIZA J2242.8+5301 (redshift $z = 0.1921$). This x-ray luminous cluster (*15*) ($L_x = 6.8 \times 10^{44}$ erg s^{-1}, between 0.1 and 2.4 keV) shows a disturbed elongated morphology in Röntgen Satellite (ROSAT) x-ray images (*16*), indicative of a major merger event. The relic is located at a distance of 1.5 Mpc from the cluster center. Unlike other known radio relics, the northern relic is extremely narrow with a width of 55 kpc. Deep Westerbork Synthesis Radio Telescope (WSRT), Giant Metrewave Radio Telescope (GMRT), and Very Large Array (VLA) observations (see supporting online material) show a clear unambiguous spectral index gradient toward the cluster center (Fig. 3). The spectral index, measured over a range of frequencies between 2.3 and 0.61 GHz, decreases from −0.6 to −2.0 across the width of the narrow relic. The gradient is visible over the entire 2-Mpc length of the relic, constituting clear evidence for shock acceleration and spectral aging of relativistic electrons in an outward-moving shock. The relic's integrated radio spectrum is a single power law, with $\alpha = -1.08 \pm 0.05$, as predicted (*5*, *6*). The relic is strongly polarized at the 50 to 60% level, indicating a well-ordered magnetic field, and polarization magnetic field vectors are aligned with the relic. In the southern part of the cluster, located symmetrically with respect to the cluster center and the northern relic, there is a second fainter broader relic. The elongated radio relics are orientated perpendicular to the major axis of the cluster's elongated x-ray–emitting ICM, as expected for a binary cluster merger event in which the second southern relic traces the opposite shock wave (*1*). Furthermore, there is a faint halo of diffuse radio emission extending all the way toward the cluster center connecting the two radio relics (Fig. 1). This emission extends over 3.1 Mpc.

The source cannot be a gravitational lens, because it is too large and located too far from the cluster center. The morphology, spectral index, and association with a cluster exclude the possibility of the source being a supernova remnant. The source is also not related to the radio AGN (active galactic nucleus) located at the eastern end of the relic. High-resolution observations show this source to be detached from the relic (Fig. 2). The spectral and polarization properties are also unlike that of any known tailed radio sources (*17*, *18*). The power-law radio spectral index, clear spectral index gradient, and enormous extent

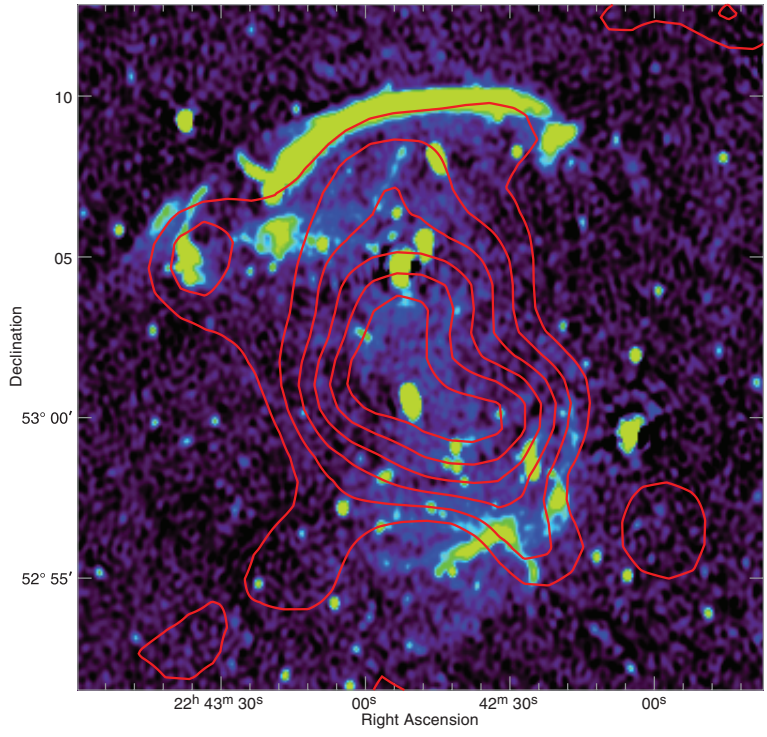

Fig. 1. WSRT radio image at 1.4 GHz. The image has a resolution of 16.5 arc sec × 12.9 arc sec and the root-mean-square (RMS) noise is 19 μJy beam^{-1}. Colors represent intensity of radio emission; red contours (linearly spaced) represent the x-ray emission from ROSAT showing the hot ICM.

[1]Leiden Observatory, Leiden University, P.O. Box 9513, NL-2300 RA Leiden, Netherlands. [2]Jacobs University Bremen, P.O. Box 750561, 28725 Bremen, Germany. [3]Thüringer Landessternwarte, Sternwarte 5, 07778 Tautenburg, Germany.

*To whom correspondence should be addressed. E-mail: rvweeren@strw.leidenuniv.nl

exclude the possibility that the source is tracing (compressed) fossil radio plasma from a radio source whose jets are now off (*19*, *20*). The integrated radio spectra of such fossil sources are very steep ($\alpha < -1.5$) and curved, because the radio-emitting plasma is old and has undergone synchrotron and inverse Compton losses. In addition, the shell-like (and not lobe-like) morphology does not support the above scenario.

Instead, all the observed properties of the relic perfectly match those of electrons accelerated at large-scale shocks via diffusive shock acceleration. The characteristics of the bright relic provide evidence that (at least some) relics are direct tracers of shock waves; moreover, the narrow width of the relic provides a way to determine the magnetic field strength at the location of the shock, using arguments similar to those that have been used for supernova remnants (*21*).

The configuration of the relic arises naturally for a head-on binary cluster merger of roughly equal masses, without much substructure, in the plane of the sky with the shock waves seen edge-on. The polarization fraction of 50% or larger can only be explained by an angle of less than 30° between the line of sight and the shock surface (*10*). Moreover, because there is evidence for spectral aging across the relic, only part of the width can be caused by projection effects.

The amount of spectral aging by synchrotron and inverse Compton losses is determined by the magnetic field strength B, the equivalent magnetic field strength of the cosmic microwave background B_{CMB}, and the observed frequency. The result is a downward spectral curvature resulting in a steeper spectral index in the post-shock region (i.e., lower α). For a relic seen edge-on, the downstream luminosity and spectral index profiles thus directly reflect the aging of the relativistic electrons (*22*). To first approximation, the width of the relic (l_{relic}) is determined by a characteristic time scale (t_{sync}) due to spectral aging, and by the downstream velocity (v_d): $l_{relic} \approx t_{sync} \times v_d$, where $t_{sync} \propto [B^{1/2}/(B^2 + B_{CMB}{}^2)] \times [\nu(1 + z)]^{-1/2}$. Conversely, from the width of the relic and its downstream velocity, a direct measurement of the magnetic field at the location of the shock can be obtained. Using standard shock jump conditions, it is possible to determine the downstream velocity from the Mach number and the downstream plasma temperature.

The spectral index at the front of the relic is -0.6 ± 0.05, which gives a Mach number of $4.6^{+1.3}_{-0.9}$ for the shock (*14*) in the linear regime. Using the $L_x - T$ scaling relation for clusters (*23*), we estimate the average temperature of the ICM to be ~9 keV. Behind the shock front, the temperature is likely to be higher. Temperatures in the range of 1.5 to 2.5 times the average value have previously been observed (*24*). The derived Mach number and the advocated temperature range imply downstream velocities between 900 and 1200 km s^{-1} (we used an adiabatic exponent of 5/3). For the remainder we adopt a value of 1000 km s^{-1}. Using the redshift, downstream velocity, spectral index, and characteristic synchrotron time scale, the width of the relic (in kpc) can be derived as

$$l_{\mathrm{relic,\ 610\ MHz}} \approx 1.2 \times 10^3 \frac{B^{1/2}}{B^2 + B_{\mathrm{CMB}}^2} \qquad (1)$$

where B and B_{CMB} are in units of μG. Because B_{CMB} is known, the measurement of l_{relic} from the radio maps directly constrains the magnetic field. From the 610-MHz image (the image with the best signal-to-noise ratio and highest angular resolution), the relic has a deconvolved width (full width at half maximum) of 55 kpc (Fig. 4). Because Eq. 1 has two solutions, the strength of the magnetic field is 5 or 1.2 μG. However, projection effects can increase the observed width of the relic and affect the derived magnetic field strength. Therefore, the true intrinsic width of the relic could be smaller, which implies that $B \geq 5$ μG or ≤ 1.2 μG (Eq. 1). We investigated the effects of projection using a curvature radius of 1.5 Mpc, the projected distance from the cluster center. Instead of using Eq. 1, we computed full radio profiles (*25*) for different angles subtended by a spherical shock front into the plane of the sky (Ψ; the total angle subtended is 2Ψ for a shell-like relic). The profile for $\Psi = 10°$ and $B = 5$ μG agrees best with the observations (Fig. 4). For $\Psi = 15°$, B is 7 μG or 0.6 μG. Values of Ψ larger

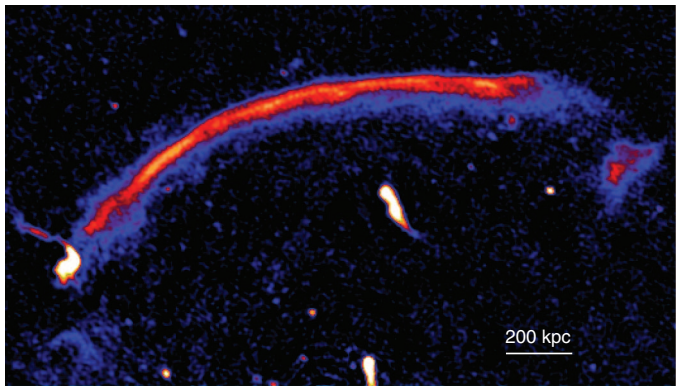

Fig. 2. GMRT 610-MHz radio image. The image has a RMS noise of 23 μJy beam^{-1} and a resolution of 4.8 arc sec × 3.9 arc sec. Colors represent intensity of radio emission.

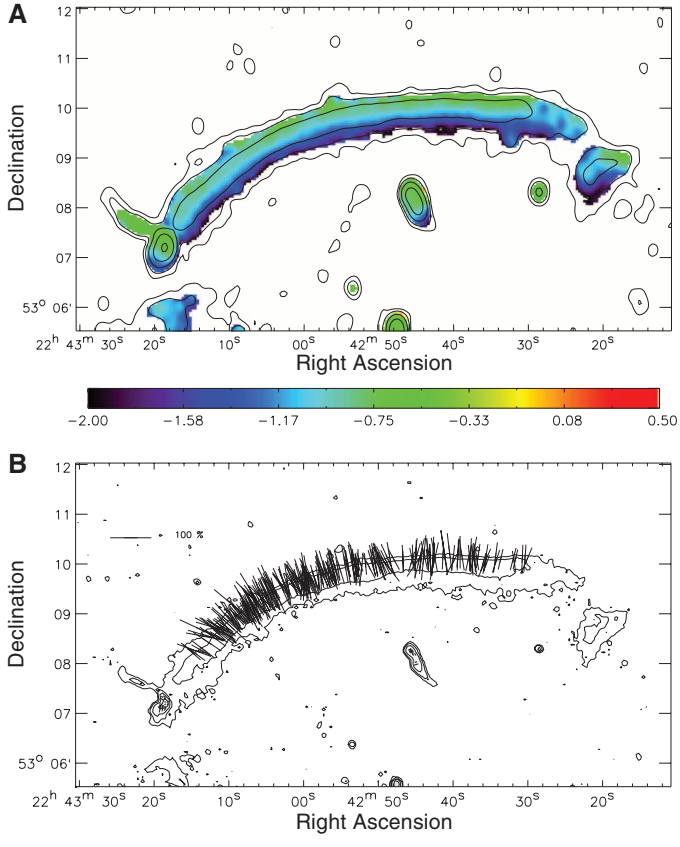

Fig. 3. Radio spectral index and polarization maps. (**A**) The spectral index was determined using matched observations at 2.3, 1.7, 1.4, 1.2, and 0.61 GHz, fitting a power-law radio spectrum to the flux density measurements. The map has a resolution of 16.7 arc sec × 12.7 arc sec. Contours are from the WSRT 1.4-GHz image and are drawn at levels of 1, 4, 16, … × 36 μJy per beam. (**B**) The polarization electric field vector map was obtained with the VLA at a frequency of 4.9 GHz and has a resolution of 5.2 arc sec × 5.1 arc sec. The contours are from Fig. 2 and are drawn at levels of 1, 4, 16, … × 70 μJy per beam. The length of the vectors is proportional the polarization fraction, which is the ratio between the total intensity and total polarized intensity. A reference vector for 100% polarization is shown in the upper left corner. The vectors were corrected for the effects of Faraday rotation using a Faraday depth of −140 rad m^{-2} determined from WSRT observations at 1.2 to 1.8 GHz.

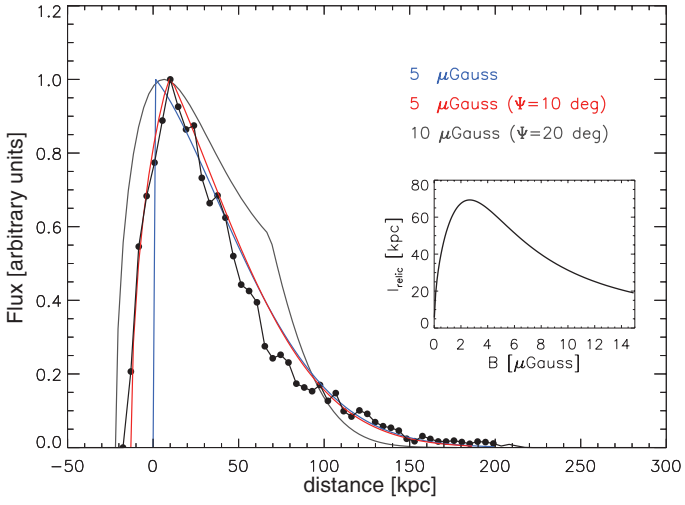

Fig. 4. The deconvolved profile at 610 MHz, averaged over the full length of the relic, is shown by the solid black line and dots. Models for different magnetic field strengths and projection angles (Ψ; i.e., the angle subtended by the relic into the plane of the sky) are overlaid. We used an equivalent magnetic field strength of the CMB at $z = 0.1921$ of 4.6 μG and a downstream velocity of 1000 km s^{-1}. The model (red) for Ψ = 10° and B = 5 μG provides the best fit. A model for $B = 5$ μG without any projection effects is overlaid in blue. For Ψ > 15°, no good fit to the data could be obtained; as an example, we have plotted the profile (gray) for Ψ = 20° and $B = 10$ μG. Inset: The intrinsic width of the relic as a function of magnetic field strength (Eq. 1); for a given width, usually two solutions for the magnetic field strength can be obtained.

than ~15° are ruled out. Lower limits placed on the inverse Compton emission (*26*, *27*) and measurements of Faraday rotation (*28*) indicate magnetic fields higher than ~2 μG. We therefore exclude the lower solutions for the magnetic field strength and conclude that the magnetic field at the location of the bright radio relic is between 5 and 7 μG.

Magnetic fields within the ICM are notoriously difficult to measure. No methods have yielded precise magnetic field strengths as far from the center as the virial radius; only lower limits using limits on inverse Compton emission have been placed. Equipartition arguments have been used as a method to determine the magnetic field strength (*9*, *10*, *12*, *14*), but this method gives only a rough estimate for the magnetic field strength and relies on various assumptions that cannot be verified. The value of 5 to 7 μG we find shows that a substantial magnetic field exists even far out from the cluster center.

Because radio relics directly pinpoint the location of shock fronts, they can be used to obtain a complete inventory of shocks and their associated properties in galaxy clusters. Such an inventory helps to clarify the impact of shocks and mergers on the general evolution of clusters. Because less energetic mergers are more common and have lower Mach numbers, there should be many fainter relics with steep spectra that have escaped detection by current instruments. Interestingly, these large-scale shocks in galaxy clusters have been suggested as acceleration sites for highly relativistic cosmic rays (*29*). As the radiation losses for relativistic cosmic ray protons are negligible, the maximum energy to which they can be accelerated is only limited by the lifetime of the shock, which can last for at least 10^9 years. This means that in merging clusters, protons can be accelerated up to extreme energies of 10^{19} eV, much higher than particles accelerated in supernova remnants.

References and Notes

1. K. Roettiger, J. O. Burns, J. M. Stone, *Astrophys. J.* **518**, 603 (1999).
2. M. Hoeft, M. Brüggen, G. Yepes, S. Gottlöber, A. Schwope, *Mon. Not. R. Astron. Soc.* **391**, 1511 (2008).
3. F. Miniati, T. W. Jones, H. Kang, D. Ryu, *Astrophys. J.* **562**, 233 (2001).
4. C. Pfrommer, T. A. Enßlin, V. Springel, *Mon. Not. R. Astron. Soc.* **385**, 1211 (2008).
5. L. O. Drury, *Rep. Prog. Phys.* **46**, 973 (1983).
6. R. Blandford, D. Eichler, *Phys. Rep.* **154**, 1 (1987).
7. T. A. Ensslin, P. L. Biermann, U. Klein, S. Kohle, *Astron. Astrophys.* **332**, 395 (1998).
8. L. Feretti, *Adv. Space Res.* **36**, 729 (2005).
9. J. Bagchi, F. Durret, G. B. L. Neto, S. Paul, *Science* **314**, 791 (2006).
10. T. E. Clarke, T. A. Ensslin, *Astron. J.* **131**, 2900 (2006).
11. A. Bonafede *et al.*, *Astron. Astrophys.* **503**, 707 (2009).
12. A. Bonafede, G. Giovannini, L. Feretti, F. Govoni, M. Murgia, *Astron. Astrophys.* **494**, 429 (2009).
13. R. J. van Weeren, H. J. A. Röttgering, M. Brüggen, A. Cohen, *Astron. Astrophys.* **505**, 991 (2009).
14. R. J. van Weeren *et al.*, *Astron. Astrophys.* **506**, 1083 (2009).
15. D. D. Kocevski, H. Ebeling, C. R. Mullis, R. B. Tully, *Astrophys. J.* **662**, 224 (2007).
16. W. Voges *et al.*, *Astron. Astrophys.* **349**, 389 (1999).
17. G. K. Miley, *Astron. Astrophys.* **26**, 413 (1973).
18. D. Sijbring, A. G. de Bruyn, *Astron. Astrophys.* **331**, 901 (1998).
19. T. A. Enßlin, Gopal-Krishna, *Astron. Astrophys.* **366**, 26 (2001).
20. T. A. Enßlin, M. Brüggen, *Mon. Not. R. Astron. Soc.* **331**, 1011 (2002).
21. J. Vink, J. M. Laming, *Astrophys. J.* **584**, 758 (2003).
22. M. Markevitch, F. Govoni, G. Brunetti, D. Jerius, *Astrophys. J.* **627**, 733 (2005).
23. M. Markevitch, *Astrophys. J.* **504**, 27 (1998).
24. C. Ma, H. Ebeling, E. Barrett, *Astrophys. J.* **693**, L56 (2009).
25. M. Hoeft, M. Brüggen, *Mon. Not. R. Astron. Soc.* **375**, 77 (2007).
26. K. Nakazawa *et al.*, *Publ. Astron. Soc. Jpn.* **61**, 339 (2009).
27. A. Finoguenov, C. L. Sarazin, K. Nakazawa, D. R. Wik, T. E. Clarke, *Astrophys. J.* **715**, 1143 (2010).
28. T. E. Clarke, P. P. Kronberg, H. Böhringer, *Astrophys. J.* **547**, L111 (2001).
29. D. Ryu, H. Kang, E. Hallman, T. W. Jones, *Astrophys. J.* **593**, 599 (2003).

30. The WSRT is operated by ASTRON (Netherlands Institute for Radio Astronomy) with support from the Netherlands Foundation for Scientific Research (NWO). We thank the staff of the GMRT who have made these observations possible. The GMRT is run by the National Centre for Radio Astrophysics of the Tata Institute of Fundamental Research. The National Radio Astronomy Observatory is a facility of the National Science Foundation operated under cooperative agreement by Associated Universities Inc. Supported by the Royal Academy of Arts and Sciences (KNAW) (R.J.v.W.). We thank G. Brunetti for discussions.

Supporting Online Material

www.sciencemag.org/cgi/content/full/science.1194293/DC1
SOM Text
Figs. S1 and S2
References

25 June 2010; accepted 7 September 2010
Published online 23 September 2010;
10.1126/science.1194293
Include this information when citing this paper.

Discovery of a Frank-Kasper σ Phase in Sphere-Forming Block Copolymer Melts

Sangwoo Lee, Michael J. Bluemle,* Frank S. Bates†

Sphere-forming block copolymers are known to self-assemble into body-centered cubic crystals near the order-disorder transition temperature. Small-angle x-ray scattering and transmission electron microscopy experiments on diblock and tetrablock copolymer melts have revealed an equilibrium phase characterized by a large tetragonal unit cell containing 30 microphase-separated spheres. This structure, referred to as the sigma (σ) phase by Frank and Kasper more than 50 years ago, nucleates and grows from the body-centered cubic phase similar to its occurrence in metal alloys and is a crystal approximant to dodecagonal quasicrystals. Formation of the σ phase in undiluted linear block copolymers (and certain branched dendrimers) appears to be mediated by macromolecular packing frustration, an entropic contribution to the interparticle interactions that control the sphere-packing geometry.

The organization of atoms, molecules, and larger aggregates into condensed phases with specific symmetries and spatial dimensions dictates the physical properties of all materials. Naïvely, spherical particles might be expected to present the simplest case. Yet filling space in three dimensions with spherical objects can produce surprisingly complex structures,

including disordered liquids, vitrified glasses, crystalline solids, and quasicrystals. Rare gas atoms, governed by attractive van der Waals interactions and strongly repulsive cores, such as argon and xenon, behave as simple hard spheres and form either face-centered cubic (fcc) or hexagonal close-packed (hcp) crystals at low temperatures and high pressures (*1*). These close-packed structures, along with body-centered cubic (bcc) packing, account for all but a few of the metallic elements in the periodic table (*2*). Colloidal crystals present a similar packing problem but at much larger length scales, typically 0.1 to 1 μm. Modern synthetic and processing techniques permit the preparation of uniformly sized spherical colloidal particles that can be arranged as fcc, hcp, or bcc crystals, depending on the surface treatment and processing strategies employed (*3*–*5*).

Many soft materials contain spherical molecular assemblies at mesoscopic length scales, intermediate to those associated with atomic and colloidal crystallization, including lipids and surfactants (*6*), dendrimers (*7*) and block copolymers (*8*). Ordering in these systems often reflects a tendency to minimize packing frustration, that is, elimination of entropically expensive molecular configurations necessitated by the incompressible nature of soft matter (*9*). These constraints are particularly evident in block copolymers (*10*), which exhibit a host of self-assembled morphologies depending on the molecular architecture (e.g., AB diblock and ABC triblock), block chemistry and composition, and overall molecular weight. Thirty years ago, Leibler anticipated that near the order-to-disorder transition (ODT), asymmetric diblock copolymer melts would form spherical microdomains ordered on a bcc lattice (*11*), a prediction that is now universally accepted (*12*).

Leibler also considered the possibility of icosahedral order in block copolymer melts, motivated in part by a provocative publication by Alexander and McTague describing a general treatment of crystal melting based on Landau theory (*13*). However, because objects with five-fold symmetry can not form periodic structures with translational order, this option was dismissed by both groups. Discovery of quasicrystalline order in multicomponent alloys in 1984 (*14*, *15*), just 4 years after Leibler's seminal contribution, heralded a new era in material design, one that continues to expand today. Hundreds of aperiodically ordered compounds have been reported with underlying 5-, 7-, 8-, 10- and 12-fold symmetry, usually generated by rapidly supercooling a multicomponent liquid (*16*). With one noteworthy exception (*17*), we are unaware of any experimental realizations of quasicrystals formed from single-component, sphere-forming liquids, although computer simulations suggest that this may be possible.

Keys and Glotzer (*18*) reported the growth of a metastable dodecagonal quasicrystal phase in molecular simulations of a supercooled liquid of spherical particles governed by an interatomic potential due to Dzugutov (*19*), known to produce local icosahedral clustering. The stable (equilibrium) state for this system is believed to be the σ phase (*20*), a crystal structure formed from coordinated polyhedra as first described by Frank and Kasper (*21*) more than 50 years ago. There is a close relationship between aperiodic order and periodic crystals with large unit cells; the Frank-Kasper σ phase represents the "periodic approximant" to certain dodecagonal quasicrystals (*18*).

Soft materials are likely candidates for the formation of Frank-Kasper phases and the corresponding quasicrystals (*22*–*24*). A tendency to minimize packing frustration should favor coordination shells among spherical particles that may be incompatible with cubic and hexagonal crystallization for certain molecular architectures. We are aware of only one example of a single-component, sphere-forming soft material (and one class of nonspherical two-component blends) (*25*) that exhibits such phase behavior. Ungar and co-workers (*26*) reported the σ and bcc phases with increasing temperature, and subsequently a dodecagonal quasicrystal (*17*), in wedge-shaped dendrimer molecules that self-assemble into approximately spherical particles. They argue that these morphologies, and a litany of other structures (*7*), are controlled by molecular shape, dictated by specific branched architectures.

Block copolymers offer nearly unlimited flexibility for the design of microphase-separated soft materials based on chain statistics common to all linear molecular architectures. In this report, we demonstrate formation of the Frank-Kasper σ phase in two different single-component, sphere-forming, block copolymer melts near the order-disorder transition temperature (T_{ODT}). This finding anticipates fresh opportunities for designing soft materials with new and potentially useful ordered, and possibly quasicrystalline, structures.

Two undiluted linear block copolymers were investigated. They were prepared by sequential anionic polymerization and characterized using well-established techniques (*27*, *28*). IL-15 is a poly(isoprene-*b*-lactide) (PI-PLA) diblock copolymer with a number-average molecular weight M_n = 3.89 kg/mol and containing 28 weight percent PLA and polydispersity index M_w/M_n = 1.12. Based on the corresponding homopolymer densities, this compound contains 22 ± 1% by volume PLA blocks. Differential scanning calorimetry measurements establish glass transition temperatures of –66°C (PI) and 5°C (PLA) for this material (fig. S1). SISO-3 is a poly(styrene-*b*-isoprene-*b*-styrene-*b*-ethylene oxide) (PS-PI-PS-PEO) tetrablock copolymer with a number-average molecular weight M_n = 23 kg/mol and polydispersity index M_w/M_n = 1.04, containing 46% by volume PS (divided equally), 46% PI and 8% PEO (each ± 1%); synthesis and characterization of this compound has been described elsewhere (*28*). This material forms PEO-rich spheres dispersed in a mixed PS and PI matrix above the melting ($T \approx 38$°C) and glass transition ($T < 100$°C) temperatures, with $T_{ODT,SISO-3} = 224 \pm 3$°C. Both molecular structures are illustrated in Fig. 1.

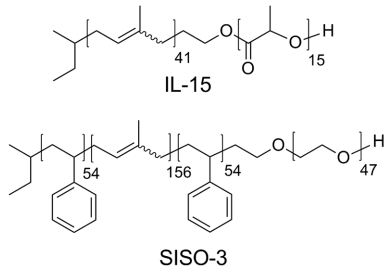

Fig. 1. Molecular architecture of poly(isoprene-*b*-lactide) (IL) and poly(styrene-*b*-isoprene-*b*-styrene-b-ethylene oxide) (SISO).

Small-angle x-ray scattering (SAXS) experiments were conducted at the Advanced Photon Source (Argonne National Laboratory) to assess the state of order in these block copolymers, employing a sample-to-detector distance of 4.04 or 6.64 m and radiation wavelength λ = 0.729 Å. Scattered x-rays were recorded on a Mar CCD area detector and azimuthally averaged to the one-dimensional form of intensity (I) versus scattering wave vector magnitude $|\vec{q}| = q = 4\pi\lambda^{-1}\sin(\theta/2)$, where θ is the scattering angle. Figure 2A shows a series of SAXS measurements obtained after rapidly cooling (≈ 100°C/min) sample IL-15 from 70°C to 40°C. Several minutes after cooling, the broad peak associated with disordered state (correlation hole scattering) spawns sharp, instrument-resolution limited, diffraction peaks that saturate after about 30 min with relative positions $q/q^* = \sqrt{1}, \sqrt{2}, \sqrt{3}, \sqrt{4}, \sqrt{5}, \sqrt{6}, \sqrt{7}$, where $q^* = 0.0648$ Å^{-1} is the location of the lowest-order reflection. This diffraction pattern is consistent with bcc symmetry (unit cell size a = 137 Å), which we associate with the self-assembly of PLA rich spheres in a PI matrix. Based on the molecular composition, the radius of these spheres is R = 41 Å, which is consistent with form-factor scattering at higher q (not shown). Each sphere incorporates approximately 193 block copolymer molecules.

Three-dimensional ordering transforms disordered block copolymer melts into soft solids accompanied by a large increase in the dynamic elastic shear modulus G′ (*29*). We monitored G′ at a frequency of 0.1 rad/s using a mechanical spectrometer after rapidly cooling IL-15 from 120° to 40°C (fig. S2). This experiment confirms that nucleation and growth of the cubic phase takes about 30 min. Upon heating the bcc ordered material from 40°C, the diffraction pattern disappears and G′ collapses at 50 ± 1°C, which is identified as $T_{ODT,IL-15}$.

A qualitatively different SAXS powder pattern develops when sample IL-15 is rapidly

Department of Chemical Engineering and Materials Science, University of Minnesota, Minneapolis, MN 55455, USA.

*Present address: Ashland Inc., Wilmington, DE 19808, USA. †To whom correspondence should be addressed. E-mail: bates@cems.umn.edu

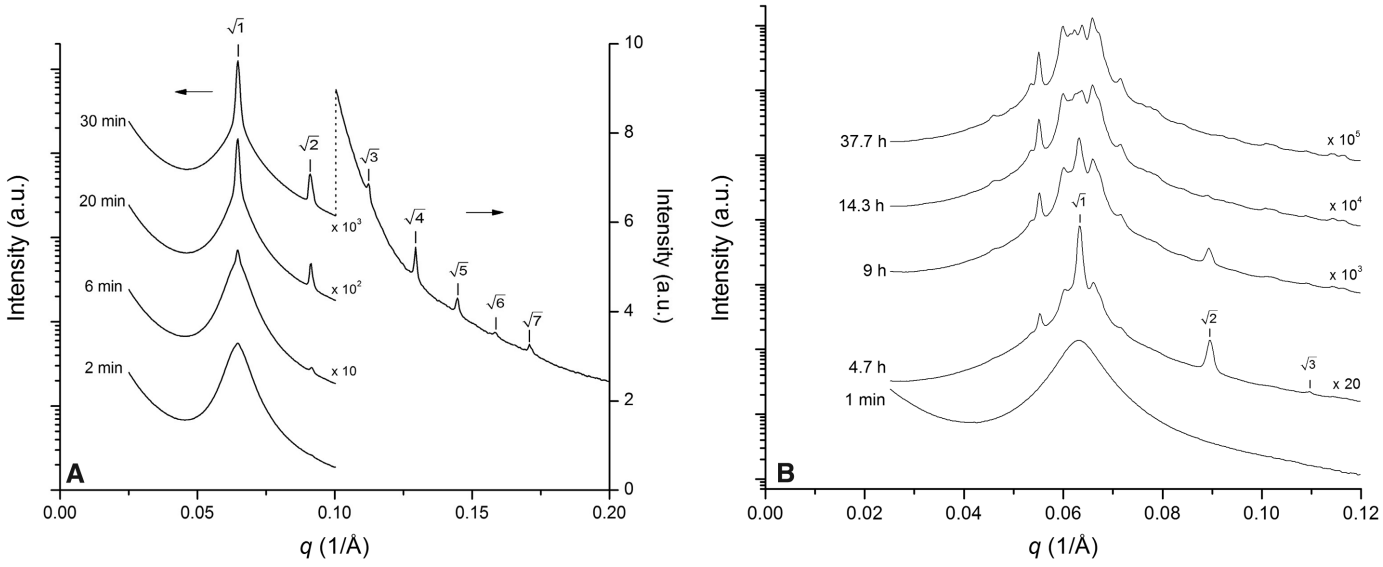

Fig. 2. Synchrotron SAXS powder patterns obtained from sample IL-15. (**A**) After cooling from 70 to 40°C. (**B**) After cooling from 120 to 25°C. Growth of bcc crystals at 40°C is evidenced by the development of Bragg peaks at $q/q^* = \sqrt{1}, \sqrt{2}, \sqrt{3}, \sqrt{4}, \sqrt{5}, \sqrt{6}, \sqrt{7}$. Initial development of cubic order at 25°C ($q/q^* = \sqrt{1}, \sqrt{2}, \sqrt{3}$) is replaced by a slowly evolving state of order that derives from the σ phase.

cooled from $T > T_{ODT,IL\text{-}15}$ to 25°C, as illustrated in Fig. 2B. Initially, scattering peaks consistent with the bcc structure appear, but these are replaced by a set of completely different reflections over the course of about 1 day. After aging this specimen at room temperature (~25°C) for 26 days, we recorded a remarkable diffraction pattern, containing at least 48 distinct peaks as shown in Fig. 3A, which cannot be indexed based on any previously reported block copolymer morphology. Dynamic elasticity measurements reveal a two-step ordering process at 25°C. Evolution of G′ (0.1 rad/s) during the first 30 min after a quench from 120°C follows the behavior documented at 40°C, then the shear modulus continues to slowly grow, by an additional 50% over the next 24-hour period (fig. S2).

We obtained the same unusual SAXS pattern shown in Fig. 3A from sample SISO-3 between 140° and 224°C (T_{ODT}), as illustrated in Fig. 3B (140°C); these data were taken after 1 day of annealing at 140°C (*30*). To facilitate comparison of the data taken from IL-15 and SISO-3, we have adjusted the q scales in Fig. 3 so that the peaks align. Although the SAXS pattern from SISO-3 contains fewer high q reflections, the relative positions and intensities of at least 15 peaks nearly duplicate those recorded with IL-15, leading us to conclude that these materials contain the same structure. Discovery of these nearly identical SAXS results was serendipitous but helped to convince us that this complicated scattering pattern was indeed characteristic of a well-defined ordered morphology.

The positions of the diffraction peaks in Fig. 3, A and B, are consistent with tetragonal symmetry yielding unit cell dimensions: a = 431 Å, c = 228 Å for IL-15 (indexing is provided in table S4), and a = 777 Å and c = 411 Å for SISO-3. Assuming identical spherical morphologies, each large unit cell would contain 30.5 domains based on the initial bcc (Fig. 2B, 4.7 hours) and final (Fig. 3A) Bragg scattering from IL-15. Ungar *et al.* (*26*) reported a SAXS pattern for undiluted wedge-shaped dendrimers that nearly duplicates the 10 most intense peaks found in Fig. 3. They determined that these branched compounds assembled into approximately spherical particles (each containing on average 11.6 molecules) on a tetragonal lattice, 30 particles per unit cell, with $P4_2/mnm$ space group symmetry. ($P\bar{4}n2$ and $P4_2nm$ symmetry are also feasible; the authors assumed the highest allowed symmetry.)

Fig. 3. Synchrotron SAXS powder patterns from (**A**) IL-15 after 26 days at room temperature, and (**B**) SISO-3 after 1 day at 140°C. The q axes have been scaled to facilitate comparison of the relative positions and intensities of these scattering patterns, which are both associated with the σ phase. A model (Rietveld) simulation of the data in (A) for $0.017 \leq q \leq 0.081$ Å^{-1} based on space group $P4_2/mnm$ is presented in (**C**).

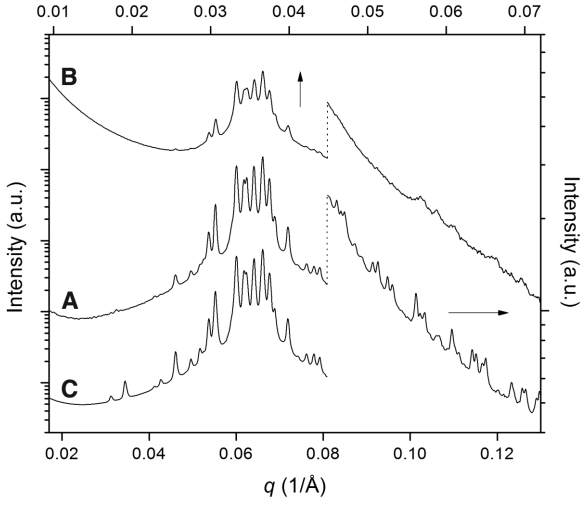

Definitive assignment of a nanoscale morphology to a material is best accomplished based on complementary reciprocal space (i.e., scattering) and real space (i.e., microscopy) analyses. Although IL-15 provides access to an impressive number of SAXS reflections, this specimen is not easily characterized by transmission electron microscopy (TEM) due to the combined effects of a low matrix molecular weight and a reduced glass transition temperature, which complicate microtoming and transferring of thin slices onto microscope grids. Fortunately, SISO-3 is sufficiently robust to permit sample preparation for TEM imaging. A specimen was annealed in vacuum at 140°C for 10 hours, then frozen by plunging into liquid nitrogen. After warming to room temperature, a small piece of the stiff glassy material was sectioned using a Reichert cryo-ultramicrotome. Thin slices (~70 nm thick) were transferred onto copper grids, stained by exposure to the vapor from a 4% aqueous osmium tetraoxide solution (OsO_4 reacts selectively with the PI blocks), and examined with a FEI F30 instrument operated at 300 kV. We found sizable areas of well-ordered morphology in this material (up to 1 μm by 0.4 μm in size), as illustrated in Fig. 4.

Real-space electron density maps were generated from the IL-15 SAXS powder diffraction

data using the Rietveld method with $P4_2/mnm$ symmetry (space group 136) and a set of 30 spherical particles per unit cell. A background intensity function, modeled after the correlation hole scattering obtained immediately after a temperature quench to 25°C (Fig. 2B and fig. S3), was employed in this analysis. Comparison of the experimental and calculated $I(q)$ patterns, determined for $0.017 \leq q \leq 0.081$ Å^{-1}, is shown in Fig. 3, A and C, respectively; optimized Wyckoff positions are listed in table S5. (Note that for $q <$ 0.04 Å^{-1} the calculation is sensitive to minor variations in the scattering power assigned to each Wykoff position, which we estimated based on the Wigner-Seitz cell volumes, as described below. We believe the minor discrepancy between the computed and experimental scattering patterns in the low q range can be attributed to this effect). The resulting crystal structure is shown in Fig. 5A, and projection of a collection of unit cells along the c axis is presented in Fig. 5B. This complex periodic structure is formed from fused dodecagonal cells (layers of alternating hexagonally coordinated rings surrounding a column of spheres) resulting in a vertical projection that closely approximates the TEM image in Fig. 4. Owing to the finite thickness of the TEM specimen, we are not able to delineate every anticipated sphere in the micrograph. Nevertheless, an array of white spots surrounded by dark and gray rings, decorated with additional white spots, are plainly evident. Comparison of the calculated and experimental unit cells indicates that the TEM specimen was sliced at an oblique angle, distorting the four-fold tetragonal symmetry apparent in the calculated projection.

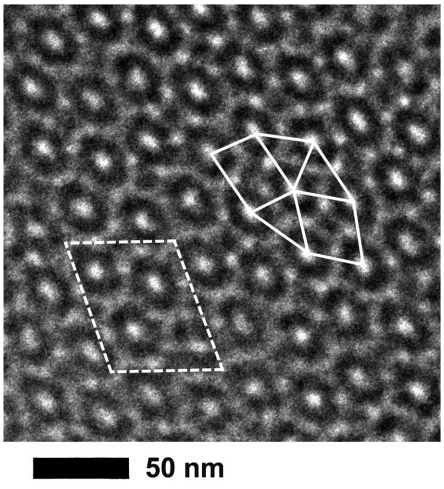

Fig. 4. TEM image recorded from a stained (OsO_4) thin section of sample SISO-3. The morphology is consistent with a tilted c-axis projection of the σ phase, where the unit cell is identified by the dashed rectangle. Isolated white spots surrounded by dark and gray rings are consistent with columns of dodecagonal units of spheres. A five-fold coordinated $3^2.4.3.4$ tiling element, formed from squares and triangles, is associated with each ring in the morphology, verifying the assignment of the σ phase to SISO-3.

Frank and Kasper (*21*) postulated a rich assortment of space-filling algorithms in an effort to rationalize the structure of complex alloys formed from spherical particles. The σ phase, which has $P4_2/mnm$ symmetry and 30 spheres per unit cell, is an important example of such a Frank-Kasper phase. We are aware of only two elemental manifestations of this structure, β-uranium (*31*) and β-tantalum (*32*), although the σ phase is common in metal alloys (*33*), particularly stainless steels, where it nucleates and grows in conjunction with bcc ferrite (*34*). A distinctive feature of this structure is the two-dimensional pattern created by tiling the four-fold plane perpendicular to the stacking (c) direction with triangles and squares. Figure 5B illustrates the basic tiling element of the σ phase: a $3^2.4.3.4$ unit containing two triangles, a square, a triangle, and a square. Five equal-length segments connect the nearest vertices of this element, identifying the five-fold coordination of dodecagonal stacks in the c-axis projection of the σ phase (Fig. 5B). After accounting for the aforementioned skewing, the TEM image can be tiled using the $3^2.4.3.4$ element (Fig. 4), corroborating our assignment of the Frank-Kasper σ phase to SISO-3 at elevated temperatures, and IL-15 at 25°C based on the SAXS identity in Fig. 3.

Ordered microphases in block copolymer melts reflect a delicate balance between enthalpic (H) and entropic (S) factors that govern the overall Gibbs free energy at a given temperature and pressure, $G = H - TS$. Self-assembly leads to ordered arrays of microdomains with specific interfacial area $\Sigma \sim d^2$ (d is the characteristic domain dimension) and interfacial tension $\gamma \sim \chi^{1/2}$ (χ is the Flory-Huggins interaction parameter), where the product $\Sigma\gamma$ determines H. To maintain constant density at fixed domain geometry, the polymer blocks must adopt a distribution of molecular configurations that collectively define the overall entropy S. The equilibrium morphology and lattice parameters are determined by a tradeoff between minimizing H and maximizing S. Until now, the phases that characterize microphase-separated diblock copolymers (spheres, cylinders, gyroid, and lamellae) contain one uniform domain type, for example, one sphere per bcc lattice site (*8*). In contrast, five distinct sphere packing geometries, distributed between ten 12-fold, sixteen 14-fold, and four 15-fold coordinated sites characterize the σ phase.

We have constructed the five different Wigner-Seitz polyhedra that make up the overall volume of the σ-phase unit cell (fig. S6), ranging in volume from 91% to 106% of the average cell volume. This arrangement, which represents a compromise between the purely icosahedron and truncated octahedron (bcc) symmetries anticipated by Landau theory, appears to create additional packing frustration (i.e., a wider range of length scales that must be accommodated by stretched and compressed block configurations), thus reducing the system entropy. Occurrence of the bcc phase at higher temperatures than those associated with the σ phase in IL-15 is consistent with this entropic argument. Based on the lattice parameters obtained at 25°C before and after the bcc-to-σ transformation (Fig. 2B), the ratio of interfacial areas per unit volume is $\langle\Sigma_\sigma\rangle/\Sigma_{bcc} = 0.99$. This implies a slightly smaller enthalpy for the σ phase relative to bcc, which would explain why it is favored over bcc packing at lower temperatures. Clearly, these simple observations must be tested with quantitative theory.

Although IL-15 and SISO-3 have relatively narrow molecular weight and composition distributions, these polymers are not strictly monomolecular and we cannot rule out the possibility that the polymer chains are distributed asymmetrically among the different sites within the σ-phase unit cell. However, the occurrence of this morphology in (presumably) pure monomolecular dendrimers argues against this entropically expensive explanation.

Finally, we are intrigued by the possibility of preparing soft quasicrystalline phases from single-

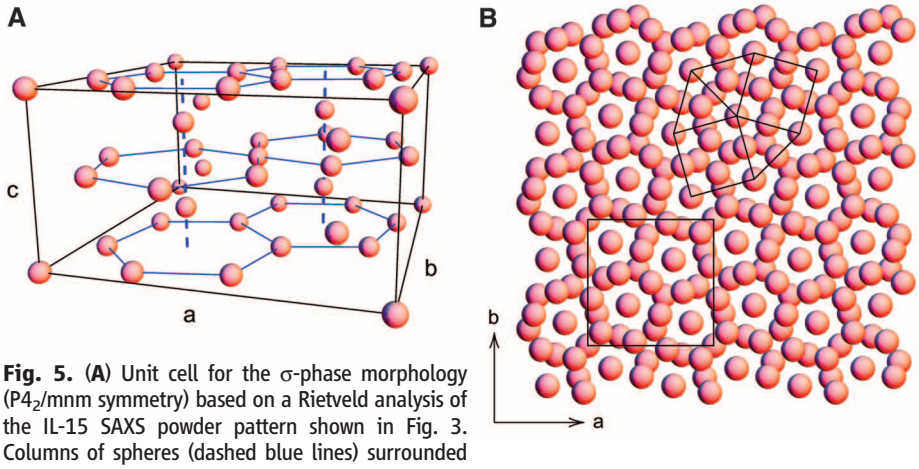

Fig. 5. (**A**) Unit cell for the σ-phase morphology ($P4_2/mnm$ symmetry) based on a Rietveld analysis of the IL-15 SAXS powder pattern shown in Fig. 3. Columns of spheres (dashed blue lines) surrounded by fused rings of hexagonally coordinated spheres (solid blue lines) produce a distinctive pattern when projected along the c axis (**B**), which is consistent with the TEM image in Fig. 4. A $3^2.4.3.4$ tiling element, characteristic of the five-fold coordination of the dodecagonal elements in the σ phase, and the tetragonal face of the unit cell, are sketched on this image.

component block copolymer melts. The σ phase is the approximant crystal structure to certain dodecagonal quasicrystals, and an example of both σ-phase and quasicrystal formation has been reported in a single-dendrimer compound (*17*, *26*). Hayashida *et al*. also reported a dodecagonal quasicrystal in cylinder forming binary blends of star block terpolymer and homopolymer based on the nonperiodic tiling of TEM micrographs with $3^2.4.3.4$ nets (*25*). Molecular simulations indicate that dodecagonal quasicrystals represent slowly evolving metastable states relative to the (equilibrium) σ phase (*18*). Our time-dependent SAXS (Figs. 2 and 3) and mechanical spectroscopy (fig. S2) experiments with IL-15 may reflect a transient quasicrystalline morphology, consistent with these simulations. Appropriately designed block copolymers could represent ideal materials with which to characterize the thermodynamic and kinetic properties of these fascinating aperiodic systems.

Identification of the σ phase in linear block copolymer melts presents the opportunity for designing interesting and useful materials from many other polymers. Decades of experimental experience and well-established theory show that single-component block copolymer melts exhibit universal phase behavior, governed by well-established molecular parameters, primarily the molecular weight, composition, and segment-segment interaction parameter χ (*8*). The σ phase has an enormous unit cell, with lattice parameters that are expected to scale with the two-thirds power of block copolymer molecular weight. Thus, an asymmetric diblock copolymer prepared with 20 times the molecular weight of IL-15 (i.e., a modest 80 kg/mol), and subject to judicious choice of block types (which controls χ), should result in a unit cell dimension of $a \approx 0.3$ μm, potentially suitable for application as a photonic crystal (*35*). More generally, the concept of guiding the growth of gigantic crystals and quasicrystals by tailoring the packing frustration of soft macromolecules might be extended to other organic and inorganic nanoparticles by attaching polymer chains with controlled molecular weight and polydispersity to the surfaces.

References and Notes

1. J. Wittlinger, R. Fischer, S. Werner, J. Schneider, H. Schulz, *Acta Crystallogr. B* **53**, 745 (1997).
2. N. W. Ashcroft, N. D. Mermin, *Solid State Physics* (Brooks/Cole, Belmont, CA, 1976).
3. N. A. Clark, A. J. Hurd, B. J. Ackerson, *Nature* **281**, 57 (1979).
4. P. N. Pusey, W. van Megen, *Nature* **320**, 340 (1986).
5. L. Meng *et al*., *Nano Lett.* **6**, 2249 (2006).
6. J. M. Seddon, *Biochim. Biophys. Acta* **1031**, 1 (1990).
7. B. M. Rosen *et al*., *J. Am. Chem. Soc.* **131**, 17500 (2009).
8. F. S. Bates, G. H. Fredrickson, *Phys. Today* **52**, 32 (1999).
9. D. M. Anderson, S. M. Gruner, S. Leibler, *Proc. Natl. Acad. Sci. U.S.A.* **85**, 5364 (1988).
10. M. Matsen, F. S. Bates, *Macromolecules* **29**, 7641 (1996).
11. L. Leibler, *Macromolecules* **13**, 1602 (1980).
12. F. S. Bates, R. E. Cohen, C. V. Berney, *Macromolecules* **15**, 589 (1982).
13. S. Alexander, J. McTague, *Phys. Rev. Lett.* **41**, 702 (1978).
14. D. Levine, P. J. Steinhardt, *Phys. Rev. Lett.* **53**, 2477 (1984).
15. D. Shechtman, I. Blech, D. Gratias, J. W. Cahn, *Phys. Rev. Lett.* **53**, 1951 (1984).
16. C. Janot, *Quasicrystals: A Primer* (Oxford Univ. Press, New York, ed. 2, 1994).
17. X. Zeng *et al*., *Nature* **428**, 157 (2004).
18. A. S. Keys, S. C. Glotzer, *Phys. Rev. Lett.* **99**, 235503 (2007).
19. M. Dzugutov, *Phys. Rev. A* **46**, R2984 (1992).
20. J. Roth, A. R. Denton, *Phys. Rev. E Stat. Phys. Plasmas Fluids Relat. Interdiscip. Topics* **61**, (6 Pt B), 6845 (2000).
21. F. C. Frank, J. S. Kasper, *Acta Crystallogr.* **12**, 483 (1959).
22. G. Ungar, X. Zeng, *Soft Matter* **1**, 95 (2005).
23. R. Lifshitz, H. Diamant, *Philos. Mag.* **87**, 3021 (2007).
24. T. Dotera, *Philos. Mag.* **87**, 3011 (2007).
25. K. Hayashida, T. Dotera, A. Takano, Y. Matsushita, *Phys. Rev. Lett.* **98**, 195502 (2007).
26. G. Ungar, Y. Liu, X. Zeng, V. Percec, W. D. Cho, *Science* **299**, 1208 (2003).
27. S. C. Schmidt, M. A. Hillmyer, *Macromolecules* **32**, 4794 (1999).
28. M. J. Bluemle, J. Zhang, T. P. Lodge, F. S. Bates, *Macromolecules* **43**, 4449 (2010).
29. M. B. Kossuth, D. C. Morse, F. S. Bates, *J. Rheol.* **43**, 167 (1999).
30. The integrity of sample SISO-3 after 24 hours of annealing under vacuum at 140°C was verified by size exclusion chromatography (SEC).
31. A. C. Lawson *et al*., *Acta Crystallogr. B* **44**, 89 (1988).
32. A. Arakcheeva, G. Chapuis, H. Birkedal, P. Pattison, V. Grinevitch, *Acta Crystallogr. B* **59**, 324 (2003).
33. G. J. Dickins, A. M. B. Douglas, W. H. Taylor, *Acta Crystallogr.* **9**, 297 (1956).
34. J. W. Elmer, T. A. Palmer, E. D. Specht, *Metall. Mater. Trans., A Phys. Metall. Mater. Sci.* **38**, 464 (2007).
35. J. D. Joannopoulos, S. G. Johnson, J. N. Winn, R. D. Meade, *Photonic Crystals: Molding the Flow of Light* (Princeton Univ. Press, Princeton, NJ, ed. 2, 2008).

36. This work was supported by the Department of Energy through a subcontract to UT-Battelle (4000041622), the National Science Foundation through grant DMR-0704192, and the University of Minnesota Materials Research Science and Engineering Center (MRSEC). Portions of this work were performed at the DuPont-Northwestern-Dow Collaborative Access Team (DND-CAT) located at Sector 5 of the Advanced Photon Source (APS). DND-CAT is supported by E. I. Dupont de Nemours & Company, the Dow Chemical Company, and the State of Illinois. Use of the APS was supported by the U.S. Department of Energy, Office of Science, Basic Energy Sciences, under contract DE-AC02-06CH11357. Parts of this work were carried out in the University of Minnesota I.T. Characterization Facility, which receives partial support from NSF through the National Nanotechnology Infrastructure Network program. The authors gratefully acknowledge helpful discussions with N. Balsara and T. P. Lodge.

Supporting Online Material

www.sciencemag.org/cgi/content/full/330/6002/349/DC1
Figs. S1 to S7
References

23 July 2010; accepted 3 September 2010
10.1126/science.1195552

Room-Temperature Detection of a Single Molecule's Absorption by Photothermal Contrast

A. Gaiduk, M. Yorulmaz, P. V. Ruijgrok, M. Orrit*

So far, single-molecule imaging has predominantly relied on fluorescence detection. We imaged single nonfluorescent azo dye molecules in room-temperature glycerol by the refractive effect of the heat that they release in their environment upon intense illumination. This photothermal technique provides contrast for the absorbing objects only, irrespective of scattering by defects or roughness, with a signal-to-noise ratio of ~10 for a single molecule in an integration time of 300 milliseconds. In the absence of oxygen, virtually no bleaching event was observed, even after more than 10 minutes of illumination. In a solution saturated with oxygen, the average bleaching time was of the order of 1 minute. No blinking was observed in the absorption signal. On the basis of bleaching steps, we obtained an average absorption cross section of 4 angstroms^2 for a single chromophore.

Single-molecule optical detection (*1*) has become an indispensable tool in molecular biology and materials science. For the past 20 years, optical single-molecule detection has relied on fluorescence (*2*, *3*) because of the low background of this technique. However, monitoring optical absorption more directly would have definite advantages. Fluorescence requires an efficient pathway for populating the emitting state and also the near absence of nonradiative relaxation to the ground state or to intermediate dark states. The fluorescent state is easily destroyed or quenched by photochemical reactions, often involving electron or proton transfer. Indeed, only a very small fraction of all absorbing molecules (called chromophores) are strongly fluorescent (then called fluorophores). Nonfluorescent chromophores include certain metal complexes and many conjugated molecules, for example, DNA bases, that are important in biology. Such molecules could become more-natural labels than fluorophores.

The first single-molecule optical detection experiment, by Kador and Moerner, was achieved by absorption (*4*) but relied on favorable cryogenic conditions, under which the absorption cross section of the narrowest molecular transition was extremely large. Their doubly modulated absorption technique was later improved on with modern optics and detectors (*5*–*7*), but the

Institute of Physics, Leiden University, Post Office Box 9504, 2300 RA Leiden, Netherlands.

*To whom correspondence should be addressed. E-mail: orrit@molphys.leidenuniv.nl

absorption signal still appears on a strong background of unabsorbed photons, resulting in a lower signal-to-noise ratio than fluorescence. Detecting the absorption of a single molecule at ambient conditions is much more challenging than at low temperature because of the reduction by 5 to 6 orders of magnitude of the cross section, essentially because of fast dephasing by thermal fluctuations. A method for the detection of single-molecule absorption at room temperature must thus solve two different problems.

First, the absorption cross section of a typical chromophore at room temperature is only of the order of 10^{-2} nm^2. The number of the absorption events varies as the ratio of the absorption cross section to the area of a diffraction-limited light beam. This ratio is about 10^{-7} for a laser spot diameter of 300 nm. Because statistical fluctuations in a number N of photons scale as $\sqrt{N}$, a change in transmitted signal of 10^{-7} requires more than 10^{14} photons to be detected. Of those, at least 10^7 have to be absorbed by the molecule. The detection of such small signals therefore requires many absorption events, which may conflict with the poor photostability of many fluorescent molecules at ambient conditions.

Second, in a direct extinction measurement, where only missing photons are identified, a molecule's absorption appears on a background of scattering by any inhomogeneities in refractive index, arising for instance from roughness of the interfaces. Therefore, for practical applications, it is vital to be able to discriminate true absorption from scattering.

Three main routes have been pursued in the past 10 years toward surmounting these obstacles.

Photothermal contrast relies on the intensity change of a probe beam caused by a modulated heating beam of a different color. Kitamori and co-workers (*8*) have detected sub-yoctomole concentrations of absorbers in solution with integration times of several seconds, that is, in conditions under which many diffusing molecules contributed in turn to the signal. Boyer *et al.* (*9*) applied a similar method to detect single immobilized gold nanoparticles down to 5 nm in diameter, a performance that was later substantially improved by Berciaud *et al.* (*10*, *11*) and has led to a number of applications in recent years.

Alternatively, various sensitive optical techniques have been applied either in interferometers (*12*) or in a reflection or transmission geometry (*13*, *14*) to detect some tens of molecules (*12*), small particles (*13*), or quantum dots (*15*). In the latter two cases, however, the use of ultraclean and stable conditions was essential to ensure the absence of scattering background.

Most recently, Xie and co-workers have explored stimulated emission to distinguish absorption from scattering (*16*). Indeed, because stimulated photons can only arise from the excited state of molecules, this method efficiently rejects scattering and fulfills the second requirement. With a modulated stimulating beam, they were able to image absorption in cells down to a few tens of molecules.

We pushed the sensitivity of photothermal detection to the single-molecule limit, demonstrating a signal-to-noise ratio of about 10 with reasonable integration times of 100 to 300 ms, joined to excellent rejection of the scattering background.

Photothermal contrast relies on a time-dependent thermal lens. This inhomogeneous refractive index profile results from the heat dissipated by a pointlike absorber in its surroundings. The local inhomogeneity of the refractive index scatters a probe beam. The resulting weak scattered field interferes with the main probe field (either transmitted or reflected), thereby slightly changing the detected probe intensity. A disadvantage of the method is that the transduction efficiency, relating the index change to the dissipated heat, is rather low. It is proportional to $\partial n/\partial T$, of the order of 10^{-4} K^{-1} or lower. However, this inefficiency is more than compensated for by a gain in applicable probe intensity and the associated reduction in photon noise. Because the probe wavelength can be chosen in a transparency region, a spectral range where absorption is negligible, the probe intensity can be very high, much higher than the saturation intensity of the heating beam. Photon noise on the probe beam is therefore considerably reduced.

Our setup for photothermal contrast imaging is shown in fig. S1 (*17*). The absorbed pump power gives rise to a temperature gradient with an amplitude $\Delta T_{surf} = \frac{\sigma_{abs} I_{heat}}{4\pi\kappa R}$ at the surface of the source, assumed to be spherical: σ_{abs} is the absorption cross section of the absorber, I_{heat} the pump intensity, κ the thermal conductivity of the medium, and R the radius of the heat source. The backward scattered probe light is collected by the focusing microscope objective, sent to a fast photodiode, and fed into the lock-in amplifier. The photothermal signal is proportional to both the heating and probe powers. We modulate the pump at rather high frequency (around 1 MHz) to reject mechanical, electronic, and laser noise. We have chosen the reflection geometry with index matching to adapt the probe signal to the characteristics of our fast low-noise detector (maximum detected intensity 18 μW). Because a good overlap of the two tightly focused beams with different colors is critical, residual chromatic aberrations of the objective must be carefully compensated.

We very recently used this setup (*18*) to improve the photothermal detection approach of

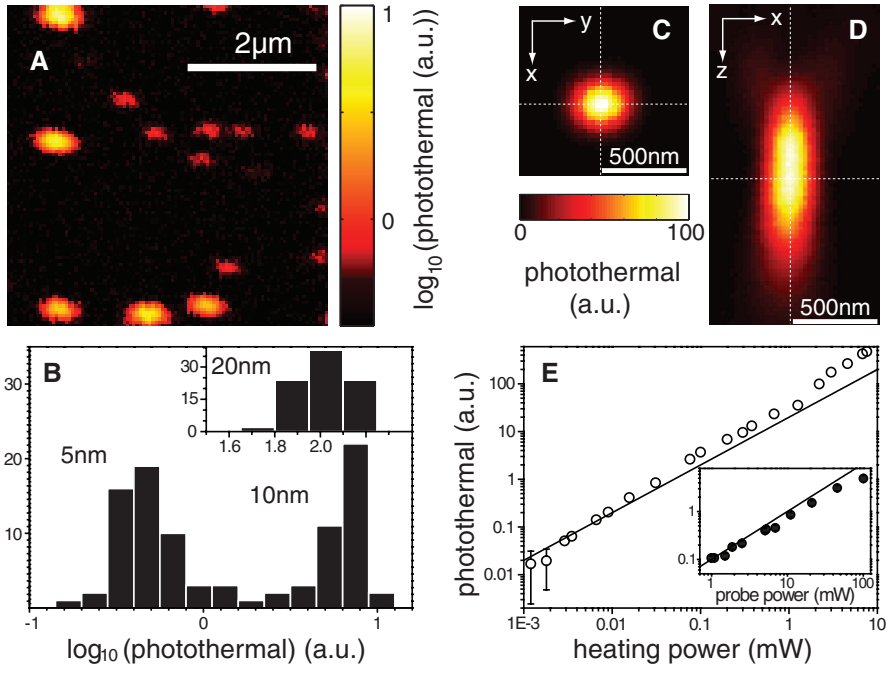

Fig. 1. Photothermal images of gold nanospheres illustrate the large dynamic range of the method and its low background. (**A**) A raster scan image of a sample containing 10-nm (yellow) and 5-nm (red) diameter gold particles in glycerol: heating power is 0.43 mW; probe power, 21 mW; integration time per pixel, 3 ms. The FWHMs of the photothermal spots are 210 nm and 370 nm. a.u., arbitrary units. (**B**) Histogram of the photothermal signals for 94 gold particles of 5-nm or 10-nm diameter. (Inset) Histogram of signals for 88 gold particles of 20-nm diameter in the same conditions. As expected, the photothermal signal roughly scales as the volume of the particles. (**C** and **D**) The point-spread function (PSF) of the photothermal signal is well fitted by a Gaussian with σ_x = 220 nm, σ_y = 250 nm, and σ_z = 670 nm, as mapped by scanning a 20-nm-diameter gold particle in three dimensions. Note the two weak lobes of the PSF in the *x*, *z* image, also observed in confocal fluorescence microscopy. These data are reproduced from (*18*). (**E**) Linear scaling of the photothermal signal of a 20-nm gold particle with heating and probe (inset) powers. Solid lines show linear fits at low heating and probe powers. Error bars indicate standard deviation values. For most of the data, they are smaller than the symbol size.

Berciaud *et al.* (*10*, *11*). Among the different points discussed in (*18*), the choice of the transducing fluid is crucial to enhance the sensitivity. We first characterized the sensitivity of our setup with gold nanoparticles used as absorption standards. Figure 1A shows an image of a sample containing 10-nm- and 5-nm-diameter gold spheres on glass surface in glycerol. We measured photothermal signals by heating at 514 nm and probing at 800 nm. The signals from different diameters differ by a factor of about 8, as expected from the volume ratio. The elongated shape of the photothermal spots in this image (210 nm and 370 nm principal half-maximum widths) arose from the shape of the pump beam, because spatial filtering was weak in this experiment. Stronger spatial filtering yielded a much better shape. In our previous work (*18*), we measured the photothermal detection volume by scanning a 20-nm gold sphere in three dimensions. The full widths at half maximum (FWHM, determined by a Gaussian fit) across *x*, *y*, and *z* are 220 nm, 250 nm, and 670 nm, respectively. These data are reproduced in Fig. 1, C and D. Last, we verified the linear relationships between pump and probe powers and photothermal signal by varying the heating power over 4 orders of magnitude (1 μW to 10 mW) and the probe power over 2 orders of magnitude (1 mW to 100 mW). Slight deviations from linear behavior at high power may be due to variations of spectra or thermal constants of the materials in the broad range of temperature changes explored (from 0.05 K up to about 500 K). Compared with our prior report (*18*), we exploit the thermal sensitivity of glycerol here but not the thermal isolation from the glass substrate.

To ascertain the possibility of detecting a single organic molecule in photothermal microscopy, we only need to compare the smallest detectable power over a given integration time to the power dissipated by a single molecule. In (*18*), we demonstrated the detection of a dissipated power as low as 3 nW with a signal-to-noise ratio of $SNR = 8$ and an integration time of 10 ms. By increasing the integration time to hundreds of ms, even smaller dissipated powers can be measured. A single molecule can release heat along two pathways: a direct nonradiative transition from the excited state and vibronic relaxation before and after a radiative fluorescent transition. The shorter the fluorescence lifetime (τ_F) and the lower the fluorescence quantum yield (η_F) are, the larger is the dissipated power at saturation. The most favorable molecules for photothermal detection should therefore have strong nonradiative channels and thus very weak fluorescence yields. This is the case for the trial molecules chosen in the present work. We calculated the dissipated power at saturation for several commercially available organic molecules (fig. S2 and table S1) (*17*). The highest dissipated power at saturation of 15 nW well above the limit of 3 nW was obtained for a high-efficiency dark quencher (Black-Hole-Quencher, BHQ1, Biosearch Technologies, Novato, California). This azo dye molecule is used in the design of oligonucleotide probes to quench the fluorescence of a dye in a DNA construct (*19*, *20*). For the present experiments, we chose a chromophore-DNA construct to increase the absorption signal by the presence of two chromophores in each construct and to secure the adhesion of the constructs to the glass surface by their single-strand DNA linker (figs. S3 and S4) (*17*).

A photothermal image obtained on a sample of spin-coated quencher-DNA construct (BHQ1-10T-BHQ1) submerged in nitrogen-bubbled glycerol is shown in Fig. 2A. The image reveals four photothermal spots with a $SNR \sim 10$ for an integration time of 300 ms. These spots persisted for as long as 1 hour without bleaching or fading. Less than 2% of the molecules bleached in the first 10 min of illumination. When the glycerol was saturated by oxygen, in contrast, one-step photobleaching was observed after an average time of ~1 min. Several typical background-corrected photothermal traces are displayed in Fig. 2B and demonstrate digital irreversible steps. We never observed any blinking or any later reappearance of a bleached photothermal signal.

The absolute value of the change in absorption cross section upon photobleaching is estimated by comparison to the photothermal signal of 20-nm gold nanoparticles. The calculated (*21*, *22*) cross section of these gold nanospheres is 460 nm^2 at 514 nm in glycerol, in good agreement with absolute cross-section measurements (*23*). The histogram in Fig. 2C summarizes the absorption cross-section changes in 30 single bleaching steps, with an average value of 4.1 $Å^2$. This value, which corresponds to the cross section of a single chromophore, is in satisfactory agreement with the isotropic value, $\sigma_{BHQ} = 2.1$ $Å^2$, deduced from the absorption spectrum of the quencher-DNA construct in glycerol. Note that the maximum value of the cross section for a favorably oriented molecule is $3\sigma_{BHQ} = 6.3$ $Å^2$. The histogram of Fig. 2C is a broad distribution without distinct maximum, in qualitative agreement with the isotropic distribution of transition dipole moments (solid line in Fig. 2C with a steplike cutoff at $3\sigma_{BHQ}$). Our observation suggests that the absorption dipoles of BHQ1 molecules are not freely rotating, even under the heavy illumination to which we subjected them, and that the molecules are fixed to the surface and/or to the DNA linker.

The histogram of survival times before digital photobleaching is shown in Fig. 2D. The average number of absorbed photons before bleaching is about 10^{11} under oxygen-saturated conditions and larger than 10^{12} under oxygen-free conditions, showing a huge reduction in the bleaching efficiency per photon compared with usual fluorophores in the same conditions. This robustness can be attributed to the much shorter dwell time in the excited singlet state resulting from the efficient internal conversion. We have attempted measurements of the polarization dependence of single-molecule absorption signals, but these

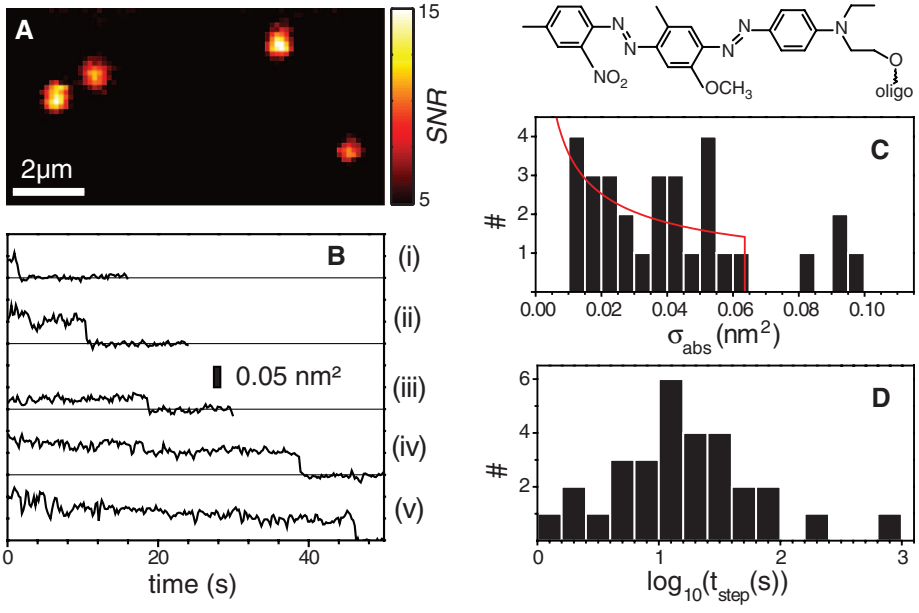

Fig. 2. (**A**) Photothermal image of four constructs (BHQ1-10T-BHQ1), consisting of two fluorescence quenchers (BHQ1) attached to a single strand of DNA (10 thymine bases): integration time per pixel, 300 ms; heating power, 5.1 mW at 514 nm; probe power, 84 mW at 800 nm. (**B**) Photothermal time traces showing single-step bleaching obtained on a sample with BHQ1-10T-BHQ1 on glass in oxygen-saturated glycerol: integration time per point, 100 ms; heating, 5.1 mW; probe, 84 mW. (**C**) Histogram of amplitude of 30 bleaching steps in the photothermal traces. The average change in absorption cross section upon bleaching is 4.1 $Å^2$. The red line represents the distribution of absorption cross sections of single chromophores corresponding to the isotropic distribution of transition dipole moments. The cutoff at 6.3 $Å^2$ is the calculated cross section for a perfectly oriented molecule. (**D**) Histogram of survival times before one-step photobleaching events for the same set of data. The average time is 49 s.

measurements were very difficult because of the buildup of a photothermal background over long illumination times by the pump beam [the probe had no noticeable effect on this buildup (figs. S6 to S8) (*17*)].

We could not observe simultaneous fluorescence and photothermal signals from the spots of Fig. 2. Such simultaneous signals arose only from abnormally bright spots, attributable to large aggregates, and showed quick correlated decays of both signals upon illumination (fig. S9) (*17*). On the sample of Fig. 2, we also observed a few spots with strong photothermal signals corresponding to an absorption cross section of about 1 nm^2, which shows one-step bleaching. Possible interpretations are aggregates of several molecules desorbing simultaneously or, more probably, another chemical species with a large absorption cross section, possibly with excited-state absorption of the intense probe beam. We only found very few examples of two-step photobleaching of the BHQ1-10T-BHQ1 constructs. We believe that this absence results from the low probability of bleaching, joined with the low probability of finding two favorable orientations in the same construct.

Our successful single molecule detection relied here on favorable conditions, the use of glycerol (with large $\partial n/\partial T$ and poor heat conduction) instead of water, with a high heating power of 5.1 mW focused into the diffraction-limited spot and with an even higher probe power of more than 70 mW. Although the conditions for single-molecule absorption in a cell, for example, would be far from these ideal ones, this result opens the way for further optimization of the technique and to a much broader variety of absorbing molecules. Interesting candidates are natural absorbers, for example, metal proteins such as hemoglobin, which would be useful for applications in analytical biochemistry and medical assays (*24*).

An intrinsic limitation of the photothermal method is the low transduction factor between pump and probe because of the relatively weak variation of refractive index with temperature. A future search for more-efficient transduction, for example, photomechanical or photoelectrical detections using micro- and nano-optomechanical systems (*25*), appears full of promise.

References and Notes

1. W. E. Moerner, M. Orrit, *Science* **283**, 1670 (1999).
2. M. Orrit, J. Bernard, *Phys. Rev. Lett.* **65**, 2716 (1990).
3. R. A. Keller *et al.*, *Appl. Spectrosc.* **50**, 12A (1996).
4. W. E. Moerner, L. Kador, *Phys. Rev. Lett.* **62**, 2535 (1989).
5. L. Kador, T. Latychevskaia, A. Renn, U. P. Wild, *J. Chem. Phys.* **111**, 8755 (1999).
6. J. Y. P. Butter, B. Hecht, B. R. Crenshaw, C. Weder, *J. Chem. Phys.* **125**, 154710 (2006).
7. I. Gerhardt *et al.*, *Phys. Rev. Lett.* **98**, 033601 (2007).
8. M. Tokeshi, M. Uchida, A. Hibara, T. Sawada, T. Kitamori, *Anal. Chem.* **73**, 2112 (2001).
9. D. Boyer, P. Tamarat, A. Maali, B. Lounis, M. Orrit, *Science* **297**, 1160 (2002).
10. S. Berciaud, L. Cognet, G. A. Blab, B. Lounis, *Phys. Rev. Lett.* **93**, 257402 (2004).
11. S. Berciaud, D. Lasne, G. A. Blab, L. Cognet, B. Lounis, *Phys. Rev. B* **73**, 045424 (2006).
12. J. Hwang, M. M. Fejer, W. E. Moerner, *Phys. Rev. A* **73**, 021802 (2006).
13. F. V. Ignatovich, L. Novotny, *Phys. Rev. Lett.* **96**, 013901 (2006).
14. G. Wrigge, J. Hwang, I. Gerhardt, G. Zumofen, V. Sandoghdar, *Opt. Express* **16**, 17358 (2008).
15. P. Kukura, M. Celebrano, A. Renn, V. Sandoghdar, *Nano Lett.* **9**, 926 (2009).
16. W. Min *et al.*, *Nature* **461**, 1105 (2009).
17. Materials and methods are available as supporting material on *Science* Online.
18. A. Gaiduk, P. V. Ruijgrok, M. Yorulmaz, M. Orrit, *Chem. Sci.* **1**, 343 (2010).
19. V. V. Didenko, Ed., *Methods in Molecular Biology: Fluorescent Energy Transfer Nucleic Acid Probes: Designs and Protocols* (Humana, Totowa, NJ, 2006).
20. S. A. E. Marras, F. R. Kramer, S. Tyagi, *Nucleic Acids Res.* **30**, e122 (2002).
21. M. A. van Dijk *et al.*, *Phys. Chem. Chem. Phys.* **8**, 3486 (2007).
22. C. F. Bohren, D. R. Huffman, *Absorption and Scattering of Light by Small Particles* (Wiley, New York, 1998).
23. A. Arbouet *et al.*, *Phys. Rev. Lett.* **93**, 127401 (2004).
24. S. Lu, W. Min, S. Chong, G. R. Holtom, X. S. Xie, *Appl. Phys. Lett.* **96**, 113701 (2010).
25. S. W. Stahl, E. M. Puchner, H. E. Gaub, *Rev. Sci. Instrum.* **80**, 073702 (2009).

26. We acknowledge financial support by European Research Council (Advanced Grant SiMoSoMa). This work is a part of the research program of the Stichting voor Fundamenteel Onderzoek der Materie, which is financially supported by the Netherlands Organization for Scientific Research. We thank H. van der Meer for precious help with the experimental setup.

Supporting Online Material

www.sciencemag.org/cgi/content/full/330/6002/353/DC1
Materials and Methods
Figs. S1 to S9
References

22 July 2010; accepted 16 September 2010
10.1126/science.1195475

Atmospheric CO_2: Principal Control Knob Governing Earth's Temperature

Andrew A. Lacis,* Gavin A. Schmidt, David Rind, Reto A. Ruedy

Ample physical evidence shows that carbon dioxide (CO_2) is the single most important climate-relevant greenhouse gas in Earth's atmosphere. This is because CO_2, like ozone, N_2O, CH_4, and chlorofluorocarbons, does not condense and precipitate from the atmosphere at current climate temperatures, whereas water vapor can and does. Noncondensing greenhouse gases, which account for 25% of the total terrestrial greenhouse effect, thus serve to provide the stable temperature structure that sustains the current levels of atmospheric water vapor and clouds via feedback processes that account for the remaining 75% of the greenhouse effect. Without the radiative forcing supplied by CO_2 and the other noncondensing greenhouse gases, the terrestrial greenhouse would collapse, plunging the global climate into an icebound Earth state.

It often is stated that water vapor is the chief greenhouse gas (GHG) in the atmosphere. For example, it has been asserted that "about 98% of the natural greenhouse effect is due to water vapour and stratiform clouds with CO_2 contributing less than 2%" (*1*). If true, this would imply that changes in atmospheric CO_2 are not important influences on the natural greenhouse capacity of Earth, and that the continuing increase in CO_2 due to human activity is therefore not relevant to climate change. This misunderstanding is resolved through simple examination of the terrestrial greenhouse.

The difference between the nominal global mean surface temperature (T_S = 288 K) and the global mean effective temperature (T_E = 255 K) is a common measure of the terrestrial greenhouse effect ($G_T = T_S - T_E$ = 33 K). Assuming global energy balance, T_E is also the Planck radiation equivalent of the 240 W/m^2 of global mean solar radiation absorbed by Earth.

The Sun is the source of energy that heats Earth. Besides direct solar heating of the ground, there is also indirect longwave (LW) warming arising from the thermal radiation that is emitted by the ground, then absorbed locally within the atmosphere, from which it is re-emitted in both upward and downward directions, further heating the ground and maintaining the temperature gradient in the atmosphere. This radiative interaction is the greenhouse effect, which was first discovered by Joseph Fourier in 1824 (*2*), experimentally verified by John Tyndall in 1863 (*3*), and quantified by Svante Arrhenius in 1896 (*4*). These studies established long ago that water vapor and CO_2 are indeed the principal terrestrial GHGs. Now, further consideration shows that CO_2 is the one that controls climate change.

CO_2 is a well-mixed gas that does not condense or precipitate from the atmosphere. Water vapor and clouds, on the other hand, are highly active components of the climate system that respond rapidly to changes in temperature and air pressure by evaporating, condensing, and precipitating. This identifies water vapor and clouds as the fast feedback processes in the climate system.

Radiative forcing experiments assuming doubled CO_2 and a 2% increase in solar irradiance (*5*) show that water vapor provides the strongest climate feedback of any of the atmospheric GHGs, but that it is not the cause (forcing) of global cli-

NASA Goddard Institute for Space Studies, 2880 Broadway, New York, NY 10025, USA.

*To whom correspondence should be addressed. E-mail: andrew.a.lacis@nasa.gov

mate change. The response of the climate system to an applied forcing is determined to be the sum of the direct (no-feedback) response to the applied forcing and the induced radiative response that is attributable to the feedback process contributions. The ratio of the total climate response to the no-feedback response is commonly known as the feedback factor, which incorporates all the complexities of the climate system feedback interactions. For the doubled CO_2 and the 2% solar irradiance forcings, for which the direct no-feedback responses of the global surface temperature are 1.2° and 1.3°C, respectively, the ~4°C surface warming implies respective feedback factors of 3.3 and 3.0 (*5*).

Because the solar-thermal energy balance of Earth [at the top of the atmosphere (TOA)] is maintained by radiative processes only, and because all the global net advective energy transports must equal zero, it follows that the global average surface temperature must be determined in full by the radiative fluxes arising from the patterns of temperature and absorption of radiation. This then is the basic underlying physics that explains the close coupling that exists between TOA radiative fluxes, the greenhouse effect, and the global mean surface temperature.

An improved understanding of the relative importance of the different contributors to the greenhouse effect comes from radiative flux experiments that we performed using Goddard Institute for Space Studies (GISS) ModelE (*6*). Figure 1 depicts the essence of these calculations, including the separation of the greenhouse contributors into feedback and forcing categories.

In round numbers, water vapor accounts for about 50% of Earth's greenhouse effect, with clouds contributing 25%, CO_2 20%, and the minor GHGs and aerosols accounting for the remaining 5%. Because CO_2, O_3, N_2O, CH_4, and chlorofluorocarbons (CFCs) do not condense and precipitate, noncondensing GHGs constitute the key 25% of the radiative forcing that supports and sustains the entire terrestrial greenhouse effect, the remaining 75% coming as fast feedback contributions from water vapor and clouds.

We used the GISS 4° × 5° ModelE to calculate changes in instantaneous LW TOA flux (annual global averages) in experiments where atmospheric constituents (including water vapor, clouds, CO_2, O_3, N_2O, CH_4, CFCs, and aerosols) were added to or subtracted from an equilibrium atmosphere with a given global temperature structure, one constituent at a time for a 1-year period. Decreases in outgoing TOA flux for each constituent relative to the empty or the full-component atmosphere define the bounds for the relative impact on the total greenhouse effect. Had the overlapping absorption been negligible, the sum of the flux differences would have been equal to the LW flux equivalent of the total greenhouse effect ($G_F = \sigma T^4_S - \sigma T^4_E = 150$ W/m^2), where σ is the Stefan-Boltzmann constant. We found the single-addition flux differences to be overestimated by a factor of 1.36, whereas in the single-subtraction cases, the sum of the TOA flux differences was underestimated by a factor of 0.734. By normalizing these fractional contributions to match the full-atmosphere value of G_F, we obtained the fractional response contributions shown in Fig. 1.

Because of overlapping absorption, the fractional attribution of the greenhouse effect is to some extent qualitative (as shown by the dashed and dotted extremum lines in Fig. 1), even though the spectral integral is a full and accurate determination of the atmospheric greenhouse strength for the specified global temperature structure. Still, the fractional attribution is sufficiently precise to clearly differentiate the radiative flux contributions due to the noncondensable GHGs from those arising from the fast feedback processes. This allows an empirical determination of the climate feedback factor as the ratio of the total global flux change to the flux change that is attributable to the radiative forcing due to the noncondensing GHGs. This empirical determination leads then to a climate feedback factor of 4, based on the noncondensing GHG forcing accounting for 25% of the outgoing flux reduction at the TOA for the full-constituent atmosphere. This implies that Earth's climate system operates with strong positive feedback that arises from the forcing-induced changes in the condensable species.

A direct consequence of this combination of feedback by the condensable and forcing by the noncondensable constituents of the atmospheric greenhouse is that the terrestrial greenhouse effect would collapse were it not for the presence of these noncondensing GHGs. If the global atmospheric temperatures were to fall to as low as $T_S = T_E$, the Clausius-Clapeyron relation would imply that the sustainable amount of atmospheric water vapor would become less than 10% of the current atmospheric value. This would result in (radiative) forcing reduced by ~30 W/m^2, causing much of the remaining water vapor to precipitate, thus enhancing the snow/ice albedo to further diminish the absorbed solar radiation. Such a condition would inevitably lead to runaway glaciation, producing an ice ball Earth.

Claims that removing all CO_2 from the atmosphere "would lead to a 1°C decrease in global warming" (*7*), or "by 3.53°C when 40% cloud cover is assumed" (*8*) are still being heard. A clear demonstration is needed to show that water vapor and clouds do indeed behave as fast feedback processes and that their atmospheric distributions are regulated by the sustained radiative forcing due to the noncondensing GHGs. To this end, we performed a simple climate experiment with the GISS 2° × 2.5° AR5 version of ModelE, using the Q-flux ocean with a mixed-layer depth of 250 m, zeroing out all the noncondensing GHGs and aerosols.

The results, summarized in Fig. 2, show unequivocally that the radiative forcing by noncondensing GHGs is essential to sustain the atmospheric temperatures that are needed for significant levels of water vapor and cloud feedback. Without this noncondensable GHG forcing, the physics of this model send the climate of Earth plunging rapidly and irrevocably to an icebound state, though perhaps not to total ocean freezeover.

The scope of the climate impact becomes apparent in just 10 years. During the first year alone, global mean surface temperature falls by 4.6°C. After 50 years, the global temperature stands at –21°C, a decrease of 34.8°C. Atmospheric water vapor is at ~10% of the control climate value (22.6 to 2.2 mm). Global cloud cover increases from its 58% control value to more than 75%, and the global sea ice fraction goes from 4.6% to 46.7%, causing the planetary albedo of Earth to also increase from ~29% to 41.8%. This has the effect of reducing the absorbed solar energy to further exacerbate the global cooling.

After 50 years, a third of the ocean surface still remains ice-free, even though the global surface temperature is colder than –21°C. At tropical latitudes, incident solar radiation is sufficient to keep the ocean from freezing. Although this thermal oasis within an otherwise icebound Earth

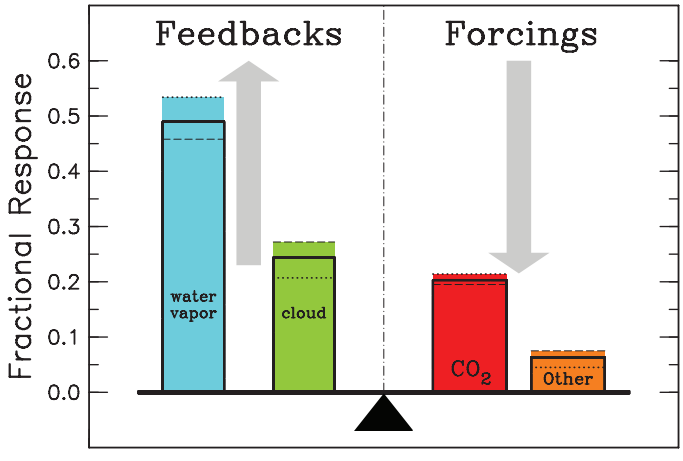

Fig. 1. Attribution of the contributions of individual atmospheric components to the total terrestrial greenhouse effect, separated into feedback and forcing categories. Horizontal dotted and dashed lines depict the fractional response for single-addition and single-subtraction of individual gases to an empty or full-component reference atmosphere, respectively. Horizontal solid black lines are the scaled averages of the dashed- and dotted-line fractional response results. The sum of the fractional responses adds up to the total greenhouse effect. The reference atmosphere is for conditions in 1980.

appears to be stable, further calculations with an interactive ocean would be needed to verify the potential for long-term stability. The surface temperatures in Fig. 3 are only marginally warmer than 1°C within the remaining low-latitude heat island.

From the foregoing, it is clear that CO_2 is the key atmospheric gas that exerts principal control over the strength of the terrestrial greenhouse effect. Water vapor and clouds are fast-acting feedback effects, and as such are controlled by the radiative forcings supplied by the noncondensing GHGs. There is telling evidence that atmospheric CO_2 also governs the temperature of Earth on geological time scales, suggesting the related question of what the geological processes that control atmospheric CO_2 are. The geological evidence of glaciation at tropical latitudes from 650 to 750 million years ago supports the snowball Earth hypothesis (*9*), and by inference, that escape from the snowball Earth condition is also achievable.

On million-year time scales, volcanoes are the principal source of atmospheric CO_2, and rock weathering is the principal sink, with the biosphere acting as both source and sink (*10*). Because the CO_2 sources and sinks operate independently, the atmospheric level of CO_2 can fluctuate. If the atmospheric CO_2 level were to fall below its critical value, snowball Earth conditions can result.

Antarctic and Greenland ice core data show atmospheric CO_2 fluctuations between 180 to 300 parts per million (ppm) over the glacial-interglacial cycles during the past 650,000 years (*11*). The relevant physical processes that turn the CO_2 control knob on thousand-year time scales between glacial and interglacial extremes are not fully understood, but appear to involve both the biosphere and the ocean chemistry, including a significant role for Milankovitch variations of the Earth-orbital parameters.

Besides CO_2, methane is another potent greenhouse control knob, being implicated in the Paleocene-Eocene thermal maximummass extinction 55 million years ago, when global warming by up to 5°C (*12*) occurred because of a massive release of methane from the disintegration of seafloor clathrates (*13*, *14*). Methane is the second most important noncondensing GHG after CO_2. Of the 2.9 W/m^2 of GHG radiative forcing from 1750 to 2000, CO_2 contributed 1.5 W/m^2, methane 0.55 W/m^2, and CFCs 0.3 W/m^2, with the rest coming from N_2O and ozone (*15*). All of these increases in noncondensing GHG forcing are attributable to human activity (*16*).

Climate control knobs on the solar side of the energy balance ledger include the steady growth in luminosity since the beginning of the Solar System (from about 70% of present luminosity, depending on the postulated early solar mass loss), as hydrogen is consumed in nuclear reactions in the solar interior (*17*, *18*). Milankovitch variations of the Earth-orbital parameters, which alter the relative seasonal distribution as well as the intensity of incident solar radiation within the polar regions, are another important solar energy control knob that is intimately associated with glacial-interglacial cycles of climate change. For solar irradiance changes over the past several centuries, an increase by about 0.1 W/m^2 is inferred since the time of the Maunder minimum, based on trends in sunspot activity and other proxies (*19*).

Of the climate control knobs relevant to current climate, those on the solar side of the energy balance ledger show only negligible impact. Several decades of solar irradiance monitoring have not detected any long-term trends in solar irradiance beyond the 11-year oscillation associated with the solar sunspot cycle. Large volcanic

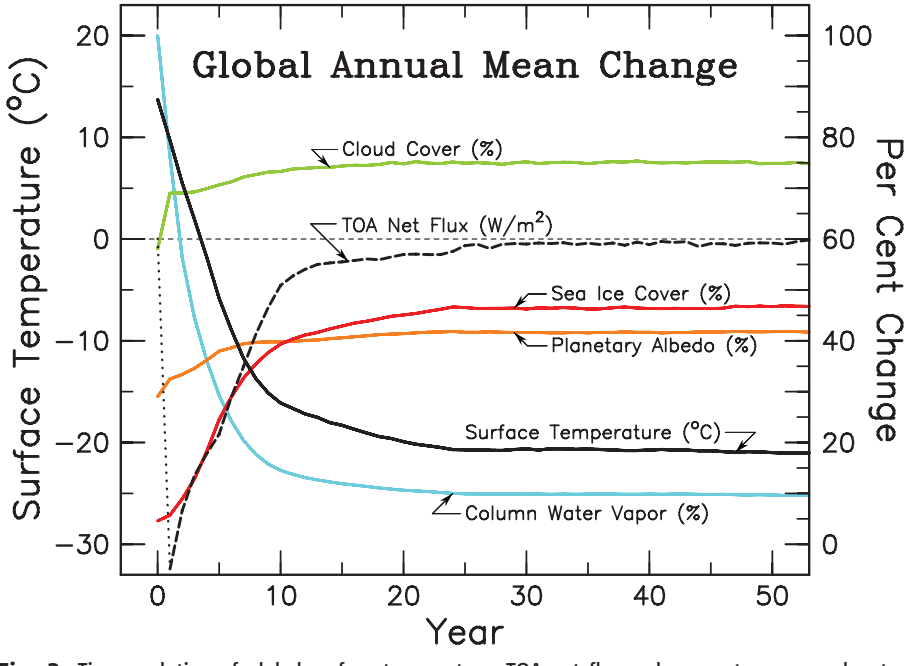

Fig. 2. Time evolution of global surface temperature, TOA net flux, column water vapor, planetary albedo, sea ice cover, and cloud cover, after the zeroing out of the noncondensing GHGs. The model used in the experiment is the GISS 2°× 2.5° AR5 version of ModelE, with the Q-flux ocean and a mixed-layer depth of 250 m. Model initial conditions are for a preindustrial atmosphere. Surface temperature and TOA net flux use the lefthand scale.

Fig. 3. Zonally averaged annual mean surface temperature change after the zeroing out of noncondensing GHGs.

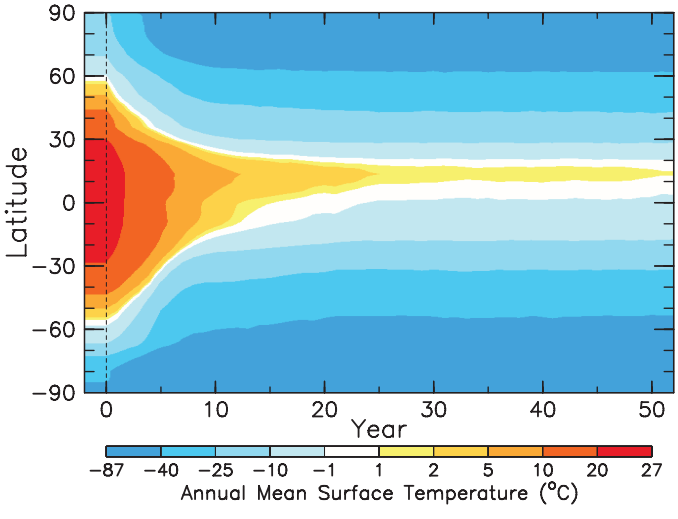

Table 1. Planetary greenhouse parameters.

Parameter	Mars	Earth	Venus
T_S (K)	215	288	730
T_E (K)	210	255	230
σT_S^4 (W/m^2)	121	390	16,100
σT_E^4 (W/m^2)	111	240	157
G_T (K)	5	33	500
G_F (W/m^2)	10	150	~16,000
P_S (bar)	0.01	1	100

eruptions can happen at any time, but no substantial eruptions have occurred since the eruption of Mt. Pinatubo in the Philippines in 1991.

In a broader perspective, CO_2 greenhouses also operate on Mars and Venus, because both planets possess atmospheres with substantial amounts of CO_2. The atmospheric greenhouse effect requires that a substantial fraction of the incident solar radiation must be absorbed at the ground in order to make the indirect greenhouse heating of the ground surface possible. Greenhouse parameters and relative surface pressure (P_S) for Mars, Earth, and Venus are summarized in Table 1.

Earth is unique among terrestrial planets in having a greenhouse effect in which water vapor provides strong amplification of the heat-trapping action of the CO_2 greenhouse. Also, N_2 and O_2, although possessing no substantial absorption bands of their own, are actually important contributors to the total greenhouse effect because of pressure-broadening of CO_2 absorption lines, as well as by providing the physical structure within which the absorbing gases can interact with the radiation field.

The anthropogenic radiative forcings that fuel the growing terrestrial greenhouse effect continue unabated. The continuing high rate of atmospheric CO_2 increase is particularly worrisome, because the present CO_2 level of 390 ppm is far in excess of the 280 ppm that is more typical for the interglacial maximum, and still the atmospheric CO_2 control knob is now being turned faster than at any time in the geological record (*20*). The concern is that we are well past even the 300- to 350-ppm target level for atmospheric CO_2, beyond which dangerous anthropogenic interference in the climate system would exceed the 25% risk tolerance for impending degradation of land and ocean ecosystems, sea-level rise, and inevitable disruption of socioeconomic and food-producing infrastructure (*21*, *22*). Furthermore, the atmospheric residence time of CO_2 is exceedingly long, being measured in thousands of years (*23*). This makes the reduction and control of atmospheric CO_2 a serious and pressing issue, worthy of real-time attention.

References and Notes

1. R. S. Lindzen, *Quart. J. R. Meteorol. Soc* **117**, 651 (1991).
2. J. Fourier, *Ann. Chemie Physique* **27**, 136 (1824).
3. J. Tyndall, *Philos. Mag.* **25**, 200 (1863).
4. S. Arrhrenius, *Philos. Mag.* **41**, 237 (1896).
5. J. Hansen *et al.*, *AGU Geophys. Monogr.* **29**, 130 (1984).
6. G. A. Schmidt *et al.*, *J. Clim.* **19**, 153 (2006).
7. J. Tomkin, *Phys. Today* **45**, 13 (1992).
8. R. S. Lindzen, H. Charnock, K. P. Shine, R. Kandel, *Phys. Today* **48**, 78 (1995).
9. J. L. Kirschvink, in *The Proterozoic Biosphere: A Multidisciplinary Study*, J. W. Schopf, C. Klein, D. Des Maris, Eds. (Cambridge Univ. Press, Cambridge, 1992), pp. 51–52.
10. R. A. Berner, *The Phanerozoic Carbon Cycle: CO_2 and O_2* (Oxford Univ. Press, New York, 2004).
11. E. Jansen *et al.*, in *Climate Change 2007: The Physical Science Basis. Contribution of Working Group I to the Fourth Assessment Report of the Intergovernmental Panel on Climate Change*, S. Solomon *et al.*, Eds. (Cambridge Univ. Press, Cambridge, 2007), pp. 433–497.
12. J. C. Zachos, G. R. Dickens, R. E. Zeebe, *Nature* **451**, 279 (2008).
13. G. R. Dickens, J. R. O'Neil, D. K. Rea, R. M. Owen, *Paleoceanography* **10**, 965 (1995).
14. G. A. Schmidt, D. T. Shindell, *Paleoceanography* **18**, 1004 (2003).
15. J. Hansen *et al.*, *J. Geophys. Res.* **110**, D18104 (2005).
16. K. L. Denman *et al.*, in *Climate Change 2007: The Physical Science Basis. Contribution of Working Group I to the Fourth Assessment Report of the Intergovernmental Panel on Climate Change*, S. Solomon *et al.*, Eds. (Cambridge Univ. Press, Cambridge, 2007), pp. 499–587.
17. I. J. Sackmann, A. I. Boothroyd, K. E. Kraemer, *Astrophys. J.* **418**, 457 (1993).
18. I. J. Sackmann, A. I. Boothroyd, *Astrophys. J.* **583**, 1024 (2003).
19. P. Forster *et al.*, in *Climate Change 2007: The Physical Science Basis. Contribution of Working Group I to the Fourth Assessment Report of the Intergovernmental Panel on Climate Change*, S. Solomon *et al.*, Eds. (Cambridge Univ. Press, Cambridge, 2007), pp. 433–497.
20. D. Archer *et al.*, *Annu. Rev. Earth Planet. Sci.* **37**, 117 (2009).
21. L. D. D. Harvey, *Clim. Change* **82**, 1 (2007).
22. J. Hansen *et al.*, *Open Atmos. Sci. J.* **2**, 217 (2008).
23. F. Joos, R. Spahni, *Proc. Natl. Acad. Sci. U.S.A.* **105**, 1425 (2008).

24. We thank B. Carlson, A. Del Genio, J. Hansen, G. Russell, R. Stothers, and L. Travis for comments and the NASA Earth Science Research Division managed by J. Kaye and D. Considine for support.

Supporting Online Material

www.sciencemag.org/cgi/content/full/330/6002/356/DC1
SOM Text
Figs. S1 and S2
Table S1
References

8 April 2010; accepted 10 September 2010
10.1126/science.1190653

The Structure of Iron in Earth's Inner Core

Shigehiko Tateno,[1,2]* Kei Hirose,[1,2]* Yasuo Ohishi,[3] Yoshiyuki Tatsumi[2]

Earth's solid inner core is mainly composed of iron (Fe). Because the relevant ultrahigh pressure and temperature conditions are difficult to produce experimentally, the preferred crystal structure of Fe at the inner core remains uncertain. Static compression experiments showed that the hexagonal close-packed (hcp) structure of Fe is stable up to 377 gigapascals and 5700 kelvin, corresponding to inner core conditions. The observed weak temperature dependence of the *c*/*a* axial ratio suggests that hcp Fe is elastically anisotropic at core temperatures. Preferred orientation of the hcp phase may explain previously observed inner core seismic anisotropy.

Determining the crystal structure of iron (Fe) under ultrahigh pressure and temperature (*P*-*T*) conditions is a key piece of information required to decipher the complex seismic structures observed in Earth's inner core (*1*–*3*). Fe adopts body-centered cubic (bcc) structure at ambient conditions and transforms into the hexagonal close-packed (hcp) phase above 15 GPa. Although hcp Fe can persist under core pressures at 300 K (*4*, *5*), a phase transition at elevated temperature is a possibility. Both theory and experiments have proposed different forms of Fe at simultaneously high *P*-*T* conditions, which include bcc (*6*, *7*), face-centered-cubic (fcc) (*8*), and hcp structures (*5*, *9*). The structure of Fe has never been examined experimentally at the inner core *P*-*T* conditions (>330 GPa and ≥5000 K), because the techniques previously used to produce such extreme conditions—dynamical shock-wave experiments—impede the ability to make simultaneous structure measurements on the order of a microsecond.

Based on a combination of static compression experiments in a laser-heated diamond-anvil cell (DAC) and synchrotron x-ray diffraction (XRD) measurements (Fig. 1), we determined the structure of Fe up to 377 GPa and 5700 K (*10*). A temperature gradient was relatively large when the sample was heated to more than 5000 K at >300 GPa (Fig. 2A); nevertheless, the variations were less than ±10% in the 6-μm region across the hot spot, which corresponds to the x-ray beam size at full width at half maximum, considering the fluctuations in temperature with time (Fig. 2B). We calculated the sample temperature by averaging the variation in the 6-μm area probed by x-rays. Pressure was determined from the unit-cell volume of hcp Fe, using its *P*-*V*-*T* (where *V* is volume) equation of state (*11*). The ±10% temperature variation leads to about ±2% uncertainty in pressure (377 ± 8.5 GPa at 5700 K). The pressure gradient in the sample was <5 GPa at ~300 GPa in a 10-μm area after heating.

To construct the phase diagram of Fe at inner core conditions, we conducted six separate sets of experiments (Fig. 3). The first experiment at 303 GPa and room temperature resulted in an XRD pattern that included peaks from hcp Fe and Re (the gasket material) (fig. S1A) (*10*). Subsequently, we heated this sam-

[1]Department of Earth and Planetary Sciences, Tokyo Institute of Technology, Ookayama, Meguro, Tokyo 152-8551, Japan. [2]Institute for Research on Earth Evolution, Japan Agency for Marine-Earth Science and Technology, Yokosuka, Kanagawa 237-0061, Japan. [3]Japan Synchrotron Radiation Research Institute, Sayo, Hyogo 679-5198, Japan.

*To whom correspondence should be addressed. E-mail: tateno.s.aa@m.titech.ac.jp (S.T.); kei@geo.titech.ac.jp (K.H.)

ple to 4820 K at 332 GPa. The one-dimensional (1D) XRD pattern did not change except for the appearance of an hcp 002 line (Fig. 1A). On the other hand, the 2D image became spotty (fig. S1B), indicating crystal growth and hence the stability of hcp Fe at these *P-T* conditions. After these measurements, the sample was temperature-quenched and then further compressed to 321 GPa at room temperature. We again heated the sample to 5520 K at 356 GPa. The XRD pattern was still dominated by the hcp phase (Fig. 1B), but minor peaks assigned to pyrite-type SiO_2 (*12*) (the pressure medium) and Fe_3C cementite appeared. The measured lattice parameters and volumes of Fe_3C are in agreement with earlier experimental results to 187 GPa (*13*) (table S1). Similar observations were made in five other experiments, which were conducted in a wide *P-T* range from 135 GPa and 2690 K to 377 GPa and 5700 K (Fig. 3). In all measurements, we obtained no evidence of a phase transition to bcc or fcc Fe phases.

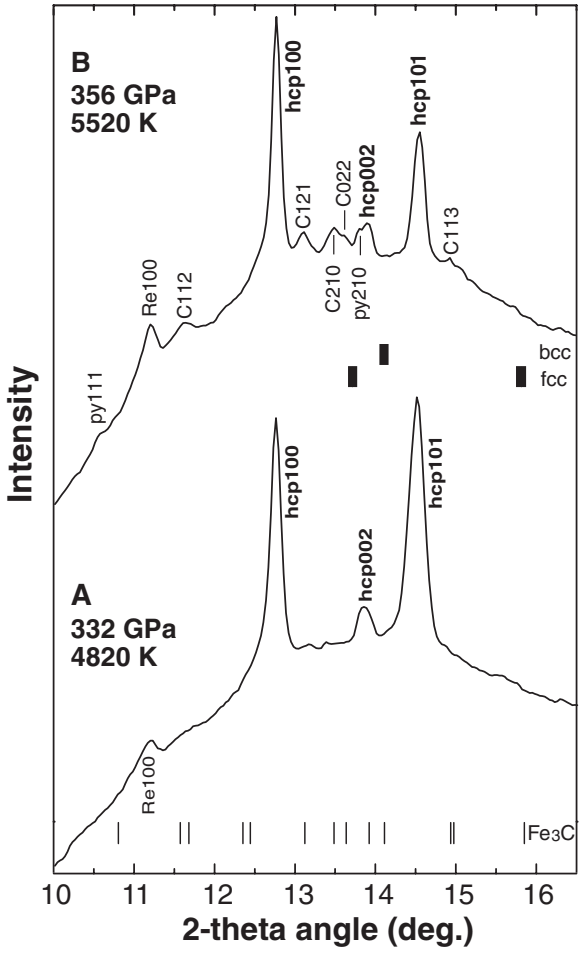

Fig. 1. Representative XRD patterns of hcp Fe at (**A**) 332 GPa and 4820 K and at (**B**) 356 GPa and 5520 K. The peak positions of the bcc and fcc phases were calculated for volumes larger by 0 to 1% than that for the observed hcp phase. hcp, hcp Fe; py, pyrite-type SiO_2 (pressure medium); C, Fe_3C cementite; Re, rhenium (gasket).

The presence of Fe_3C in the XRD pattern indicates contamination by carbon from the diamond anvils, which has been reported in several earlier DAC studies (*14*–*16*). Nevertheless, the maximum solubility of carbon in solid Fe is already low (<0.6%) at 44 GPa and further decreases with increasing pressure (*17*). Moreover, although previous ab initio calculations (*18*) demonstrated that the addition of a small amount of carbon to Fe strongly stabilizes the bcc phase relative to the hcp phase, we did not observe XRD peaks from bcc Fe. These suggest that the effect of carbon contamination on the phase relation of Fe was negligible.

These experiments were performed at temperatures near the melting curve of Fe (*19*, *20*) (Fig. 3). We observed a temperature jump from 3220 K to ~4000 K at 135 GPa by a small increase in laser output power (fig. S2). Large fluctuations in temperature and the elevation of background intensity in the XRD patterns were also noticed after the temperature jump. These are usually interpreted as a sign of melting (*21*, *22*). The melting temperature at 135 GPa should thus be little higher than 3220 K, which is somewhat higher than the previous experimental determinations by Boehler (*19*, *22*) but lower than those by Ma *et al.* (*20*), considering the effect of thermal pressure contributions. At >350 GPa, on the other hand, 2D XRD images showed the extensive grain growth above 5700 K, suggesting that this temperature is close to the melting point. In addition, we found no anomalies up to 4120 K at 210 GPa. These observations place constraints on the melting curve of Fe, which previously existed only up to 200 GPa.

These results indicate that hcp Fe is a stable form of Fe up to 377 GPa and 5700 K, which is compatible with previous ab initio calculations by Vočadlo *et al.* (*9*). The estimation of temperature at the inner/outer core boundary ranges from 4850 to 5700 K, depending on the melting temperature of Fe and the effect of light alloying elements (*19*, *23*, *24*). The temperature gradient should be very small within the inner core (*24*). Our experiments thus represent a range of inner core *P-T* conditions. One limitation of these ex-

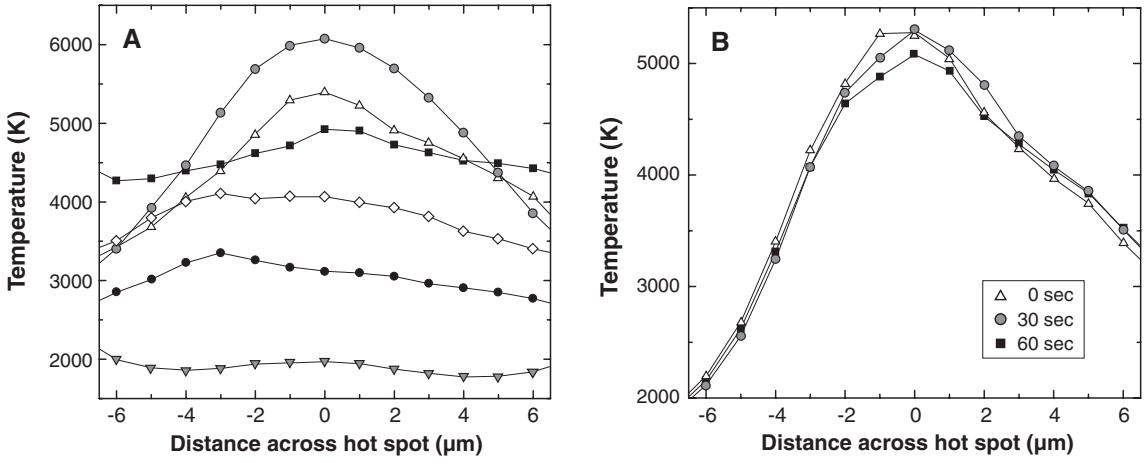

Fig. 2. (**A**) Typical temperature profiles across the laser-heated spot obtained at pressures above 300 GPa. (**B**) Fluctuations in temperature with time in 60 s.

periments is that chemical impurities such as silicon and sulfur, which have the ability to change the stable crystal structure (*9*, *18*, *25*), were not accounted for.

Strong seismic anisotropy exists in the inner core, with longitudinal waves traveling ~3% faster along the polar axis than in the equatorial plane (*1*). This was originally attributed to the preferred orientation of hcp Fe, which exhibits a strong single-crystal elastic anisotropy, at least at low temperature (*26*). However, Steinle-Neumann *et al.* (*27*) demonstrated that the *c*/*a* axial ratio of hcp Fe increases substantially with increasing temperature (Fig. 4), which has a significant influence on its elastic anisotropy. More recent calculations (*6*, *28*) reported that the *c*/*a* ratio approaches the value of 1.6299 for the ideal hcp structure at high temperature, and consequently elastic anisotropy of hcp Fe no longer exists at inner core conditions. On the other hand, experimental evidence previously suggested weak temperature dependence of the *c*/*a* ratio at 140 GPa (*22*), as do our data at ~330 GPa (Fig. 4). The *c*/*a* ratio of 1.602 at 332 GPa and 4820 K, which is substantially lower than the ideal value, suggests that hcp Fe should be elastically anisotropic even at the high temperature conditions of the inner core. The observed seismic anisotropy may therefore result from the preferred orientation of the hcp phase with the *c* axis parallel to Earth's rotation axis (*26*).

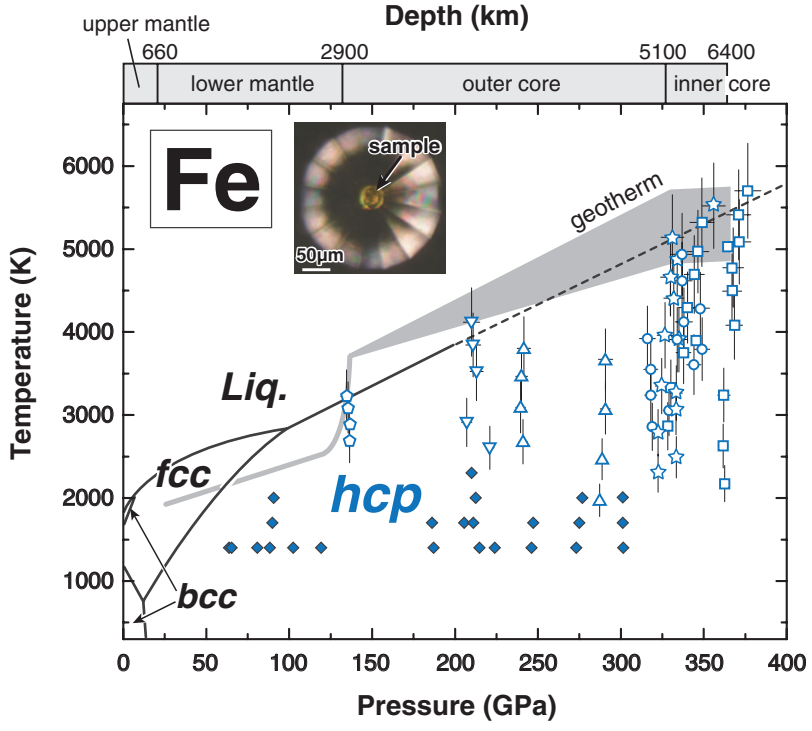

Fig. 3. Phase diagram of Fe and the inferred temperature profile inside Earth (*19*, *23*, *24*). Open symbols indicate the present results (different symbols indicate different runs), and solid diamonds indicate data from previous experimental work (*5*). The low-pressure solid-solid phase transition boundaries and melting curve are from Boehler (*19*). Liq., liquid. (**Inset**) Sample photograph at 335 GPa in the DAC.

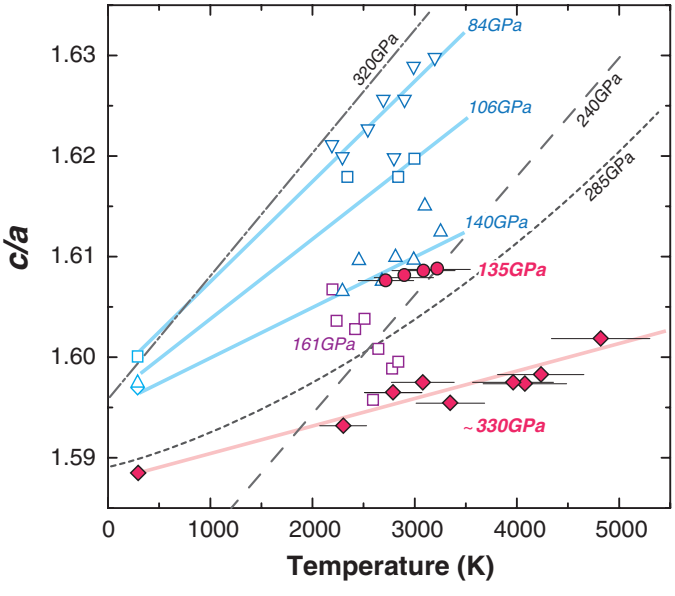

Fig. 4. Temperature dependence of the *c*/*a* axial ratio of hcp Fe collected at 135 GPa (red circles) and ~330 GPa (red diamonds) (table S2). Previous experimental results at 84, 106, and 140 GPa are from Boehler *et al.* (*22*) (blue open symbols), and those at 161 GPa are from Ma *et al.* (*20*) (purple open squares). The results of theoretical calculations are also shown by the dot-dashed curve (*27*), dashed curve (*6*), and dotted curve (*28*).

References and Notes

1. A. Morelli, A. M. Dziewonski, J. H. Woodhouse, *Geophys. Res. Lett.* **13**, 1545 (1986).
2. M. Mattesini *et al.*, *Proc. Natl. Acad. Sci. U.S.A.* **107**, 9507 (2010).
3. M. Monnereau, M. Calvet, L. Margerin, A. Souriau, *Science* **328**, 1014 (2010).
4. H. K. Mao, Y. Wu, L. C. Chen, J. F. Shu, A. P. Jephcoat, *J. Geophys. Res.* **95**, 21737 (1990).
5. Y. Kuwayama, K. Hirose, N. Sata, Y. Ohishi, *Earth Planet. Sci. Lett.* **273**, 379 (2008).
6. A. B. Belonoshko, R. Ahuja, B. Johansson, *Nature* **424**, 1032 (2003).
7. W. Luo *et al.*, *Proc. Natl. Acad. Sci. U.S.A.* **107**, 9962 (2010).
8. A. S. Mikhaylushkin *et al.*, *Phys. Rev. Lett.* **99**, 165505 (2007).
9. L. Vočadlo *et al.*, *Nature* **424**, 536 (2003).
10. Materials and methods are available on *Science* Online.
11. L. S. Dubrovinsky, S. K. Saxena, F. Tutti, S. Rekhi, T. LeBehan, *Phys. Rev. Lett.* **84**, 1720 (2000).
12. Y. Kuwayama, K. Hirose, N. Sata, Y. Ohishi, *Science* **309**, 923 (2005).
13. N. Sata *et al.*, *J. Geophys. Res.* **115**, B09204 (2010).
14. V. B. Prakapenka, G. Shen, L. S. Dubrovinsky, *High Temp. High Press.* **35/36**, 237 (2003).
15. J. Rouquette *et al.*, *Appl. Phys. Lett.* **92**, 121912 (2008).
16. D. Frost *et al.*, *J. Geophys. Res.* **115**, B02202 (2010).
17. O. T. Lord, M. J. Walter, R. Dasgupta, D. Walker, S. M. Clark, *Earth Planet. Sci. Lett.* **284**, 157 (2009).
18. A. S. Côté, L. Vočadlo, J. P. Brodholt, *Geophys. Res. Lett.* **35**, L05306 (2008).
19. R. Boehler, *Nature* **363**, 534 (1993).
20. Y. Ma *et al.*, *Phys. Earth Planet. Inter.* **143–144**, 455 (2004).
21. R. Boehler, N. von Bargen, A. Chopelas, *J. Geophys. Res.* **95**, 21731 (1990).
22. R. Boehler, D. Santamaría-Pérez, D. Errandonea, M. Mezouar, *J. Phys. Conf. Ser.* **121**, 022018 (2008).
23. D. Alfè, M. J. Gillan, G. D. Price, *Contemp. Phys.* **48**, 63 (2007).
24. F. D. Stacey, P. M. Davis, *Physics of the Earth* (Cambridge Univ. Press, ed. 4, Cambridge, 2008).
25. L. Dubrovinsky *et al.*, *Science* **316**, 1880 (2007).
26. L. Stixrude, R. E. Cohen, *Science* **267**, 1972 (1995).
27. G. Steinle-Neumann, L. Stixrude, R. E. Cohen, O. Gülseren, *Nature* **413**, 57 (2001).
28. C. M. S. Gannarelli, D. Alfe, M. J. Gillan, *Phys. Earth Planet. Inter.* **152**, 67 (2005).

29. We thank N. Sata, T. Komabayashi, and Y. Tanaka for technical support. The synchrotron XRD measurements were conducted at beamline BL10XU of the SPring-8 synchrotron radiation facility (proposal nos. 2009B0087 and 2010A0087). S.T. was supported by the JSPS Research Fellowships for Young Scientists.

Supporting Online Material

www.sciencemag.org/cgi/content/full/330/6002/359/DC1
Materials and Methods
Figs. S1 to S3
Tables S1 and S2
References

6 July 2010; accepted 9 September 2010
10.1126/science.1194662

Intravascular Danger Signals Guide Neutrophils to Sites of Sterile Inflammation

Braedon McDonald,[1] Keir Pittman,[1] Gustavo B. Menezes,[1]* Simon A. Hirota,[2] Ingrid Slaba,[1] Christopher C. M. Waterhouse,[1,3] Paul L. Beck,[2,4] Daniel A. Muruve,[1,4] Paul Kubes[1]†

Neutrophils are recruited from the blood to sites of sterile inflammation, where they contribute to wound healing but may also cause tissue damage. By using spinning disk confocal intravital microscopy, we examined the kinetics and molecular mechanisms of neutrophil recruitment to sites of focal hepatic necrosis in vivo. Adenosine triphosphate released from necrotic cells activated the Nlrp3 inflammasome to generate an inflammatory microenvironment that alerted circulating neutrophils to adhere within liver sinusoids. Subsequently, generation of an intravascular chemokine gradient directed neutrophil migration through healthy tissue toward foci of damage. Lastly, formyl-peptide signals released from necrotic cells guided neutrophils through nonperfused sinusoids into the injury. Thus, dynamic in vivo imaging revealed a multistep hierarchy of directional cues that guide neutrophil localization to sites of sterile inflammation.

Sterile inflammation, characterized by redness, heat, swelling, and pain, occurs when tissues are injured in the absence of infection. Necrotic cell death can generate profound sterile inflammation characterized by the accumulation of innate immune effector cells, namely neutrophils, within the affected tissue. Such responses are classically considered homeostatic "wound healing" reactions to tissue injury, in which the phagocytic functions of neutrophils contribute to the clearance of debris (*1*). Neutrophils, however, possess a vast arsenal of hydrolytic, oxidative, and pore-forming molecules capable of causing profound collateral tissue destruction (*2*). As such, overexuberant neutrophil recruitment in response to sterile inflammatory stimuli contributes to the immunopathology observed in many diseases, including ischemic injuries/infarction, trauma, autoimmunity, drug-induced liver injury, and others (*1*, *3*–*7*). Therefore, understanding the mechanisms that allow neutrophils to respond to sterile tissue injury and cell death is fundamental to our understanding of both homeostatic innate immune functions and pathogenic immune responses in disease.

[1]Immunology Research Group, University of Calgary, Alberta T2N 4N1, Canada. [2]Gastrointestinal Research Group, Snyder Institute of Infection, Immunity and Inflammation, University of Calgary, Alberta T2N 4N1, Canada. [3]Department of Pediatrics, Division of Pediatric Gastroenterology, University of Calgary, Alberta T2N 4N1, Canada. [4]Department of Medicine, University of Calgary, Alberta T2N 4N1, Canada.

*Present address: Departamento de Morfologia, Instituto de Ciências Biológicas, Universidade Federal de Minas Gerais, Brazil.

†To whom correspondence should be addressed. E-mail: pkubes@ucalgary.ca

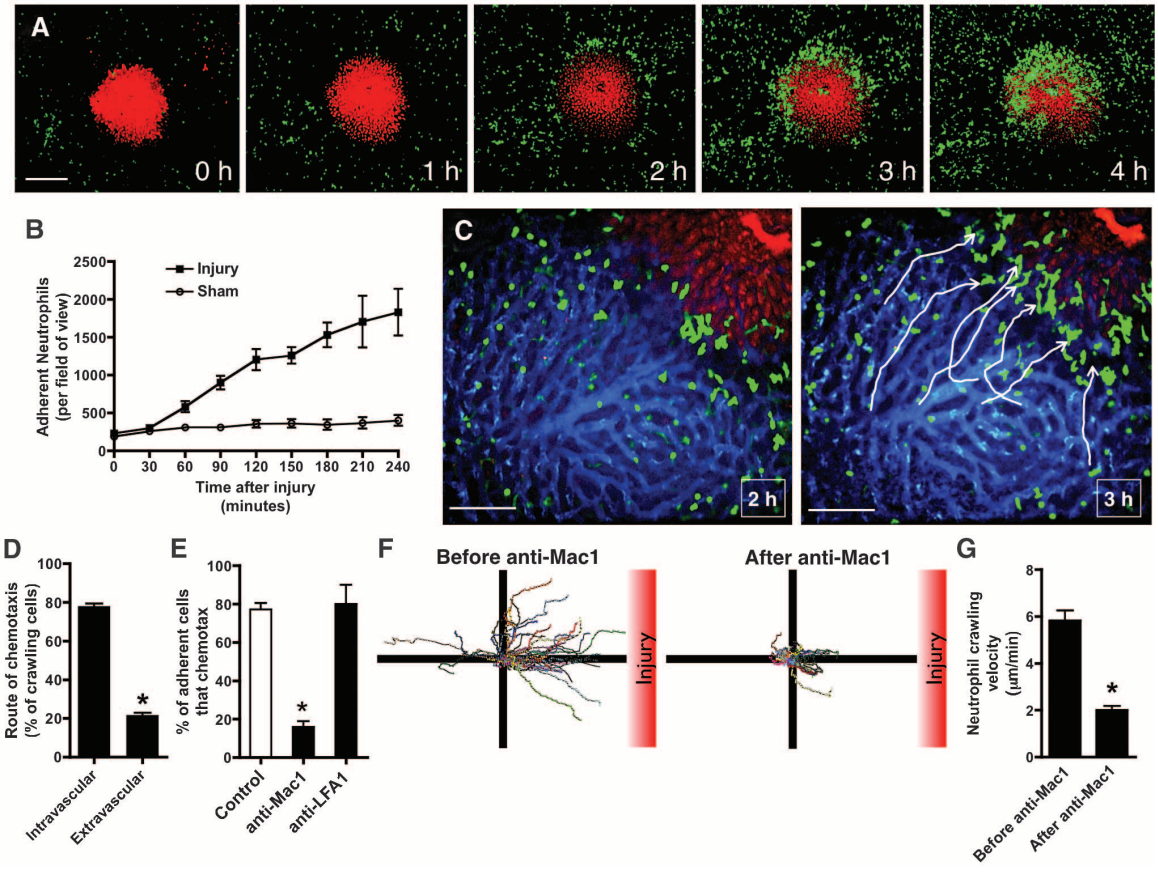

Fig. 1. Neutrophils home in to sites of sterile injury by intravascular crawling. (**A**) Time-lapse images from SD-IVM demonstrating the response of neutrophils (green) to focal hepatic necrosis (red, propidium iodide). Scale bar indicates 200 μm. (**B**) Number of adherent neutrophils per field of view in response to sterile injury or sham procedure. $N = 5$ individual mice per group for all time points. Error bars show SEM. (**C**) Representative SD-IVM images at 2 and 3 hours after injury, demonstrating the intravascular (blue, Alexa-647-BSA) route taken by neutrophils (green) to reach necrotic foci (red). Arrows show path of travel of selected neutrophils. Scale bars, 100 μm. (**D**) Quantitative representation of the route of migration taken by neutrophils en route to tissue injury. $N = 5$ individual mice; error bars, SEM; $^*P < 0.01$ by *t* test. (**E**) Animals treated with blocking antibodies against Mac1, LFA1, or isotype control (administered before injury) were imaged 2.5 hours postinjury to determine the percentage of adherent neutrophils that directionally chemotax toward the injury site. $N \geq 5$ individual mice per treatment group; error bars show SEM; $^*P < 0.01$ by one-way analysis of variance (ANOVA) with Bonferroni's posttest. (**F** and **G**) Migration paths (F) and crawling velocities (G) of neutrophils responding to tissue injury before and 10 min after administration of Mac1 antibody. Experiments were conducted 2.5 hours postinjury. Paths are normalized for their origins (site of adhesion) and position relative to the center of the necrotic focus. $N = 3$ individual mice; error bars, SEM; $^*P < 0.01$ by *t* test.

Cell death by necrosis releases multiple endogenous pro-inflammatory damage-associated molecular patterns (DAMPs), including proteins, nucleic acids, extracellular matrix components, and lipid mediators (*1*, *4*, *8*–*10*). When injected into mice, purified DAMPs or necrotic cells mobilize neutrophils to the site of inoculation (*9*, *11*, *12*). Bona fide sterile tissue injury, however, results in the death of multiple cell types, release of many DAMPs, and formation of hemostatic barriers (coagulation and thrombosis), culminating in a complex milieu of inflammatory and chemoattractant danger signals that must be translated into precise directional cues to guide neutrophil trafficking. We used in vivo imaging of the early innate immune response to reveal a multistep cascade of molecular events that guide the recruitment of neutrophils to locations of sterile injury.

We generated a murine model of focal hepatic necrosis induced by localized thermal injury on the surface of the liver and used spinning disk confocal intravital microscopy (SD-IVM) to visualize the subsequent response of neutrophils (*13*). Mice expressing enhanced green fluorescent protein under the control of the endogenous lysozyme M promoter (LysM-eGFP) were used to visualize the kinetics of eGFP-expressing (and $Gr1^{+}$) neutrophils to a 0.022 ± 0.001 (SEM) mm^3 necrotic lesion visualized by superfusion of propidium iodide over the injury area (Fig. 1A and movie S1). Within 30 to 60 min after injury, neutrophils began adhering to the microvascular endothelium (Fig. 1B). Neutrophil recruitment occurred in response to necrotic cells, because sham operation and imaging did not result in neutrophil accumulation (Fig. 1B). Neutrophil adhesion within liver sinusoids was mediated by interactions between the integrin αMβ2 (Mac1) and its endothelial ligand intercellular adhesion molecule–1 (ICAM-1) (fig. S1, A and B). In contrast, when *Escherichia coli* was applied to the liver surface rather than a necrotic injury, neutrophil adhesion in sinusoids was dependent on CD44 rather than Mac1, revealing different mechanisms of neutrophil recruitment to infection versus sterile inflammation (fig. S1, C to F). The sterility of the inflammatory response was confirmed by depleting mice of culturable gut flora with use of antibiotics (*14*) and finding no alteration in the response to hepatic necrosis (fig. S2).

Neutrophils initially adhered within sinusoids around foci of injury and over time were observed to gradually accumulate within the area of necrosis (Fig. 1A and fig. S3). Of adherent neutrophils, 77.3% ± 3.3 were observed to directionally chemotax toward the necrotic tissue, ultimately infiltrating into the area of cell death (Fig. 1C). Instead of transmigrating out of the vasculature to take the shortest path toward the site of danger, the majority of neutrophils migrated via the intravascular route, which was often a less-direct course (Fig. 1, C and D, and movies S2 and S3). Inhibitory antibodies against Mac1 but not the closely related αLβ2-integrin LFA1 significantly reduced the number of neutrophils that chemotaxed intravascularly toward tissue injury compared with the number in isotype control-treated animals (Fig. 1E and movie S4). Furthermore, administration of Mac1 antibody 2.5 hours after injury abruptly stopped migrating neutrophils, demonstrating a role for Mac1 in mediating crawling and adhesion (Fig. 1, F and G). Thus, neutrophils use the vascular channels as highways to guide their transit through healthy tissue toward sites of sterile injury.

Analysis of the microvascular hemodynamics revealed an absence of perfused sinusoids within the area of necrosis and occlusion of the sinus-

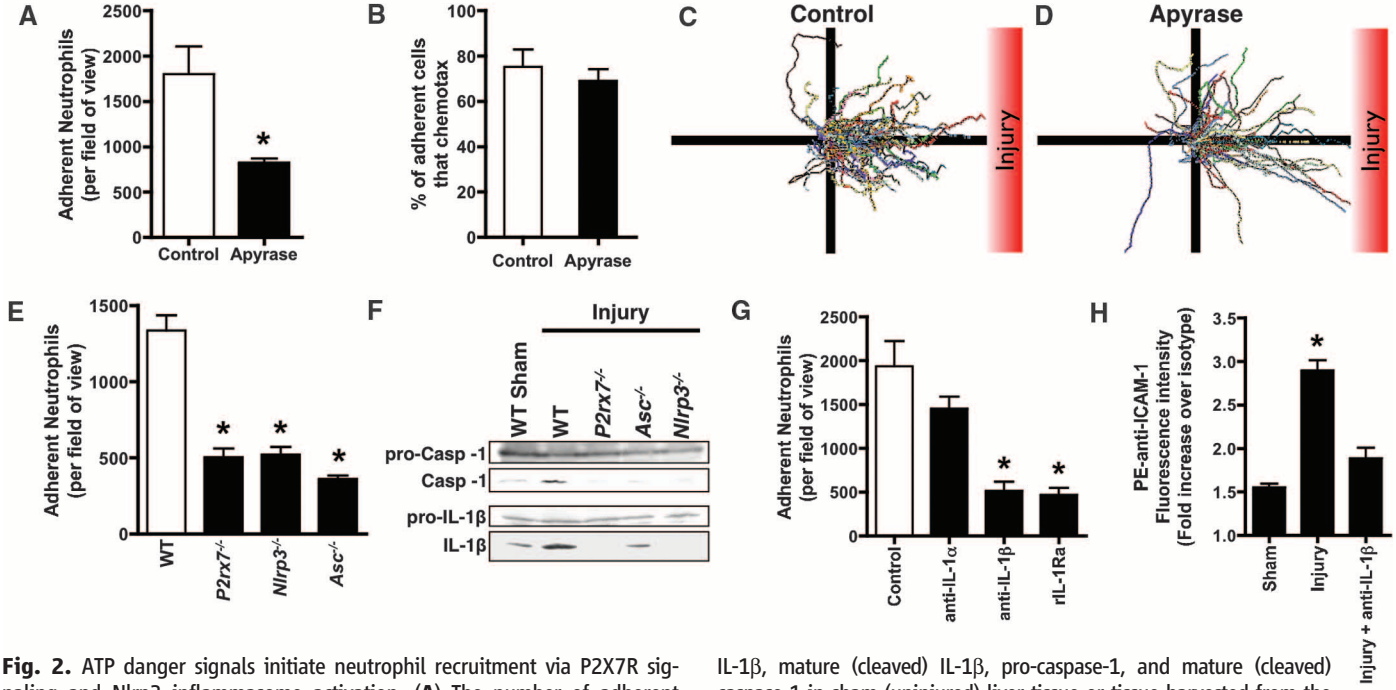

Fig. 2. ATP danger signals initiate neutrophil recruitment via P2X7R signaling and Nlrp3 inflammasome activation. (**A**) The number of adherent neutrophils per field of view 4 hours after focal hepatic injury in mice treated with apyrase or vehicle control. $N = 5$ individual mice per treatment group; error bars, SEM; $^*P < 0.05$ by t test. (**B** to **D**) Mice treated with apyrase or vehicle control were imaged 2.5 hours postinjury to determine the percentage of adherent neutrophils that chemotax toward the injury site (B) and migration paths for chemotaxing neutrophils [(C) and (D)]. Paths are normalized for their origins (site of adhesion) and position relative to the center of the necrotic focus. $N = 5$ individual mice per group; error bars, SEM. (**E**) Number of adherent neutrophils per field of view 4 hours after focal hepatic injury in indicated mouse strains [wild type (WT) and C57BL/6]. $N = 5$ individual mice per genotype; error bars, SEM; $^*P < 0.01$ versus WT by one-way ANOVA with Bonferroni's posttest. (**F**) Representative immunoblots for the detection of pro-IL-1β, mature (cleaved) IL-1β, pro-caspase-1, and mature (cleaved) caspase-1 in sham (uninjured) liver tissue or tissue harvested from the site of injury in the indicated mice. Representative of two independent experiments. (**G**) Number of adherent neutrophils per field of view 4 hours after focal hepatic injury in mice treated with recombinant IL-1R antagonist (rIL-1Ra) or antibodies against IL-1β or IL-1α. $N = 5$ individual mice per treatment group; error bars, SEM; $^*P < 0.01$ versus control by one-way ANOVA with Bonferroni's posttest. (**H**) Fluorescence intensity was quantified from SD-IVM images after administration of phycoerythrin (PE)–labeled antibody against ICAM-1 (PE-anti-ICAM-1), expressed as -fold increase in fluorescence intensity relative to equivalently labeled isotype control. Experiments were conducted 2.5 hours postinjury (or sham procedure) in the presence and absence of IL-1β blocking antibody. $N = 3$ individual mice per treatment group; error bars, SEM; $^*P < 0.001$ versus control by one-way ANOVA with Bonferroni's posttest.

oids immediately adjacent to the necrotic core (surrounding ~150 μm) by platelet thrombi (fig. S4, A to C). Although neutrophil crawling velocity was reduced within these areas (fig. S4D), this did not limit their ability to home into the injury site (movie S2). Beyond 150 μm from the injury border, more than 80% of sinusoids were actively perfused, and as such the majority of neutrophils migrated via perfused sinusoids without any preference for vessels flowing toward or away from the necrotic focus (fig. S4, E and F).

To investigate the molecular signals that direct neutrophil migration, we hypothesized that purinergic danger signals such as extracellular adenosine triphosphate (ATP) released by damaged cells act as a find-me signal to guide neutrophils to sites of necrosis. Previous studies have suggested that this function of ATP may be due to its ability to induce cytokine production and/or its ability to promote leukocyte migration (*3*, *15*–*17*). Administration of an exogenous ATPase (apyrase), which hydrolyzed extracellular ATP released after injury (fig. S5A), resulted in a marked reduction in the total number of neutrophils recruited into the liver in response to tissue injury (Fig. 2A and movie S5). In contrast, apyrase did not inhibit the ability of recruited neutrophils to chemotax toward the focus of injury (Fig. 2, B to D), demonstrating that ATP does not function as a chemotactic signal. Similarly, administration of suramin to block heterotrimeric guanine nucleotide–binding protein (G protein)–coupled P2Y purinergic receptors that have been implicated in the chemotactic response to ATP (*15*–*17*) did not affect the recruitment or migration of neutrophils (fig. S5B).

Extracellular ATP, via P2X7 receptor signaling, is one of the best-characterized activators of the Nlrp3 inflammasome, which mediates the generation of inflammatory cytokines such as interleukin (IL)-1β (*1*, *18*, *19*). Similar to apyrase treatment, selective inhibition of P2X7 receptors with oxidized ATP or genetic deficiency in *P2rx7*$^{-/-}$ mice resulted in reduced neutrophil recruitment in response to tissue injury, without impairing the chemotactic response of the few recruited neutrophils (Fig. 2E and figs. S5B and S6). Bone marrow chimeric mice demonstrated that the target cells of P2X7R signaling were of hematopoietic origin but were not neutrophils because isolated *P2rx7*$^{-/-}$ and wild-type neutrophils were recruited equivalently to foci of necrosis after adoptive transfer (fig. S7). Furthermore, the quantity of neutrophils recruited to areas of necrosis was significantly reduced in mice deficient in inflammasome component Nlrp3 or ASC compared with wild-type animals (Fig. 2E). Consistent with recent reports that macrophages are the primary sentinel cells that sense cell death and generate pro-inflammatory cytokines (*20*), mice that were depleted of liver-resident intravascular macrophages (Kupffer cells) by admin-

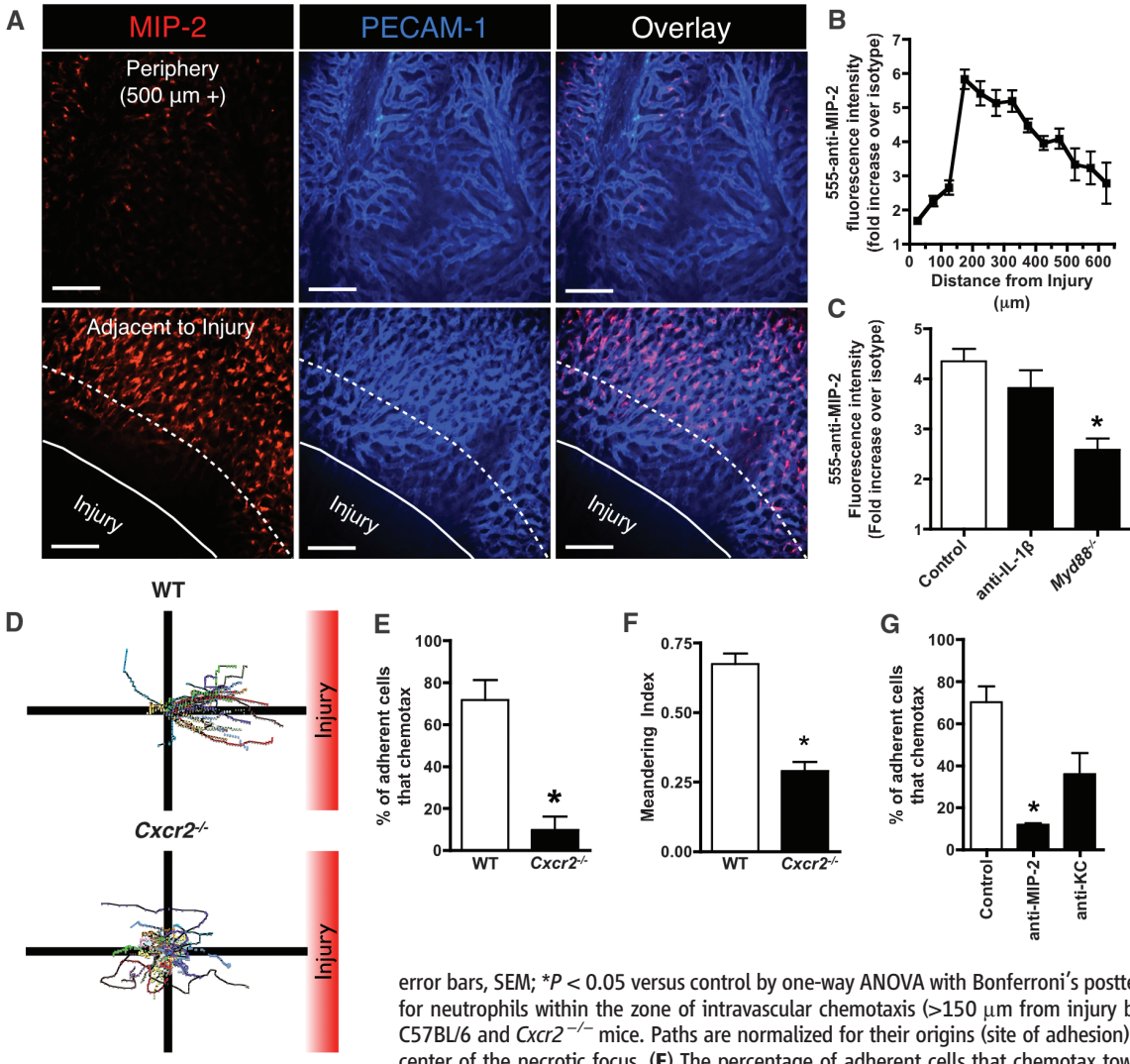

Fig. 3. An intravascular chemokine gradient guides neutrophil chemotaxis within the vasculature toward foci of sterile injury. (**A**) MIP-2 expression (red) and PECAM-1^{+} endothelium (blue) were visualized 2.5 hours after injury in the distant periphery and directly adjacent to the injury (indicated by solid white lines). Scale bars, 100 μm. (**B**) Fluorescence intensity of MIP-2 antibody staining from SD-IVM images was quantified within individual sinusoids at various distances from the border of necrotic injury 2.5 hours postinjury and expressed as -fold increase in fluorescence intensity relative to equivalently labeled isotype control. *N* = 103 sinusoids compiled from three individual mice; error bars, SEM. (**C**) Fluorescence intensity of MIP-2 antibody staining in sinusoids surrounding injury in mice left untreated (control) or treated with IL-1β blocking antibody before injury or in *Myd88*$^{-/-}$ mice. *N* ≥ 3 individual mice per treatment group; error bars, SEM; **P* < 0.05 versus control by one-way ANOVA with Bonferroni's posttest. (**D**) Cell migration paths for neutrophils within the zone of intravascular chemotaxis (>150 μm from injury border, see fig. S10C) in WT C57BL/6 and *Cxcr2*$^{-/-}$ mice. Paths are normalized for their origins (site of adhesion) and position relative to the center of the necrotic focus. (**E**) The percentage of adherent cells that chemotax toward the injury site in WT or *Cxcr2*$^{-/-}$ mice. (**F**) Meandering index of migrating neutrophils depicted in (D). In (D) to (F), imaging was conducted 2.5 hours postinjury; *N* ≥ 3 individual mice per group; error bars, SEM; **P* < 0.01 by *t* test. (**G**) Mice treated with antibodies against MIP-2, KC, or isotype control were imaged 2.5 hours postinjury, and the percentage of adherent cells that chemotax toward the injury site was determined. *N* = 3 individual mice per treatment group; error bars, SEM; **P* < 0.01 versus control by one-way ANOVA with Bonferroni's posttest.

istration of liposome-encapsulated clodronate (*21*) demonstrated reduced neutrophil recruitment similar to animals with impaired P2X7R signaling (fig. S8). Western blots of injured liver tissue confirmed that Nlrp3-dependent activation of caspase-1 and IL-1β processing at sites of focal hepatic necrosis was entirely dependent on P2X7R signaling (Fig. 2F). Mice that received blocking antibodies against IL-1β, a recombinant antagonist of the IL-1-receptor (IL-1R), or animals that were deficient of the signaling adaptor MyD88 (required for signaling through IL-1R) showed similarly reduced neutrophil accumulation (Fig. 2G and fig. S9A). Neutrophil adoptive transfer experiments revealed that MyD88-deficient and wild-type neutrophils were recruited equivalently to sites of injury, indicating that neutrophils were not a target of IL-1β (fig. S9B). Instead, IL-1β blockade prevented ICAM-1 up-regulation on the surface of sinusoidal endothelium in response to tissue injury (Fig. 2H). Thus, ATP danger signals activate a pathway that initiates neutrophil adhesion but do not guide neutrophil chemotaxis toward necrotic cells.

We next hypothesized that chemokines produced in response to tissue injury may guide intravascular neutrophil migration to foci of sterile inflammation. Previous studies have demonstrated that chemokines may be expressed and immobilized on the luminal surface of microvascular endothelium in vivo (*22*). Intravital immunofluorescence using SD-IVM revealed MIP-2 (macrophage inflammatory protein 2, CXCL2) expression on the luminal surface of the liver sinusoids that was maximal at about 150 μm from the injury border and gradually decreased out to 650 μm, demonstrating the presence of an intravascular gradient that leads toward the injured area (Fig. 3, A and B). Graded MIP-2 expression was not dependent on IL-1β but did require signaling through a MyD88-dependent pathway within nonhematopoietic cells (Fig. 3C and fig. S10A). Within the region of high intravascular MIP-2 expression, neutrophils in CXCR2-deficient animals that were unable to detect MIP-2 failed to directionally chemotax (Fig. 3, D and E) but rather migrated randomly in the vasculature (meandering index 0.29 ± 0.03, Fig. 3F). Inhibitory antibodies against MIP-2, and to a lesser extent CXCL1 (KC), prevented intravascular chemotaxis toward foci of damage, confirming that neutrophil chemotaxis is directed by a functional gradient of intravascular chemokines (Fig. 3G).

The intravascular gradient of MIP-2 was consistently observed to abruptly end ~100 to 150 μm proximal to the border of necrotic tissue, despite the presence of intact platelet endothelial cell adhesion molecule 1–positive (PECAM-1^{+}) endothelium (Fig. 3, A and B). Intravenous administration of a PECAM-1–specific antibody demonstrated that sinusoidal endothelium in this malperfused area is accessible to circulating proteins. Circulating recombinant MIP-2 failed to bind within this proximal zone (fig. S10B), suggesting that the absence of MIP-2 may be due to an inability of the chemokine to become immobilized on endothelial surface glycosaminoglycans near the injury. Furthermore, within this proximal 150 μm surrounding the injury, directional neutrophil migration was independent of CXCR2 (Fig. 4, A and B).

Given that neutrophils migrate directly into the area of cell death, we hypothesized that necrotic cells released a CXCR2-independent chemoattractant, or "necrotaxis" signal, that directs neutrophil migration beyond the intravascular che-

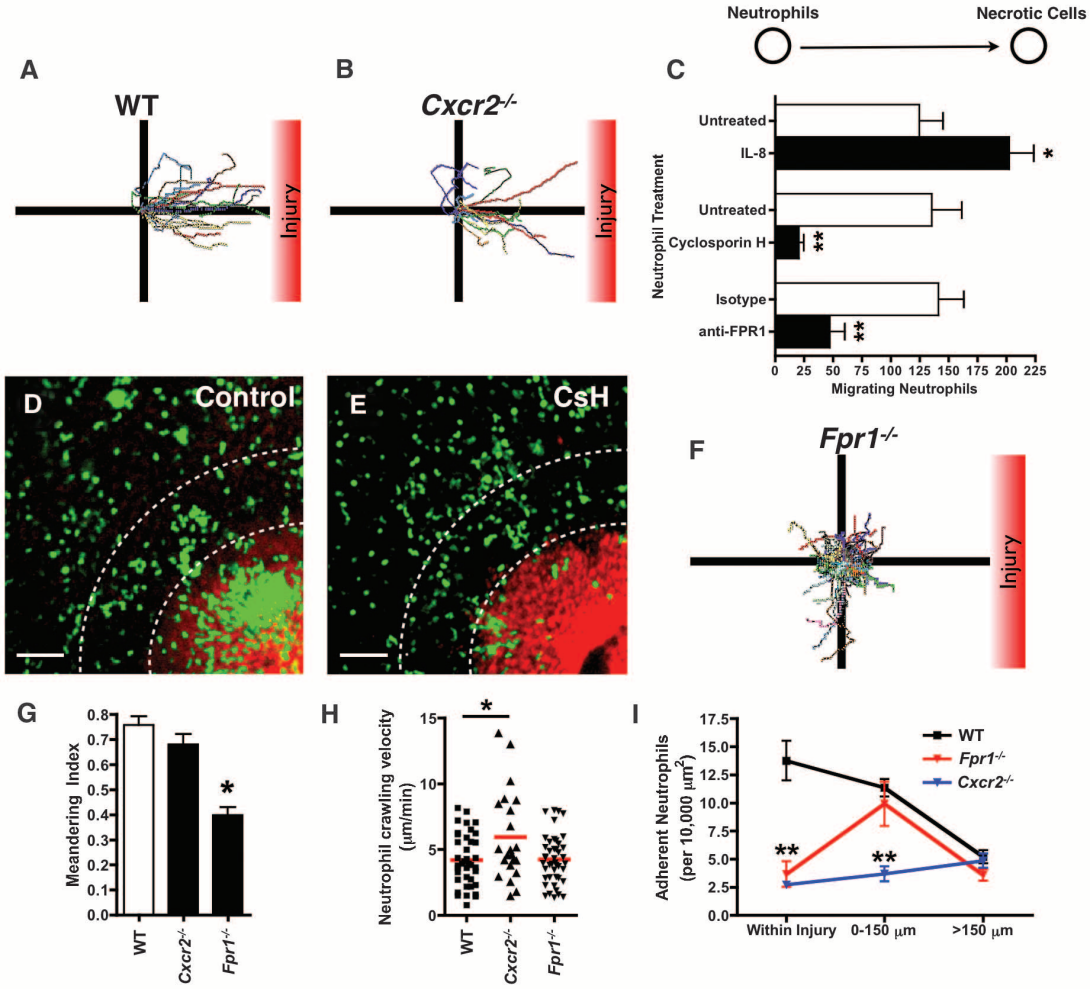

Fig. 4. FPR1-dependent necrotaxis guides precise localization of neutrophils into areas of sterile tissue necrosis. (**A** and **B**) Cell migration paths for neutrophils within the zone of necrotaxis (proximal 150 μm surrounding injury, see fig. S10C) in WT (A) and *Cxcr2*$^{-/-}$ (B) mice 2.5 hours postinjury. Paths are normalized for their origins (site of adhesion) and position relative to the center of the necrotic focus ($N \geq 3$ individual mice per group). (**C**) The number of human neutrophils that chemotaxed toward necrotic HEK 293 cells in vitro. Neutrophils were left untreated or incubated with IL-8, CsH, anti-FPR1, or isotype control. $N \geq 5$ independent experiments; error bars, SEM; *$P < 0.05$ or **$P < 0.01$ versus control by one-way ANOVA with Bonferroni's posttest. (**D** and **E**) Representative SD-IVM images of neutrophils (green) responding to a focus of tissue injury (red) in animals treated with vehicle control (D) or the FPR1 antagonist CsH (E). Dashed lines are at injury border and 150 μm. Scale bars, 100 μm. Representative of three animals per group. (**F**) Cell migration paths for neutrophils within the zone of necrotaxis in *Fpr1*$^{-/-}$ mice 2.5 hours postinjury ($N = 4$ independent mice). (**G** and **H**) Meandering index [(G) error bars, SEM] and crawling velocity [(H) lines, means] of migrating neutrophils depicted in (A), (B), and (F). *$P < 0.05$ versus WT by one-way ANOVA with Bonferroni's posttest. (**I**) Number of adherent neutrophils per 10,000 μm^2 within the indicated regions around necrotic foci (4× field of view) 4 hours after injury in WT, *Cxcr2*$^{-/-}$, and *Fpr1*$^{-/-}$ mice. $N \geq 3$ independent mice per genotype; error bars, SEM; **$P < 0.01$ versus WT by one-way ANOVA with Bonferroni's posttest.

mokine gradient (fig. S10C). In support of this, neutrophils failed to enter into a focus of sterile inflammation that did not contain necrotic cells (focal vascular occlusion generated by localized compression of sinusoids) and instead simply accumulated around the injury (fig. S11). Furthermore, the observation that neutrophils rapidly migrated away from high concentrations of CXCR2 ligands implies that the necrotactic stimulus must hierarchically override CXCR2 signaling. In an in vitro under agarose chemotaxis assay, necrotic cells potently attracted human neutrophils (Fig. 4C). This attraction overrode CXCR2 signals, because incubation of neutrophils in IL-8 (human homolog of MIP-2) did not inhibit chemotaxis toward necrotic cells (Fig. 4C). Mitochondria contain DAMPs, including formylated peptides, that can direct neutrophil chemotaxis via signaling through the formyl-peptide receptor 1 [FPR1 (*7*)]. In vitro, blockade of neutrophil FPR1 with inhibitory antibodies or the selective antagonist cyclosporin H (CsH) significantly attenuated neutrophil chemotaxis toward necrotic cells (Fig. 4C). In vivo, treatment of LysM-eGFP mice with CsH (Fig. 4, D and E, and fig. S12) or genetic deficiency of FPR1 ($Fpr1^{-/-}$, Fig. 4, F and G) resulted in nondirectional random migration within the necrotaxis zone. Importantly, FPR1 signals controlled only directionality within the necrotaxis zone, because neutrophil crawling velocities were unchanged in $Fpr1^{-/-}$ mice compared with those in wild-type mice (Fig. 4H). Overall, although the majority of neutrophils in wild-type mice accumulated within the necrotic focus, neutrophils in $Fpr1^{-/-}$ mice homed in to the proximal 150 μm around the injury, where they migrated randomly and accumulated (Fig. 4I). This pattern of neutrophil accumulation was equivalent to that seen in response to foci of vascular occlusion, where both wild-type and $Fpr1^{-/-}$ neutrophils accumulated in the proximal 150 μm but failed to migrate into the area of injury, presumably because of a lack of FPR1 ligands in the absence of dead cells (fig. S11).

We have identified a multistep cascade of intravascular events that allow neutrophils to sense and home in to sites of sterile inflammation in vivo (fig. S13). In contrast to recent reports (*17*), we show that ATP does not function as a chemoattractant but rather initiates the inflammatory response through mechanisms that lead to neutrophil adhesion. We have recently reported that signals through formyl peptide receptors in neutrophils hierarchically override signals through CXCR2, allowing neutrophils to preferentially migrate toward end-target chemoattractants in vitro (*23*). Our present study provides evidence that this hierarchy of neutrophil chemoattraction functions in vivo. Importantly, the migration patterns and molecular guidance cues that direct neutrophils to sites of sterile inflammation in the liver also function similarly in other organs such as the skin, which contains a vastly different cellular composition and vascular architecture (fig. S14).

Neutrophil extravasation out of the vasculature into tissues can cause substantial collateral damage during pathological inflammatory responses (*1*, *24*). We propose that the intravascular danger sensing and recruitment mechanisms identified in this study have evolved to limit collateral damage during responses to sterile injury by allowing neutrophils to remain intravascular as they navigate through healthy tissue to sites of injury. Furthermore, necrotaxis cues are released from necrotic cells to promote localization of neutrophils directly into existing areas of injury. This is likely a means to focus the innate immune response on damaged areas and away from healthy tissue, providing an additional safeguard against collateral damage during sterile inflammatory responses.

References and Notes

1. H. Kono, K. L. Rock, *Nat. Rev. Immunol.* **8**, 279 (2008).
2. A. W. Segal, *Annu. Rev. Immunol.* **23**, 197 (2005).
3. M. C. Hyman *et al.*, *J. Clin. Invest.* **119**, 1136 (2009).
4. A. B. Imaeda *et al.*, *J. Clin. Invest.* **119**, 305 (2009).
5. Z. X. Liu, D. Han, B. Gunawan, N. Kaplowitz, *Hepatology* **43**, 1220 (2006).
6. A. Tsung *et al.*, *J. Exp. Med.* **201**, 1135 (2005).
7. Q. Zhang *et al.*, *Nature* **464**, 104 (2010).
8. D. Jiang *et al.*, *Nat. Med.* **11**, 1173 (2005).
9. P. Scaffidi, T. Misteli, M. E. Bianchi, *Nature* **418**, 191 (2002).
10. Y. Shi, J. E. Evans, K. L. Rock, *Nature* **425**, 516 (2003).
11. F. Martinon, V. Pétrilli, A. Mayor, A. Tardivel, J. Tschopp, *Nature* **440**, 237 (2006).
12. C. J. Chen *et al.*, *Nat. Med.* **13**, 851 (2007).
13. Material and methods are available as supporting online material at *Science* Online.
14. S. Rakoff-Nahoum, J. Paglino, F. Eslami-Varzaneh, S. Edberg, R. Medzhitov, *Cell* **118**, 229 (2004).
15. D. Davalos *et al.*, *Nat. Neurosci.* **8**, 752 (2005).
16. M. R. Elliott *et al.*, *Nature* **461**, 282 (2009).
17. Y. Chen *et al.*, *Science* **314**, 1792 (2006).
18. J. Tschopp, K. Schroder, *Nat. Rev. Immunol.* **10**, 210 (2010).
19. S. S. Iyer *et al.*, *Proc. Natl. Acad. Sci. U.S.A.* **106**, 20388 (2009).
20. H. Kono, D. Karmarkar, Y. Iwakura, K. L. Rock, *J. Immunol.* **184**, 4470 (2010).
21. W. Y. Lee *et al.*, *Nat. Immunol.* **11**, 295 (2010).
22. J. Middleton *et al.*, *Cell* **91**, 385 (1997).
23. B. Heit *et al.*, *Nat. Immunol.* **9**, 743 (2008).
24. C. Nathan, *Nat. Rev. Immunol.* **6**, 173 (2006).

25. We thank C. Badick for excellent technical support. This study was supported by grants from the Canadian Institutes of Health Research and Alberta Innovates (Health Solutions).

Supporting Online Material

www.sciencemag.org/cgi/content/full/330/6002/362/DC1
Materials and Methods
Figs. S1 to S14
References
Movies S1 to S5

22 July 2010; accepted 30 August 2010
10.1126/science.1195491

Granulosa Cell Ligand NPPC and Its Receptor NPR2 Maintain Meiotic Arrest in Mouse Oocytes

Meijia Zhang,[1,2] You-Qiang Su,[2] Koji Sugiura,[2]* Guoliang Xia,[1]† John J. Eppig[2]†

Granulosa cells of mammalian Graafian follicles maintain oocytes in meiotic arrest, which prevents their precocious maturation. We show that mouse mural granulosa cells, which line the follicle wall, express natriuretic peptide precursor type C (*Nppc*) messenger RNA (mRNA), whereas cumulus cells surrounding oocytes express mRNA of the NPPC receptor NPR2, a guanylyl cyclase. NPPC increased cGMP levels in cumulus cells and oocytes and inhibited meiotic resumption in vitro. Meiotic arrest was not sustained in most Graafian follicles of *Nppc* or *Npr2* mutant mice, and meiosis resumed precociously. Oocyte-derived paracrine factors promoted cumulus cell expression of *Npr2* mRNA. Therefore, the granulosa cell ligand NPPC and its receptor NPR2 in cumulus cells prevent precocious meiotic maturation, which is critical for maturation and ovulation synchrony and for normal female fertility.

Meiosis is a germ cell–specific process that reduces the number of chromosomes from the diploid to the haploid number. It begins in human and mouse ovaries during fetal life, but meiotic progression becomes arrested for prolonged periods at the diplotene stage of meiotic prophase. Fully grown mammalian oocytes in Graafian follicles are maintained in meiotic prophase arrest until the preovulatory surge of luteinizing hormone (LH) triggers the resumption of meiosis and ovulation. The mature oocytes (eggs) are then available for fertilization within the oviduct. The somatic cell compartment of Graafian follicles, consisting of mural granulosa cells lining the inside of the follicle wall and cumulus cells surrounding the oocyte, plays a crucial role in maintaining oocyte meiotic arrest in mammals because removal of the oocyte-cumulus cell complex from these follicles results in gonadotropin-independent meiotic resumption in culture (*1*, *2*). Cyclic nucleotides cAMP (adenosine 3′,5′-monophosphate) and

[1]State Key Laboratory for Agrobiotechnology, College of Biological Sciences, China Agricultural University, Beijing 100193, People's Republic of China. [2]The Jackson Laboratory, Bar Harbor, ME 04609, USA.

*Present address: Laboratory of Applied Genetics, Graduate School of Agricultural and Life Science, University of Tokyo, Tokyo, Japan.

†To whom correspondence should be addressed. E-mail: john.eppig@jax.org (J.J.E.); glxia@cau.edu.cn (G.X.)

cGMP (cyclic guanosine 5′-monophosphate) are crucial for maintaining meiotic arrest. Cyclic AMP is generated within oocytes downstream of GPR3 and GPR12, regulators of G_s proteins controlling adenylyl cyclase (*3*, *4*). Inability to sustain oocyte cAMP concentrations leads to precocious gonadotropin-independent resumption of meiosis, which interrupts the synchrony between oocyte maturation and ovulation and compromises female fertility (*3*–*5*). PDE3A, an oocyte-specific phosphodiesterase, becomes activated after the LH surge to decrease cAMP concentrations in oocytes and thereby initiates pathways governing meiotic resumption (*6*). Before the LH surge, cGMP, originating in granulosa cells of the follicular somatic compartment and transferred to the oocyte via gap junctions, inhibits activity of PDE3A in the oocyte (*7*, *8*). Therefore, control of cGMP production by granulosa cells is essential for maintaining meiotic arrest in fully grown oocytes.

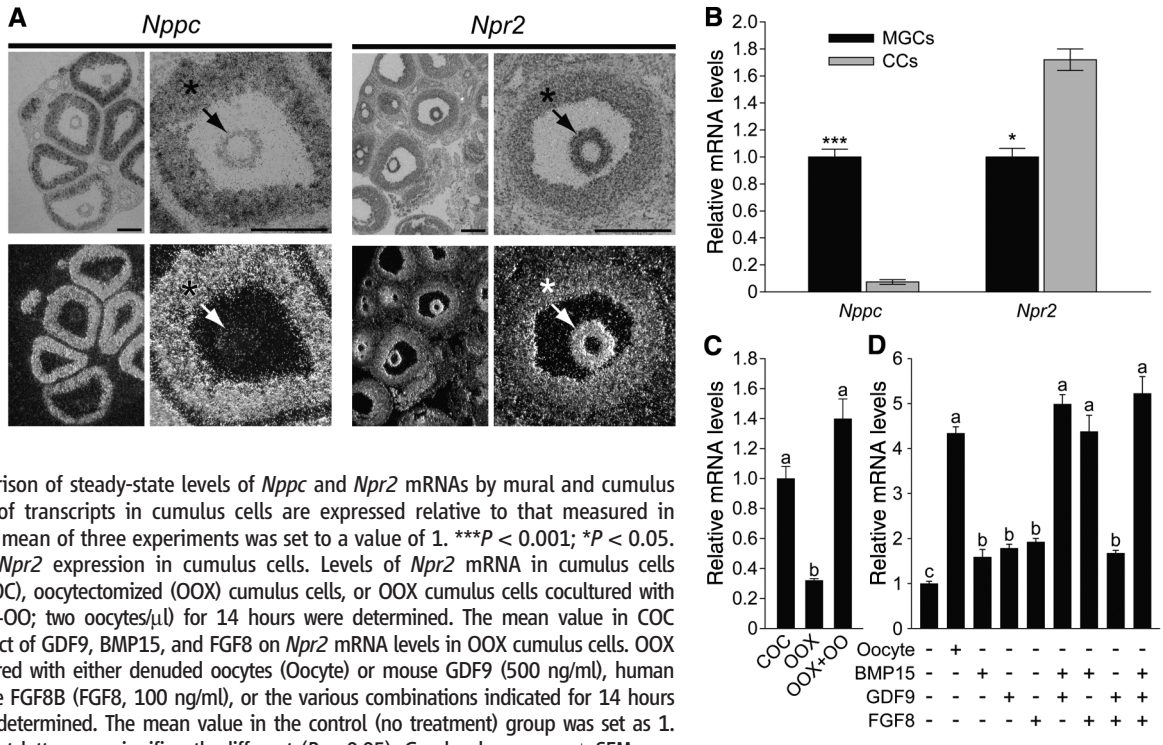

Fig. 1. Expression of *Nppc* and *Npr2* mRNA by granulosa cells. (**A**) In situ hybridization showing localization of *Nppc* and *Npr2* mRNA expression in prepubertal mouse ovaries 48 hours after eCG injection. Histology is shown in bright-field images (upper panels), and localization of specific mRNAs is shown in dark-field images (lower panels). Asterisks (*) indicate mural granulosa cells (MGCs); arrows indicate cumulus cells (CCs). Bars, 200 μm. (**B**) Comparison of steady-state levels of *Nppc* and *Npr2* mRNAs by mural and cumulus cells by qRT-PCR. Levels of transcripts in cumulus cells are expressed relative to that measured in mural granulosa cells; the mean of three experiments was set to a value of 1. ***$P < 0.001$; *$P < 0.05$. (**C**) Effect of oocytes on *Npr2* expression in cumulus cells. Levels of *Npr2* mRNA in cumulus cells cultured as intact COCs (COC), oocytectomized (OOX) cumulus cells, or OOX cumulus cells cocultured with fully grown oocytes (OOX+OO; two oocytes/μl) for 14 hours were determined. The mean value in COC group was set as 1. (**D**) Effect of GDF9, BMP15, and FGF8 on *Npr2* mRNA levels in OOX cumulus cells. OOX cumulus cells were cocultured with either denuded oocytes (Oocyte) or mouse GDF9 (500 ng/ml), human BMP15 (500 ng/ml), mouse FGF8B (FGF8, 100 ng/ml), or the various combinations indicated for 14 hours and levels of *Npr2* mRNA determined. The mean value in the control (no treatment) group was set as 1. Values indicated by different letters are significantly different ($P < 0.05$). Graphs show mean ± SEM.

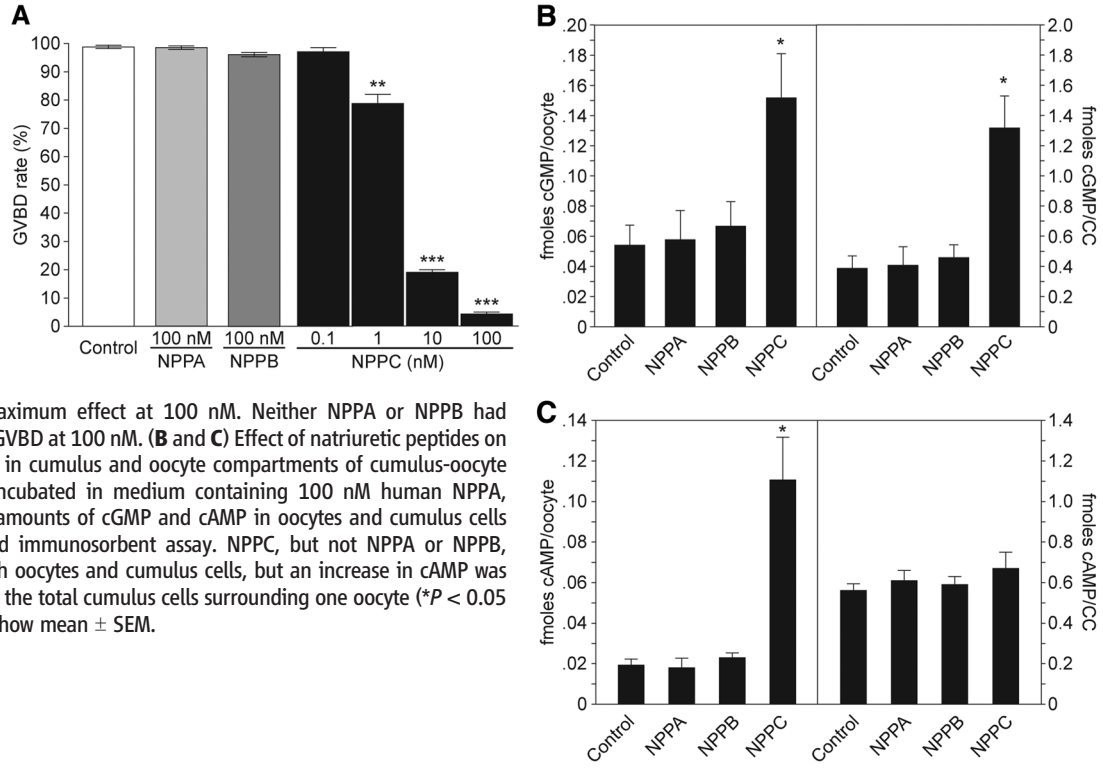

Fig. 2. Effect of natriuretic peptides on gonadotopin-independent (spontaneous) resumption of meiosis and production of cAMP and cGMP in vitro. (**A**) Effect of natriuretic peptides on spontaneous maturation of cumulus cell–enclosed oocytes in vitro. Oocytes were cultured for 4 hours in medium containing human NPPA, NPPB, or NPPC and assessed for GVBD indicative of the resumption of meiosis. NPPC dose-dependently inhibited resumption of cumulus cell–enclosed oocytes with a maximum effect at 100 nM. Neither NPPA or NPPB had detectable activity in preventing GVBD at 100 nM. (**B** and **C**) Effect of natriuretic peptides on levels of cGMP (B) and cAMP (C) in cumulus and oocyte compartments of cumulus-oocyte complexes (COCs). COCs were incubated in medium containing 100 nM human NPPA, NPPB, or NPPC for 1 hour, and amounts of cGMP and cAMP in oocytes and cumulus cells were evaluated by enzyme-linked immunosorbent assay. NPPC, but not NPPA or NPPB, promoted increased cGMP in both oocytes and cumulus cells, but an increase in cAMP was seen only in oocytes. CC indicates the total cumulus cells surrounding one oocyte (*$P < 0.05$ compared with control). Graphs show mean ± SEM.

Exploration of the mouse cumulus cell transcriptome for mRNAs encoding guanylyl cyclases by microarray analysis (*9*) revealed abundant expression of natriuretic peptide receptor 2 (*Npr2*, also called GC-B) mRNA. The presence of this guanylyl cyclase was reported in rat follicles, and the binding of its ligand, NPPC (also known as CNP), to granulosa cells varied during the estrous cycle (*10*). Moreover, NPPA (ANP) was reported to inhibit resumption of meiosis in rat oocytes (*11*). Therefore, expression of *Nppc* and *Npr2* mRNAs in mouse ovarian follicles was determined by in situ hybridization. *Nppc* mRNA was expressed predominantly by mural granulosa cells, which line the inside of the follicular wall, and, in contrast, *Npr2* mRNA was expressed predominantly by cumulus cells; outwardly decreasing levels of expression included some periantral mural granulosa cells (Fig. 1A). Quantitative reverse transcription–polymerase chain reaction (qRT-PCR) confirmed that the steady-state levels of *Nppc* mRNA were at least a factor of 10 higher in mural granulosa cells than in cumulus cells, and levels of *Npr2* mRNA were about twice as high in cumulus cells as compared with mural granulosa cells (Fig. 1B). Because the isolation and collection of mural granulosa cells from follicles are unavoidably biased to those that line the antrum, and as shown by in situ hybridization these periantral mural granulosa cells express *Npr2* mRNA at levels much higher than the larger population of outermost mural granulosa cells (Fig. 1A), this difference in *Npr2* expression is really much greater than a factor of 2.

The intriguing juxtaposition of the cell types expressing the ligand mRNA (*Nppc*) and its cognate receptor (*Npr2*) suggests a functional relationship. Supporting this idea, we found that NPPC peptide, but not the related NPPA or NPPB, prevented spontaneous (gonadotropin-independent) resumption of cumulus cell–enclosed (Fig. 2A), but not denuded (fig. S1), mouse oocytes in vitro. Likewise, NPPC, but not NPPA or NPPB, increased cumulus cell and oocyte cGMP levels in cultured cumulus cell–oocyte complexes (Fig. 2B). Cyclic AMP levels were elevated in oocytes but not in cumulus cells (Fig. 2C). Because oocytes do not express detectable NPR2 receptors, effects of NPPC on cGMP levels in oocytes probably

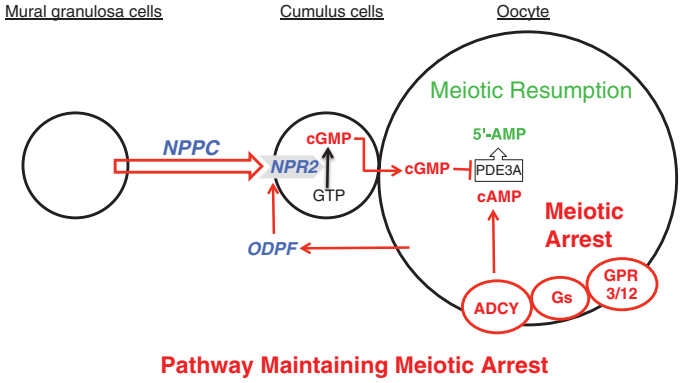

Fig. 4. Model depicting the role of NPPC and NPR2 and oocyte-derived paracrine factors (ODPF) in the maintenance of oocyte meiotic arrest. See text for details. ADCY, adenylyl cyclase; GPR3/12, G protein–coupled receptors 3 and 12; Gs, GNAS (guanine nucleotide binding protein, α stimulating) complex.

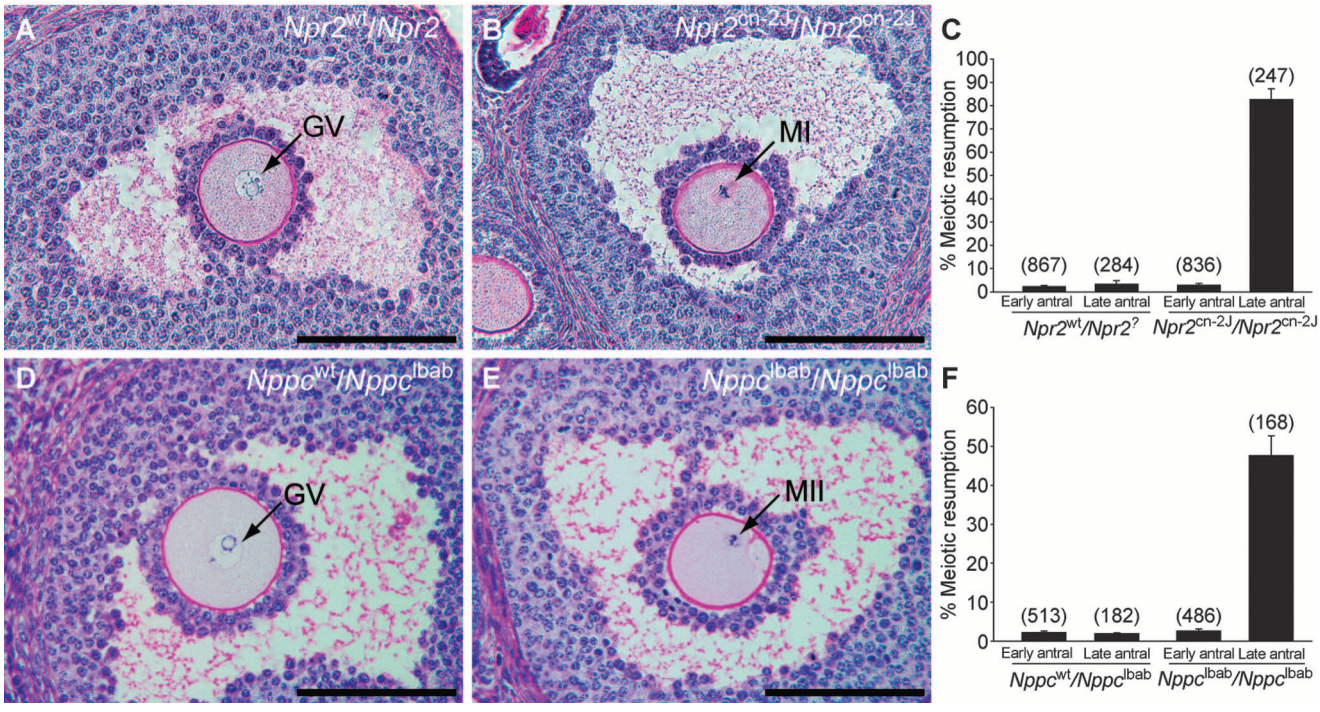

Fig. 3. Failure to maintain meiotic arrest in Graafian (late antral) follicles of $Npr2^{cn\text{-}2J}/Npr2^{cn\text{-}2J}$ and $Nppc^{lbab}/Nppc^{lbab}$ mutant mouse ovaries. (**A**) A prophase-arrested oocyte (GV, germinal vesicle) within a late antral follicle of a control $Npr2^{wt}/Npr2^{?}$ ovary. (**B**) An oocyte with metaphase I (MI) chromosomes within a late antral follicle of an $Npr2^{cn\text{-}2J}/Npr2^{cn\text{-}2J}$ mutant ovary. (**C**) Percentages of oocytes that had resumed meiosis, counted in sections of ovaries from control $Npr2^{wt}/Npr2^{?}$ and mutant $Npr2^{cn\text{-}2J}/Npr2^{cn\text{-}2J}$ mice that were treated with eCG for 44 hours. Graph shows mean ± SEM of six ovaries; numbers above bars indicate number of follicles examined. (**D** and **E**) Ovarian follicles after development as grafts under kidney capsules of immunodeficient hosts for 30 days. (D) A prophase-arrested oocyte within a late antral follicle of a heterozygous control $Nppc^{wt}/Nppc^{lbab}$ ovary. (E) An oocyte with metaphase II (MII) chromosomes and a polar body, within a late antral follicle of a mutant $Nppc^{lbab}/Nppc^{lbab}$ ovary. (**F**) Percentages of oocytes that had resumed meiosis, counted in sections of $Nppc^{wt}/Nppc^{lbab}$ and $Nppc^{lbab}/Nppc^{lbab}$ grafted ovaries. Graph shows mean ± SEM of six ovaries; numbers above bars indicate number of follicles examined. The terms "early" and "late" antral follicles are used as defined by Pedersen and Peters (*15*). Bars, 100 μm.

result from the generation of cGMP by cumulus cells and subsequent transfer to oocytes via gap junctions. Most likely, increased oocyte cAMP resulted from higher amounts of oocyte cGMP suppressing oocyte cAMP phosphodiesterase activity.

If the function of the NPPC/NPR2 pathway is to participate in the maintenance of meiotic arrest, then oocytes within Graafian (large antral) follicles of *Nppc* and *Npr2* mutant mice should exhibit precocious gonadotropin-independent resumption of meiosis. Ovaries were removed from 22- to 24-day-old $Npr2^{cn\text{-}2J}/Npr2^{cn\text{-}2J}$ homozygous mutant and $Npr2^{wt}/Npr2^{?}$ control mice 44 hours after injection of equine chorionic gonadotropin (eCG) to promote follicular development and prepared for histological analysis. Because homozygous $Nppc^{lbab}/Nppc^{lbab}$ mice exhibit early postnatal lethality, ovaries of 5-day-old mutant and wild-type control mice were grafted to the kidney capsules of immunodeficient CBySmn.CB17-$Prkdc^{scid}$/J ovariectomized adult mice, a procedure that supports ovarian growth and development. Ovaries were removed 30 days later. The percentages of germinal vesicle (GV) intact (meiosis arrested) and germinal vesicle breakdown (GVBD, meiosis resumed) oocytes in antral follicles were determined by examining serial sections. There were no major morphological differences in ovarian histology in wild-type or mutant ovaries (see low-magnification images in fig. S2). Oocytes in early antral follicles of both mutant ovaries were at the GV stage, the same as in the wild-type controls. However, whereas oocytes in Graafian (late antral) follicles in control ovaries were maintained at the GV stage, 50% of oocytes in $Nppc^{lbab}/Nppc^{lbab}$ and 80% of oocytes in $Npr2^{cn\text{-}2J}/Npr2^{cn\text{-}2J}$ mutant late antral follicles had resumed meiosis (Fig. 3). The finding that the precocious resumption of meiosis phenotype is expressed by only 50% of the oocytes in ovaries of the *Nppc* mutant is likely because $Nppc^{lbab}$ is a hypomorphic mutation, producing a peptide with slight guanylyl cyclase–stimulating activity (*12*). Also, NPPC may circulate in the normal mouse recipients for the mutant ovarian grafts. Cumulus cells in mutant ovaries were tightly packed around maturing oocytes and showed no evidence of cumulus expansion, which would be indicative of gonadotropin-stimulated maturation. Therefore, NPPC and its receptor NPR2 play a major role in maintaining meiotic arrest.

Higher expression of transcripts in cumulus cells than in mural granulosa cells often indicates that oocyte-derived paracrine factors promote cumulus cell expression (*13*). Therefore, the possible role of oocyte-derived paracrine factors in regulating levels of *Npr2* mRNA in cumulus cells was determined. Microsurgical extirpation of oocytes from complexes (oocytectomy, OOX) significantly reduced expression of *Npr2* mRNA in cumulus cells (Fig. 1C). Coculture of cumulus cells with fully grown denuded oocytes (two oocytes/μl) restored levels of *Npr2* mRNA to that observed in intact complexes (Fig. 1C). Therefore, levels of *Npr2* mRNA in cumulus cells are regulated, at least in part, by oocyte-derived paracrine factors. GDF9, BMP15, and FGF8B are paracrine growth factors secreted by oocytes (*14*). Each of these alone only slightly promoted expression of *Npr2* mRNA by cumulus cells in vitro (Fig. 1D). However, combinations of BMP15 + GDF9, BMP15 + FGF8B, or all three proteins promoted levels of *Npr2* mRNA expression in cumulus cells equivalent to those promoted by coculture with cumulus cell–denuded oocytes (Fig. 1D).

Cumulus cells function to support oocyte development, whereas mural granulosa cells have important endocrine functions and become corpora luteal cells after ovulation. Oocyte-derived paracrine factors regulate cumulus cell expression of transcripts at levels different from those in mural granulosa cells (*13*). Thus, the two populations of granulosa cells have distinct roles, and the oocyte profoundly affects the differentiation of cumulus cells to promote its own development. This study demonstrates a complex regulatory network among mural granulosa cells, cumulus cells, and oocytes before the LH surge, one that is essential for maintaining oocyte meiotic arrest.

On the basis of findings presented here and key studies by others, we put forward the following model for the maintenance of meiotic arrest in fully grown mammalian oocytes (Fig. 4). Oocyte cAMP is crucial for maintaining meiotic arrest and is generated by oocyte adenylyl cyclase, which is controlled by the constitutive action of GPR3 and GPR12 via G_s protein (*3*, *4*). Inhibition of oocyte cAMP-phosphodiesterase (PDE3A) activity is essential for sustaining elevated cAMP concentrations (*6*). Cyclic GMP diffuses into the oocyte from companion cumulus cells via gap junctions and inhibits oocyte PDE3A activity and cAMP hydrolysis and maintains meiotic arrest (*7*, *8*). We show here that NPPC produced by follicular mural granulosa cells stimulates the generation of cGMP by cumulus cell NPR2. Oocytes themselves participate in this meiosis-arresting pathway not only by producing cAMP, but also by promoting cumulus cell expression of NPR2 receptors, which generate the cGMP needed to inhibit oocyte PDE3A activity and thereby maintain meiotic arrest.

References and Notes

1. G. Pincus, E. V. Enzmann, *J. Exp. Med.* **62**, 665 (1935).
2. R. G. Edwards, *Nature* **208**, 349 (1965).
3. L. M. Mehlmann *et al.*, *Science* **306**, 1947 (2004).
4. M. Hinckley, S. Vaccari, K. Horner, R. Chen, M. Conti, *Dev. Biol.* **287**, 249 (2005).
5. C. Ledent *et al.*, *Proc. Natl. Acad. Sci. U.S.A.* **102**, 8922 (2005).
6. F. J. Richard, A. Tsafriri, M. Conti, *Biol. Reprod.* **65**, 1444 (2001).
7. S. Vaccari, J. L. Weeks 2nd, M. Hsieh, F. S. Menniti, M. Conti, *Biol. Reprod.* **81**, 595 (2009).
8. R. P. Norris *et al.*, *Development* **136**, 1869 (2009).
9. Y.-Q. Su *et al.*, *Development* **135**, 111 (2008).
10. M. Jankowski *et al.*, *Biol. Reprod.* **56**, 59 (1997).
11. J. Törnell, B. Carlsson, H. Billig, *Endocrinology* **126**, 1504 (1990).
12. T. Tsuji *et al.*, *Biochem. Biophys. Res. Commun.* **376**, 186 (2008).
13. F. J. Diaz, K. Wigglesworth, J. J. Eppig, *J. Cell Sci.* **120**, 1330 (2007).
14. K. Sugiura *et al.*, *Development* **134**, 2593 (2007).
15. T. Pedersen, H. Peters, *J. Reprod. Fertil.* **17**, 555 (1968).

16. We thank G. Cox, T. Gridley, and M. A. Handel for comments in preparation of the manuscript and L. Jaffe for helpful discussions. J.J.E., K.S., and Y.-Q.S. were supported by grants HD23839 and HD21970 from Eunice Kennedy Shriver National Institute of Child Health and Human Development. M.Z. and G.X. received support from National Basic Research Program of China (grants 2007CB947401 and 2006CB504003) and grant 2009SKLAB07-5 from State Key Laboratory for Agrobiotechnology of China. We also thank M. Mazuk, Baylor College of Medicine, for providing GDF9 and BMP15 and M. O'Brien and K. Wigglesworth for technical assistance.

Supporting Online Material

www.sciencemag.org/cgi/content/full/330/6002/366/DC1
Materials and Methods
Figs. S1 and S2
Table S1
References

10 June 2010; accepted 31 August 2010
10.1126/science.1193573

Dom34:Hbs1 Promotes Subunit Dissociation and Peptidyl-tRNA Drop-Off to Initiate No-Go Decay

Christopher J. Shoemaker, Daniel E. Eyler, Rachel Green*

No-go decay (NGD) is one of several messenger RNA (mRNA) surveillance systems dedicated to the removal of defective mRNAs from the available pool. Two interacting factors, Dom34 and Hbs1, are genetically implicated in NGD in yeast. Using a reconstituted yeast translation system, we show that Dom34:Hbs1 interacts with the ribosome to promote subunit dissociation and peptidyl-tRNA drop-off. Our data further indicate that these recycling activities are shared by the homologous translation termination factor complex eRF1:eRF3, suggesting a common ancestral function. Because Dom34:Hbs1 activity exhibits no dependence on either peptide length or A-site codon identity, we propose that this quality-control system functions broadly to recycle ribosomes throughout the translation cycle whenever stalls occur.

The quality of actively translated mRNA is monitored through multiple cellular mechanisms including nonsense-mediated decay (NMD) (*1*), non-stop decay (NSD) (*2*, *3*), and no-go decay (NGD) (*4*). NMD and NSD target transcripts containing premature stop codons or lacking stop codons, respectively. The in vivo targets of NGD are poorly characterized, but appear to include a broad range of stalled translation complexes containing, for example, mRNAs with

inhibitory secondary structure (*4*), chemical damage (*5*), premature stop or rare codons (*4*), or ribosomal defects [a process more broadly referred to as nonfunctional ribosome decay (NRD)] (*6*, *7*).

In *Saccharomyces cerevisiae*, two proteins, Dom34 (Pelota in higher eukaryotes) and Hbs1, were previously implicated in the endonucleolytic event characteristic of NGD (*4*), although neither factor directly catalyzes this cleavage (*8*). These proteins associate both in vivo (*9*) and in vitro (*10*), and although neither protein is essential in yeast, both deletion strains (*DOM34*Δ and *HBS1*Δ) exhibit synthetic growth defects with strains lacking a subset of 40*S* ribosomal subunit proteins (*9*), suggesting involvement in a common process. Dom34 is evolutionarily related to the eukaryotic translation termination factor eRF1, with two notable differences: The central domain of Dom34 lacks the conserved Gly-Gly-Gln (GGQ) motif required for catalysis of peptide release, and the N-terminal domain of Dom34 lacks the Asn-Ile-Lys-Ser (NIKS) motif involved in codon recognition (fig. S1) (*10*–*12*). Hbs1 exhibits substantial sequence identity to eRF3-related guanosine triphosphatases, including eEF1a, which delivers aminoacylated-tRNA to the A site of the ribosome, and Ski7, a factor implicated in NSD in yeast (*3*, *11*). These observations suggested that a Dom34:Hbs1 complex may directly engage the ribosome (similar to eRF1:eRF3) to initiate the events of NGD that ultimately result in mRNA degradation.

To determine whether Dom34:Hbs1 productively interacts with the ribosome, we measured the guanosine 5′-triphosphate (GTP) hydrolysis activity of purified recombinant protein (fig. S2) in the presence or absence of *S. cerevisiae* ribosomal subunits (*13*). Robust hydrolysis occurred only when both Dom34 and Hbs1 were incubated together with both ribosomal subunits (40*S* and 60*S*) (Fig. 1A). This activity parallels the stimulation observed with the homologous translation termination factors eRF1 and eRF3 (*14*). To further characterize the reaction catalyzed by Dom34:Hbs1 on eukaryotic ribosomes, we used an in vitro–reconstituted yeast translation system (*13*, *15*). Programmed complexes were typically composed of 80*S* ribosomes stalled on a defined mRNA with a peptidyl-tRNA in the P site, and either a sense or a stop codon poised in the A site (for "elongation" and "termination" complexes, respectively). We followed the fate of various components by labeling the peptidyl-tRNA either on the peptide moiety (with ^{35}S-methionine) or on the P-site tRNA itself (with ^{32}P at the terminal adenosine) (Fig. 1B).

Radiolabeled dipeptidyl 80*S* termination complexes were treated with either eRF1:eRF3:GTP

Howard Hughes Medical Institute and Department of Molecular Biology and Genetics, Johns Hopkins University School of Medicine, Baltimore, MD 21205, USA.

*To whom correspondence should be addressed. E-mail: ragreen@jhmi.edu

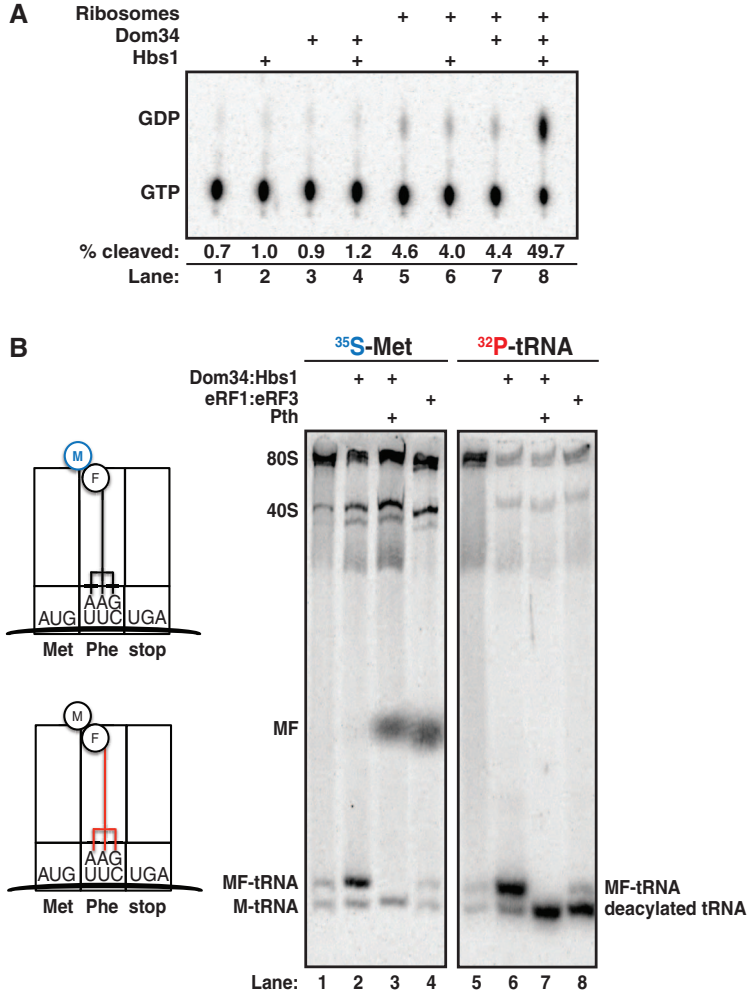

Fig. 1. (**A**) Ribosome stimulation of GTP hydrolysis by Dom34:Hbs1 as visualized by thin-layer chromatogram. (**B**) Native gel analysis of ribosomal termination complexes incubated with indicated components. Stylized diagrams of differentially labeled [^{35}S-Met (blue) or ^{32}P[CCA]-tRNA (red)] ribosome complexes are on the left. Pth, peptidyl-tRNA hydrolase.

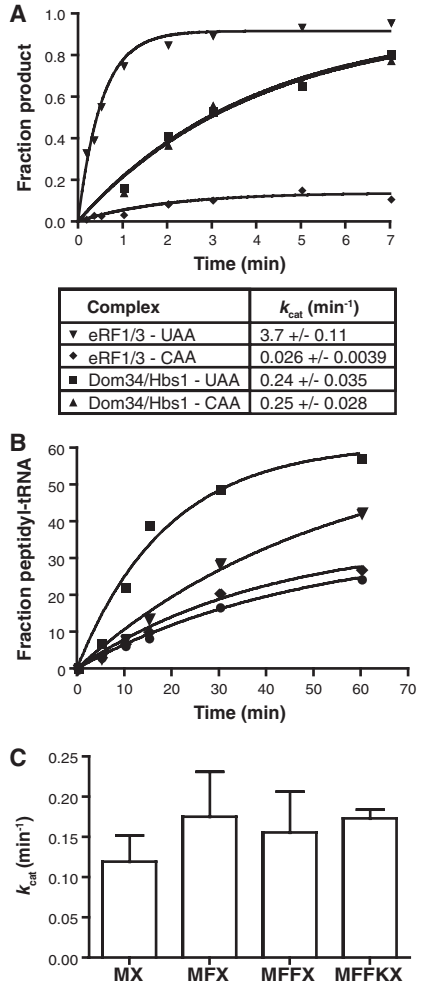

Complex	k_{cat} (min^{-1})
▼ eRF1/3 - UAA	3.7 +/- 0.11
◆ eRF1/3 - CAA	0.026 +/- 0.0039
■ Dom34/Hbs1 - UAA	0.24 +/- 0.035
▲ Dom34/Hbs1 - CAA	0.25 +/- 0.028

Fig. 2. Effects of codon identity and peptide length on Dom34:Hbs1-mediated peptidyl-tRNA release activity. (**A**) Kinetics of release reactions mediated by Dom34:Hbs1 and eRF1:eRF3 on UAA and CAA A-site–programmed ribosome complexes. k_{cat} values are the means ± SD (n = 3). (**B**) Inhibition of Dom34:Hbs1-mediated reaction by a release-defective eRF1 variant [eRF1(AGQ)] on UAA-programmed ribosomes. (■) Dom34/Hbs1 only; (▼) +5 μM eRF1 (AGQ); (◆) +20 μM eRF1 (AGQ); (●) 20 μM eRF1(AGQ) only. (**C**) Rate constants for Dom34:Hbs1-mediated peptidyl-tRNA release on programmed complexes containing Met-tRNA^{iMet}, di-, tri-, or tetra-peptidyl tRNA in the P site (n = 4, ±SD).

or Dom34:Hbs1:GTP, and the products of the reaction were followed by native gel electrophoresis (*16*). eRF1:eRF3:GTP ternary complex promoted the release of two distinct species from 80*S* complexes: ^{35}S-Met-Phe dipeptide (Fig. 1B, lane 4) and ^{32}P-deacylated-tRNA^{Phe} (Fig. 1B, lane 8). By contrast, Dom34:Hbs1:GTP ternary complex promoted the release of a distinct product that migrated at the same position under both labeling conditions (Fig. 1B, lanes 2 and 6), suggesting that it represented intact peptidyl-tRNA. This was confirmed by treatment with recombinant peptidyl-tRNA hydrolase (Pth) (Fig. 1B, lanes 3 and 7), which produced the predicted shifts in product identity (*17*).

The kinetic parameters of the Dom34:Hbs1-promoted reaction were determined with a Pth-coupled reaction and an electrophoretic thin-layer chromatography system (fig. S3) (*18*). Ribosome termination complexes (containing tripeptidyl-tRNA in the P site and a stop codon in the A site) were treated with various factors, and the rate constants for the corresponding reactions were determined. The rate constant for peptide release by eRF1:eRF3 was about 3.7 min^{-1} [as previously reported in the yeast system (*15*)], whereas that of Dom34:Hbs1-promoted peptidyl-tRNA release was slower by a factor of ~15 (Fig. 2A), in a reaction that was dependent on the presence of both factors (fig. S4). Notably, the rate of peptidyl-tRNA hydrolysis by Pth substantially exceeds that of the Dom34:Hbs1-catalyzed peptidyl-tRNA release from the ribosome (fig. S5). As previously observed for eRF1:eRF3 (*19*), catalysis by Dom34:Hbs1 was strongly inhibited in the presence of the nonhydrolyzable GTP analog, GDPNP. The observed inhibition of product formation by both GDPNP and heat inactivation of Dom34:Hbs1 (fig. S6) excludes the uninteresting possibility that nonspecific ribosome dissociation might account for the observed peptidyl-tRNA release.

To test the specificity of these reactions, we compared the reactivity of Dom34:Hbs1 on complexes containing stop (UAA) or non-stop (CAA) codons in the A site. eRF1:eRF3 exhibits a high degree of specificity for stop codons relative to near-stop with rate constants for peptide release differing by about two orders of magnitude (Fig. 2A). By contrast, Dom34:Hbs1 exhibits no specificity for these complexes as the rate constants (and reaction endpoints) are indistinguishable (Fig. 2A). Given the codon-independent nature of the Dom34:Hbs1 reaction, we wanted to confirm that these factors engage the A site of the ribosome. This was accomplished by successfully competing Dom34:Hbs1 activity on termination complexes with increasing amounts of a catalytically inactive eRF1 variant, eRF1(AGQ) (*20*) (Fig. 2B).

Based on the known activities of other A-site–binding factors (e.g., eEF2), we investigated whether Dom34:Hbs1 facilitates a translocation-like process on the ribosome, effectively pushing peptidyl-tRNAs out through the E site. However, because neither length of the peptide (Fig. 2C) nor E-site–bound inhibitors (fig. S7) affected the release reaction, this model seemed unlikely.

A subunit dissociation model was next considered based on the lack of influence of peptide length on the peptidyl-tRNA release reaction, and the likely difficulty of directly releasing such topologically constrained species from intact 80*S* particles. Subunit dissociation was followed with ribosome termination complexes containing either ^{32}P-labeled 40*S* subunits or ^{35}S-Met–labeled peptidyl-tRNA. eIF6, a yeast protein known to bind to the interface region of the 60*S* subunit, served as an anti-association factor that "trapped" dissociation events (*21*, *22*). Indeed, subunit dissociation was promoted by Dom34:Hbs1 (Fig. 3A, lane 5) and correlated nicely with peptidyl-tRNA release activity (Fig. 3A, lane 2). Both reactions were inhibited by the addition of GDPNP (Fig. 3A, lanes 3 and 6) and exhibited similar magnesium dependencies (Fig. 3B). We also followed Dom34:Hbs1-mediated subunit dissocia-

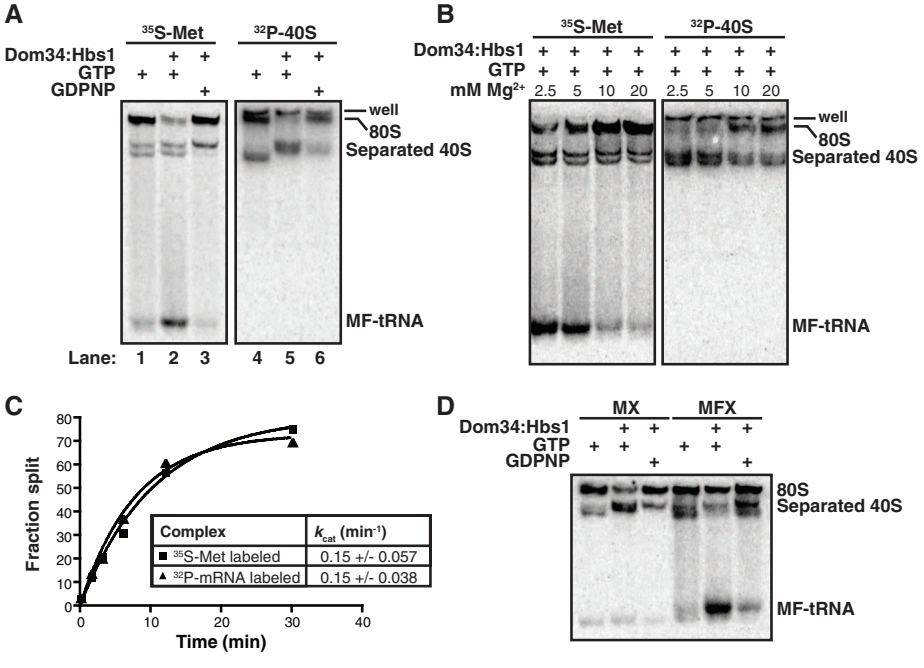

Fig. 3. Dom34:Hbs1 promotes ribosome subunit dissociation. (**A**) Native gel analysis demonstrating GTP dependence of Dom34:Hbs1-mediated products on differentially labeled ribosome complexes. (**B**) Native gel analysis indicating similar magnesium sensitivities for Dom34:Hbs1-mediated formation of peptidyl-tRNA and separation of subunits. (**C**) Rates of peptidyl-tRNA formation and subunit separation are similar. k_{cat} values are the means ± SD (n = 3). (**D**) Native gel analysis reveals distinct products generated from Dom34:Hbs1 treatment of initiation (MX) and elongation (MFX) complexes. Met-tRNA^{iMet} partitions with 40*S* subunits, whereas Met-Phe-peptidyl-tRNA is fully liberated from the ribosome.

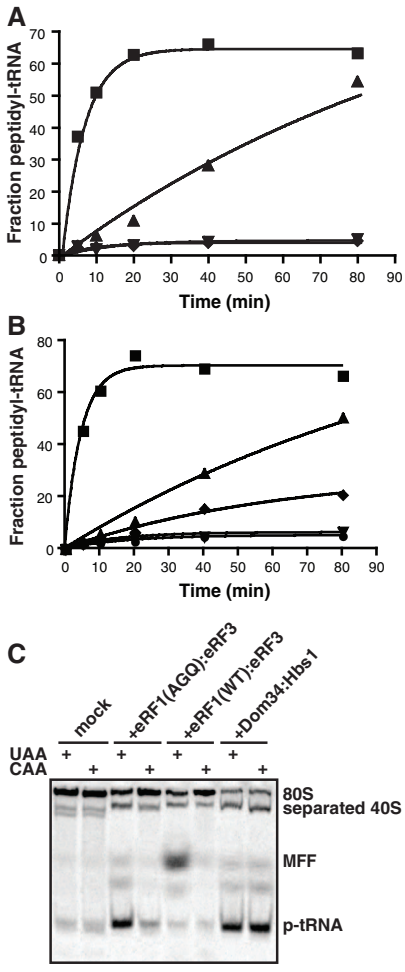

Fig. 4. Intrinsic subunit separation activity associated with eRF1:eRF3. (**A**) Kinetics of peptidyl-tRNA release stimulated by eRF1(AGQ):eRF3. (■) Dom34:Hbs1; (▲) eRF1(AGQ)/eRF3; (▼) mock; (◆) eRF1(AGQ)/eRF3 (GDPNP). (**B**) Stimulation of subunit separation capacity of eRF1(AGQ) by eRF3. (■) Dom34/Hbs1; (▲) eRF1(AGQ)/eRF3; (◆) eRF1(AGQ); (▼) eRF3; (●) mock. (**C**) Native gel analysis of the codon dependence (UAA versus CAA) of eRF1(AGQ):eRF3 recycling activity.

tion using complexes formed with ^{32}P-labeled mRNA and found that the mRNA segregated predominantly with 40*S* subunits (fig. S8), consistent with the previously reported dependence of mRNA dissociation on additional initiation factors (*23*). Additionally, no cleavage of mRNA was observed during Dom34:Hbs1-mediated processes (fig. S9), consistent with an earlier report (*8*).

Because Dom34:Hbs1-driven subunit dissociation and peptidyl-tRNA release are correlated events (Fig. 3, A and B), we sought to determine their order by measuring the rate constants of the two reactions using ribosome complexes containing either ^{32}P-labeled mRNA or ^{35}S-Met–labeled peptidyl-tRNA (Fig. 3C). The observed rate constants for the disappearance of 80*S* ribosomes in a native gel were closely matched (~0.15 min^{-1}) when either the labeled mRNA or peptidyl-tRNA was monitored. These data indicate that subunit dissociation and peptidyl-tRNA formation by Dom34:Hbs1 are tightly coupled to one another, with one likely serving as the rate-limiting step for the other [e.g., (*24*)].

If subunit dissociation occurs first, it seemed possible that an intermediate product might be generated in which subunits have dissociated but peptidyl-tRNA has not yet departed (i.e., peptidyl-tRNA:40*S* subunit conjugates). In a comparison of Dom34:Hbs1 activity on an initiation-like ribosome complex (carrying initiator Met-tRNA^{iMet} in the P site) and on an elongated ribosome complex (carrying Met-Phe-tRNA^{Phe} in the P site), free Met-Phe-tRNA^{Phe} was the predominant product from the Dom34:Hbs1-treated elongated ribosome complex, whereas Met-tRNA^{iMet}–bound 40*S* subunit was the predominant product from the Dom34:Hbs1-treated initiation complexes (Fig. 3D and fig. S10A). The appearance of a Met-tRNA^{iMet}–bound 40*S* complex suggests that subunit separation can take place independently of peptidyl-tRNA release. To confirm that the observed Met-tRNA^{iMet}–bound 40*S* complex represented an authentic stable product of the Dom34:Hbs1-catalyzed reaction, rather than reassociation of Met-tRNA^{iMet} with ribosomes after initial dissociation, we repeated the Dom34:Hbs1-catalyzed reaction in the presence of a large excess of unlabeled Met-tRNA^{iMet} and found that the chase had no effect on the reaction products (fig. S10B). These data are broadly consistent with the previously reported high affinity of 40*S* subunits for Met-tRNA^{iMet} (*25*) and show that the Dom34:Hbs1 complex initially promotes subunit dissociation and that peptidyl-tRNA dissociation typically follows.

Given the structural similarities between Dom34:Hbs1 and eRF1:eRF3, we wondered whether the canonical eukaryotic release factors might also promote subunit separation, independent of peptide release, and thereby contribute to ribosome recycling during termination. Treatment of termination complexes (with ^{35}S-Met–labeled peptidyl-tRNA) with catalytically inactive eRF1(AGQ):eRF3 led to the formation of free peptidyl-tRNA in a reaction inhibited by GDPNP. This activity was distinguished from that promoted by Dom34:Hbs1 only by its slower rate (0.012 min^{-1} versus 0.21 min^{-1}) (Fig. 4A). Like the Dom34:Hbs1-catalyzed reaction, the eRF1(AGQ):eRF3 reaction depended on both protein components for full activity (Fig. 4B). Lastly, we found that eRF1(AGQ):eRF3-mediated peptidyl-tRNA release exhibited robust codon specificity, taking place only when a stop codon was presented in the A site (Fig. 4C).

Canonical recycling, which occurs after termination, involves subunit dissociation, and mRNA and tRNA release, thus allowing for subsequent reinitiation of translation. In bacteria, a specialized ribosome recycling factor, RRF, is central to this GTP-dependent process (*26*). However, in eukaryotes, no RRF has been identified. Our results indicate that eRF1:eRF3 and Dom34:Hbs1 directly destabilize the subunit interface to promote recycling. Although additional factors (including translation elongation factors) appear to promote or accelerate various aspects of recycling in yeast and mammals (*23*, *27*–*29*), our observations could explain why no true RRF homolog is present in eukaryotes where "termination-like" factors instead play the key role in destabilizing the subunit interface. We further argue that Dom34:Hbs1 acts as a specialized recycling factor on malfunctioning ribosome complexes that, for example, do not appropriately engage the next factor in the translation cycle or are inherently defective and thus unable to properly elongate (i.e., NRD) (*6*). Subsequent to Dom34:Hbs1-mediated recycling, kinetic competition between translation reinitiation and mRNA decay (or rRNA decay in the case of NRD) will determine the partitioning of defective RNAs, with the opportunities for degradation accumulating with each passage through the quality-control pathway.

References and Notes

1. S. W. Peltz, A. H. Brown, A. Jacobson, *Genes Dev.* **7**, 1737 (1993).
2. P. A. Frischmeyer *et al.*, *Science* **295**, 2258 (2002).
3. A. van Hoof, P. A. Frischmeyer, H. C. Dietz, R. Parker, *Science* **295**, 2262 (2002).
4. M. K. Doma, R. Parker, *Nature* **440**, 561 (2006).
5. R. Gandhi, M. Manzoor, K. A. Hudak, *J. Biol. Chem.* **283**, 32218 (2008).
6. S. E. Cole, F. J. LaRiviere, C. N. Merrikh, M. J. Moore, *Mol. Cell* **34**, 440 (2009).
7. J. Soudet, J. P. Gélugne, K. Belhabich-Baumas, M. Caizergues-Ferrer, A. Mougin, *EMBO J.* **29**, 80 (2010).
8. D. O. Passos *et al.*, *Mol. Biol. Cell* **20**, 3025 (2009).
9. A. Carr-Schmid, C. Pfund, E. A. Craig, T. G. Kinzy, *Mol. Cell. Biol.* **22**, 2564 (2002).
10. M. Graille, M. Chaillet, H. van Tilbeurgh, *J. Biol. Chem.* **283**, 7145 (2008).
11. G. C. Atkinson, S. L. Baldauf, V. Hauryliuk, *BMC Evol. Biol.* **8**, 290 (2008).
12. H. H. Lee *et al.*, *Mol. Cell* **27**, 938 (2007).
13. M. G. Acker, S. E. Kolitz, S. F. Mitchell, J. S. Nanda, J. R. Lorsch, *Methods Enzymol.* **430**, 111 (2007).
14. L. Frolova *et al.*, *RNA* **2**, 334 (1996).
15. P. Saini, D. E. Eyler, R. Green, T. E. Dever, *Nature* **459**, 118 (2009).
16. M. A. Algire *et al.*, *RNA* **8**, 382 (2002).
17. Z. Vogel, T. Vogel, A. Zamir, D. Elson, *Eur. J. Biochem.* **21**, 582 (1971).
18. E. M. Youngman, J. L. Brunelle, A. B. Kochaniak, R. Green, *Cell* **117**, 589 (2004).
19. E. Z. Alkalaeva, A. V. Pisarev, L. Y. Frolova, L. L. Kisselev, T. V. Pestova, *Cell* **125**, 1125 (2006).
20. L. Y. Frolova *et al.*, *RNA* **5**, 1014 (1999).
21. M. Gartmann *et al.*, *J. Biol. Chem.* **285**, 14848 (2010).
22. K. Si, U. Maitra, *Mol. Cell. Biol.* **19**, 1416 (1999).
23. A. V. Pisarev, C. U. Hellen, T. V. Pestova, *Cell* **131**, 286 (2007).
24. A. Savelsbergh *et al.*, *Mol. Cell* **11**, 1517 (2003).
25. S. E. Kolitz, J. E. Takacs, J. R. Lorsch, *RNA* **15**, 138 (2009).
26. A. V. Zavialov, V. V. Hauryliuk, M. Ehrenberg, *Mol. Cell* **18**, 675 (2005).
27. A. V. Pisarev *et al.*, *Mol. Cell* **37**, 196 (2010).
28. S. Khoshnevis *et al.*, *EMBO Rep.* **11**, 214 (2010).
29. S. Kurata *et al.*, *Proc. Natl. Acad. Sci. U.S.A.* **107**, 10854 (2010).

30. We thank J. Lorsch and his lab members R. Parker and M. Moore for valuable discussions, H. Zaher and N. Guydosh for thoughtful comments on the manuscript, and B. Rogers for cloning and purification of Pth and eIF6.

Supporting Online Material

www.sciencemag.org/cgi/content/full/330/6002/369/DC1
Materials and Methods
Figs. S1 to S10
Tables S1 and S2
References

18 May 2010; accepted 16 August 2010
10.1126/science.1192430

Selection at Linked Sites Shapes Heritable Phenotypic Variation in *C. elegans*

Matthew V. Rockman,[1,2]* Sonja S. Skrovanek,[2,3] Leonid Kruglyak[2,3]*

Mutation generates the heritable variation that genetic drift and natural selection shape. In classical quantitative genetic models, drift is a function of the effective population size and acts uniformly across traits, whereas mutation and selection act trait-specifically. We identified thousands of quantitative trait loci (QTLs) influencing transcript abundance traits in a cross of two *Caenorhabditis elegans* strains; although trait-specific mutation and selection explained some of the observed pattern of QTL distribution, the pattern was better explained by trait-independent variation in the intensity of selection on linked sites. Our results suggest that traits in *C. elegans* exhibit different levels of variation less because of their own attributes than because of differences in the effective population sizes of the genomic regions harboring their underlying loci.

Some phenotypes exhibit abundant heritable variation and others almost none. As heritable variation is the raw material for adaptation, the forces that shape its distribution across traits are a central concern of evolutionary genetics (*1*). Among wild strains of the partially

selfing nematode *Caenorhabditis elegans*, transcript abundance traits—model quantitative phenotypes (*2*–*7*)—differ in their levels of heritable variation (*4*, *8*) and, on the basis of experimental measurements of the rate at which mutation increases their variance, they exhibit lower levels of heritable variation than expected under neutral mutation-drift equilibrium (*4*). These findings and similar results in other species are consistent with the prediction that trait-dependent stabilizing selection should result in different levels of variation among traits (*3*–*7*).

To genetically dissect the causes of different variabilities among *C. elegans* traits, we measured transcript abundances by microarray in developmentally synchronized young adult hermaphrodites of 208 recombinant inbred advanced intercross lines from a cross between the laboratory strain, N2, and a wild isolate from Hawaii, CB4856 (*9*). These strains, though relatively divergent for *C. elegans*, are closely related, differing at roughly 1 base pair per 900 (*10*). Each line was genotyped at 1455 single-nucleotide polymorphism (SNP) markers. Interval mapping for each of 15,888 traits identified 2309 quantitative trait loci (QTLs) at a false discovery rate (FDR) of 5% (Fig. 1A) (*11*).

The majority of QTLs (65%) are local; that is, these QTLs occur at the genomic locations of the genes whose transcript abundances they influence [the spatial coincidence is defined here by overlap between the l-lod (logarithm of the odds ratio for linkage) QTL support interval and the gene]. Nearly a quarter of the remaining QTLs (distant QTLs) map to three statistically robust hotspots (*11*) (Fig. 1A and fig. S1). The X-linked hotspot encompasses more than a megabase and probably contains multiple causal variants, one of which may be the known pleiotropic mutation of phenylalanine to valine at residue 215 in the neuropeptide receptor *npr-1* (*12*). Candidate genes for the other hotspots include *Y17G9B.8*, a putative component of a chromatin regulatory complex whose transcript abundance maps strongly to a local QTL at its position in the hotspot on the left side of chromosome IV, and *Y105C5A.15*, a putative zinc-finger transcription factor whose transcript abundance maps locally to a QTL at its position in the hotspot on the right side of chromosome IV.

The global distribution of QTLs is markedly nonuniform. Both local and distant QTLs are strongly enriched in the arms of the chromosomes relative to the centers (Table 1). *C. elegans* lacks heterochromatic centromeres, and the chromosomes are structured in semidiscrete domains that exhibit correlated variation in gene density, evolutionary conservation, repeat sequence density, and recombination rate (*9*, *13*, *14*). The chromosomal centers have high gene density and low recombination rates, whereas chromosome arms have lower gene density and higher recombination rates. Chromosome tips have an intermediate gene density but effectively no recombination (*9*). Under a simple mutational null model, QTL density is expected to correlate with the density

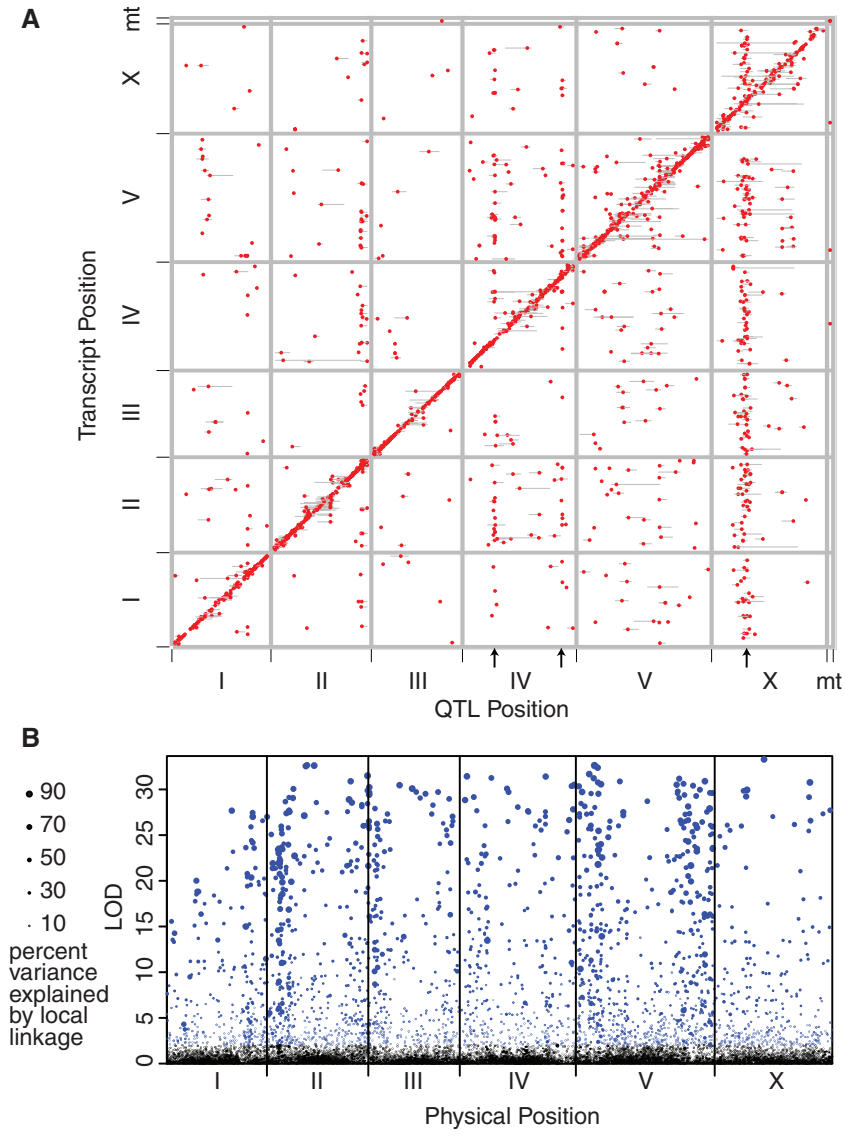

Fig. 1. (**A**) QTLs for each transcript abundance phenotype, significant at an FDR of 5%, are plotted in rows located at the genomic positions of the transcripts. Gray bars represent 1-lod support intervals. The diagonal includes local QTLs, those that colocalize with the transcript they affect. Three robust QTL hotspots are indicated with arrows. (**B**) Local lod score is plotted for each probe at its physical position along the chromosomes. Points in blue are significant at a 5% FDR according to a single-marker linkage test. Points are scaled according to the fraction of variance in transcript abundance explained by the local QTL.

Table 1. Both distant and local QTLs are overrepresented in chromosome arms relative to centers.

Domain	Distant QTLs	Local QTLs	Genome	Probes
Tip	25 (3.1%)	93 (6.2%)	7.4 Mb (7.3%)	987 (6.2%)
Arm	508 (62.5%)	935 (62.5%)	45.9 Mb (45.8%)	6049 (38.1%)
Center	277 (34.1%)	466 (31.1%)	47.0 Mb (46.9%)	8843 (55.7%)
Mitochondrial	3 (0.4%)	2 (0.1%)	0.014 Mb (0.01%)	9 (0.1%)
Total	813	1496	100.3 Mb (100%)	15888

[1]Department of Biology and Center for Genomics and Systems Biology, New York University, 100 Washington Square East, New York, NY 10003, USA. [2]Lewis-Sigler Institute for Integrative Genomics and Department of Ecology and Evolutionary Biology, Carl Icahn Laboratory, Princeton University, Princeton, NJ 08544, USA. [3]Howard Hughes Medical Institute, Princeton University, Princeton, NJ 08544, USA.

*To whom correspondence should be addressed. E-mail: mrockman@nyu.edu (M.V.R.); leonid@genomics.princeton.edu (L.K.)

of potentially functional sites and hence to be higher in chromosomal centers than in arms, contrary to the observed pattern. Furthermore, as QTL detection is most favored in low-recombination areas (*15*, *16*), the observed pattern also runs counter to the expected effect of mapping bias.

The chromosomal patterning of causal variants is particularly pronounced for local QTLs, which we confirmed in a focused single-marker analysis (*17*), which increased detection power over our initial genome scan. We identified 2538 transcripts affected by QTLs that are linked to their own genomic locations at a 5% FDR (Fig. 1B). We found that 23.7% of transcripts in chromosome arms and 20.1% of those in chromosome tips have local QTLs, compared to only 10.2% of those in chromosome centers (χ^2_2 = 495.7, $P < 10^{-107}$). The chromosomal patterning is robust to confounding by potential hybridization artifacts, as demonstrated by analysis of only the 7694 transcripts for which the CB4856 genotype is associated with higher expression than the reference N2 genotype. The 1057 significant local QTLs among these exhibit the same pattern of enrichment: 20.0% of arm transcripts, 17.9% of tip transcripts, and 9.6% of center transcripts have significant local QTLs (χ^2_2 = 162.7, $P < 10^{-35}$).

We corroborated the results of linkage mapping by estimating the amount of heritable phenotypic variation attributable to each type of chromosomal domain, using a genome-partitioning approach that avoids assumptions about the number, location, and effect sizes of QTLs (*11*, *18*). We estimated the amount of genetic variance attributable to chromosomal arms versus centers for each of the 1191 traits that are significantly heritable by this method (FDR = 0.05; fig. S2), and we observed an excess of both arm-biased and center-biased traits (fig. S3), consistent with contributions from large-effect or spatially clustered loci. A significant majority of heritable traits are arm-biased (permutation two-tailed P = 0.0325). The arm bias remains when the effects of local QTLs are removed by linear regression ($P \leq 0.0025$), and the pattern is not driven by the QTL hotspots (*11*) (fig. S7).

Several nonexclusive models may explain global patterns of variation in the density of functional variants influencing transcript abundance traits (*1*, *3*–*7*, *19*–*21*). In standard multivariate quantitative genetic models, equilibrium trait

Table 2. Logistic regression models implicate mutation, stabilizing selection, and linked selection in explaining the distribution of local linkages. LRT: likelihood ratio test statistic comparing the logistic regression model in which the specified term has been dropped to the model in which all terms are included. LRT is equivalent to the drop in explained deviance due to excluding the term from the model. The null deviance is 12897.5. The LRT was tested against a χ^2 distribution to yield the associated P values. Δdf: difference in degrees of freedom between the specified model and the null model, including only the intercept. Chromosomal domain is a factor with three levels and hence contributes two degrees of freedom. AIC: Akaike information criterion. Model 4 includes all two-, three-, and four-way interactions among the variables. Consequently the LRT and P values for dropping single terms cannot be calculated.

	Model 1		Model 2		Model 3		Model 4	
	LRT	$-\log_{10}(P)$	LRT	$-\log_{10}(P)$	LRT	$-\log_{10}(P)$	LRT	$-\log_{10}(P)$
Gene size	149	33.5	38.7	9.30	–	–	X	X
RNAi	13.1	3.5	10.8	3.00	–	–	X	X
Conservation	222.6	49.6	81.6	18.77	–	–	X	X
Distant linkage	36.2	8.7	35.1	8.51	–	–	X	X
Interaction terms	–	–	–	–	–	–	X	X
Recombination rate	–	–	–	–	–	–	–	–
Chromosomal domain	–	–	263.1	57.12	444.8	96.59	–	–
Background selection	–	–	–	–	–	–	–	–
Explained deviance	337.8		600.9		444.8		370.6	
Residual deviance	12,559.7		12,296.6		12,452.7		12,526.9	
Δdf	4		6		2		15	
AIC	12,569.7		12,310.6		12,458.7		12,558.9	

	Model 5		Model 6		Model 7		Model 8	
	LRT	$-\log_{10}(P)$	LRT	$-\log_{10}(P)$	LRT	$-\log_{10}(P)$	LRT	$-\log_{10}(P)$
Gene size	121.9	27.62	38.4	9.23	22.6	5.71	22.5	5.68
RNAi	14.4	3.83	11.1	3.06	11.8	3.23	11.9	3.25
Conservation	193.6	38.94	81.6	18.78	44.2	10.54	44	10.49
Distant linkage	35.9	8.68	35.1	8.50	33.4	8.12	33.3	8.11
Interaction terms	–	–	–	–	–	–	–	–
Recombination rate	52.1	12.27	1.2	0.56	–	–	–	–
Chromosomal domain	–	–	212.2	46.07	–	–	0.3	0.06
Background selection	–	–	–	–	363.6	80.32	100.7	22.98
Explained deviance	389.9		602.1		701.4		701.6	
Residual deviance	12,507.6		12,295.4		12,196.1		12,195.9	
Δdf	5		7		5		7	
AIC	12,519.6		12,311.4		12,208.1		12,211.9	

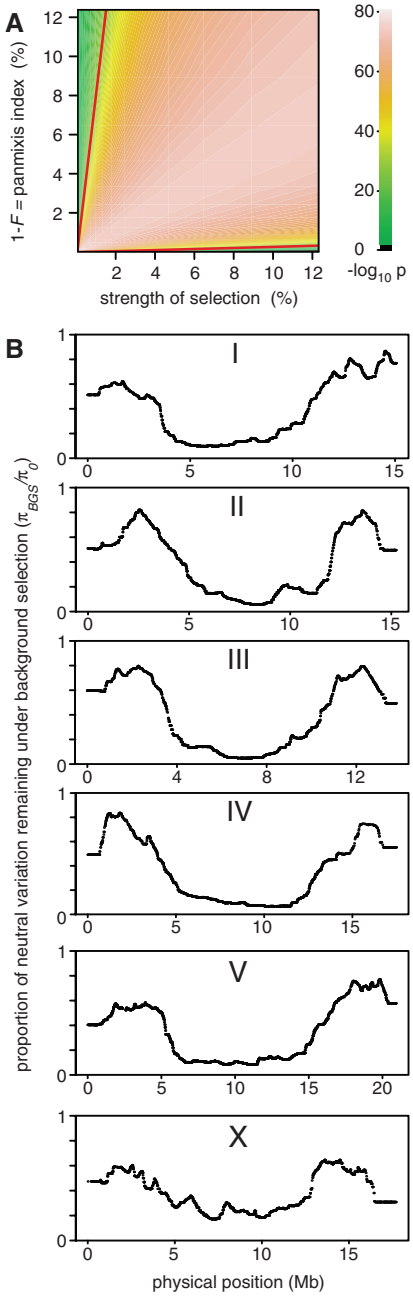

Fig. 2. (**A**) The significance of background selection in a logistic regression model (which includes gene-specific mutation and selection variables) is plotted as a function of the index of panmixis and strength of selection against deleterious mutations. Background selection is significant at $P < 0.01$ across all but a small slice of parameter space corresponding to very low rates of outcrossing (black). The red lines bracket the region of parameter space over which background selection explains more of the local linkage probability than any other variable in the model. See fig. S4. (**B**) Effects of background selection on levels of variation along the chromosomes under the best-fitting background selection model.

variation results from mutation, selection, and drift, the last governed by effective population size (N_e) and acting uniformly across traits (*22*). We asked whether mutation and selection could explain why some transcript abundance traits are influenced by their own genomic loci and why others are not. We focused on these local QTLs because they represent largely independent genetic variants, are precisely localized, and account for a large fraction of the phenotypic variance in traits with local QTLs (Fig. 1B).

Variation in local QTL density should reflect variation in rates of local mutational input. In *C. elegans*, the rate of spontaneous single-base mutation has been directly measured and is uniform on a chromosomal scale, with no dependence on recombination rate or domain structure (*23*). Consequently, the rate of mutation that generates local QTLs probably depends on the local mutational target size. Indeed, genes with local QTLs are longer than those without (*t* test on log-transformed lengths, $P = 0.004$).

Variation in QTL density should also reflect variation in the intensity of purifying selection, which eliminates mutations that adversely affect the phenotype. We used measurable correlates of purifying selection to test this model. Genes that exhibit phenotypes when their expression is knocked down by RNA interference (RNAi) [effectively essential genes; nearly all characterized RNAi phenotypes would be lethal in nature (*11*)] are less likely to have local QTLs than genes with no RNAi phenotype ($\chi^2 = 55.1$, $P < 2 \times 10^{-13}$). Moreover, we observed fewer evolutionarily constrained nucleotides in genes with local QTLs [(*11*); genes include introns and flanking sequence] than in genes without (*t* test on Box-Cox transformed values, $P < 4 \times 10^{-23}$).

Phenotypic variance not attributable to local QTLs, including measurement error and environmental variance as well as distant genetic effects, does not differ significantly between transcripts with and without local QTLs (*t* test on log-transformed data, $P = 0.93$). However, traits with local QTLs are more likely than traits without to also map to additional QTLs ($\chi^2 = 63.2$, $P < 2 \times 10^{-15}$). Thus, traits that can withstand local genetic variation can also withstand other genetic perturbations, consistent with these transcript abundances experiencing weaker stabilizing selection compared to other genes.

To determine whether the variables associated with mutational target size and strength of selection have independent effects on local QTL probability, we tested their explanatory value in multiple logistic regression models. Gene interval length, number of conserved bases, RNAi phenotype, and presence of distant QTLs are all significant predictors of local QTL probability in a model that includes them all (model M1 in Table 2).

However, when the chromosomal domain of each gene (tip, arm, or center) was included as a factor (model M2), it was by far the most explanatory variable. Indeed, chromosomal domain alone (model M3) explained the QTL data better than a model incorporating all of the gene-level attributes, even when all interactions among the variables were included (model M4). Genic point estimates of the recombination rate, although significant if domain type was excluded (model M5), had no significant explanatory value after taking the domains into account (M6). Thus, the domain patterning of local QTLs is not explained by gene-level measures of mutation, selection, or recombination.

Although the effective population size (N_e), which governs genetic drift, is shared by all measured traits, natural selection can cause variation in apparent N_e along the genome. Selection—positive or negative—causes alleles in future generations to be descended from a smaller subset of current alleles than would occur without selection, decreasing the N_e of the linked genomic interval (*24*–*26*). In *C. elegans*, high levels of self-fertilization reduce the effective recombination rate, increasing the effect of selection at linked sites on standing variation at the level of sequence polymorphism (*23*, *27*–*29*).

In primarily selfing species with small effective population sizes, such as *C. elegans*, background selection, the reduction in neutral variation due to linkage between neutral variants and deleterious mutations undergoing deterministic elimination from the population (*26*), is likely to be the predominant form of linked selection (*28*, *30*), and it provides a parsimonious explanation for patterns of variation given the certainty that deleterious mutations arise and are eliminated by selection. Although hitchhiking due to positive selection may also be operating, data from *C. briggsae*, a nematode that shares *C. elegans*'s mating system, strongly favor background selection over the alternative models of selection at linked sites (*30*). Under background selection, the level of neutral variation at a gene is a function of the number of linked sites susceptible to deleterious mutation and the effective rate of recombination between each such site and the gene. We fitted an explicit model of background selection to each gene (*26*, *31*), estimating the physical distribution of deleterious mutations from comparative genomic data and considering a range of values for two poorly constrained parameters: the strength of selection against deleterious mutations and the inbreeding coefficient, F, whose complement ($P = 1 - F$) rescales the meiotic recombination rate to yield the effective rate in partially selfing species (*11*).

Background selection was a highly significant ($P < 10^{-80}$, model M7) predictor of local QTL probability in logistic regression analyses that include all of the gene-specific mutation and selection variables, and it entirely accounts for the effect of domain type (model M8). Background selection accounts for more of the explained deviance than all gene-specific variables combined, across nearly all of the parameter space of inbreeding and selection intensity (Fig. 2A and fig. S4).

These results were robust to variation in deleterious mutation rate, alternative treatments of the genetic map and genic variables, different significance thresholds for linkage, alternative modeling methods, and exclusion of all genes susceptible to hybridization artifacts (fig. S5). Although our model omits the effects of Hill-Robertson interference between linked mutations, such effects are expected to operate primarily as a scaling factor on the expected reduction in variation due to background selection (*32*). The background selection model that best explains the data predicts high levels of neutral variation on the chromosome arms and low levels in the centers (Fig. 2B). The low-recombination chromosome tips are more similar to the high-recombination arms than to the low-recombination centers because they are linked to deleterious mutations only on one side.

Although the effects of selection on linked neutral nucleotide polymorphism are widely recognized, we have shown that such selection at linked sites is also a major factor shaping heritable phenotypic variation. Consequently, quantitative genetic models predicated on uniform effects of genetic drift across traits are not valid in *C. elegans*.

Transcript abundances in *C. elegans*, as in other species, are undoubtedly shaped by trait-specific mutation rates and selection pressures (*3*–*7*, *19*–*21*). At the global level, however, the propensity of traits to vary in *C. elegans* is explained by processes independent of the functions of the individual transcripts. These findings provide an alternative explanation for the observed discordance between standing phenotypic variation in *C. elegans* and that predicted from neutral mutation-drift equilibrium (*4*). It may also explain the fine-scale correlation between cis-acting regulatory polymorphism and gene density in humans (*20*).

Natural selection and quantitative genetic analyses both rely on replicated measurements of the marginal effects of alleles across randomized genetic backgrounds. We have used quantitative genetics in *C. elegans* to show that randomization in this partially selfing species is ineffective, diminishing the ability of natural selection to evaluate individual alleles. Consequently the evolutionary fates of alleles—and hence phenotypes—are determined less by their own effects than by the genomic company they keep.

References and Notes

1. D. Houle, *Genetica* **102–103**, 241 (1998).
2. R. B. Brem, L. Kruglyak, *Proc. Natl. Acad. Sci. U.S.A.* **102**, 1572 (2005).
3. S. A. Rifkin, J. Kim, K. P. White, *Nat. Genet.* **33**, 138 (2003).
4. D. R. Denver *et al.*, *Nat. Genet.* **37**, 544 (2005).
5. J. Ronald, J. M. Akey, *PLoS ONE* **2**, e678 (2007).
6. C. R. Landry, B. Lemos, S. A. Rifkin, W. J. Dickinson, D. L. Hartl, *Science* **317**, 118 (2007).
7. J. C. Fay, P. J. Wittkopp, *Heredity* **100**, 191 (2008).
8. Y. Li *et al.*, *PLoS Genet.* **2**, e222 (2006).
9. M. V. Rockman, L. Kruglyak, *PLoS Genet.* **5**, e1000419 (2009).

10. S. R. Wicks, R. T. Yeh, W. R. Gish, R. H. Waterston, R. H. Plasterk, *Nat. Genet.* **28**, 160 (2001).
11. Information on materials and methods is available on *Science* Online.
12. M. de Bono, C. I. Bargmann, *Cell* **94**, 679 (1998).
13. T. M. Barnes, Y. Kohara, A. Coulson, S. Hekimi, *Genetics* **141**, 159 (1995).
14. The C. elegans Sequencing Consortium, *Science* **282**, 2012 (1998).
15. A. Genissel, L. M. McIntyre, M. L. Wayne, S. V. Nuzhdin, *Mol. Biol. Evol.* **25**, 101 (2008).
16. M. A. Noor, A. L. Cunningham, J. C. Larkin, *Genetics* **159**, 581 (2001).
17. J. Ronald, R. B. Brem, J. Whittle, L. Kruglyak, *PLoS Genet.* **1**, e25 (2005).
18. P. M. Visscher *et al.*, *Am. J. Hum. Genet.* **81**, 1104 (2007).
19. M. K. Lawniczak, A. K. Holloway, D. J. Begun, C. D. Jones, *Genome Biol.* **9**, R125 (2008).
20. J. Tung, O. Fédrigo, R. Haygood, S. Mukherjee, G. A. Wray, *Mol. Biol. Evol.* **26**, 2047 (2009).
21. J. F. Ayroles *et al.*, *Nat. Genet.* **41**, 299 (2009).
22. S. J. Arnold, R. Bürger, P. A. Hohenlohe, B. C. Ajie, A. G. Jones, *Evolution* **62**, 2451 (2008).
23. D. R. Denver *et al.*, *Proc. Natl. Acad. Sci. U.S.A.* **106**, 16310 (2009).
24. W. G. Hill, A. Robertson, *Genet. Res.* **8**, 269 (1966).
25. J. M. Smith, J. Haigh, *Genet. Res.* **23**, 23 (1974).
26. B. Charlesworth, M. T. Morgan, D. Charlesworth, *Genetics* **134**, 1289 (1993).
27. A. Graustein, J. M. Gaspar, J. R. Walters, M. F. Palopoli, *Genetics* **161**, 99 (2002).
28. A. D. Cutter, B. A. Payseur, *Mol. Biol. Evol.* **20**, 665 (2003).
29. R. Jovelin, *Mol. Biol. Evol.* **26**, 2373 (2009).
30. A. D. Cutter, J. Y. Choi, *Genome Res.* **20**, 1103 (2010).
31. R. R. Hudson, N. L. Kaplan, *Genetics* **141**, 1605 (1995).
32. V. B. Kaiser, B. Charlesworth, *Trends Genet.* **25**, 9 (2009).
33. We thank E. Andersen, A. Chang, J. Gerke, R. Ghosh, D. Gresham, M. Hahn, A. Paaby, D. Pollard, H. Seidel, and J. Shapiro for comments on the manuscript. We thank the *Caenorhabditis* Genetics Center, funded by the NIH National Center for Research Resources, for strains. Our work was supported by the NIH (grants R01 HG004321 to L.K., R01 GM089972 to M.V.R., and P50 GM071508 to the Lewis-Sigler Institute), a Jane Coffin Childs Fellowship (M.V.R.), an Ellison Foundation New Scholar Award (M.V.R.), and a James S. McDonnell Foundation Centennial Fellowship (L.K.). L.K. is an investigator of the Howard Hughes Medical Institute. Microarray data have been deposited at the Gene Expression Omnibus with accession number GSE23857.

Supporting Online Material

www.sciencemag.org/cgi/content/full/330/6002/372/DC1
Materials and Methods
Figs. S1 to S7
References

24 June 2010; accepted 31 August 2010
10.1126/science.1194208

Rapid Construction of Empirical RNA Fitness Landscapes

Jason N. Pitt and Adrian R. Ferré-D'Amaré*

Evolution is an adaptive walk through a hypothetical fitness landscape, which depicts the relationship between genotypes and the fitness of each corresponding phenotype. We constructed an empirical fitness landscape for a catalytic RNA by combining next-generation sequencing, computational analysis, and "serial depletion," an in vitro selection protocol. By determining the reaction rate constant for every point mutant of a catalytic RNA, we demonstrated that abundance in serially depleted pools correlates with biochemical activity (correlation coefficient $r = 0.67$, standard score $Z = 7.4$). Therefore, enumeration of each genotype by deep sequencing yielded a fitness landscape containing ~10^7 unique sequences, without requiring measurement of the phenotypic fitness for each sequence. High-throughput mapping between genotype and phenotype may apply to artificial selections, host-pathogen interactions, and other biomedically relevant evolutionary phenomena.

In vitro selection of RNA has led to the isolation of aptamers and ribozymes expanding our understanding of the biochemical capabilities of this nucleic acid (*1*). Systematic evolution of ligands by exponential enrichment (SELEX) methodology also allows the study of the process of evolutionary adaptation (*2*), which has been conceptualized as an optimizing walk through a fitness landscape (*3*). In molecular evolution, such a landscape represents the sequence space of a macromolecule and the fitness associated with each genotype (*4*, *5*). Two major difficulties have been identified in the empirical construction of macromolecular fitness landscapes. First, even for macromolecules of modest length, the sequence space is vast; a 20-mer RNA or protein has ~10^{12} or ~10^{26} possible sequences, respectively. Second, to characterize the landscape, the phenotypic fitness of each individual genotype needs to be measured, or an indirect measure of fitness needs to be validated. Therefore, although fitness landscapes have been constructed through computer simulations [see, for example, (*6*–*8*)], experimental analyses of fitness landscapes have typically been limited to dozens to hundreds of genotypes [reviewed in (*9*)].

Advances in DNA sequencing methodology allow us to sequence ~10^8 individual molecules of lengths up to ~50 nucleotides (nt) with high accuracy, producing larger accessible experimental sequence spaces (*10*). During an in vitro selection experiment, the representation of RNA molecules that are more active should increase. Thus, we hypothesize that the abundance (or "fecundity") of a particular sequence in an RNA pool undergoing selection, or its rate of increase, may serve as a surrogate fitness metric. Therefore, deep sequencing of earlier stages of an in vitro RNA selection experiment (before the pool became dominated by the most active species) and enumeration of the frequency of each genotype may directly provide an experimental fitness landscape.

To establish the validity of this approach, we mutagenized a well-characterized in vitro selected RNA ligase ribozyme and subjected the resulting pool to reselection. We chose the class II ligase (*11*), because its length (54 nt) is comparable to those of reliable individual reads by the Illumina genome analyzer and because the wild type [isolate a4-11, hereafter "master sequence;" fig. S1 and (*11*)] of this catalytic RNA is extremely active, likely being near-optimal. The mutagenized pool (45 nt at a degeneracy of 21% per position; expected frequency of master sequence = 0.0025%) can be analogous to a viral population arising because of error-prone replication (*12*). Our class II ligase construct catalyzes the formation of a 2′-5′ phosphodiester bond between its 5′ triphosphate and the 3′ terminus of a substrate RNA that is immobilized on a magnetic bead (fig. S1) (*13*). Additional sequence pools served as negative controls: One was composed of ~10^{13} random RNAs; the other was made up of mutants of a sequence variant of the class II ligase that has been engineered to favor 3′-5′ bond formation, but which is crippled in catalytic activity (fig. S1) (*14*).

Our control pools were flanked by constant sequences allowing their members to be distinguished from those of the master-sequence pool, and neither was expected to be substantially enriched during the course of selection. The three RNA pools were mixed to generate a starting pool with a complexity of ~6×10^{13} sequences (*13*), with the genotypes of members of each pool centered on a characteristic sequence distance (number of mutations) from the master sequence (Fig. 1A).

To separate individual sequences by their reactivity, we incubated the RNA pool with substrate RNA linked to beads, depleting the most active species from the population. RNAs were allowed to react for 24 hours. Then, we sequenced species capable of ligation to the beads, and we analyzed their genotypes and frequencies (Fig. 1 and table S1) (*13*). This one-step selection experiment resulted in an enrichment of the master-sequence pool at the detriment of the random and engineered pools. The most abundant sequences in the starting pool are polymerase chain reaction artifacts from the random pool (Fig. 1B). These disappear in the 24-hour selected pool (Fig. 1D). Moreover, the representation of the master sequence (Hamming distance = 0) increased markedly, from 0.0015 to 0.28% of the total population (Fig. 1, C and E).

Because the enrichment of a sequence in the selection experiment should be proportional to its catalytic activity, we successively depleted an

Howard Hughes Medical Institute and Division of Basic Sciences, Fred Hutchinson Cancer Research Center, 1100 Fairview Avenue North, Seattle, WA 98109–1024, USA.

*To whom correspondence should be addressed. E-mail: aferre@fhcrc.org

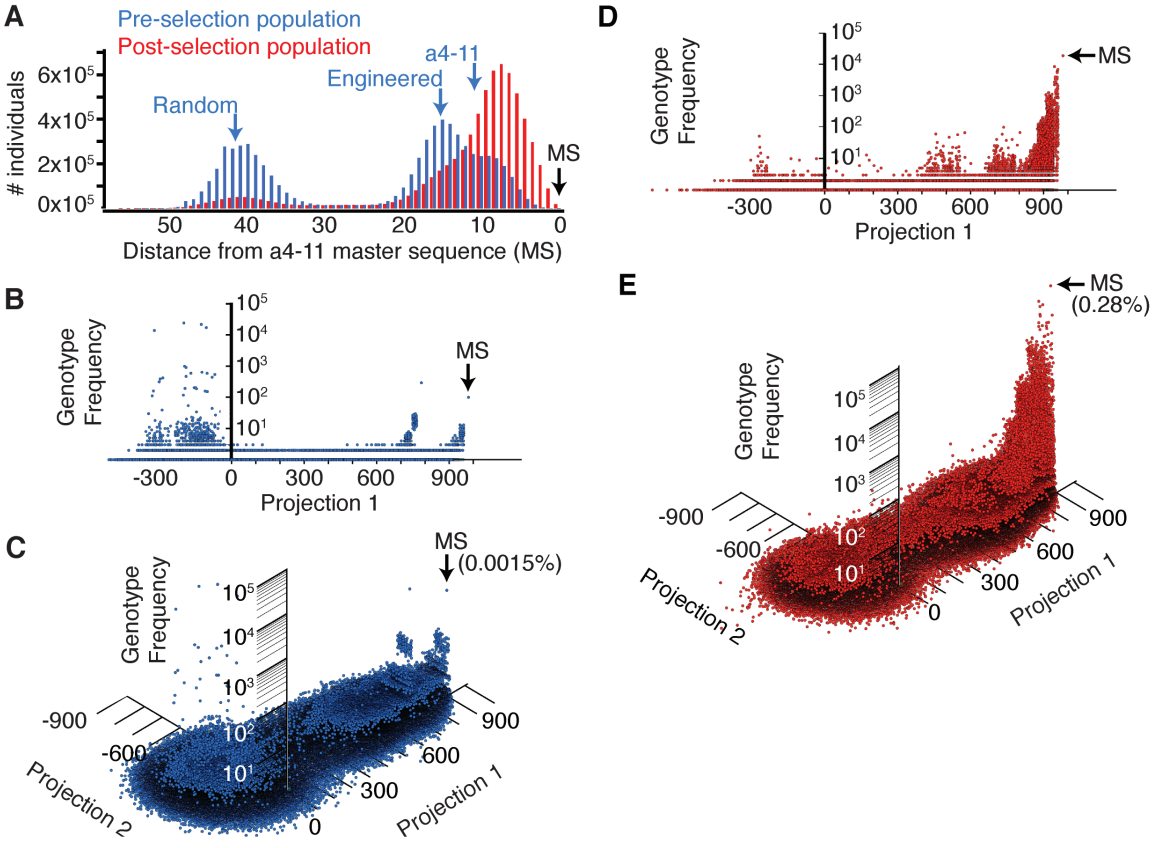

Fig. 1. Population structure before and after one round of in vitro selection. (**A**) Histograms of RNA ligase ribozyme populations before (blue) and after (red) in vitro selection (6.7×10^6 sequences each). Sequences are binned according to their Hamming distance (*28*) from the a4-11 (*11*) master sequence (MS) (*13*). (**B** and **C**) Pre-selection mutant spectrum (*13*, *19*). Each spot is a unique species. Projection axes 1 and 2 are hash scores to the master sequence and an arbitrary string, respectively. Genotype frequency is the number of times a sequence was observed (*13*). (**D** and **E**) Mutant spectrum after one 24-hour in vitro selection step.

RNA pool with a stoichiometric excess of immobilized substrate for increasing time intervals in a "serial depletion" experiment. Comparison of the population captured after a 1-min incubation with that captured after 24 hours shows that the former is composed of sequences that are markedly closer to the master sequence (Fig. 2A). If the fecundity of genotypes is proportional to their activity, then the rate of change of their frequency over the time course, plotted as a function of genotype space, would represent a fitness landscape (Fig. 2B and figs. S2 and S3). Populations selected early were more active than those selected at the longest time point, as evidenced by their bulk reaction rate constants (k_{obs}) (Fig. 3A). The populations selected at the three shortest time points had comparable activity to each other, but the serially depleted population that was allowed to react for 24 hours was only one-third as active. Consistent with early selection of the most active sequences, the information content (*15*, *16*) of the early time points is also highest (Fig. 3A) (*13*).

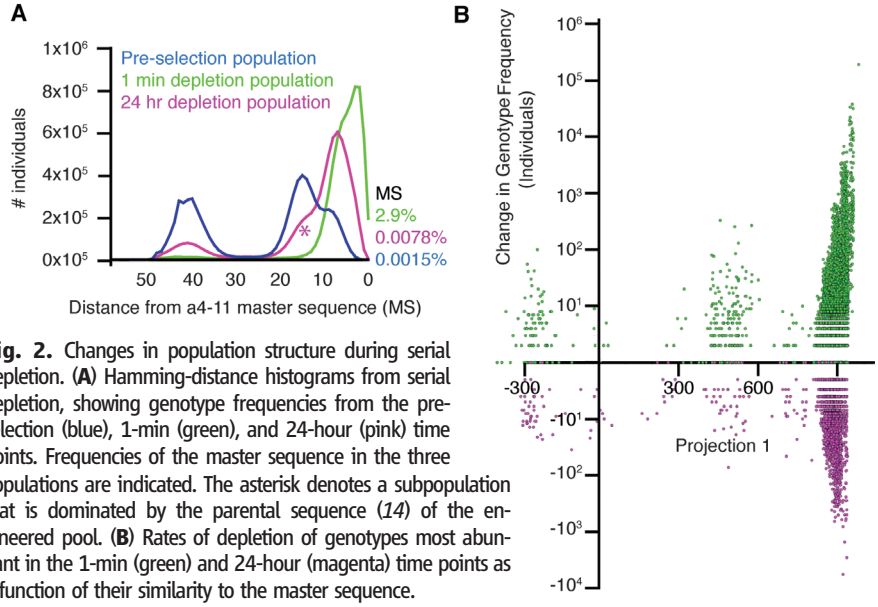

Fig. 2. Changes in population structure during serial depletion. (**A**) Hamming-distance histograms from serial depletion, showing genotype frequencies from the pre-selection (blue), 1-min (green), and 24-hour (pink) time points. Frequencies of the master sequence in the three populations are indicated. The asterisk denotes a subpopulation that is dominated by the parental sequence (*14*) of the engineered pool. (**B**) Rates of depletion of genotypes most abundant in the 1-min (green) and 24-hour (magenta) time points as a function of their similarity to the master sequence.

To demonstrate experimentally that the frequency of each sequence is indicative of its catalytic activity and not due to interactions within the RNA population, we synthesized all 162 possible single point mutations of the master sequence and measured their k_{obs} values (fig. S4 and table S3) (*13*). The k_{obs} of point mutants in all positions varied in the library ($n = 135$ point mutants) correlated positively (correlation coefficient $r = 0.67$) with the frequency of sequences containing the mutations in the 24-hour incubation (Fig. 3B). We tested the significance of this correlation through computation of the distribution of the correlation coefficients of randomly assorted experimental k_{obs} and observed mutation frequencies (mean = 0.0088, SD = 0.089) (Fig. 3B and table S4) (*17*). This analysis indicates a significant regression coefficient ($Z = 7.4$, $p << 0.0001$, t test). Therefore, the fecundity of any individual sequence provides a metric of its fitness, and we can create an experimental fitness landscape composed of ~10^7 different RNA genotypes in a single experiment (Fig. 2B)

The empirical fitness landscape we generated is a high-dimensional object. We visualized it by computing the information content per residue of the master sequence, in essence projecting the landscape onto the ribozyme sequence. We plotted the information content for sequences most abundant in the 1-min time point (maximal representation $D_{max} = 1$ min), as well as those most abundant

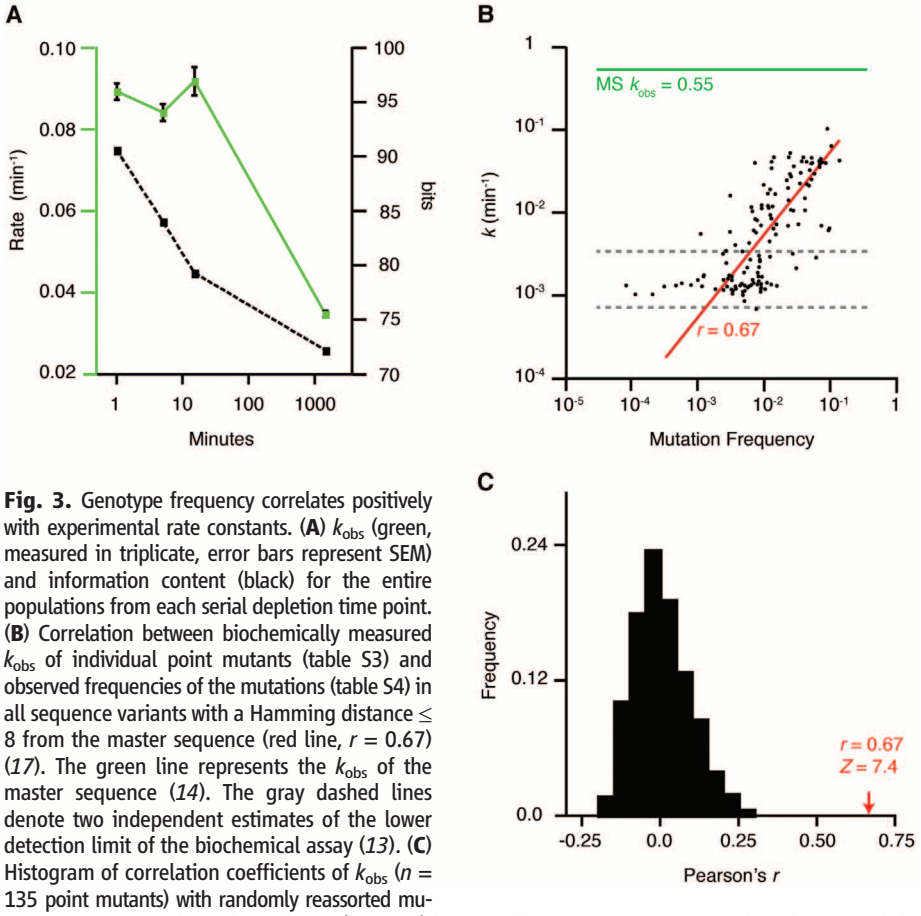

Fig. 3. Genotype frequency correlates positively with experimental rate constants. (**A**) k_{obs} (green, measured in triplicate, error bars represent SEM) and information content (black) for the entire populations from each serial depletion time point. (**B**) Correlation between biochemically measured k_{obs} of individual point mutants (table S3) and observed frequencies of the mutations (table S4) in all sequence variants with a Hamming distance ≤ 8 from the master sequence (red line, r = 0.67) (*17*). The green line represents the k_{obs} of the master sequence (*14*). The gray dashed lines denote two independent estimates of the lower detection limit of the biochemical assay (*13*). (**C**) Histogram of correlation coefficients of k_{obs} (n = 135 point mutants) with randomly reassorted mutation frequencies. The real correlation (r = 0.67) between the mutant frequencies in the selection and the experimental k_{obs} is 7.4 standard deviations from the mean.

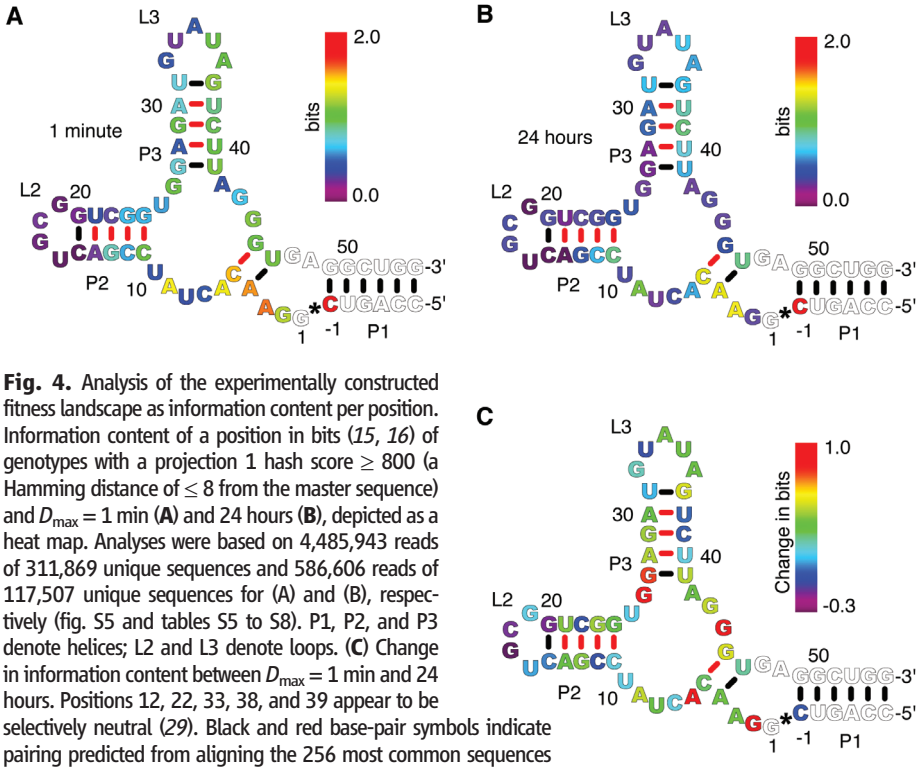

Fig. 4. Analysis of the experimentally constructed fitness landscape as information content per position. Information content of a position in bits (*15*, *16*) of genotypes with a projection 1 hash score ≥ 800 (a Hamming distance of ≤ 8 from the master sequence) and D_{max} = 1 min (**A**) and 24 hours (**B**), depicted as a heat map. Analyses were based on 4,485,943 reads of 311,869 unique sequences and 586,606 reads of 117,507 unique sequences for (A) and (B), respectively (fig. S5 and tables S5 to S8). P1, P2, and P3 denote helices; L2 and L3 denote loops. (**C**) Change in information content between D_{max} = 1 min and 24 hours. Positions 12, 22, 33, 38, and 39 appear to be selectively neutral (*29*). Black and red base-pair symbols indicate pairing predicted from aligning the 256 most common sequences and from analysis of the Watson-Crick covariation of all sequences with a projection 1 hash score ≥ 800 (*13*).

in the 24-hour time point (D_{max} = 24 hours), on a revised secondary structure of the ribozyme generated from sequence-covariation information implicit in our data (Fig. 4, A and B, fig. S5, and tables S5 to S9) (*13*). This analysis reveals that, in addition to the previously characterized key residues surrounding the ligation junction (*11*, *14*), sequences in the central bulge of the RNA and the distal end of paired region (helix) 3 (P3) are important for maximal activity. The location of these residues under purifying selection suggests that the class II ligase may fold into a Y-shaped structure (*18*) that brings the ligation junction and L3 into close proximity. The difference in information content between members of the slow- and fast-reacting populations (Fig. 4C) provided a measure of the slope of the landscape that the evolving population must traverse to achieve maximum fitness. As expected, the catalytic rates measured for each point mutation (fig. S5D) support the functional importance of P1, P3, and L3.

In addition to studying the phenotypic fitness and positional information content of populations composed of closely related sequences, our methodology (which produces three to five orders of magnitude more sequence information than was practical before) could also be used to query the early rounds of SELEX experiments, starting with random pools. The locality-sensitive hash algorithm that we implemented is more efficient in analyzing libraries with greater sequence diversity (*19*). A typical SELEX experiment employs multiple rounds of purifying selection and amplification to separate highly active sequences from other members of the starting population, assumed to be inactive (*20*–*22*). However, this assumption is only rarely tested (*2*). Though aggregate activity of the population in earlier rounds of selection is low, there may be many sequences present that represent suboptimal solutions. Recent experiments demonstrated that minute RNAs, working alone or in ensembles, can be highly active catalysts (*23*, *24*). For such small functional nucleic acids (≤13 nt), our methodology can determine the fitness of every possible RNA (4^{13} or 6.7 × 10^7 possible genotypes).

One application of empirically generated fitness landscapes is the analysis of systems in genetic conflict (*25*): for example, a host immune response and an infecting viral quasi-species (*26*, *27*). In such systems, positive selection drives phenotypic variation that maximizes sampling of their respective fitness landscapes. However, these systems are dynamic, with changes in one population leading to changes in the other. By analyzing regions of the fitness landscapes that remain fixed between multiple conditions, we predict that critical regions of the molecules in question can be identified for vaccine or drug development.

References and Notes

1. D. S. Wilson, J. W. Szostak, *Annu. Rev. Biochem.* **68**, 611 (1999).
2. N. Lehman, G. F. Joyce, *Curr. Biol.* **3**, 723 (1993).
3. S. Wright, *Proc. Sixth Int. Congress Genet.* **1**, 356 (1932).
4. J. Maynard Smith, *Nature* **225**, 563 (1970).

5. P. Schuster, *Eur. Rev.* **17**, 281 (2009).
6. P. Schuster, *Biol. Chem.* **382**, 1301 (2001).
7. M. A. Huynen, P. F. Stadler, W. Fontana, *Proc. Natl. Acad. Sci. U.S.A.* **93**, 397 (1996).
8. M. Stich, E. Lázaro, S. C. Manrubia, *BMC Evol. Biol.* **10**, 46 (2010).
9. F. J. Poelwijk, D. J. Kiviet, D. M. Weinreich, S. J. Tans, *Nature* **445**, 383 (2007).
10. D. R. Bentley, *Curr. Opin. Genet. Dev.* **16**, 545 (2006).
11. E. H. Ekland, J. W. Szostak, D. P. Bartel, *Science* **269**, 364 (1995).
12. E. Domingo, S. Wain-Hobson, *EMBO Rep.* **10**, 444 (2009).
13. Materials and methods are available as supporting material on *Science* Online.
14. J. N. Pitt, A. R. Ferré-'Amaré, *J. Am. Chem. Soc.* **131**, 3532 (2009).
15. J. M. Carothers, S. C. Oestreich, J. H. Davis, J. W. Szostak, *J. Am. Chem. Soc.* **126**, 5130 (2004).
16. T. D. Schneider, G. D. Stormo, L. Gold, A. Ehrenfeucht, *J. Mol. Biol.* **188**, 415 (1986).
17. The correlation was calculated using the frequencies of all haplotypes containing up to eight mutations (projection 1 hash score ≥ 800; 706,899 reads of 106,012 unique genotypes). The value of r is statistically unchanged ($p \geq 5\%$, two-tailed t test) if the analysis is limited to sequences with 1, 2, ..., 6 mutations, indicating that higher-order effects are not detectable (table S2).
18. M. de la Peña, D. Dufour, J. Gallego, *RNA* **15**, 1949 (2009).
19. J. N. Pitt, I. Rajapakse, A. R. Ferré-D'Amaré, *Nucleic Acids Res.*, published online 6 August 2010 (10.1093/nar/gkq661).
20. G. F. Joyce, *Gene* **82**, 83 (1989).
21. A. D. Ellington, J. W. Szostak, *Nature* **346**, 818 (1990).
22. C. Tuerk, L. Gold, *Science* **249**, 505 (1990).
23. R. M. Turk, N. V. Chumachenko, M. Yarus, *Proc. Natl. Acad. Sci. U.S.A.* **107**, 4585 (2010).
24. A. Vlassov, A. Khvorova, M. Yarus, *Proc. Natl. Acad. Sci. U.S.A.* **98**, 7706 (2001).
25. L. D. Hurst, A. Atlan, B. O. Bengtsson, *Q. Rev. Biol.* **71**, 317 (1996).
26. G. Fernàndez, B. Clotet, M. A. Martínez, *J. Virol.* **81**, 2485 (2007).
27. H. S. Robins *et al.*, *Blood* **114**, 4099 (2009).
28. R. Hamming, *Bell Syst. Tech. J.* **29**, 147 (1950).
29. M. Kimura, *Nature* **217**, 624 (1968).

30. We thank R. Basom, A. Marty, and the staff of the Fred Hutchison Cancer Research Center Genomics Shared Resource for performing the Illumina sequencing and D. Bartel, B. Fritz, R. Knight, H. Malik, W. Noble, H. Robins, A. Roll-Mecak, and M. Tewari for discussions. This work was supported by the W.M. Keck Foundation and the Howard Hughes Medical Institute (HHMI). A.R.F.-D. is an investigator of the HHMI. Illumina sequence data have been deposited with the National Center for Biotechnology Information Sequence Read Archive with accession code SRA020870.

Supporting Online Material

www.sciencemag.org/cgi/content/full/330/6002/376/DC1
Materials and Methods
Figs. S1 to S5
Tables S1 to S10
References

7 May 2010; accepted 6 August 2010
10.1126/science.1192001

Temperature as a Universal Resetting Cue for Mammalian Circadian Oscillators

Ethan D. Buhr,[1,2] Seung-Hee Yoo,[1,2,3] Joseph S. Takahashi[1,2,3,4]*

Environmental temperature cycles are a universal entraining cue for all circadian systems at the organismal level with the exception of homeothermic vertebrates. We report here that resistance to temperature entrainment is a property of the suprachiasmatic nucleus (SCN) network and is not a cell-autonomous property of mammalian clocks. This differential sensitivity to temperature allows the SCN to drive circadian rhythms in body temperature, which can then act as a universal cue for the entrainment of cell-autonomous oscillators throughout the body. Pharmacological experiments show that network interactions in the SCN are required for temperature resistance and that the heat shock pathway is integral to temperature resetting and temperature compensation in mammalian cells. These results suggest that the evolutionarily ancient temperature resetting response can be used in homeothermic animals to enhance internal circadian synchronization.

Daily cycles of light and temperature are perhaps the two most reliable environmental timing cues for living systems on Earth. As a consequence, organisms use these cues to entrain their endogenous circadian rhythms to the solar day (*1*). Recent work suggests that most cells in the mammalian body similarly use internal entraining cues to synchronize circadian patterns of gene expression to the rest of the body (*2*–*5*). It is now understood that most cells in the mammalian body contain cell-autonomous circadian oscillators (*6*–*10*). These cellular oscillators are synchronized at the organismal level by the suprachiasmatic nucleus (SCN) of the hypothalamus (*11*). Although a number of factors have been implicated in the resetting of peripheral tissues, no universal entraining mechanism for peripheral oscillators has been defined (*2*, *4*, *12*, *13*).

Temperature is a primordial entraining agent for circadian rhythms in all organisms with the exception of homeothermic vertebrates (*14*–*18*). Although mammals do not normally entrain to external environmental temperature cycles (*19*), this cue would be ideal as a global internal entraining cue in mammals because of the existence of circadian rhythms of body temperature driven by the SCN. Indeed, externally applied temperature cycles can sustain rhythmic clock gene expression in Rat-1 fibroblasts and primary glial cells in vitro, as well as in peripheral clocks in the whole animal (*12*, *20*). For such a system to function in vivo, two requirements would be necessary: (i) peripheral oscillators must be sensitive to subtle variations in temperature within the physiologic range (36°C to 38.5°C in mice) and (ii) the SCN itself must be resistant to subtle temperature changes or it would be susceptible to feedback that could interfere with entrainment. Consistent with this idea, Brown *et al*. (*12*) have shown that altered ambient temperature cycles can shift the phase of rhythms in other brain regions, but the SCN remained in phase with the light cycle.

We tested this hypothesis by assessing temperature resetting of the circadian rhythms of tissues from $Per2^{Luciferase}$ mice ex vivo using real-time analysis of PER2::LUC bioluminescence (*10*). $Per2^{Luc}$ tissues were cultured in Lumicycle (Actimetrics, Wilmette, Illinois) machines equipped with photomultiplier tubes (PMT). Tissues were maintained at the lower set point of body temperature, 36°C, and then pulsed with temperatures that correspond to the peak set point of 38.5°C (fig. S1A). All peripheral tissues tested were highly responsive to 38.5°C temperature pulses and exhibited high-amplitude, type 0 resetting. Type 0 phase resetting is characterized by resetting of oscillators to a common new phase after pulses occurring at all phases. Phase transition curves show that both 1-hour and 6-hour 38.5°C pulses strongly reset the rhythms of peripheral tissues to new phases clustered around CT12-18 and increased the peak to trough amplitude (Fig. 1A and fig. S2). However, at the majority of times across the circadian cycle, the phase of the adult SCN was resistant to identical physiological temperature changes [in contrast to neonatal and juvenile rat SCN tissue, which appear more sensitive to temperature cycles (*21*)]. Tissues of all types that were held at a constant 36°C but removed from the bioluminescence recording device for 6 hours as handling controls showed no phase shifts (fig. S1, B to H).

To test whether the sensitivity of peripheral tissues and the resistance of the SCN also occur under conditions of entrainment to temperature cycles, pituitary and lung cultures from the same animals were exposed to oppositely phased temperature cycles composed of 12 hours of 36°C and 12 hours of 38.5°C. Within 3 days, the phase of PER2 bioluminescence of lung and pituitary cultures had assumed the phase of the correspond-

[1]Department of Neurobiology and Physiology, Northwestern University, Evanston, IL 60208–3520, USA. [2]Center for Functional Genomics, Northwestern University, Evanston, IL 60208–3520, USA. [3]Department of Neuroscience, University of Texas Southwestern Medical Center, Dallas, TX 75390–9111, USA. [4]Howard Hughes Medical Institute, University of Texas Southwestern Medical Center, Dallas, TX 75390–9111, USA

*To whom correspondence should be addressed. E-mail: joseph.takahashi@utsouthwestern.edu

ing temperature cycle (either shifted or unshifted) so that they were ~180° out of phase with each other (Fig. 1B). By contrast, SCN that were cultured in opposing temperature cycles remained unshifted even after 4 days, demonstrating that the SCN is resistant to cyclic temperature changes within the physiologic range (Fig. 1B). The entrainment of peripheral tissues was also observed in response to temperature cycles that mimicked body temperature cycles (*22*) (fig. S3). Taken together, these results demonstrate that circadian changes in temperature comparable to that seen with core body temperature rhythms are capable of entraining and enhancing the amplitude of the circadian rhythms of peripheral tissues while the adult SCN remains resistant.

To explore the possible mechanisms of the SCN resistance to temperature pulses, we tested the role of intercellular communication and coupling in the SCN. When communication among neurons in the SCN was impaired by application of the voltage-gated Na^+ channel blocker, tetrodotoxin (TTX), temperature pulses strongly reset the SCN and this effect of TTX was reversible (Fig. 2, A and B). To assess the properties of the individual cells within an SCN in its networked state and in the presence of TTX, SCN bioluminescence was imaged with a dual microchannel plate–intensified gallium arsenide phosphide–cooled charge-coupled device (CCD) camera system. Individual cells within an SCN were typically locked in phase throughout an experiment, but in TTX cells in the same SCN "free run" and eventually became scattered in phase (*23*) (Fig. 2C). After a 6-hour pulse the cells were resynchronized, as can be seen as vertical alignment of peak bioluminescence after the pulse in the heatmap in Fig. 2C (right panel). The resistance of individual cells was restored after the removal of TTX (fig. S4D). Thus, TTX treatment rendered the SCN sensitive to temperature resetting.

Because of the presence of voltage-gated calcium channels in the SCN and the role that L-type calcium channels play in the membrane potential of SCN neurons, we tested whether the blockade of L-type calcium channels contributed to the insensitivity of the SCN to temperature pulses (*24*). Similar to TTX, treatment with an L-type calcium channel blocker, nimodipine, caused a marked decrease in amplitude of $Per2^{Luc}$ bioluminescence and reversibly revealed the temperature sensitivity of the SCN to 6-hour pulses of 38.5°C (Fig. 2, D and E, and fig. S5A). Mibefradil, a T-type calcium channel blocker, did not sensitize the SCN to temperature-induced phase shifts (Fig. 2F and fig. S5B). This suggests that L-type calcium channels play a role in maintaining the SCN's phase in the presence of temperature, possibly through a contribution to intercellular communication.

The ventrolateral and dorsomedial regions of the SCN differ in their expression of the peptides vasoactive intestinal polypeptide (VIP) and arginine vasopressin (AVP), in their efferent and afferent projections, and in the timing of their development (*25*, *26*). Because of this regional difference, the dorsomedial and ventrolateral regions of the SCN were cultured separately and tested for thermal sensitivity (Fig. 3, A and B). Surprisingly, both the ventral and dorsal regions exhibited large phase shifts in response to 6-hour 38.5°C pulses very similar to those of SCN slices in the presence of TTX (Fig. 3C). This did not occur if the SCN were split from one another sagittally by a cut from the third ventricle ventrally down through the optic chiasm (Fig. 3D). The sagittally separated SCN were resistant to phase shifts by 6-hour 38.5°C pulses (Fig. 3, E and F). Pharmacologic blockade of VIP and AVP signaling in the SCN did not reveal strong temperature resetting, however greatly increased the variance of the phase shifts in response to temperature pulses (*22*) (fig. S6, A and B). The blockade of γ-aminobutyric acid (GABA) signaling did not reveal any change in the SCN's resistance to temperature changes (*22*) (fig. S6, D to F). Thus, the cellular architecture that renders the

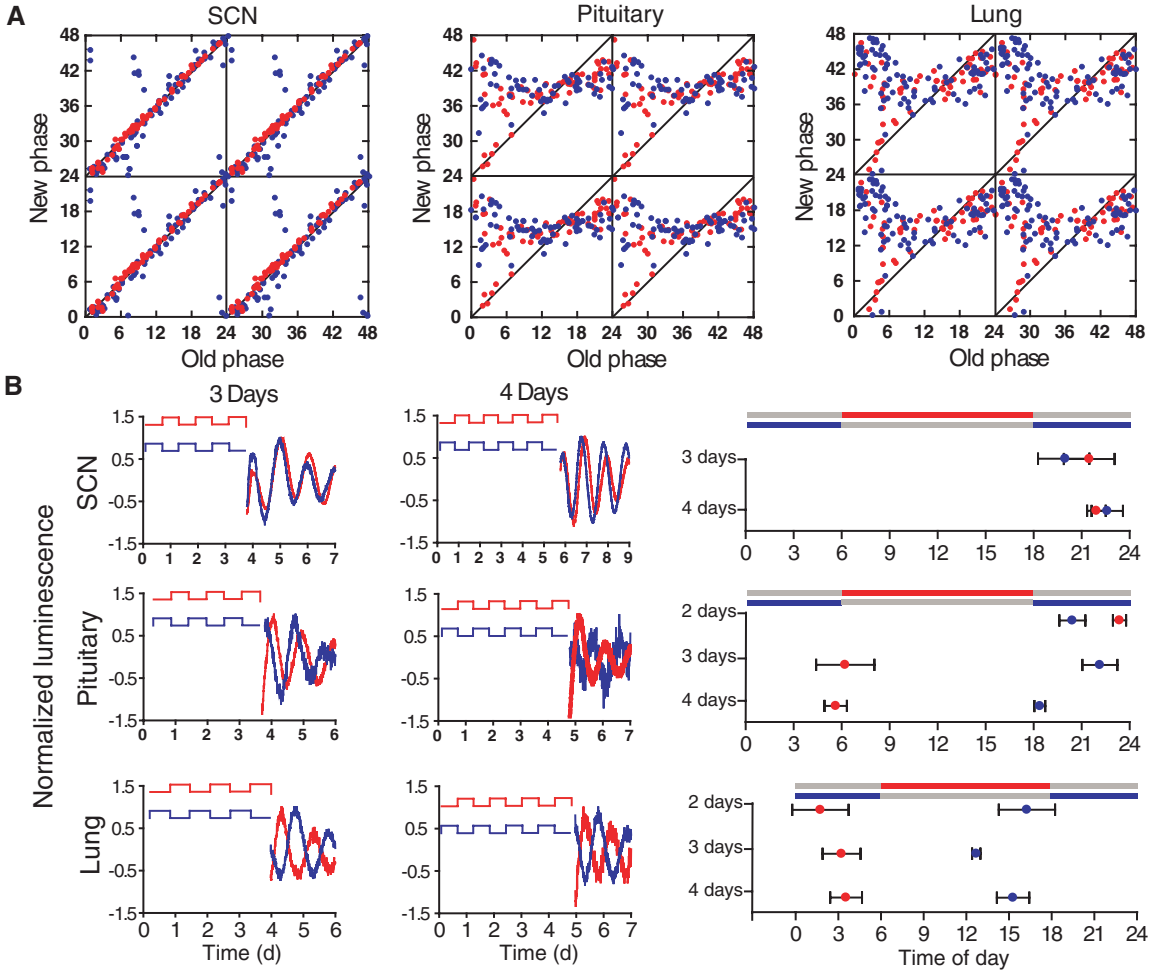

Fig. 1. Peripheral tissues, but not SCN, are sensitive to temperature changes within the physiological temperature range. (**A**) Phase transition curves for SCN, pituitary, and lung in response to 6-hour (blue) or 1-hour (red) 38.5°C temperature pulses from 36°C. Pulse times are plotted as the time in circadian hours of the end of the pulse from the previous trough of bioluminescence. (**B**) SCN, pituitary, and lung cultures exposed to opposing square-wave 12-hour:12-hour 36°C:38.5°C temperature cycles. Phase graphs show time of peak $PER2^{LUC}$ bioluminescence the day after the temperature cycle. Colored bars above represent the times of warm temperature for the points of corresponding color below. Data are mean ± SEM. $n = 4$ for each SCN point and $n = 5$ for each pituitary and lung point.

SCN resistant to temperature resetting is contained within a single SCN and requires communication between the ventrolateral and dorsomedial regions using a GABA-independent signaling pathway that may involve VIP and AVP. Furthermore, cell-autonomous circadian oscillators are temperature sensitive in all cell types, including the SCN. Logically, this argues that the temperature resistance of the SCN must originate as a higher-order network property of the mammalian SCN circadian system.

The mechanism of the cell-autonomous molecular clock involves a transcription-translation negative feedback loop (*27*). Recent work shows that heat shock factor 1 (HSF1) and components of the heat shock response pathway are involved in circadian gene expression in mouse liver (*13*, *28*). To test the role of the heat shock response pathway in temperature resetting, we used the benzylidene lactam drug, KNK437, which is a highly potent antagonist of the heat shock signaling pathway (*22*, *29*). One-hour pulses of 100 μM KNK437 alone given to pituitary and lung cultures caused strong type 0 phase shifts

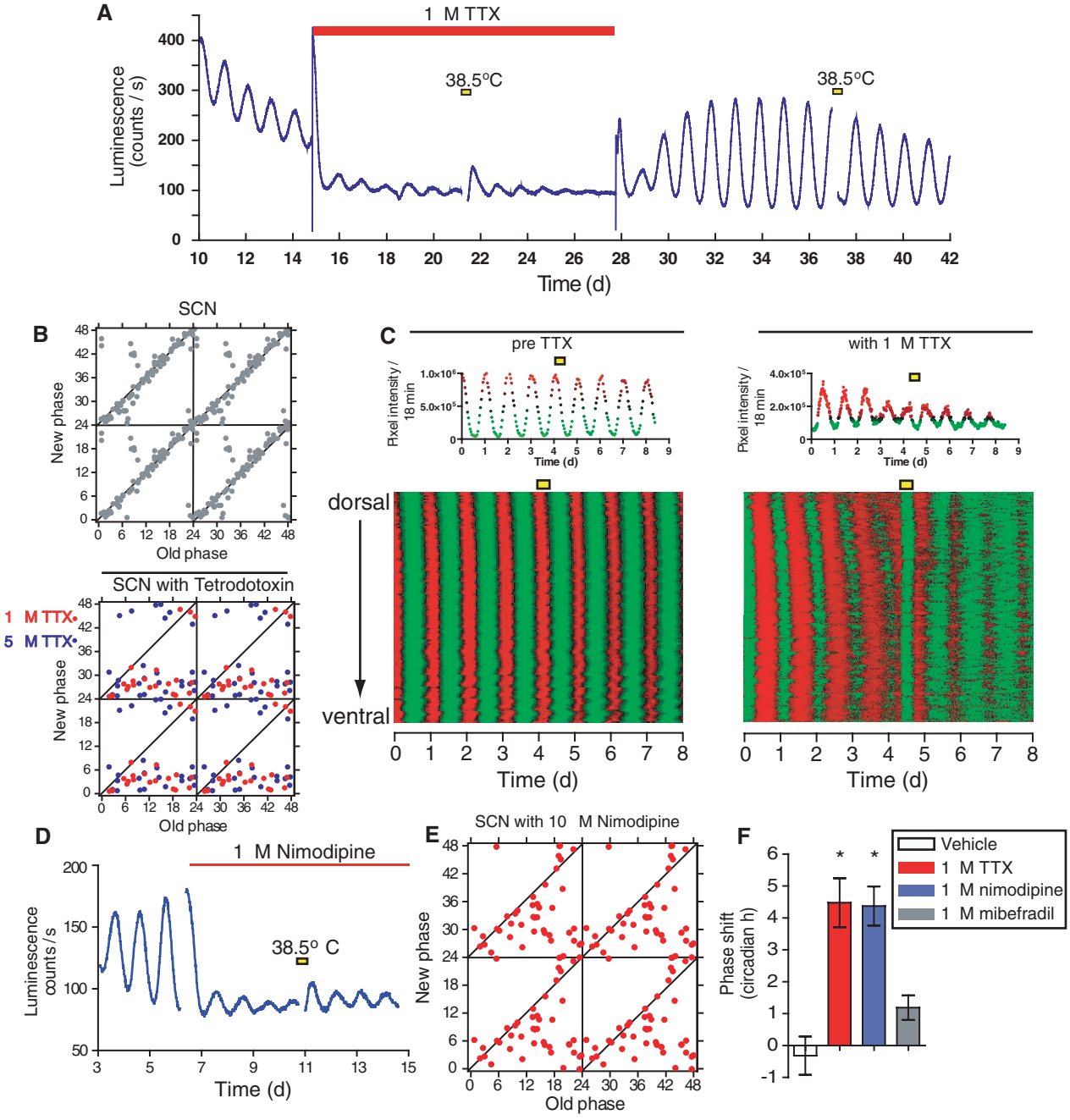

Fig. 2. Tetrodotoxin reveals temperature sensitivity of SCN cultures. (**A**) Bioluminescence record from a *Per2*^{Luc} SCN treated with 1 μM TTX as indicated. Six-hour 38.5°C pulses noted with yellow bars. (**B**) Phase transition curve of individual SCN cultures containing 5 μM (blue) or 1 μM (red) TTX or without drug (gray). (**C**) A *Per2*^{Luc} SCN was imaged using an intensified CCD camera. Identical regions of interest equal to or smaller than the size of a single cell were measured. Heat maps display voxels measured from dorsal (top) to ventral (bottom), where red corresponds to peak bioluminescence and green to trough with and without TTX for the same SCN. (**D**) 1 μM nimodipine reduces amplitude of bioluminescence rhythms and reveals temperature sensitivity. (**E**) Phase transition curve of individual SCN cultures receiving a 6-hour temperature pulse of 38.5°C in 10 μM nimodipine. (**F**) Phase shifts in response to 6-hour 38.5°C pulses that ended 22 hours after the trough of bioluminescence displayed as mean ± SEM. Vehicle (n = 14), 1 μM TTX (n = 11), 1 μM nimodipine (n = 13), 1 μM mibefradil (n = 11). *, $P < 0.05$, analysis of variance (ANOVA), Tukey post hoc analysis.

in *Per2*^{Luc} rhythms but did not affect the phase of SCN cultures (Fig. 4A). To explore the possible mechanisms of phase shifting by KNK437, we compared the phase response curves for resetting by 1-hour KNK437 pulses alone with either 1-hour 38.5°C "warm" pulses or 1-hour 33.5°C "cool" pulses. Because warm pulses induce HSF-mediated transcription and KNK437 blocks this transcription, it is reasonable to expect that the pulses induced by KNK437 alone would mimic cool pulses (or a reduction of HSF-mediated transcription). Indeed, when the phase-response curves of 1-hour KNK437, 1-hour cool (33.5°C), and 1-hour warm (38.5°C) pulses were compared, the responses of pituitary and lung to KNK437 and cool pulses were overlapping with breakpoints between delays and advances occurring at ~CT21. In contrast, the phase response curves for warm pulses were distinctly different with breakpoints at ~CT3 (Fig. 4B). Thus, KNK437 pulses mimic a reduction in temperature, which is consistent with a role of HSF1 in temperature resetting to cool pulses.

To test for a role of HSF1 in mediating temperature resetting to warm pulses, we used KNK437 to block HSF1 induction and determined whether temperature-induced phase shifts could be blocked by KNK437 treatment. We first validated that 38.6°C temperature pulses induced a heat shock response and that KNK437 could block this (*22*) (fig. S7). To test the ability of KNK437 to block temperature-induced phase shifts, 38.5°C temperature pulses were given in the presence of KNK437 in lung and pituitary cultures. At phases at which KNK437 alone produced no shift, but warm pulses alone caused a phase advance, simultaneous application of KNK437 and a warm pulse completely blocked resetting by temperature (Fig. 4C). To confirm the pharmacological blockade by KNK437, we used a second classical HSF1 inhibitor, quercetin (*22*). Quercetin also completely blocked temperature-induced phase shifts in a manner indistinguishable from KNK437 (Fig. 4C). Thus, two independent inhibitors of HSF1 blocked temperature resetting. To explore the KNK437 blockade at other phases of the circadian cycle, the KNK437 blocking experiment was performed at all phases, and KNK437 completely blocked the phase-shifting effects of temperature pulses on peripheral clocks at every phase of the cycle (Fig. 4D and fig. S7, D and E). We can also rule out saturation effects in this experiment because nonsaturating 1-hour temperature pulses were used. By contrast and as observed with temperature pulses, the SCN was also resistant to the phase-shifting effects of KNK437 pulses, highlighting another similarity in the differential actions of temperature and KNK437 on central and peripheral oscillators (Fig. 4D). Finally, to circumvent the phase-shifting effects of KNK437 pulses, we conducted blocking experiments using chronic application of KNK437. Under these conditions, temperature pulses given to peripheral clocks such as liver, lung, and U2-OS cultures could not induce phase shifts nor induce increases in the amplitude of oscillations (fig. S8). Taken together, these experiments demonstrate that inhibition of HSF1 mimics the effects of cool pulses and that blockade of HSF1 induction is associated with a loss of resetting to warm pulses, implicating a critical role of this pathway in temperature entrainment of mammalian clocks.

In addition to the phase-shifting effects of KNK437, the circadian period increased dramatically with increasing concentration of the drug when administered chronically to SCN cultures, and this effect on period was reversible (Fig. 5, A and B). Cultures of pituitary and lung displayed similar period lengthening effects in chronic KNK437 (Fig. 5C). The period lengthening caused by KNK437 inhibition of HSF-mediated transcription is consistent with the long free-running period observed in mice carrying a null allele of *Hsf1* (*28*). In addition to the entraining effects of temperature, a canonical property of circadian clocks is temperature compensation, which is the ability of the period of a rhythm to remain fairly constant at various physiologically permissive temperatures (*1*, *18*, *22*). Intriguingly, treatment with KNK437 greatly impaired the temperature compensation of circadian period of SCN and pituitary. In control media containing dimethyl sulfoxide (DMSO) vehicle, circadian rhythms were compensated with temperature coefficient values, Q_{10}, of 1.04 and 0.97 in the SCN and pituitary, respectively. However, in the presence of 100 μM KNK437, the Q_{10} values became 1.34 for the SCN and 1.38 for the pituitary, which fall significantly outside the Q_{10} range for temperature compensation (typically between 0.9 and 1.2) (Fig. 5D) (*1*, *18*). In contrast, SCN cultures treated with 1 μM TTX displayed a Q_{10} of 1.06, demonstrating that the temperature compensation of the SCN is a cell-autonomous phenomenon and does not depend on intercellular coupling (Fig. 5D).

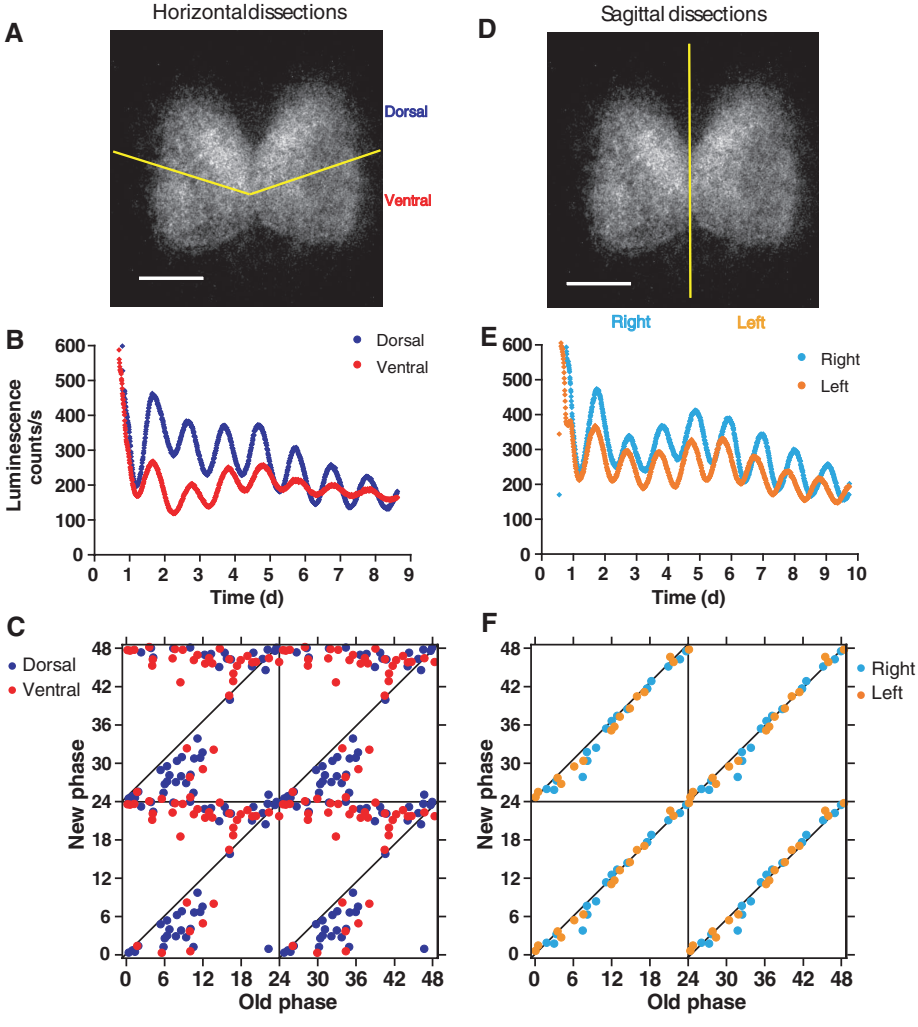

Fig. 3. SCN resistance to temperature pulses relies on the integrity of the ventral and dorsal regions. (**A**) Yellow line shows approximate dissection of the dorsomedial and ventrolateral regions of a coronal SCN slice. Scale bar, 500 μm. (**B**) Dorsal (blue) and ventral (red) sections from the same SCN cultured in separate dishes. (**C**) Phase transition curves of dorsal and ventral SCN sections in response to 6-hour pulses of 38.5°C. (**D**) Coronal sections of the SCN were also dissected sagittally so that the left and right SCN were cultured separately. (**E**) Bioluminescence of right and left SCN from the same animal. (**F**) Phase transition curves of right (blue) and left (orange) SCN sections in response to 6-hour pulses of 38.5°C.

Thus, changes in temperature comparable to the circadian body temperature rhythm are a potent cue for resetting in peripheral tissues. Although it has been reported that more than one cue may reset peripheral tissues and that different tissues may use different cues for their entrainment, many of these resetting stimuli appear to involve changes in body temperature or may converge on temperature response pathways (Fig. 5E). For example, although in vivo experiments are important for the understanding of entrainment and resetting of rhythms at the organismal level, it is extremely difficult, if not impossible, to separate the effects of activity, sleep, feeding, and metabolic and redox state from the effects of temperature. Paradigms that involve induction of rhythms in the absence of circadian cues from the SCN—such as chronic administration of methamphetamine to *Cry1*$^{-/-}$/*Cry2*$^{-/-}$ mice or wild-type mice with SCN lesions—always involve a change in both body temperature and activity (*30*–*32*). Restricted feeding regimens that alter circadian gene expression in the liver are also associated with deep depressions of body temperature at times when food is unavailable (*3*). Glucocorticoids, which reset peripheral circadian oscillators (*2*), also cause an inhibition of the HSF1-mediated transcription, and Hsp90 and Hsp70 act as molecular chaperones for inactive glucocorticoid receptors (*33*, *34*). Redox state, which fluctuates on a circadian basis (*35*), also regulates HSF1 activation (*36*). In addition, signaling pathways involving cyclic adenosine monophosphate and calcium, which regulate circadian oscillators (*37*, *38*), also activate the heat shock pathway (*39*, *40*). Thus, changes in body temper-

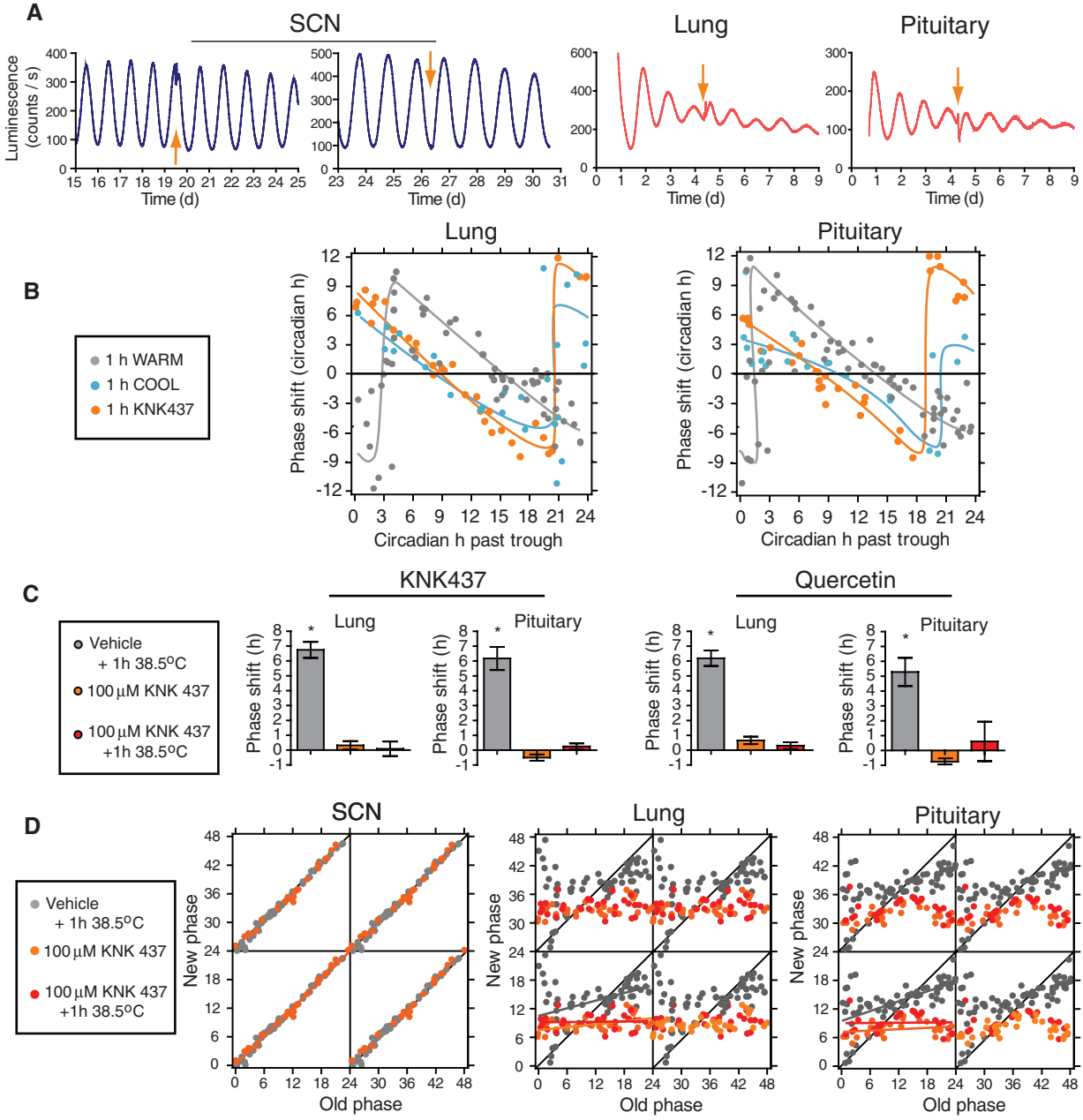

Fig. 4. KNK437 phase shifts the clock and blocks temperature-induced phase changes. (**A**) SCN, lung, or pituitary cultures receiving a 1-hour pulse of 100 μM KNK437 indicated by an orange arrow. (**B**) Phase response curves of lung and pituitary receiving a 1-hour 38.5°C "warm" pulse, 33.5°C "cool" pulse, or 100 μM KNK437 pulse. (**C**) Average phase shifts (mean ± SEM) from lung or pituitary cultures receiving a 1-hour 38.5°C pulse in DMSO (n = 6), 1-hour 38.5°C pulse in 100 μM KNK437 or 100 μM Quercetin (n = 5), or a 1-hour pulse of 100 μM KNK437 or 100 μM Quercetin alone (n = 4) given 9 to 11 hours (lung) or 4 to 8 hours (pituitary) past peak luminescence. *, $P < 0.01$, ANOVA, Tukey post hoc analysis. (**D**) Phase transition curves of SCN, lung, and pituitary receiving 1-hour pulses of indicated treatments.

ature and/or activation of the heat shock pathway may be a final common pathway for resetting circadian clocks in mammals. The experiments presented here show that temperature can act as a universal entraining agent for circadian rhythms throughout the body. This is consistent with the rhythmic binding of HSF1 to heat shock elements (HSE) in vivo and the presence of HSE motifs in the upstream region of the *Per2* gene in many mammalian species (*13*, *28*).

Temperature serves as an important entrainment cue for invertebrates at the organismal level (*18*). Conidiation rhythms in *Neurospora* can be entrained by either light or temperature cycles, and in some instances temperature cycles can override light cycles (*16*). The pathways of light and temperature entrainment in *Neurospora* are mechanistically distinct. Temperature changes cause a posttranscriptional, temperature-dependent alternate splicing event in which alternate isoforms of the FRQ protein result from one of two translation initiation sites, whereas light entrainment appears to act through a light-induced increase in *frq* transcription (*41*–*43*). In *Drosophila*, temperature pulses act through a similar mechanism to light pulses, which are both associated with a CRYPTOCHROME-mediated degradation of TIMELESS, and the cry^b mutation causes reduced circadian resetting to both temperature and light pulses (*44*, *45*). The *Drosophila per* gene also undergoes temperature-dependent splicing, which regulates midday activity (*46*, *47*). Finally, temperature entrainment in *Drosophila* also relies on *nocte* expression (*14*, *48*). Interestingly, this *nocte*-mediated temperature entrainment of clock neurons in *Drosophila* is distinct from that of peripheral oscillators so that the brain clocks require the mechano- and thermo-sensitive chordotonal organs for proper temperature entrainment (*48*). Thus, the temperature entrainment of *Drosophila* requires both the cell-autonomous response to temperature changes and neuronal

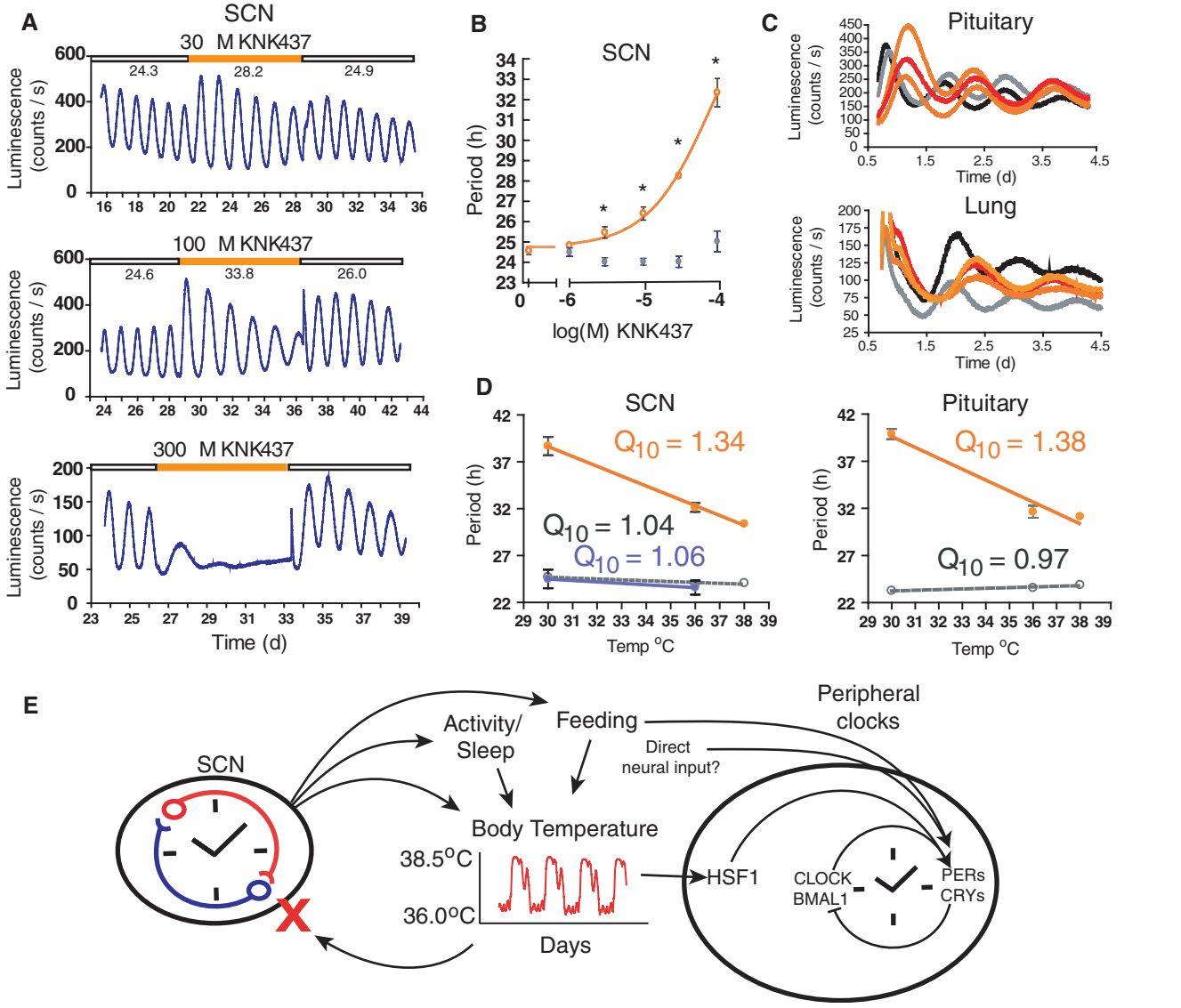

Fig. 5. Inhibiting HSF-mediated transcription lengthens circadian period and impairs temperature compensation. (**A**) SCN in KNK437 where marked by an orange line. Numbers indicate the period of the rhythm under the line. (**B**) Periods of SCN in KNK437 (orange) at 100 μM ($n = 5$), 30 μM ($n = 5$), 10 μM ($n = 5$), 3 μM ($n = 5$), and 1 μM ($n = 5$) displayed as mean ± SEM. Gray points indicate the periods of the same SCN cultures after KNK437 was removed. *, $P < 0.05$ from paired t tests corrected for multiple measures. (**C**) Traces of bioluminescence from pituitary or lung cultured with DMSO (black/gray) or 100 μM KNK437 (orange/red). (**D**) Periods (mean ± SEM) of SCN or pituitary in 100 μM KNK437 or DMSO. SCN: 30°C DMSO $n = 8$, KNK $n = 5$, and TTX $n = 6$; 36°C DMSO $n = 9$, KNK $n = 8$, and TTX $n = 8$; 38°C DMSO $n = 8$ and KNK $n = 8$. Pituitary: 30°C DMSO $n = 6$ and KNK $n = 6$; 36°C DMSO $n = 9$ and KNK $n = 7$; 38°C DMSO $n = 7$ and KNK $n = 8$. $P < 0.05$ comparing drug treatment or temperature within KNK groups (ANOVA); not significant for temperature in vehicle groups (ANOVA). (**E**) Model representing the communication between dorsal and ventral SCN, which confers phase resistance to body temperature changes regulated by the SCN. Body temperature then entrains peripheral oscillators by acting through HSF-mediated transcription.

communication. It is possible that among mammals a difference in cellular communication within the SCN exists. For example, in rats the expression of clock genes in the ventrolateral and dorsomedial regions of the SCN can be split in vivo under 22-hour light-dark conditions (*49*). It is possible that this same susceptibility to dissociation within the tissue allows for increased sensitivity to temperature changes in this species (*21*).

We have shown that cellular communication within the SCN and between the ventrolateral and dorsomedial SCN confers resistance to temperature resetting. This observation is consistent with the ability of an animal's behavioral rhythms to "free-run" through environmental temperature cycles (*18*, *19*) and suggests that resistance to temperature entrainment in vivo is conferred by the SCN. When communication between cells within the SCN is blocked, the tissue exhibits temperature sensitivity equal in magnitude to that of peripheral tissue, revealing that temperature-sensitive resetting is a cell-autonomous property. Finally, the sensitivity of peripheral clocks to small temperature changes is abolished in the presence of KNK437 or quercetin, thus revealing a critical role of the heat shock response pathway in resetting of circadian clocks to thermal stimuli and in temperature compensation of circadian period.

References and Notes

1. C. S. Pittendrigh, *Cold Spring Harb. Symp. Quant. Biol.* **25**, 159 (1960).
2. A. Balsalobre *et al.*, *Science* **289**, 2344 (2000).
3. F. Damiola *et al.*, *Genes Dev.* **14**, 2950 (2000).
4. K. A. Stokkan, S. Yamazaki, H. Tei, Y. Sakaki, M. Menaker, *Science* **291**, 490 (2001).
5. S. Yamazaki *et al.*, *Science* **288**, 682 (2000).
6. D. K. Welsh, D. E. Logothetis, M. Meister, S. M. Reppert, *Neuron* **14**, 697 (1995).
7. A. Balsalobre, F. Damiola, U. Schibler, *Cell* **93**, 929 (1998).
8. S. H. Yoo *et al.*, *Proc. Natl. Acad. Sci. U.S.A.* **101**, 5339 (2004).
9. E. Nagoshi *et al.*, *Cell* **119**, 693 (2004).
10. D. K. Welsh, S. H. Yoo, A. C. Liu, J. S. Takahashi, S. A. Kay, *Curr. Biol.* **14**, 2289 (2004).
11. M. Stratmann, U. Schibler, *J. Biol. Rhythms* **21**, 494 (2006).
12. S. A. Brown, G. Zumbrunn, F. Fleury-Olela, N. Preitner, U. Schibler, *Curr. Biol.* **12**, 1574 (2002).
13. B. Kornmann, O. Schaad, H. Bujard, J. S. Takahashi, U. Schibler, *PLoS Biol.* **5**, e34 (2007).
14. F. T. Glaser, R. Stanewsky, *Curr. Biol.* **15**, 1352 (2005).
15. K. Lahiri *et al.*, *PLoS Biol.* **3**, e351 (2005).
16. Y. Liu, M. Merrow, J. J. Loros, J. C. Dunlap, *Science* **281**, 825 (1998).
17. T. Yoshida, Y. Murayama, H. Ito, H. Kageyama, T. Kondo, *Proc. Natl. Acad. Sci. U.S.A.* **106**, 1648 (2009).
18. L. Rensing, P. Ruoff, *Chronobiol. Int.* **19**, 807 (2002).
19. K. Hoffmann, *Oecologia* **3**, 184 (1969).
20. L. M. Prolo, J. S. Takahashi, E. D. Herzog, *J. Neurosci.* **25**, 404 (2005).
21. E. D. Herzog, R. M. Huckfeldt, *J. Neurophysiol.* **90**, 763 (2003).
22. Materials and methods are available as supporting material on *Science* Online.
23. S. Yamaguchi *et al.*, *Science* **302**, 1408 (2003).
24. C. M. Pennartz, M. T. de Jeu, N. P. Bos, J. Schaap, A. M. Geurtsen, *Nature* **416**, 286 (2002).
25. E. E. Abrahamson, R. Y. Moore, *Brain Res.* **916**, 172 (2001).
26. C. S. Kabrita, F. C. Davis, *Brain Res.* **1195**, 20 (2008).
27. P. L. Lowrey, J. S. Takahashi, *Annu. Rev. Genomics Hum. Genet.* **5**, 407 (2004).
28. H. Reinke *et al.*, *Genes Dev.* **22**, 331 (2008).
29. S. Yokota, M. Kitahara, K. Nagata, *Cancer Res.* **60**, 2942 (2000).
30. S. Honma, K. Honma, T. Shirakawa, T. Hiroshige, *Physiol. Behav.* **44**, 247 (1988).
31. S. Honma, T. Yasuda, A. Yasui, G. T. van der Horst, K. Honma, *J. Biol. Rhythms* **23**, 91 (2008).
32. O. Tataroglu, A. J. Davidson, L. J. Benvenuto, M. Menaker, *J. Biol. Rhythms* **21**, 185 (2006).
33. I. Grad, D. Picard, *Mol. Cell. Endocrinol.* **275**, 2 (2007).
34. S. A. Wadekar, D. Li, E. R. Sánchez, *Mol. Endocrinol.* **18**, 500 (2004).
35. J. Rutter, M. Reick, S. L. McKnight, *Annu. Rev. Biochem.* **71**, 307 (2002).
36. S. G. Ahn, D. J. Thiele, *Genes Dev.* **17**, 516 (2003).
37. A. Balsalobre, L. Marcacci, U. Schibler, *Curr. Biol.* **10**, 1291 (2000).
38. J. S. O'Neill, E. S. Maywood, J. E. Chesham, J. S. Takahashi, M. H. Hastings, *Science* **320**, 949 (2008).
39. H. S. Choi, B. Li, Z. Lin, E. Huang, A. Y. Liu, *J. Biol. Chem.* **266**, 11858 (1991).
40. D. D. Mosser, P. T. Kotzbauer, K. D. Sarge, R. I. Morimoto, *Proc. Natl. Acad. Sci. U.S.A.* **87**, 3748 (1990).
41. S. K. Crosthwaite, J. J. Loros, J. C. Dunlap, *Cell* **81**, 1003 (1995).
42. A. C. Diernfellner, T. Schafmeier, M. W. Merrow, M. Brunner, *Genes Dev.* **19**, 1968 (2005).
43. Y. Liu, N. Y. Garceau, J. J. Loros, J. C. Dunlap, *Cell* **89**, 477 (1997).
44. R. Kaushik *et al.*, *PLoS Biol.* **5**, e146 (2007).
45. R. Stanewsky *et al.*, *Cell* **95**, 681 (1998).
46. K. H. Low, C. Lim, H. W. Ko, I. Edery, *Neuron* **60**, 1054 (2008).
47. J. Majercak, D. Sidote, P. E. Hardin, I. Edery, *Neuron* **24**, 219 (1999).
48. H. Sehadova *et al.*, *Neuron* **64**, 251 (2009).
49. H. O. de la Iglesia, T. Cambras, W. J. Schwartz, A. Díez-Noguera, *Curr. Biol.* **14**, 796 (2004).

50. We thank members of the Takahashi laboratory for helpful discussions; S. Panda and J. B. Hogenesch for providing the U-2 OS cells; S. A. Kay for providing PG 99-465; and R. I. Morimoto for providing HSP70 antibody. We especially thank V. Kumar and K. Shimomura for suggestions and discussion on the manuscript. This work was supported by NIH P50 MH074924 to J.S.T. and T32 AG 20418 to E.D.B. J.S.T. is an Investigator and S.H.Y. was an Associate in the Howard Hughes Medical Institute. J.S.T. has a paid consulting relationship with, and owns stock in, ReSet Therapeutics, Inc., a biotechnology company that works on circadian rhythms and metabolism.

Supporting Online Material

www.sciencemag.org/cgi/content/full/330/6002/379/DC1
Materials and Methods
SOM Text
Figs. S1 to S8
References

29 January 2010; accepted 26 August 2010
10.1126/science.1195262

Cell Type–Specific Loss of BDNF Signaling Mimics Optogenetic Control of Cocaine Reward

Mary Kay Lobo,[1] Herbert E. Covington III,[1] Dipesh Chaudhury,[2] Allyson K. Friedman,[2] HaoSheng Sun,[1] Diane Damez-Werno,[1] David M. Dietz,[1] Samir Zaman,[1] Ja Wook Koo,[1] Pamela J. Kennedy,[1] Ezekiell Mouzon,[1] Murtaza Mogri,[3] Rachael L. Neve,[4] Karl Deisseroth,[3] Ming-Hu Han,[1,2] Eric J. Nestler[1,2]*

The nucleus accumbens is a key mediator of cocaine reward, but the distinct roles of the two subpopulations of nucleus accumbens projection neurons, those expressing dopamine D1 versus D2 receptors, are poorly understood. We show that deletion of TrkB, the brain-derived neurotrophic factor (BDNF) receptor, selectively from D1+ or D2+ neurons oppositely affects cocaine reward. Because loss of TrkB in D2+ neurons increases their neuronal excitability, we next used optogenetic tools to control selectively the firing rate of D1+ and D2+ nucleus accumbens neurons and studied consequent effects on cocaine reward. Activation of D2+ neurons, mimicking the loss of TrkB, suppresses cocaine reward, with opposite effects induced by activation of D1+ neurons. These results provide insight into the molecular control of D1+ and D2+ neuronal activity as well as the circuit-level contribution of these cell types to cocaine reward.

The nucleus accumbens (NAc) plays a crucial role in mediating the rewarding effects of drugs of abuse (*1*). However, little is known about the specific function of the two major populations of NAc projection neurons, which together make up >95% of all NAc neurons, in regulating these behaviors. These neurons, like those in the dorsal striatum, are medium spiny neurons (MSNs) divided into two subtypes based on their distinct projections through cortical-basal ganglia circuits and their differential gene expression, including enrichment of dopamine D1 versus D2 receptors (*2*). These two MSN subtypes, in dorsal striatum, exert balanced but antagonistic influences on their downstream outputs and behaviors, most notably motor behaviors (*3*–*5*), but their role, in NAc, in regulating reward behaviors still needs to be determined.

Although activation of both D1 and D2 receptors contributes to the rewarding effects of cocaine (*6*), current biochemical evidence has focused primarily on cocaine-induced molecular and structural changes in D1+ MSNs (*7*–*11*). For example, the extracellular signal-regulated kinase (ERK) pathway is induced in D1+ MSNs after cocaine exposure (*8*), an effect thought to be mediated directly via activation of D1 receptors (*12*, *13*). How-

[1]Fishberg Department of Neuroscience, Mount Sinai School of Medicine, New York, NY 10029, USA. [2]Pharmacology and System Therapeutics, Mount Sinai School of Medicine, New York, NY 10029, USA. [3]Department of Bioengineering, Stanford University, Stanford, CA 94305, USA. [4]Department of Brain and Cognitive Sciences, Massachusetts Institute of Technology, Cambridge, MA 02139, USA.

*To whom correspondence should be addressed. E-mail: eric.nestler@mssm.edu

ever, ERK activation by cocaine may occur through other mechanisms, such as brain-derived neurotrophic factor (BDNF) signaling (*13*), because BDNF and the activated form of its receptor, TrkB, are both up-regulated in the NAc after cocaine exposure (*14*–*16*). Furthermore, manipulations of BDNF and its TrkB receptor in this brain region potently modify rewarding responses to cocaine (*15*–*19*). Despite these important insights into BDNF signaling and dopaminergic transmission in the NAc, it remains unclear which MSN subtype is involved in these phenomena.

We first determined whether TrkB mRNA is differentially expressed in either MSN subtype using fluorescence activated cell sorting (FACS) to purify each MSN population from NAc and dorsal striatum of bacterial artificial chromosome (BAC) transgenic mice (*20*, *21*) expressing enhanced green fluorescent protein (eGFP) in D1+ or D2+ MSNs (D1-GFP or D2-GFP mice) (fig. S1) (*22*). TrkB gene expression was observed in both neuron populations (Fig. 1A), similar to previous studies demonstrating TrkB protein in each MSN subtype (*23*), but we observed a significant enrichment of TrkB mRNA in D2+ MSNs (Fig. 1A). Further studies are needed to confirm this enrichment in D2+ MSNs of the NAc specifically (*8*).

To assess the functional role of BDNF-TrkB signaling in D1+ and D2+ MSNs, we used D1-Cre or D2-Cre BAC transgenic mice in which Cre recombinase is expressed under D1 or D2 promoters and their regulatory elements (fig. S2) (*21*, *24*), combined with conditional floxed TrkB mice (flTrkB) (*25*). We then evaluated behavioral responses to cocaine in these mice when TrkB was selectively deleted from D1+ MSNs (D1-

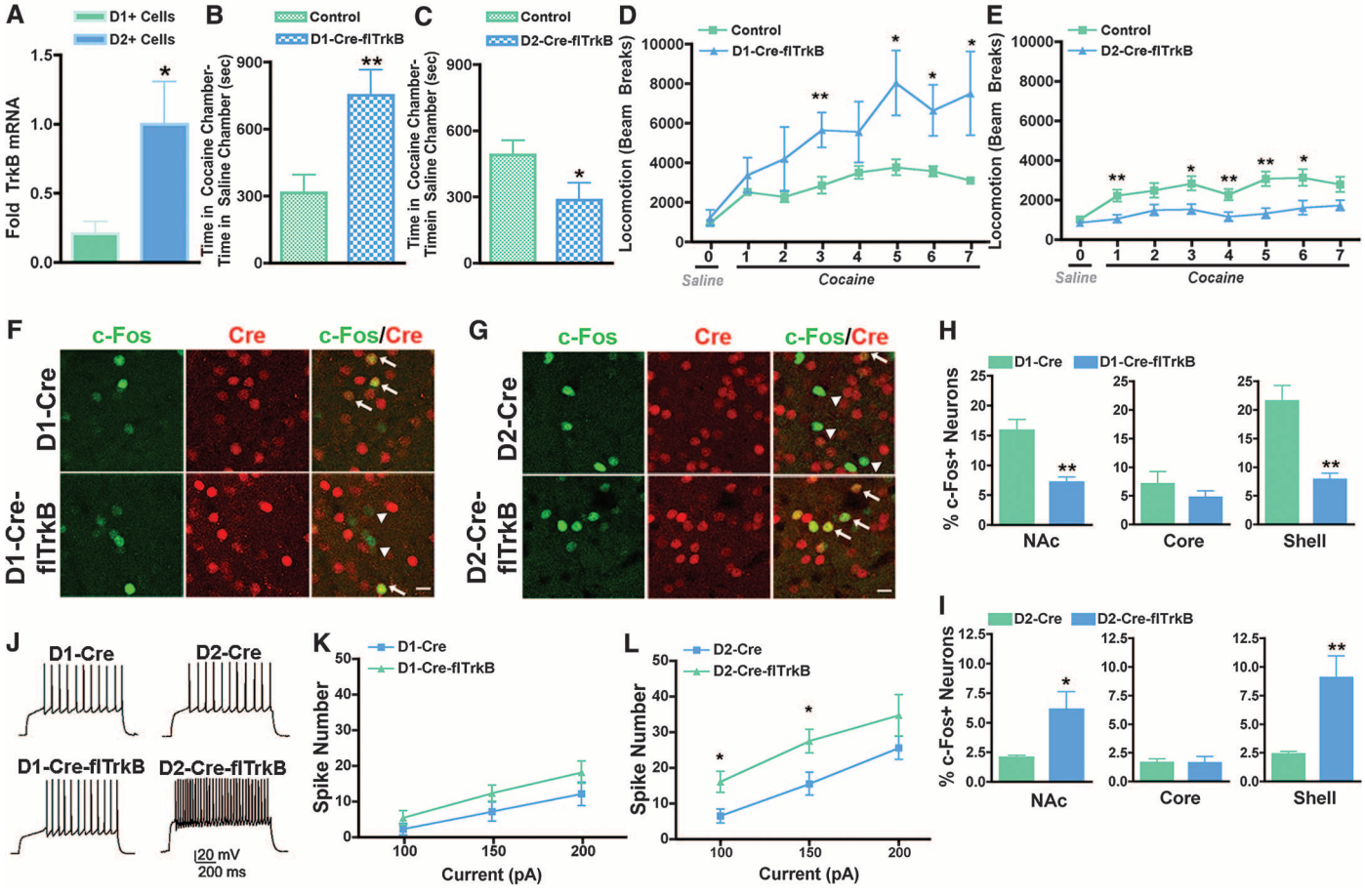

Fig. 1. Effect of selective deletion of TrkB from D1+ or D2+ MSNs on behavioral effects of cocaine, c-Fos induction, and neuronal excitability. (**A**) TrkB mRNA is expressed in D1+ and D2+ MSNs FACS-purified from D1-GFP and D2-GFP transgenic mice but is significantly enriched in D2+ MSNs (n = 4 per group; Student's t test, $P < 0.05$). (**B**) D1-Cre–flTrkB (n = 9) mice displayed enhanced cocaine conditioned place preference (CPP) relative to littermate controls (n = 10), whereas (**C**) D2-Cre–flTrkB mice (n = 14) exhibited decreased cocaine CPP compared with littermate controls (n = 16) (cocaine dose: 7.5 mg/kg intraperitoneally; Student's t test, $^{**}P < 0.01$, $^{*}P < 0.05$). (**D** and **E**) D1-Cre–flTrkB and D2-Cre–flTrkB mice and littermate controls were treated with saline on day 0 and with cocaine (10 mg/kg) on days 1 to 7, and locomotor activity was assessed over a 30-min time period. (D) D1-Cre–flTrkB mice (n = 6) displayed enhanced cocaine-induced locomotor activity after repeated cocaine administration compared with littermate controls (n = 7) [repeated measures two-way analysis of variance (ANOVA), genotype effect: $F_{(1,11)} = 6.20$, $P < 0.05$; day effect: $F_{(6,66)} = 5.50$, $P < 0.01$], while (E) D2-Cre–flTrkB mice (n = 10) showed decreased locomotor activity to acute and repeated cocaine relative to controls (n = 14) (repeated measures two-way ANOVA, genotype effect: $F_{(1,22)} = 9.98$, $P < 0.01$; day effect: $F_{(6,132)} = 4.00$, $P < 0.01$). Post hoc analysis reveals significant differences on specific cocaine days (Student's t test, $^{**}P < 0.01$, $^{*}P < 0.05$). Data represented as mean ± SEM. (**F** to **I**) c-Fos induction was examined 90 min after acute cocaine (20 mg/kg) by double immunolabeling of c-Fos and Cre in the NAc. (F and H) D1-Cre–flTrkB mice exhibited a significant decrease in double-labeled c-Fos (green) and Cre (red) neurons in the NAc after cocaine exposure compared with D1-Cre control mice, and this down-regulation is specific to the NAc shell. (G and I) In contrast, D2-Cre–flTrkB mice, relative to D2-Cre controls, displayed an increase in double-labeled c-Fos and Cre neurons in the NAc, an effect also specific to the NAc shell (n = 4 per group, Student's t test, $^{**}P < 0.01$, $^{*}P < 0.05$). Images displayed are from the NAc shell. Arrows represent neurons double labeled with c-Fos and Cre. Arrowheads represent c-Fos neurons that are not Cre positive. Scale bars, 20 μm. Data represented as mean ± SEM. (**J**) Sample traces obtained by 200 pA current injection (holding potential at −80 mV) in NAc shell MSNs in D1-Cre-flTrkB, D2-Cre-flTrkB, and their control mice injected with DIO-AAV-EYFP into the NAc for visualization of D1+ or D2+ MSNs. (**K** and **L**) D2+ MSNs in D2-Cre-flTrkB NAc (n = 3 animals), but not from D1+ MSNs in D1-Cre-flTrkB NAc (n = 4), display increased cell excitability after incremental steps in current injections (100, 150, and 200 pA) compared with respective controls, D2-Cre (n = 5) and D1-Cre (n = 8). Two-way ANOVA, $F_{(1,7)} = 13.23$, $P = 0.002$ (for D2+ MSNs), $F_{(1,11)} = 4.04$, $P = 0.054$ (for D1+ MSNs). Post hoc analysis reveals significant effects for 100 and 150 pA currents in D2+ MSNs, Student's t test, $^{*}P < 0.05$.

Cre–flTrkB) or D2+ MSNs (D2-Cre–flTrkB) in the NAc and dorsal striatum. In an unbiased cocaine conditioned place preference (CPP) paradigm, D1-Cre–flTrkB mice displayed a significant increase in cocaine preference relative to littermate controls (Fig. 1B). This increase in preference is opposite to findings from previous studies that disrupted BDNF-TrkB signaling nonselectively (i.e., in both MSN subtypes) in the NAc (*15*–*19*). However, our observations in the D2-Cre–flTrkB mice parallel these previous studies: D2-Cre–flTrkB mice exhibited a significant decrease in cocaine preference compared with their littermate controls (Fig. 1C). Importantly, these behavioral responses are likely mediated by loss of TrkB in D1+ and D2+ MSNs in the adult NAc, because both phenotypes were rescued by expressing TrkB, using herpes simplex virus (HSV-TrkB-GFP-mCherry), in the NAc of each mutant mouse line (fig. S3). The lack of developmental consequences of the TrkB deletion is also supported by several normal baseline behaviors in these mice (fig. S4).

To further explore the effects of selective deficits in BDNF-TrkB signaling on cocaine action, we analyzed locomotor activity and sensitization in the D1-Cre–flTrkB and D2-Cre–flTrkB mice. Cocaine and other stimulants increase locomotor activity upon initial exposures, with further increases (sensitization) seen after repeated exposure to the drug. Locomotor sensitization is thought to reflect biochemical adaptations that contribute to drug addiction and relapse (*26*). In agreement with our CPP experiments, we observed increased locomotor sensitization in D1-Cre–flTrkB mice compared with littermate controls and the opposite effect in D2-Cre–flTrkB mice (Fig. 1, D and E, and fig. S5).

To gain insight into the functional effect of the loss of BDNF-TrkB signaling from D1+ and D2+ neurons, we first measured c-Fos induction, a marker of neuronal function, in the NAc of D1-

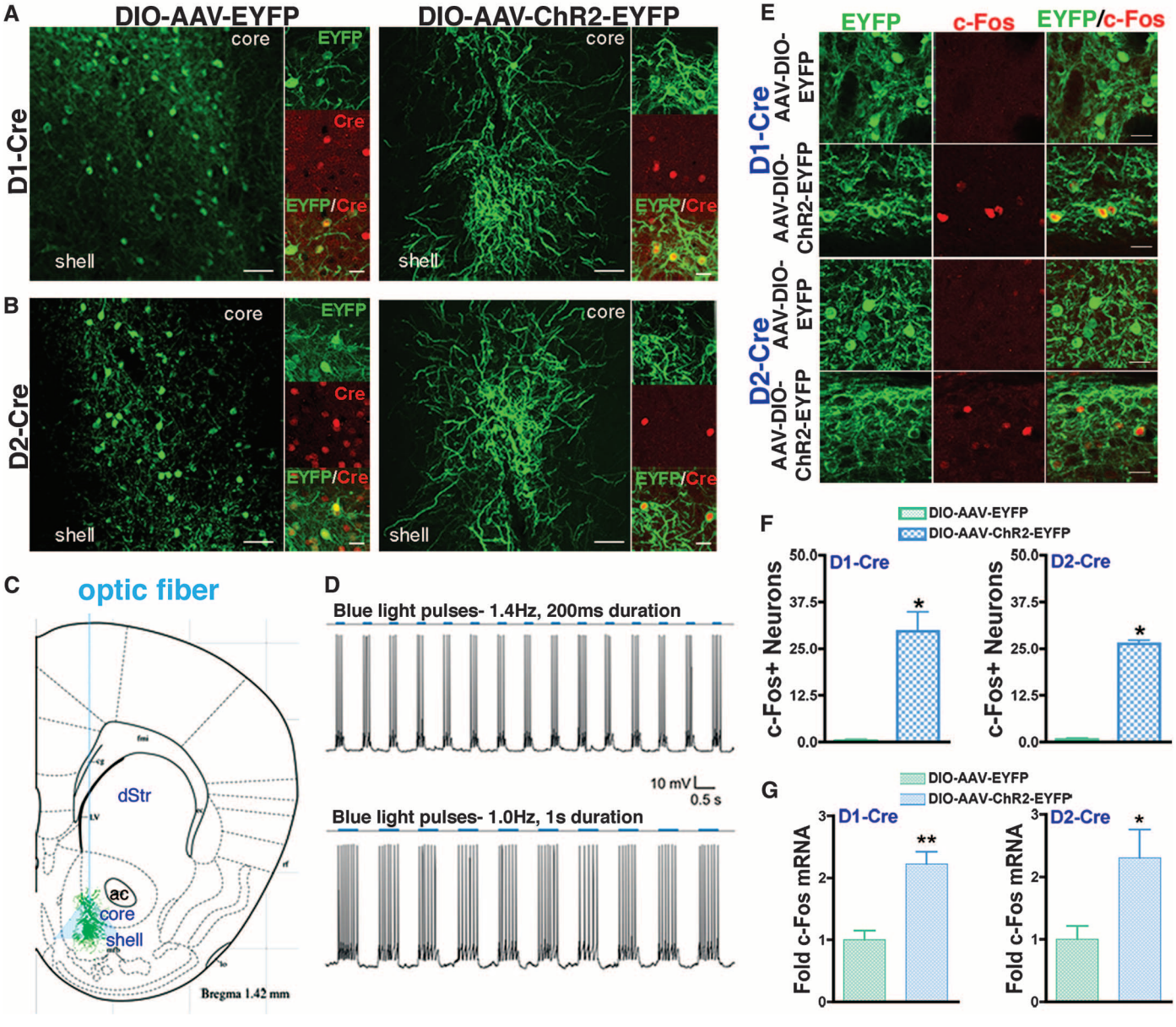

Fig. 2. In vivo and in vitro optogenetic control of D1+ or D2+ MSNs. (**A** and **B**) DIO-AAV-ChR2-EYFP or DIO-AAV-EYFP was injected into the NAc of D1-Cre and D2-Cre mice, resulting in ChR2-EYFP or EYFP expressing neurons (green) that also express Cre (red). Scale bars, 50 μm (low-power images) and 20 μm (high-power images). (**C**) Diagram of D1+ or D2+ ChR2 expressing MSNs and blue-light emission from the optic fiber. (**D**) Control of neuronal firing when a NAc MSN expressing DIO-AAV-ChR2-EYFP is exposed to blue light at 1.4 or 1.0 Hz. (**E**) c-Fos (red) expression is induced in D1+ or D2+ MSNs expressing ChR2 (green) that have been activated with 10-Hz blue-light stimulation but not EYFP expressing MSNs. Scale bars, 20 μm. (**F**) Quantification of (E) shows a significant increase in c-Fos expressing ChR2 expressing D1+ and D2+ MSNs compared with EYFP expressing controls after blue-light exposure ($n = 3$ per group, Student's t test, $^{*}P < 0.01$). (**G**) c-Fos mRNA is significantly up-regulated in the NAc after blue-light pulses in DIO-AAV-ChR2-EYFP expressing D1-Cre and D2-Cre mice ($n = 4$ to 5 per group, Student's t test, $^{**}P < 0.01$, $^{*}P < 0.05$).

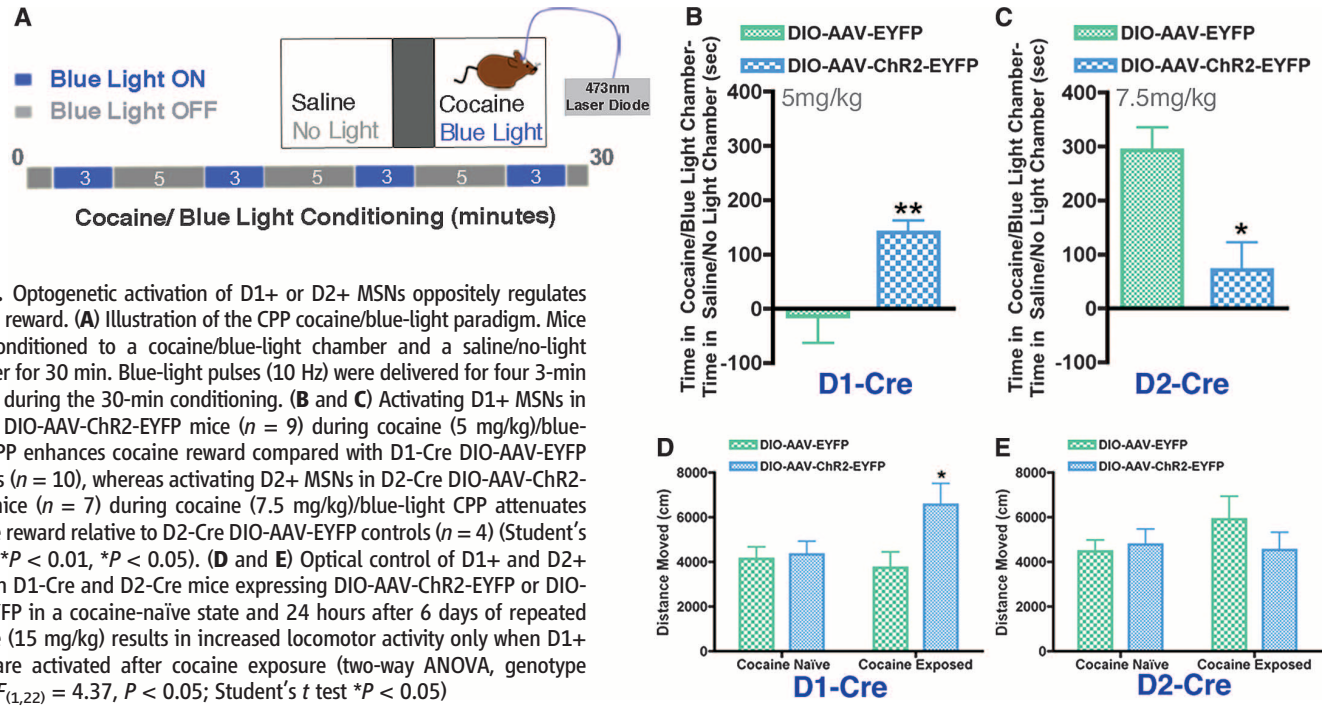

Fig. 3. Optogenetic activation of D1+ or D2+ MSNs oppositely regulates cocaine reward. (**A**) Illustration of the CPP cocaine/blue-light paradigm. Mice were conditioned to a cocaine/blue-light chamber and a saline/no-light chamber for 30 min. Blue-light pulses (10 Hz) were delivered for four 3-min periods during the 30-min conditioning. (**B** and **C**) Activating D1+ MSNs in D1-Cre DIO-AAV-ChR2-EYFP mice (n = 9) during cocaine (5 mg/kg)/blue-light CPP enhances cocaine reward compared with D1-Cre DIO-AAV-EYFP controls (n = 10), whereas activating D2+ MSNs in D2-Cre DIO-AAV-ChR2-EYFP mice (n = 7) during cocaine (7.5 mg/kg)/blue-light CPP attenuates cocaine reward relative to D2-Cre DIO-AAV-EYFP controls (n = 4) (Student's t test, $^{**}P < 0.01$, $^{*}P < 0.05$). (**D** and **E**) Optical control of D1+ and D2+ MSNs in D1-Cre and D2-Cre mice expressing DIO-AAV-ChR2-EYFP or DIO-AAV-EYFP in a cocaine-naïve state and 24 hours after 6 days of repeated cocaine (15 mg/kg) results in increased locomotor activity only when D1+ MSNs are activated after cocaine exposure (two-way ANOVA, genotype effect: $F_{(1,22)} = 4.37$, $P < 0.05$; Student's t test $^{*}P < 0.05$)

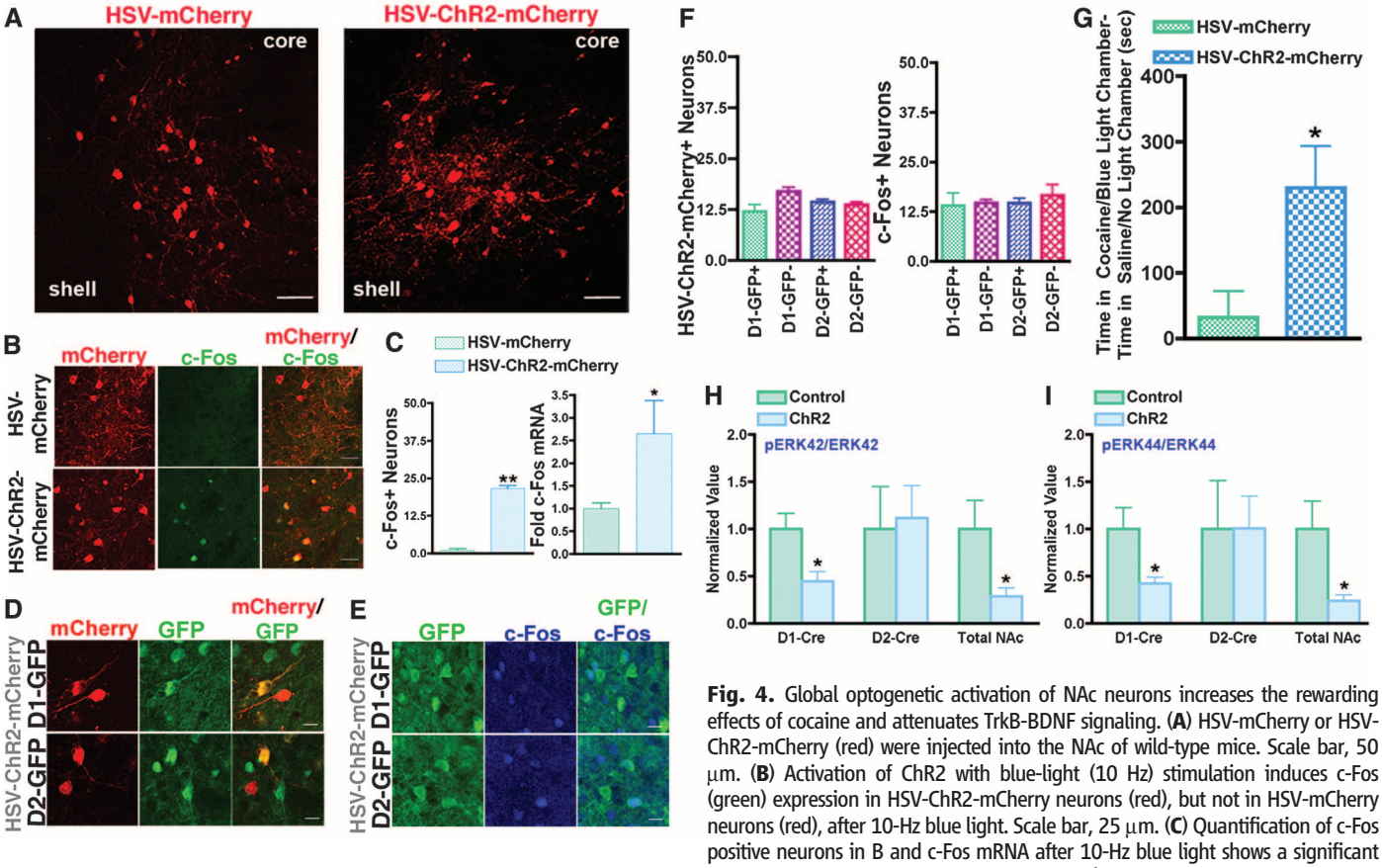

Fig. 4. Global optogenetic activation of NAc neurons increases the rewarding effects of cocaine and attenuates TrkB-BDNF signaling. (**A**) HSV-mCherry or HSV-ChR2-mCherry (red) were injected into the NAc of wild-type mice. Scale bar, 50 μm. (**B**) Activation of ChR2 with blue-light (10 Hz) stimulation induces c-Fos (green) expression in HSV-ChR2-mCherry neurons (red), but not in HSV-mCherry neurons (red), after 10-Hz blue light. Scale bar, 25 μm. (**C**) Quantification of c-Fos positive neurons in B and c-Fos mRNA after 10-Hz blue light shows a significant increase in c-Fos in HSV-ChR2-mCherry expressing NAc compared to HSV-mCherry expressing controls (n = 3 to 5 per group, Student's t test, $^{**}P < 0.01$, $^{*}P < 0.05$). (**D**) HSV-ChR2-mCherry (red) injection into the NAc of D1-GFP and D2-GFP mice mediates transgene expression in both D1+ and D2+ MSNs (GFP, green) and (**E**) c-Fos (blue) is induced by light in each MSN (green). Scale bar, 10 μm. (**F**) Quantification of (D) and (E) shows HSV-ChR2-mCherry and blue light induced c-Fos equally in D1+ and D2+ MSNs. (**G**) Mice expressing HSV-ChR2-mCherry (n = 9) in the NAc displayed enhanced preference for the cocaine (5 mg/kg)/blue-light chamber compared with control mice expressing HSV-mCherry (n = 8) (Student's t test, $P < 0.05$). (**H** and **I**) Blue-light simulation results in a significant decrease in phospho:total ERK levels (pERK42/ERK42 and pERK44/ERK44) in the NAc of D1-Cre DIO-AAV-ChR2-EYFP mice and mice expressing HSV-ChR2-mCherry relative to their controls (DIO-AAV-EYFP or HSV-mCherry) (n = 5 to 8 per group, Student's t test, $^{*}P < 0.05$).

Cre–flTrkB and D2-Cre–flTrkB mice after acute cocaine exposure (Fig. 1, F to I, and fig. S6). Previous studies have shown the selective induction of c-Fos in D1+ MSNs in response to cocaine (*8*, *12*). D1-Cre–flTrkB mice exhibited a significant decrease in c-Fos+ D1+ MSNs in the NAc, an effect specific to the NAc shell and not seen in the NAc core, relative to control mice (Fig. 1, F and H, and fig. S6). In striking contrast, D2-Cre–flTrkB mice displayed a significant increase in c-Fos+ D2+ MSNs in the NAc, also specific to shell, compared to controls (Fig. 1, G and I, and fig. S6). We observed no difference in c-Fos expression in dorsal striatum, and saline-treated controls displayed minimal c-Fos induction (fig. S6).

The c-Fos data suggest that loss of BDNF-TrkB signaling alters the function of both D1+ and D2+ NAc neurons, although the nature of the functional changes are difficult to infer, because c-Fos induction, which is often used as a marker of neuronal activation, can also indicate changes in signaling cascades without a change in firing or even neuronal inhibition (*27*, *28*). We thus directly investigated the excitability of each MSN subtype in the NAc shell after loss of TrkB. We observed a dramatic increase in neuronal firing in response to current injections in D2+ MSNs in the D2-Cre-flTrkB mice (Fig. 1, J and L). Although no significant change in baseline excitability was observed in D1+ MSNs in the D1-Cre-flTrkB mice, there was a trend for increased excitability ($P = 0.054$) (Fig. 1, J and K), and we found down-regulation of five K^+ channel subunits in the NAc of D1-Cre-flTrkB mice after repeated exposure to cocaine (table S1), consistent with enhanced excitability of these MSNs as well.

Given these direct links between loss of TrkB and enhanced excitability of NAc MSNs, we next studied directly the influence of increased activity of these MSN subtypes on behavioral responses to cocaine using optogenetic technologies (*29*–*31*). We expressed channelrhodopsin-2 (ChR2), a 473-nm blue light–activated cation channel (*29*), in D1+ or D2+ MSNs in the NAc using D1-Cre and D2-Cre mice and conditional adeno-associated viruses (AAVs), DIO-AAV-ChR2-EYFP and the control DIO-AAV-EYFP, that express only in the presence of Cre recombinase (*31*) (Fig. 2, A and B). The vectors were stereotaxically injected into the NAc of D1-Cre and D2-Cre mice, followed by a cannula implant to which an optic fiber was secured to deliver blue light directly into the virus-infected NAc (Fig. 2, A to C). This approach enables temporally precise control of NAc neuronal firing (Fig. 2D). To further validate the technique in vivo, we demonstrated c-Fos induction after 10-Hz blue-light pulses in D1+ and D2+ MSNs expressing DIO-AAV-ChR2-EYFP (Fig. 2, E to G, and fig. S7).

To evaluate the behavioral response to cocaine when D1+ versus D2+ MSNs are activated selectively, we used a CPP paradigm, in which D1-Cre and D2-Cre mice, expressing DIO-AAV-ChR2-EYFP or DIO-AAV-EYFP in the NAc, were conditioned to cocaine plus 10-Hz blue-light pulses in one chamber, with saline and no light used for the opposite chamber (Fig. 3A). D1-Cre mice expressing DIO-AAV-ChR2-EYFP in the NAc displayed a significant increase in cocaine/blue-light preference compared with the D1-Cre DIO-AAV-EYFP control group (Fig. 3B). In contrast, D2-Cre mice expressing DIO-AAV-ChR2-EYFP exhibited a significant attenuation of cocaine/blue-light preference relative to controls (Fig. 3C). We observed no difference in blue-light preference in D1-Cre or D2-Cre mice expressing DIO-AAV-ChR2-EYFP in the absence of cocaine (fig. S8). These data implicate a role for activation of D1+ MSNs in enhancing the rewarding effects of cocaine, with activation of D2+ MSNs antagonizing cocaine reward. These findings are consistent with previous studies, in which disruption of glutamatergic NMDA receptor signaling or loss of c-Fos in D1+ MSNs reduced cocaine sensitization or CPP (*11*, *32*). Conversely, ablation of D2+ MSNs increases the locomotor and rewarding effects of another stimulant, amphetamine (*33*).

We next evaluated locomotor activity when the two NAc MSN subtypes are activated under cocaine-naïve and exposed conditions. We detected no change in locomotion in cocaine-naïve mice when either MSN subtype was activated relative to nonstimulated controls (Fig. 3, D and E). However, 24 hours after 6 days of repeated cocaine administration (15 mg/kg), blue-light pulses to the NAc in D1-Cre mice expressing DIO-AAV-ChR2-EYFP increased locomotor activity compared with controls (Fig. 3D), with no change observed upon activation of D2+ MSNs (Fig. 3E). These data are in accordance with the prevailing model of dorsal striatal function (*3*–*5*), which implicates activation of D1+ MSNs in promoting motor function and suggests that repeated exposure to cocaine enhances the output of D1+ MSNs of the NAc.

It is unclear what behavioral effects occur when both MSN subtypes in the NAc are activated during cocaine exposure, which likely occurs through glutamatergic inputs to this brain region. There is evidence implicating a hypoactive NAc in the cocaine-addicted state (*34*, *35*), but data also support activation of some neurons during operant cocaine behaviors and context-dependent cocaine sensitization (*34*, *36*). Additionally, high-frequency deep-brain stimulation of the NAc, which may inhibit neuronal activity, attenuates an animal's reinstatement to cocaine seeking, and excitatory AMPA receptor-mediated glutamatergic transmission has been shown to induce relapse to cocaine addiction (*37*, *38*). We injected herpes simplex viruses, HSV-ChR2-mCherry or HSV-mCherry, into the NAc of wild-type mice (Fig. 4A) to optically control global NAc neuronal activity during cocaine/blue-light CPP (Fig. 3A). We found that HSV-ChR2-mCherry is expressed equally in D1+ and D2+ MSNs (Fig. 4, D and F) and that blue-light exposure induces equivalent c-Fos levels in these neurons (Fig. 4, B, C, E, and F, and fig. S7). Mice expressing HSV-ChR2-mCherry in the NAc displayed enhanced reward to cocaine/blue light relative to control mice (Fig. 4G).

Finally, we probed for changes in the phosphorylated (active) form of ERK (pERK), which is downstream of BDNF-TrkB signaling (*13*) and is dynamically regulated by both neuronal activation and inhibition (*39*–*41*), to further link loss of TrkB with ChR2-induced activation of D1+ and D2+ MSNs. We observed down-regulation of pERK42 and pERK44 in D1-Cre DIO-AAV-ChR2-EYFP–activated NAc compared with controls, with no change seen in D2-Cre DIO-AAV-ChR2-EYFP–activated NAc (Fig. 4, H and I). Similar to selective activation of D1+ MSNs, we observed decreased pERK42 and pERK44 in HSV-ChR2-mCherry activated NAc (Fig. 4, H and I). Thus, optogenetic stimulation of D1+ MSNs impairs a downstream target of BDNF-TrkB signaling, which implicates common downstream effects upon loss of TrkB, and optogenetic activation, in D1+ MSNs, consistent with the common behavioral effects seen under these conditions. Although no change in pERK was observed in stimulated D2+ MSNs, data cited above revealed common induction of c-Fos and increased neuronal excitability upon loss of TrkB and optogenetic stimulation (Fig. 1, G, I, J, and L, and Fig. 2, D to G).

The present study indicates opposite roles for D1+ and D2+ MSNs in mediating the behavioral effects of cocaine. The potent influence of BDNF-TrkB signaling in the NAc on cocaine reward (*15*–*19*) is mediated through D2+ MSNs, because TrkB mRNA is enriched in these neurons and selective deletion of TrkB from D2+ MSNs attenuates cocaine reward. Furthermore, deletion of TrkB from D2+ MSNs increases their neuronal excitability and reactivity to cocaine (as evidenced by increased c-Fos induction), and mimics the ability of direct activation of these neurons, via optogenetic tools, to attenuate behavioral responses to cocaine.

Our D1+ MSN data are more complex. We observe enhanced cocaine reward when D1+ MSNs are activated optogenetically and when TrkB is deleted selectively from them; however, the latter results in decreased c-Fos induction by cocaine without a significant change in baseline neuronal excitability. Nonetheless, the down-regulation of several K^+ channel subunits in the NAc of D1-Cre-flTrkB mice suggests enhanced neuronal activity in response to cocaine exposure, which is consistent with the behavioral effects seen with optogenetic activation of D1+ MSNs. Our finding of enhanced behavioral responses to cocaine in the D1 TrkB knockouts, when cocaine induction of c-Fos is lost, is partly consistent with the report that deletion of c-Fos in D1+ MSNs potentiates cocaine reward (*11*), although our data contrast with other observations of this previous study, which may be due to loss of c-Fos in whole striatum in that report. Furthermore, the ability of acute cocaine to induce c-Fos, which occurs selectively in D1+ MSNs, declines with repeated drug administration (*8*, *12*, *42*). The blunted c-Fos response, which we see after acute cocaine exposure in D1+ MSNs lacking TrkB, is therefore similar to wild-type D1+ MSNs that have been exposed to repeated cocaine. Finally, we cannot

rule out trans-synaptic effects in these phenomena, for example, the possibility that D2+ MSNs, expressing normal levels of TrkB, may alter cocaine responses of D1+ MSNs in the D1-CreflTrkB mice, resulting in loss of c-Fos induction.

Together, our data support a model in which loss of TrkB in D2+ MSNs enhances their excitability, which then directly desensitizes the rewarding effects of cocaine. In contrast, loss of TrkB in D1+ MSNs may similarly enhance their activity, but only when exposed to cocaine, as evidenced by K^+ channel down-regulation, with such activity increasing the rewarding effects of cocaine. These opposite effects exerted by activation of each MSN subtype on cocaine reward is consistent with current models of basal ganglia function, which posit that D1+ versus D2+ MSNs act in opposition through the direct and indirect pathways, respectively, to produce balanced behavioral output (*3*–*5*). It is plausible that, in the addicted brain, there may be an imbalance of these two MSNs. This imbalance may occur through an overactive D1+ MSN pathway as well as through decreased activity of D2+ MSNs, the latter mediated via enhanced BDNF-TrkB signaling. Expanding our understanding of the complex control of drug reward by the two main subtypes of NAc MSNs could help steer the development of treatments of drug addiction targeted selectively to D1+ versus D2+ MSN subtypes.

References and Notes

1. S. E. Hyman, R. C. Malenka, E. J. Nestler, *Annu. Rev. Neurosci.* **29**, 565 (2006).
2. C. R. Gerfen, *Annu. Rev. Neurosci.* **15**, 285 (1992).
3. R. L. Albin, A. B. Young, J. B. Penney, *Trends Neurosci.* **12**, 366 (1989).
4. G. E. Alexander, M. R. DeLong, P. L. Strick, *Annu. Rev. Neurosci.* **9**, 357 (1986).
5. A. M. Graybiel, *Curr. Biol.* **10**, R509 (2000).
6. D. W. Self, in *The Dopamine Receptors*, K. A. Neve, Ed. (Humana Press, New York, 2010), pp. 479–524.
7. K. W. Lee *et al.*, *Proc. Natl. Acad. Sci. U.S.A.* **103**, 3399 (2006).
8. J. Bertran-Gonzalez *et al.*, *J. Neurosci.* **28**, 5671 (2008).
9. M. B. Kelz *et al.*, *Nature* **401**, 272 (1999).
10. F. Ambroggi *et al.*, *Nat. Neurosci.* **12**, 247 (2009).
11. J. Zhang *et al.*, *J. Neurosci.* **26**, 13287 (2006).
12. E. Valjent *et al.*, *J. Neurosci.* **20**, 8701 (2000).
13. L. Lu, E. Koya, H. Zhai, B. T. Hope, Y. Shaham, *Trends Neurosci.* **29**, 695 (2006).
14. J. W. Grimm *et al.*, *J. Neurosci.* **23**, 742 (2003).
15. D. L. Graham *et al.*, *Nat. Neurosci.* **10**, 1029 (2007).
16. K. R. Crooks, D. T. Kleven, R. M. Rodriguiz, W. C. Wetsel, J. O. McNamara, *Neuropharmacology* **58**, 1067 (2010).
17. D. L. Graham *et al.*, *Biol. Psychiatry* **65**, 696 (2009).
18. A. Bahi, F. Boyer, V. Chandrasekar, J. L. Dreyer, *Psychopharmacology (Berl.)* **199**, 169 (2008).
19. B. A. Horger *et al.*, *J. Neurosci.* **19**, 4110 (1999).
20. S. Gong *et al.*, *Nature* **425**, 917 (2003).
21. E. Valjent, J. Bertran-Gonzalez, D. Hervé, G. Fisone, J. A. Girault, *Trends Neurosci.* **32**, 538 (2009).
22. M. K. Lobo, S. L. Karsten, M. Gray, D. H. Geschwind, X. W. Yang, *Nat. Neurosci.* **9**, 443 (2006).
23. A. Y. Freeman, J. J. Soghomonian, R. C. Pierce, *Neuroscience* **117**, 147 (2003).
24. S. Gong *et al.*, *J. Neurosci.* **27**, 9817 (2007).
25. B. W. Luikart, S. Nef, T. Shipman, L. F. Parada, *Neuroscience* **117**, 847 (2003).
26. T. E. Robinson, K. C. Berridge, *Philos. Trans. R. Soc. Lond. B Biol. Sci.* **363**, 3137 (2008).
27. J. I. Morgan, T. Curran, *Annu. Rev. Neurosci.* **14**, 421 (1991).
28. J. D. Mikkelsen, A. Søderman, A. Kiss, N. Mirza, *Eur. J. Pharmacol.* **519**, 223 (2005).
29. V. Gradinaru *et al.*, *J. Neurosci.* **27**, 14231 (2007).
30. R. D. Airan, K. R. Thompson, L. E. Fenno, H. Bernstein, K. Deisseroth, *Nature* **458**, 1025 (2009).
31. J. A. Cardin *et al.*, *Nat. Protoc.* **5**, 247 (2010).
32. C. L. Heusner, R. D. Palmiter, *J. Neurosci.* **25**, 6651 (2005).
33. P. F. Durieux *et al.*, *Nat. Neurosci.* **12**, 393 (2009).
34. L. L. Peoples, A. V. Kravitz, K. Guillem, *ScientificWorldJournal* **7**, 22 (2007).
35. W. A. Carlezon Jr., M. J. Thomas, *Neuropharmacology* **56** (suppl. 1), 122 (2009).
36. E. Koya *et al.*, *Nat. Neurosci.* **12**, 1069 (2009).
37. J. L. Cornish, P. W. Kalivas, *J. Neurosci.* **20**, RC89 (2000).
38. F. M. Vassoler *et al.*, *J. Neurosci.* **28**, 8735 (2008).
39. S. Impey, K. Obrietan, D. R. Storm, *Neuron* **23**, 11 (1999).
40. S. Paul, A. C. Nairn, P. Wang, P. J. Lombroso, *Nat. Neurosci.* **6**, 34 (2003).
41. J.-L. Cao *et al.*, *Proc. Natl. Acad. Sci. U.S.A.*, in press (2010).
42. W. Renthal *et al.*, *J. Neurosci.* **28**, 7344 (2008).

43. We thank N. Heintz and P. Greengard (Rockefeller University) and C.R. Gerfen (NIH/NIMH) for providing us with D1-Cre, D2-Cre, D1-GFP, and D2-GFP mice. We thank M. S. Levine and X. W. Yang (UCLA) for providing us with D1-GFP and D2-GFP mice. We thank L. Parada (UTSouthwestern) for providing us with the flTrkB mice. We thank V. Lessman (Otto-von-Guericke-Universität) for providing us with the TrkB (full length)-GFP construct. This work was supported by grants from the National Institute on Drug Abuse, and M.K.L. is supported by the Drug Abuse Research Training Program at MSSM (NIDA T32 DA007135-26A2).

Supporting Online Material

www.sciencemag.org/cgi/content/full/330/6002/385/DC1
Materials and Methods
Figs. S1 to S8
Table S1
References

17 February 2010; accepted 8 September 2010
10.1126/science.1188472

Salmonella Pathogenesis and Processing of Secreted Effectors by Caspase-3

C. V. Srikanth,[1,2]* Daniel M. Wall,[1,3]* Ana Maldonado-Contreras,[2] Hai Ning Shi,[1] Daoguo Zhou,[4] Zachary Demma,[2] Karen L. Mumy,[1,2] Beth A. McCormick[1,2]†

The enteric pathogen *Salmonella enterica* serovar Typhimurium causes food poisoning resulting in gastroenteritis. The *S.* Typhimurium effector *Salmonella* invasion protein A (SipA) promotes gastroenteritis by functional motifs that trigger either mechanisms of inflammation or bacterial entry. During infection of intestinal epithelial cells, SipA was found to be responsible for the early activation of caspase-3, an enzyme that is required for SipA cleavage at a specific recognition motif that divided the protein into its two functional domains and activated SipA in a manner necessary for pathogenicity. Other caspase-3 cleavage sites identified in *S.* Typhimurium appeared to be restricted to secreted effector proteins, which indicates that this may be a general strategy used by this pathogen for processing of its secreted effectors.

Salmonella enterica serovar Typhimurium acquires virulence via a 40-kb segment of the bacterial chromosome designated *Salmonella* pathogenicity island 1 (SPI-1) (*1*). SPI-1 contains more than 25 genes encoding structural components and substrates of a type III protein-secretion system that mediates the translocation of effector proteins from *Salmonella* into mammalian cells (*1*). One of these, *Salmonella* invasion protein A (SipA), is a bifunctional molecule responsible for promoting actin polymerization, a process that facilitates bacterial entry into epithelial cells (*2*), and is required to trigger signal transduction cascades that promote polymorphonuclear leukocyte (PMN) migration across the intestinal epithelium (*3*). The actin binding function of SipA is known to be localized to a C-terminal fragment (amino acids 426 to 684) termed SipAb (*4*). We have reported that the N-terminal fragment of the SipA effector protein (amino acids 2 to 425) harbors the functional domain that induces PMN transepithelial migration (*5*), which underlies the clinical manifestations of salmonellosis.

We found a caspase-3 motif, DEVD (*6*), at amino acid positions 431 to 434 (Fig. 1A) of SipA at the junction between the two functional domains (*7*). Treatment of a purified fraction of SipA to activated caspase-3 enzyme generated a predicted fragment (55 kD; Fig. 1B) and confirmed that the SipA DEVD cleavage motif was functionally active. The expected lower molecular weight band was not seen, most likely from lack of antibody recognition; however, mutation of the caspase-3 site by changing aspartic acid at position four to alanine (A) (DEVD→DEVA; termed caspase site mutant, csm-SipA) rendered SipA insensitive to caspase-3 cleavage (Fig. 1B).

Although caspase-3 is a frequently activated death protease, this enzyme also catalyzes specific cleavage of many cellular proteins (*8*) and promotes cell proliferation and inflammation

[1]Department of Pediatric Gastroenterology and Nutrition, Harvard Medical School and Massachusetts General Hospital, Boston, MA 02129, USA. [2]Department of Molecular Genetics and Microbiology, University of Massachusetts Medical School, 55 Lake Avenue North, Worcester, MA 01655, USA. [3]Institute of Infection, Immunity and Inflammation, College of Medical, Veterinary, and Life Sciences, University of Glasgow, Glasgow G12 8QQ, UK. [4]Department of Biological Sciences, Purdue University, West Lafayette, IN 47907, USA.

*These authors contributed equally to this work.
†To whom correspondence should be addressed. E-mail: Beth.McCormick@umassmed.edu

without inducing apoptosis (*9*). We found that *S.* Typhimurium infection of model intestinal epithelia induced the activated form of the caspase-3 enzyme within 2 hours and persisted for at least 4 hours (Fig. 1C and fig. S1, A and B). Apoptosis occurred 24 hours after infection of epithelial cells (*10*). No activation of other initiator cysteine proteases known to play essential roles in apoptosis (i.e., caspase-1 or caspase-8) (Fig. 1C) was observed. Staurosporine treatment, which induces apoptosis and was used as a positive control, showed significant annexin V staining, whereas the *S.* Typhimurium treated T84 cells showed minimal annexin V binding and no propidium iodide staining (Fig. 1D), confirming that early after infection this pathogen can activate caspase-3 without inducing apoptosis or necrosis.

A plasmid bearing the mutant clone pCSM-SipA (for plasmid caspase site mutant) was transformed into both *Escherichia coli* F-18, an intestinal commensal isolate (*11*), and *Salmonella*. Because *E. coli* F-18 secretes SipA through the flagella basal body (*5*), we used this strain to assess the ability of the caspase-3 site mutant to drive PMN transepithelial migration in the absence of other *S.* Typhimurium virulence determinants. By using our in vitro inflammatory model system (*12*), we found that the mutant had a reduced capacity to induce PMN transepithelial migration (>95%; $P < 0.01$) compared with the *E. coli* F-18 strain expressing the wild-type SipA protein (pSipA) (Fig. 1E).

Salmonella enterica serovar Dublin was used in the in vivo enteritis model because this strain constitutively expresses proteins from the pBH plasmid and allows the expression of proteins of interest in animal infections (*5*, *13*, *14*). Macroscopic inspection of the intestines revealed inflammation of the cecum in infections with both wild-type *Salmonella* and the ΔSipA mutant strain expressing SipA (ΔSipA/pSipA) (Fig. 2A). By contrast, no overt signs of intestinal inflammation were observed in mice infected with the ΔSipA mutant strain expressing the caspase-3 site mutant (ΔSipA/pCSM-SipA), the ΔSipA mutant strain, or the buffer negative control (Fig. 2A). Histological evaluation of hematoxylin and eosin (H&E)–stained tissue sections and the pathology scores for disease severity showed significant inflammation of the proximal colons of mice infected with either wild-type *Salmonella* or ΔSipA/pSipA, as determined by colonic wall thickening, crypt elongation, PMN infiltration, epithelial erosion, and edema (Fig. 2, A and C). By contrast, infections with both ΔSipA/pCSM-SipA and ΔSipA mutant strains did not cause pronounced intestinal inflammation (Fig. 2, A and C). Quantification of infiltrating PMNs, as determined by myeloperoxidase (MPO) activity, supported these observations (fig. S2).

Cleavage of the SipA DEVD recognition site appears to be important for promoting proinflammatory responses and suggests a role for caspase-3. Consistent with this notion, *Salmonella* is less virulent in caspase-3 knockout (caspase-$3^{-/-}$) mice, as judged by gross cecal and histopathologic examination of the proximal colons of *Salmonella*-infected caspase-$3^{-/-}$ mice, which reveals significantly less intestinal pathology compared with *Salmonella*-infected wild-type mice (Fig. 2, B and D). In addition, reduced *S.* Typhimurium invasiveness in bone marrow–derived macrophages from caspase-$3^{-/-}$ mice, compared with wild-type macrophages, further indicates that a lack of caspase-3 has an impact on the infection outcome (fig. S2C). Likewise, in vitro inhibition of epithelial-derived caspase-3 by small interfering RNA (siRNA) significantly reduced *S.* Typhimurium–induced PMN transepithelial migration (Fig. 2E), as did pharmacologic inhibition of caspase-3 (fig. S3).

Remarkably, the SipA effector itself stimulated activation of caspase-3, whereas the ΔSipA mutant strain was not able to (Fig. 3, A and B), which indicates that the effector is necessary and sufficient to promote activation of caspase-3. Moreover, *S.* Typhimurium nonpolar, isogenic mutant strains defective in SipA expression and secretion (ΔSPI-1 and ΔInvG, respectively) or lacking transcription factors controlling SipA expression (ΔHilA) also failed to induce caspase-3 activation (Fig. 3C). Mutations in genes encoding other effector proteins not associated with SipA expression, such as *avrA*, did not adversely affect the expression of activated caspase-3 (Fig. 3C). Caspase-3 expression measured during *S.* Typhimurium infection of epithelial cells by quantitative polymerase chain reaction showed that no new pro-caspase-3 was being produced (fig. S4). However, activated caspase-3 does appear in the membrane-insoluble fraction (Fig. 2D), suggesting that *S.* Typhimurium infection modifies existing pools of caspase-3.

In the intestinal lumen, several environmental cues trigger the up-regulation of the *Salmonella* SPI-1 type III secretion system (e.g., osmolarity and oxygen tension) (*15*, *16*). Therefore, upon colonization, it is likely that *Salmonella* has begun to secrete effector proteins into the intestinal milieu. Although SipA is a type III secreted protein, it is unique in its ability to act extracellularly and elicit a proinflammatory response (*5*). We hypothesized that processing of SipA by caspase-3 cleavage occurs at the apical epithelial surface, liberating the N-terminal SipA domain for its extracellular function, which presumably requires binding to a surface receptor (*3*). This offers an explanation of why the N-terminal domain, when expressed independently of the C-terminal domain, is a more potent inflammatory stimulus than the full-length protein (*5*).

In support of this hypothesis, *S.* Typhimurium infection of polarized T84 monolayers resulted in the preferential secretion of activated caspase-3 in a SipA-dependent manner into the apical epithelial compartment but not the basolateral com-

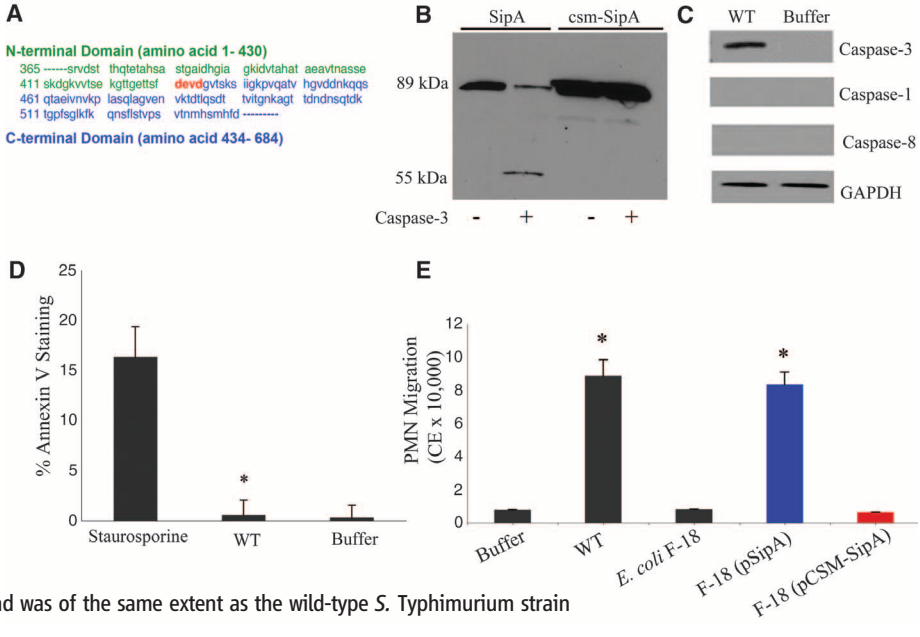

Fig. 1. The effector protein SipA harbors a functional caspase-3 cleavage site. (**A**) Primary amino acid sequence (*7*) of SipA showing the caspase-3 cleavage site (highlighted in red) between the N-terminal (green) and C-terminal (blue) domains. (**B**) Immunoblot of SipA in the absence and presence of caspase-3. The full-length 89-kD SipA effector is cleaved, resulting in production of the 55-kD truncated N-terminal domain. The caspase site mutant SipA (csm-SipA) is not cleaved by caspase-3. (**C**) Whole-cell extracts from T84 cells that were uninfected or infected with wild-type *S.* Typhimurium (WT) were probed with antibody against caspase-3, -1, or -8 and a glyceraldehyde-3-phosphate dehydrogenase (GAPDH) control showing equal loading of lanes. (**D**) Annexin V staining as a measurement of apoptosis in T84 cells 2 hours postinfection with wild-type *S.* Typhimurium (WT). Staurosporine treatment served as the positive control for apoptosis. *$P < 0.01$. (**E**) Alteration of the SipA caspase-3 motif rendered SipA resistant to cleavage and attenuated the ability of *S.* Typhimurium to induce neutrophil (PMN) movement. PMN migration induced by SipA (blue bars) was far greater than with the pCSM-SipA (red bars) and was of the same extent as the wild-type *S.* Typhimurium strain (WT). *$P < 0.01$; CE, cellular equivalent.

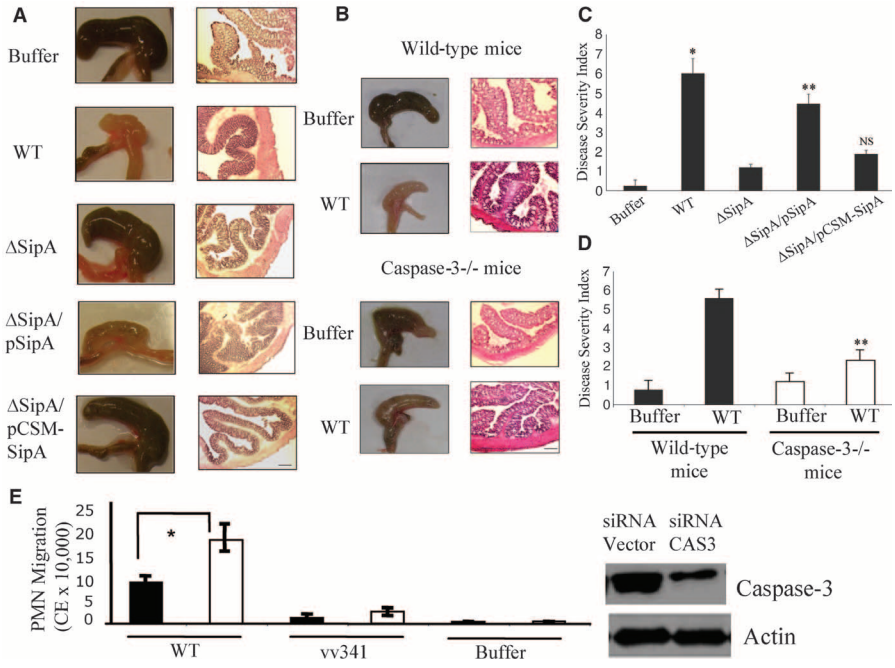

Fig. 2. Mutation of the caspase-3 cleavage site attenuates the ability of the SipA effector to promote inflammation in an in vivo mouse model. (**A**) Disease pathology after a 48-hour infection of mice with different strains of *Salmonella*. The left images show gross morphology of the cecum, whereas the right images show the histopathology of the sections stained with H&E. The magnification bar indicates 100 μM. The ΔSipA mutant strain was complemented with either SipA (pSipA) or pCSM-SipA. Phosphate-buffered saline (PBS) treatment was the negative control. (**B**) Disease pathology after a 48-hour infection of wild-type mice and caspase-3 knockout mice (both on C57BL/6 background). The left images show the gross morphology of the cecum, and H&E-stained sections of the proximal colon are shown on the right. Magnification bar, 100 μM. WT refers to the wild-type *Salmonella* strain used for infection, and buffer refers to the PBS-treated negative control. (**C**) The colonic histopathology for the sections shown in (A) was quantified by using a disease severity index (scale from 0 to 8), with 0 scored normal and a score of 8 showing the most substantial level of disease pathology ($n = 5$). Sections were scored blinded by a trained pathologist. Data represent means ± SD. *$P <$ 0.01; **$P < 0.05$; NS, not significant. (**D**) The colonic histopathology for sections in (B) was quantified by using the same disease severity index (scale 0 to 8, $n = 5$). Data represent means ±SD. **$P < 0.05$. (**E**) PMN transepithelial migration after siRNA knockdown of caspase-3 in HCT8 cells expressing siRNA against caspase-3 (black bars) or containing a vector control (white bars). Cells were infected with either wild-type *S.* Typhimurium (WT) or a ΔHilA isogenic negative mutant (vv341), which is incapable of inducing migration (*$P < 0.05$). Immunoblot shows knockdown of caspase-3 expression by siRNA directed against caspase-3; actin was used as a loading control.

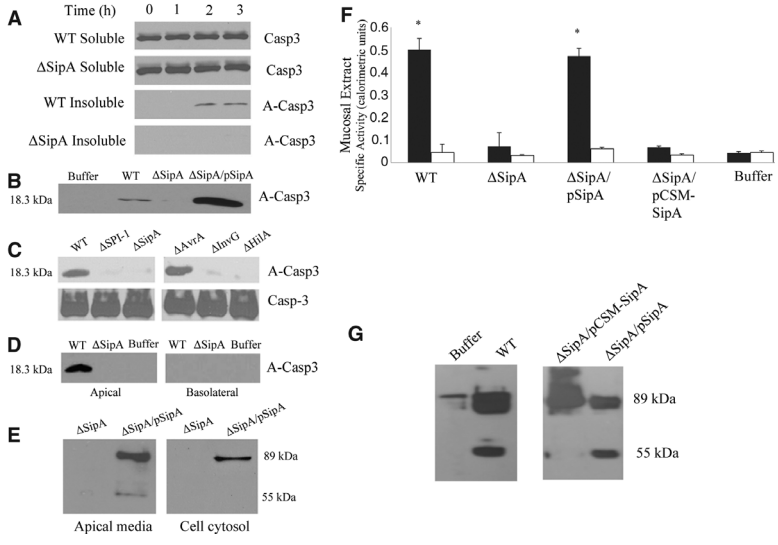

Fig. 3. SipA causes activation of caspase-3 and its release at the apical surface of the epithelium. (**A**) Time course of caspase-3 activation during *S.* Typhimurium infection of T84 cell monolayers. Cells were infected with either wild-type *S.* Typhimurium (WT) or the ΔSipA mutant. Casp3 refers to pro-caspase-3, whereas A-Casp3 represents the activated form of the enzyme; soluble and insoluble refer to the respective membrane fractions. (**B**) The ΔSipA mutant strain complemented with a vector expressing SipA (ΔSipA/pSipA) rescued the ability to induce the activation of caspase-3 after a 2-hour infection. Buffer refers to the buffer control. (**C**) Infection of T84 cells with different isogenic mutant strains of *S.* Typhimurium. Immunoblots were performed on cell extracts 3 hours postinfection with antibody against caspase-3 (anti-caspase-3). Casp3 refers to pro-caspase-3; A-Casp3 represents the activated form of the enzyme. (**D**) Activated caspase-3 was released at the apical but not basolateral surface during in vitro infection of T84 cells with wild-type *S.* Typhimurium (WT). No caspase-3 was detected in ΔSipA mutant–infected wells or in the buffer control, uninfected wells. (**E**) Cleaved SipA was detected in apical media but not in the cell cytosol after infection with the ΔSipA mutant complemented with SipA (ΔSipA/pSipA). No SipA is detected in the SipA negative mutant–infected cells. (**F**) Caspase-3 (black) or caspase-1 (white) activity was measured in mucosal extracts post–in vivo infection of WT mice. Infection was carried out with WT *Salmonella*, a ΔSipA mutant, and ΔSipA complemented with either SipA (ΔSipA/pSipA) or pCSM-SipA (ΔSipA/pCSM-SipA). Buffer refers to the uninfected buffer control. Values shown indicate means ± SD. (**G**) Immunoblots showing cleavage of SipA after addition of mucosal extract isolated from mice infected with various indicated strains. WT refers to wild-type *Salmonella*, and ΔSipA is the ΔSipA strain complemented with either WT SipA (SipA/pSipA) or the pCSM-SipA (ΔSipA/pCSM-SipA). Buffer refers to the negative control.

partment (Fig. 3D). SipA processing also occurs extracellularly at the apical surface, because SipA cleavage products were recovered within apical supernatants after *S.* Typhimurium infection but were not observed within the epithelial cell (Fig. 3E). Colonic mucus extracts were analyzed after *Salmonella*-induced colitis for the functional activity of caspase-3 and caspase-1 (a nonspecific control) (*11*). Consistent with our in vitro findings, only caspase-3 activity could be isolated from colonic mucus infected with *Salmonella* bearing a functional SipA (Fig. 3F), and *Salmonella*-infected mice were capable of cleaving only SipA possessing an intact caspase-3 recognition motif (Fig. 3G). Because these data demonstrate a novel mode of caspase-3 action, we attempted to model these interactions in vitro. Exogenous addition of the caspase-3 enzyme to *S.* Typhimurium infected T84 monolayers significantly and specifically enhanced PMN transepithelial migration (fig. S5). Although these results validate the concept that caspase-3–dependent processing plays an important role in bacterial-induced inflammation, the underlying molecular mechanism of how caspase-3 becomes activated remains to be defined. However, during infection, caspase-3 secretion does not appear to correlate with cell lysis (fig. S6).

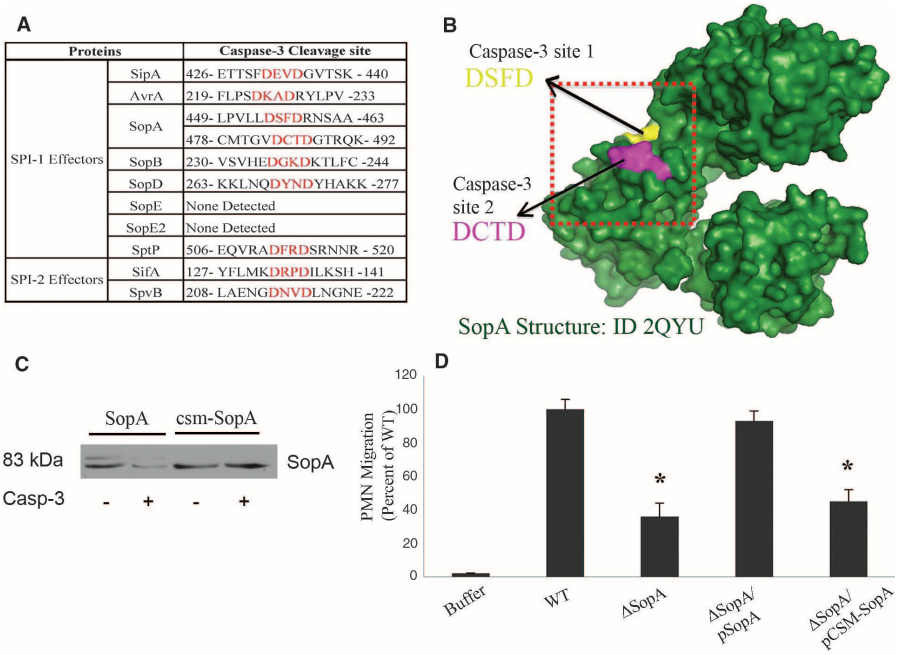

Fig. 4. Cleavage sites have been identified in numerous other *S.* Typhimurium effectors. (**A**) Functional caspase-3 cleavage sites in SipA, SopA, and putative caspase-3 cleavage sites in other *S.* Typhimurium effectors (*7*). (**B**) Three-dimensional image of the WT SopA protein showing the position of the two caspase-3 cleavage sites that are surface-exposed. ID 2QYU is Protein Data Bank identification for the given structure. (**C**) Immunoblot showing cleavage of SopA with caspase-3 and the absence of cleavage in the SopA caspase site double mutant. (**D**) PMN transepithelial migration induced in vitro by infection with WT *S.* Typhimurium and a SopA mutant strain (ΔSopA). ΔSopA/pCSM-SopA and ΔSopA/pSopA are the ΔSopA strain complemented with the caspase site mutant of SopA (csm-SopA) and wild-type SopA, respectively. *$P < 0.01$. Migration levels shown are presented as the percentage of the WT *S.* Typhimurium strain. Error bars indicate SD.

A detailed analysis of *S.* Typhimurium SPI-1 proteins revealed the existence of caspase-3 recognition and cleavage sites in other secreted *S.* Typhimurium effectors (i.e., AvrA, SopB, SifA, SipB, and SopA) but not type III secretion system structural proteins, chaperones, or transcriptional regulators. Like SipA, many of the caspase-3 cleavage sites in these other effector proteins are centrally located within the protein sequence, dividing the effectors into what, at least in the case of SifA, have been identified as two functional domains (*17*). These observations are further supported by studies with the effector protein, SopA, resembling HECT-like E3 ubiquitin ligase, which is also involved in inducing transepithelial migration of PMNs (*18*, *19*). SopA harbors two caspase-3 recognition motifs (449 to 463 and 478 to 492) that not only are positioned close to each other (Fig. 4A) but also are located in an exposed domain of the effector molecule (Fig. 4B). These SopA caspase-3 cleavage sites are functional, because exposure of SopA to the activated caspase-3 enzyme led to nearly complete digestion of the effector (Fig. 4C). By contrast, single amino acid substitution at position four of the caspase-3 recognition site to a motif not recognized by the enzyme [aspartic acid to alanine, DSFD to DSFA and DCTD to DCTA (*7*)] was refractory to caspase-3 digestion (Fig. 4C). The inability to visualize the digested fragments is most likely due to instability of the resulting fragments or poor antibody recognition. Nonetheless, the SopA caspase-3 site double mutant had significantly less capacity to induce PMN transepithelial migration than did the *S.* Typhimurium wild-type strain (>50%; $P < 0.01$).

Secreted effector proteins from other enteric pathogens, such as *Shigella flexneri* and enteropathogenic *Escherichia coli* (EPEC), also harbor potential caspase-3 recognition sites (tables S1 and S2). Although some protein sequences were found to contain multiple caspase-3 cleavage sites (i.e., IpaA and EspC), other sequences such as EPEC EspB protein, which is involved in the translocation of effector proteins during EPEC infection (*20*), exhibit discrete localization of the caspase-3 sites depending on whether the strain is isolated from humans or other mammals (rabbits or mice). Of potential importance, most of the proteins having a putative caspase-3 recognition and cleavage site exhibit a dual function, like SipA, with distinct activities of the N or C terminus of the protein (*21*–*24*). Future studies will determine whether these secreted effectors are also processed posttranscriptionally by caspase-3.

Our work reveals that *S.* Typhimurium has evolved a mechanism to deliver effector proteins in a precursor form to the host cell, where they are subsequently processed into independent functionally active domains. Alteration of the caspase-3 motif or modulation of caspase-3 expression attenuates the ability of *S.* Typhimurium to induce gastroenteritis. Many effector proteins secreted by bacteria share caspase-3 cleavage motifs, inviting speculation that caspase-3 processing may be a common host-pathogen interaction. The intestinal epithelium is a barrier against invading pathogens, and caspase-3 induction and release may have evolved as a rapid innate immune response to pathogens, perhaps in an attempt to kill or disarm the intruder (i.e., defensins). However, some pathogens such as *S.* Typhimurium appear to be able to subvert such defenses.

References and Notes

1. C. J. Hueck, *Microbiol. Mol. Biol. Rev.* **62**, 379 (1998).
2. D. Zhou, M. S. Mooseker, J. E. Galán, *Proc. Natl. Acad. Sci. U.S.A.* **96**, 10176 (1999).
3. C. A. Lee *et al.*, *Proc. Natl. Acad. Sci. U.S.A.* **97**, 12283 (2000).
4. M. Lilic *et al.*, *Science* **301**, 1918 (2003).
5. D. M. Wall *et al.*, *Cell. Microbiol.* **9**, 2299 (2007).
6. Single-letter abbreviations for the amino acid residues are as follows: A, Ala; C, Cys; D, Asp; E, Glu; F, Phe; G, Gly; H, His; I, Ile; K, Lys; L, Leu; M, Met; N, Asn; P, Pro; Q, Gln; R, Arg; S, Ser; T, Thr; V, Val; W, Trp; and Y, Tyr.
7. Materials and methods are available as supporting material on *Science* Online.
8. Z. Zakeri, R. A. Lockshin, *Adv. Exp. Med. Biol.* **615**, 1 (2008).
9. T. Q. Nhan, W. C. Liles, S. M. Schwartz, *Am. J. Pathol.* **169**, 729 (2006).
10. J. M. Kim *et al.*, *J. Clin. Investig.* **102**, 1815 (1998).
11. B. A. McCormick, B. A. Stocker, D. C. Laux, P. S. Cohen, *Infect. Immun.* **56**, 2209 (1988).
12. B. A. McCormick, S. P. Colgan, C. Delp-Archer, S. I. Miller, J. L. Madara, *J. Cell Biol.* **123**, 895 (1993).
13. M. Barthel *et al.*, *Infect. Immun.* **71**, 2839 (2003).
14. B. J. Cherayil, B. A. McCormick, J. Bosley, *Infect. Immun.* **68**, 5567 (2000).
15. C. A. Lee, S. Falkow, *Proc. Natl. Acad. Sci. U.S.A.* **87**, 4304 (1990).
16. C. A. Lee, B. D. Jones, S. Falkow, *Proc. Natl. Acad. Sci. U.S.A.* **89**, 1847 (1992).
17. M. B. Ohlson *et al.*, *Cell Host Microbe* **4**, 434 (2008).
18. M. W. Wood *et al.*, *Cell. Microbiol.* **2**, 293 (2000).
19. Y. Zhang, W. M. Higashide, B. A. McCormick, J. Chen, D. Zhou, *Mol. Microbiol.* **62**, 786 (2006).
20. W. Deng *et al.*, *Proc. Natl. Acad. Sci. U.S.A.* **101**, 3597 (2004).
21. H. J. Chiu, W. J. Syu, *Microbiology* **151**, 3277 (2005).
22. J. E. Deane, P. Roversi, C. King, S. Johnson, S. M. Lea, *J. Mol. Biol.* **377**, 985 (2008).
23. N. Ramarao *et al.*, *FEBS Lett.* **581**, 853 (2007).
24. G. Tran Van Nhieu, E. Caron, A. Hall, P. J. Sansonetti, *EMBO J.* **18**, 3249 (1999).

25. The research was supported by grants from the NIH (DK56754 and DK33506) and the Crohn's and Colitis Foundation of America to B.A.M. Additional grant support was provided by Tenovus Scotland and a Society for General Microbiology travel award to D.M.W. The use of human volunteers in this study was in accordance with appropriate guidelines and was approved by the University of Massachusetts Medical School Review Board for the Protection of Human Subjects (approval no. 13006).

Supporting Online Material

www.sciencemag.org/cgi/content/full/330/6002/390/DC1
Materials and Methods
Figs. S1 to S6
Tables S1 and S2
References

2 July 2010; accepted 6 September 2010
10.1126/science.1194598

NEW PRODUCTS FOCUS: PCR/RT-PCR

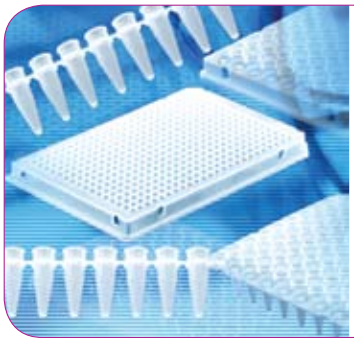

PCR CONSUMABLES

The new white PCR consumables are designed to optimize results for real-time polymerase chain reactions (qPCR). Uniformly colored with Titanium dioxide, these PCR products offer significantly better results in the analysis of fluorescence signals and consequently with the quantification of the replicated DNA. Extra-thin wall dimensions provide optimal thermal transfer and short cycle times. Reflection of the fluorescence signal is optimized by smooth surfaces. The consumables are available in strips of 8-, 24-, 48-, 96-, and 384-well plates suitable for use in most thermal cyclers. Manufactured in clean room conditions these PCR products are DNase-, DNA-, and RNAse-free.

BrandTech Scientific, Inc.
For info: 888-522-2726 | www.brandtech.com

REAL-TIME PCR SYSTEM

The Eco Real-Time PCR System is a novel platform that sets new standards in performance and simplicity for real-time polymerase chain reactions (qPCR), while offering unprecedented access to a wide range of applications at an affordable price. The Eco Real-Time PCR System offers true four-color multiplexing, high-resolution melting analysis (HRM), use of all standard qPCR chemistries, and the ability to perform fast PCR using standard chemistries. The Eco system has a compact design, 48-well plate format, and an intuitive, icon-driven software interface with smart default protocols. It offers ease-of-use for both experienced and novice qPCR users, and affordability to make it accessible to individual researchers around the world.

Illumina, Inc.
For info: 800-809-4566 | www.illumina.com/ecoqpcr

DOUBLE-QUENCHED PROBE

A new double-quenched probe increases the accuracy and reliability of 5′ nuclease real-time polymerase chain reaction (qPCR) experiments. While traditional probes have 20 to 30 bases between the dye and quencher, this novel proprietary probe design positions an internal ZEN quencher only 9 bases from the 5′ fluorophore. This shortened distance, particularly when combined with the standard 3′ quencher, significantly decreases background fluorescence and increases sensitivity. The chemical structure of the ZEN quencher stabilizes duplex formation which allows for its use in previously validated sequences. The improved functionality significantly increases qPCR accuracy and sensitivity when compared to traditional probes.

Integrated DNA Technologies
For info: 800-328-2661 | www.idtdna.com

THERMAL CYCLER

The FC1 Cycler is designed to reduce thermal cycling time and reduce overall system configuration costs for researchers conducting high sample throughput single-nucleotide polymorphism genotyping. Adding this ultrafast thermal cycler to today's existing Fluidigm system offered, provides users with the ability to double the number of microfluidic chips that can be processed in a single day. The FC1 Cycler also integrates a self-contained vacuum source and touch screen interface (that offers easy editing of thermal protocols) in a streamlined design that minimizes lab space requirements while maximizing productivity. This thermal cycler is fully compatible with Fluidigm's 96.96 and 48.48 Dynamic Array IFCs and its 12.765 Digital Array IFC. When combined with either the Fluidigm EP1 Reader or BioMark Real-Time PCR system, the FC1 Cycler can complete the entire workflow of the system in a matter of hours with only minutes of hands-on time for loading the chips.

Fluidigm
For info: +33-160-924240 | www.fluidigm.com

SEGMENTED PCR PLATES

Twin.tec PCR plates are designed to be easily divisible to save material and money when running smaller-scale experiments. These segmented 96-well plates fit almost all available polymerase chain reaction instruments and can be snapped into four separate 24-well sections. Twenty-four, 48, or 72 wells can be used as required and the empty wells are saved for future use—reducing waste and bringing significant cost savings. The frame is manufactured from rigid polycarbonate for enhanced mechanical stability, while the flexible polypropylene wells are thin-walled to ensure a snug fit to the thermal block for optimal heat transfer. The inert surface of the wells prevents DNA, RNA, and enzymes from binding and improves recovery when working with small volumes.

Eppendorf
For info: 800-645-3050 | www.eppendorf.com

PCR ARRAYS

Several new RT^2 Profiler PCR Arrays are available for gene expression profiling in nephrotoxicity, hepatotoxicology, differentiation, and embryonic stem cells markers as well as analysis of epigenetic modulators and enzymes. The arrays make expression profiling accessible for routine use in every lab with a real-time polymerase chain reaction (qPCR) instrument. The experiment is simple to perform and provides sensitive, reproducible, and reliable results to accurately profile multiple genes simultaneously. The RT^2 Profiler PCR Array provides gene expression data from the RNA within three hours and is composed of PCR Array plates, RT^2 first strand kit, RT^2 SYBR Green Master Mix, and the free PCR Array data analysis software.

Qiagen
For info: 800-426-8157 | www.qiagen.com

Electronically submit your new product description or product literature information! Go to www.sciencemag.org/products/newproducts.dtl for more information.

Newly offered instrumentation, apparatus, and laboratory materials of interest to researchers in all disciplines in academic, industrial, and governmental organizations are featured in this space. Emphasis is given to purpose, chief characteristics, and availability of products and materials. Endorsement by *Science* or AAAS of any products or materials mentioned is not implied. Additional information may be obtained from the manufacturer or supplier.

POSITIONS OPEN

NEUROBIOLOGIST
ASSISTANT PROFESSOR
California State University, Fresno
Department of Biology

Position requires development of a research program involving both Master's level and undergraduate students, a commitment to teaching and scholarly activities. This tenure-track position is part of a University-wide cohort of new faculty with a broad health emphasis. An earned doctorate (Ph.D.) in neurobiology or related field is required for appointment. Preference will be given to candidates with postdoctoral research experience. Visit **website: http://jobs.csufresno.edu** for full announcement and application details. Contact **Dr. Larry Riley** (**e-mail: lriley@csufresno.edu**) for questions. Application deadline is January 17, 2011. *California State University, Fresno is an Affirmative Action/Equal Opportunity Institution.*

DEVELOPMENTAL NEUROBIOLOGIST
University of Wyoming

The Department of Zoology and Physiology at the University of Wyoming invites applications for a full-time, nine-month, tenure-track FACULTY POSITION at the rank of **Assistant Professor,** or at a higher rank for an individual with outstanding accomplishments, starting August 2011. We seek applications from individuals working on any fundamental aspect of nervous system development. Individuals whose research compliments the system-level approaches within the department are especially encouraged to apply. The successful candidate must have a Ph.D. or equivalent in neuroscience, zoology or an appropriate field, show strong evidence of research productivity, and a strong commitment to teaching. As a member of the Graduate Neuroscience Program, the NIH funded Neuroscience Center of Biomedical Research Excellence, and the Department of Zoology and Physiology; the candidate will be expected to develop an externally funded research program, and to teach an upper level developmental biology course as well as a course in their area of expertise. A competitive start-up package and access to outstanding microscopy and cellular analytical facilities is available.

Interested applicants should e-mail: a curriculum vitae, a statement or research and teaching interests, three publications, and three letters of recommendation as pdf files to: **e-mail: zprequest@uwyo.edu** for the attention of **Developmental Neurobiology Search Committee. Websites: http://wyo.edu/Zoology; http://uwyo.edu/NeuroScience.** Review of applications will begin October 20, 2010 and continue until the position is filled. *The University of Wyoming is committed to diversity and endorses principles of Affirmative Action. We welcome applications from individuals of all backgrounds, experiences and perspectives.*

POSTDOCTORAL POSITION in the Laboratory of **Guillermo Calero** in the Department of Structural Biology at the University of Pittsburgh. The candidate will work on structural studies of multiprotein complexes involved in Transcription/DNA repair. Our group is working on novel biochemical methods that allow reconstitution of multi-protein complexes ranging from 3-28 polypeptides (MW 100 kDa–1.5 MDa). The laboratory is equipped with a state-of-the-art facility to express, solubilize, purify, and crystallize biological samples. The laboratory equipment includes a 120 lts. yeast fermenter; a 15 lt. bioreactor for insect and mammalian cell expression; light scattering, mass spectroscopy, and chromatography equipment; crystallization robots; and X-ray home sources. The position requires a Ph.D. in any area of Biology/Physics/Chemistry and strong backgrounds in biochemistry and X-ray crystallography. Please send curriculum vitae and three reference letters to **Dr. Guillermo Calero** by **e-mail: guc9@pitt.edu.** *The University of Pittsburgh is an Affirmative Action, Equal Opportunity Employer.*

POSITIONS OPEN

ASSISTANT PROFESSOR

The MIT Department of Earth, Atmospheric, and Planetary Sciences announces a major expansion of its activities in climate science and seeks applicants for up to four faculty positions in Climate-related fields. Preference will be given to junior appointments at the assistant professor level, but a senior appointment can be considered for an individual with exceptional qualifications. Areas of specific interest include observations, models, and theories of the atmosphere, ocean, and cryosphere; past and present climates; biogeochemical cycles; and ecology.

The successful candidates will have to have a strong record of accomplishment in their discipline, a strong commitment to teaching and student advising, a keen interest in relating their work to complementary research in the Department and in the MIT/Woods Hole Joint Program in Oceanography. Joint appointments with other MIT departments are also potentially negotiable where appropriate.

More information about this position can be obtained by writing **Professor Maria T. Zuber** at **e-mail: mtz@mit.edu** or **Professor Kerry A. Emanuel** at **e-mail: emanuel@mit.edu.**

A completed application will include curriculum vitae, a statement of research and teaching objectives, and the names of five potential references. Applications are being accepted at Academic Jobs Online (**website: https://academicjobsonline.org/ajo**). Please do not ask your references to upload letters at the time of application. Letters will be requested directly by MIT. To receive consideration, a completed application must be received.

Search Contact:
Mr. Michael Richard, Human Resources Administrator, EAPS, 54-926 Massachusetts Institute of Technology, 77 Massachusetts Avenue, Cambridge, MA 02139 mjr@mit.edu
Telephone: 617-253-5184
Fax: 617-253-8298

MIT is an Equal Opportunity/Affirmative Action Employer. Applications from women, minorities, veterans, older workers, and individuals with disabilities are strongly encouraged.

FACULTY POSITION

The Department of Molecular and Cell Biology at the Boston University Henry M. Goldman School of Dental Medicine occupies a completely renovated floor adjacent to basic science departments of the Medical School. We have an opening at the **ASSISTANT, ASSOCIATE** or **FULL PROFESSOR** level. We seek individuals with an outstanding publication record and an ongoing NIH RO1 or K99/ROO-funded research program as principal investigators. We seek qualified candidates with research interests in cell and developmental biology, molecular genetics, biochemistry, immunology, or microbiology. Interest in craniofacial and or oral biology is encouraged but not necessary. Excellent laboratory facilities and startup funds are available as well as joint appointments with appropriate departments at the Medical School and participation in the Bioinformatics Program at the School of Engineering. Electronically send curriculum vitae including a 250-word summary of present and future research plans and names and e-mail addresses of three to five references, no later than December 31, 2010, to: **Dr. P.W. Robbins,** Search Committee Chair (**e-mail: robbinsp@bu.edu**) or **Dr. C.B. Hirschberg,** Department Founding Chair (**e-mail: chirschb@bu.edu**). Please visit our **website: http://dentalschool.bu.edu/research/molecular/index.html.** *Boston University is an Affirmative Action and Equal Opportunity Employer.*

POSTDOCTORAL POSITION

One postdoctoral position available to study neural development and axon guidance mechanisms using molecular and genetic approaches. Candidates with a Ph.D. degree in molecular biology and related fields are encouraged to send their curriculum vitae, statement of research interests, and the names of three references to: **Dr. Renping Zhou, Laboratory for Cancer Research, School of Pharmacy, Rutgers University, 164 Frelinghuysen Road, Piscataway, NJ 08854. E-mail: bachorik@rci.rutgers.edu.**

SIGNAL TRANSDUCTION
DEPARTMENT OF SURGERY

The Department of Surgery in the College of Human Medicine at Michigan State University seeks candidates for an academic-year position at a Faculty Rank to be determined in signal transduction. Applicants are sought with demonstrated expertise in cellular signal transduction, with preference toward those with a background in mechanotransduction and physical force effects or intestinal epithelial biology. In addition to individual research efforts, the person who fills this position will be expected to collaborate actively with and mentor clinical surgical faculty and trainees as well as other MSU faculty. A strong record of research accomplishment and an independent externally funded research program are required. The position includes competitive salary and startup package, academic rank commensurate with previous experience, and the possibility of a co-appointment in one of the basic science department at MSU.

MICHIGAN STATE UNIVERSITY

Applications will only be accepted from candidates with current NIH funding or the equivalent. Applicants should submit a letter of interest, CV including complete publication list, history of research funding, statement of current and future research plans, and contact information (address, email and phone) for three referees to **Dr. Marc D. Basson, Professor and Chair, Department of Surgery, Michigan State University, Suite 655, 1200 East Michigan Ave, Lansing, MI 48912.** We would prefer electronic submission to **marc.basson@hc.msu.edu**. Applications will be accepted until the position is filled.

MSU is committed to achieving excellence through cultural diversity. The university actively encourages applications and/or nominations of women, persons of color, veterans and persons with disabilities.

Harvard Medical School
Assistant Professor

The Harvard Medical School Department of Biological Chemistry and Molecular Pharmacology announces a search for a tenure-track Assistant Professor. We seek a colleague who uses twenty-first century methodologies to study molecular mechanisms in biology and medicine and whose research program will complement and expand our strengths and those of the closely allied Department of Cell Biology.

Interested candidates should summit a CV, a 3 to 5 page statement of research interests, and have 4 letters of recommendation sent via e-mail to: **faculty_search@hms.harvard.edu**.

Application deadline is **November 24, 2010**.

Harvard Medical School is an Equal Opportunity/Affirmative Action Employer. We are actively committed to increasing the diversity of our faculty. Women and members of underrepresented minority groups are therefore strongly encouraged to apply.

Faculty Position
Molecular Biology
Sloan-Kettering Institute

The Molecular Biology Program of the Sloan-Kettering Institute, Memorial Sloan-Kettering Cancer Center (www.ski.edu), has initiated a faculty search at the Assistant Member level (equivalent to Assistant Professor). We are interested in outstanding individuals who have demonstrated records of significant accomplishment and the potential to make substantial contributions to the biological sciences as independent investigators. Successful applicants will have research interests that move the Program into exciting new areas that complement and expand our existing strengths in the areas of maintenance of genomic integrity, regulation of the cell cycle, and regulation of gene expression. Faculty will be eligible to hold appointments in the Gerstner Sloan-Kettering Graduate School of Biomedical Sciences, the Weill Cornell Graduate School of Medical Sciences, as well as the Tri-Institutional MD/PhD Training Program.

The deadline for applications is **November 1, 2010**. Interested candidates should visit **http://facultysearch.ski.edu** to access the on-line faculty application. Please visit the site as soon as possible, as it contains important information on the required application materials, including deadlines for submission of letters of reference.

Informal inquiries may be sent to **Julie Kwan at kwanj@mskcc.org** or to **Dr. Kenneth Marians, Chair, Molecular Biology Program at kmarians@sloankettering.edu**. MSKCC is an equal opportunity and affirmative action employer committed to diversity and inclusion in all aspects of recruiting and employment. All qualified individuals are encouraged to apply.

Memorial Sloan-Kettering Cancer Center
www.mskcc.org

MIAMI UNIVERSITY

Director of the Institute for the Environment and Sustainability

Tenured Full or Associate Professor, to provide leadership for the programs of the Institute, coordinate among the Institute and other academic units and centers of the University, and enhance our national profile of excellence in the environment and sustainability.

The Institute was founded in 1970 as the Institute of Environmental Science and its master's program has produced over 600 alumni who are today working in the commercial, governmental, and non-profit sectors to make our environments healthier and natural resource use more sustainable. It is being restructured to include a PhD program in Ecology, Evolution, and Environmental Biology and two undergraduate co-majors focusing on environmental science and sustainability. It includes 4 staff and more than 45 faculty drawn from 13 departments and 4 divisions of the University.

The Director will coordinate with chairs and directors of other academic units in furthering the work of the Institute, pursue external funding, maintain active scholarship, teach appropriate courses, and supervise the Institute staff. Requirements include a doctorate in an area of environmental science, engineering, policy, or related field; a strong record of scholarship; success in extramurally funded research; and professional experience with applied environmental and sustainability issues. Teaching experience and demonstrated success in administrative duties desired.

Please send letter of nominations or application, curriculum vitae, statement of research and teaching interests, and contact information for three referees to **Dr. Bill Renwick, Search Committee Chair, Department of Geography, 216 Shideler Hall, Miami University, Oxford, OH 45056. For more information, phone 513-529-5811 or 513-529-5010** or e-mail **renwicwh@muohio.edu**. Review of applications will begin **December 1, 2010**. Position available August 2011. For more information about the University and the Institute see **http://www.miami.muohio.edu/** and **http://www.cas.muohio.edu/ies/**. For information regarding campus crime and safety, visit **www.muohio.edu/righttoknow**.

Miami University is an Equal Opportunity Employer with smoke-free campuses.

Jiangsu Academy of Agricultural Sciences

Seeking Distinguished Scientists in Various Agriculture Areas

Jiangsu Academy of Agricultural Sciences (JAAS) is a professional agricultural research and extension institution that has been established since 1932. JAAS ranks at the top of provincial agricultural academies in China in terms of the comprehensive strength in agriculture. JAAS's headquarter and main research facilities are located in Nanjing, Jiangsu, China.

Currently, there are 3 distinguished full professor positions available for application in the following areas: breeding, food processing, bioenergy, facility agriculture, and large-scale farming for modern animal husbandry. Applicants should have a faculty position already beyond the assistant professor level in a university or the equivalent position in a research institution. In addition, all candidates should demonstrate excellent records of research accomplishment and have a command of bilingual language for English and Chinese, both in spoken and written.

Successful applicants will be offered a competitive package, including sufficient laboratory space, startup funding, relocation fee and competitive salary commensurate with experience, in addition to a housing allowance, and other employee benefit. Applicants can go to www.jaas.ac.cn for application details.

In addition, more information for other regular faculty positions from JAAS relevant to a variety of disciplines in agriculture is also available at www.jaas.ac.cn.

Contact information

E-mail: rsc-gbk@jaas.ac.cn; Tel: 086-25-84390037

FACULTY POSITIONS

Kimmel Cancer Center

Jefferson Medical College of Thomas Jefferson University

The Kimmel Cancer Center is recruiting for several tenure-track faculty positions. Candidates for appointment at the level of Associate or Full Professor will be considered, and would receive an academic appointment in an appropriate basic science and/or clinical department (s) affiliated with the Center. We seek individuals with interest and expertise in the following areas of translational cancer research: tumor immunology, immunotherapy, tumor vaccines, GVH/GVL, tumor virology and viral pathogenesis in transplant/immunosuppressed settings. Successful candidates will be established investigators with the motivation to collaborate with other investigators at Jefferson towards the development of joint grant initiatives and clinical trials.

Cancer Center affiliated Departments host large graduate and postdoctoral programs supported by NIH training grants. Jefferson also has a fully funded MD/PhD Program. The Kimmel Cancer Center also provides a variety of core facilities to its investigators. All facilities are described at **www.kimmelcancercenter.org**. Applicants should send a curriculum vita with description of research interests and three letters of reference via email to:

Tim L. Manser, PhD, Plimpton-Pugh Professor and Chair
Department of Microbiology & Immunology
Leader, Immunological Mechanisms in Cancer Program
Kimmel Cancer Center
c/o Kathy Reinersmann
Jefferson Medical College
233 South 10th Street/Room 302 BLSB
Philadelphia, Pa 19107
K_Reinersmann@kimmelcancercenter.org
or apply online at www.jefferson.edu/careers
referencing position ID# 101010

Jefferson Medical College is located in Center City Philadelphia adjacent to a variety of cultural, entertainment and historical attractions.

Jefferson Kimmel Cancer Center

THE CHINESE UNIVERSITY OF HONG KONG

Applications are invited for:-

School of Chinese Medicine
Professor / Associate Professor / Assistant Professor

(Ref. 1011/029(665)/2) (Closing date: November 8, 2010)

Applicants should have (i) a PhD degree in life science, preferably in Chinese medicine or related areas; (ii) established scholarship with a track record of high-quality publications and award of competitive research grants; and (iii) teaching and clinical experience in Chinese medicine. Applicants for Professorship should also have extensive teaching experience and an outstanding publication record in related fields. Duties include (a) teaching undergraduate and postgraduate courses; (b) supervising research projects; (c) conducting research in own field(s) of specialization; and (d) assisting in administration of the School and curriculum development. Appointment will normally be made on contract basis for up to three years initially commencing January 2011, which, subject to mutual agreement, may lead to longer-term appointment or substantiation later.

Salary and Fringe Benefits

Salary will be highly competitive, commensurate with qualifications and experience. The University offers a comprehensive fringe benefit package, including medical care, plus a contract-end gratuity for an appointment of two years or longer, and housing benefits for eligible appointee. Further information about the University and the general terms of service for appointments is available at *http://www.cuhk.edu.hk/personnel*. The terms mentioned herein are for reference only and are subject to revision by the University.

Application Procedure

Please send full resume, copies of academic credentials, a publication list and/or abstracts of selected published papers together with names, addresses and fax numbers/e-mail addresses of three referees to whom the applicants' consent has been given for their providing references (unless otherwise specified), to the Personnel Office, The Chinese University of Hong Kong, Shatin, N.T., Hong Kong (Fax: (852) 2696 1462) by the closing date. The Personal Information Collection Statement will be provided upon request. Please quote the reference number and mark 'Application - Confidential' on cover.

UMDNJ Robert Wood Johnson Medical School — University of Medicine & Dentistry of New Jersey

The Cancer Institute of New Jersey

NCI CCC

The Cancer Institute of New Jersey

FACULTY POSITION AVAILABLE

Cancer Metabolism

The Cancer Institute of New Jersey (CINJ) invites applications for a tenure-track faculty position at the **Assistant Professor** rank specializing in cancer metabolism. CINJ is an NCI-designated comprehensive and consortium cancer center that includes faculty members from UMDNJ-Robert Wood Medical School, Rutgers and Princeton Universities.

CINJ website **http://www.cinj.org**

New faculty are expected to establish an innovative, independent and collaborative research program addressing important, fundamental questions in the area of cancer biology and the role of cellular and mammalian metabolism in health, disease and therapy. Interdisciplinary approaches are encouraged and the combined CINJ-Princeton University consortium faculty has complementary expertise and strength in cancer biology, signal transduction, systems biology, and metabolism. The CINJ-Princeton University consortium has state-of-the-art mass spectrometry for metabolomic and metabolic analysis, in addition to advanced microscopy, live cell and animal imaging, tissue analysis, functional genomics and mutant mouse facilities. Qualified candidates must have a Ph.D. and/or M.D., or equivalent graduate degree, and outstanding academic credentials. We seek candidates who are independent investigators interested in collaboration with basic scientists and with clinical faculty for translational research.

Interested applicants should send their CV, a brief description of their research interests and plans, and the names of three references, addressed to both **Dr. Eileen White, Associate Director, Basic Science, The Cancer Institute of New Jersey, 195 Little Albany Street, New Brunswick, NJ 08901 and Dr. Joshua D. Rabinowitz, Department of Chemistry, Lewis-Sigler Institute for Integrative Genomics, 241 Carl Icahn Laboratory, Washington Road, Princeton University, Princeton, NJ 08544. If via email: cinjrecruitment@gmail.com.** UMDNJ is an EEO/AA employer, m/f/h/v, and a member of the University Health System of New Jersey

Professor, Tenure Track

The Department of Pathology, Anatomy and Cell Biology invites applications for a tenure-track position at the Associate or Full Professor level with research strength in the areas of Neurodegeneration/Regeneration/Stem Cells as related to Vision. Candidates should have research programs that complement existing faculty interests in the areas of neurodegenerative diseases, degenerative diseases/injury repair of the eye, and basic biology of cell death and cell/tissue repair.

Candidates must have a PhD or MD degree and a commitment to teaching in Departmental education programs. Applicants should have a successful independent research program and a strong record of extramural funding.

As an employer, Thomas Jefferson University maintains a commitment to provide equal access to employment. All present and future employees at Thomas Jefferson University can be assured that they will not be judged on the basis of race, color, national or ethnic origin, ancestry, sex, sexual orientation, religion, age disability or veteran's status, but by their individual performances.

Interested candidates are invited to apply online at **www.jefferson.edu/careers** and reference Job Id # 42101 in addition to submitting a curriculum vitae and names of three academic references to: **Susan Menko, Ph.D., Professor Pathology, Anatomy and Cell Biology, Thomas Jefferson University, JAH 571, 1020 Locust Street, Philadelphia, PA 19107.**

Jefferson™ University

The University of Texas at Austin

Stem Cell Biology Position

The Institute for Cellular and Molecular Biology

The Institute for Cellular and Molecular Biology, Alan Lambowitz, Director, invites applications for a tenure-track/tenured position in Stem Cell Biology. Academic appointments at the level of Assistant, Associate, or Full Professor will be in the Section of Molecular Cell and Developmental Biology.

Candidates should have an outstanding record of research productivity and a research plan based on molecular mechanisms in any area of Stem Cell Biology. Building on a strong existing faculty, the Institute has recruited more than 50 new faculty members over the past ten years. In addition to its highly interactive and interdisciplinary research environment, the Institute provides administrative and financial support for the Graduate Programs in Cell and Molecular Biology, Microbiology, and Biochemistry, as well as state-of-the art core facilities including DNA and next-gen sequencing, mass spectrometry, electron and confocal microscopy, DNA microarrays, robotics, and mouse genetic engineering. An MD-PhD program with the UT Medical Branch and UT-Austin's new Dell Pediatrics Research Institute enhance the environment for Biomedical Research.

Austin is located in the Texas hill country and is widely recognized as one of America's most beautiful and livable cities.

Applications received before November 1, 2010 will receive first consideration, but applications will be accepted until the position is filled. Please send a single PDF file containing your curriculum vitae, summary of research interests and names of three references to: **MCDB_stem_cell@biosci.utexas.edu.** References may also send their letters directly to the same email address.

Homepages • http://www.biosci.utexas.edu/MCDB/ • http://www.icmb.utexas.edu/

The University of Texas at Austin is an Equal Opportunity Employer. Qualified women and minorities are encouraged to apply; a background check will be conducted on applicant selected.

TENURE-TRACK FACULTY POSITION

Department of Molecular Medicine

The Department of Molecular Medicine at Cornell University invites applications for a tenure-track faculty position at the rank of Assistant Professor. Applications from individuals at a more advanced rank may also be considered. We seek candidates dedicated to a mechanistic understanding of cellular signal transduction. Areas of interest include, but are not limited to, cancer biology, structural biology of membrane proteins, as well as the interface of structural, chemical and cell biology. The successful candidate is expected to develop a strong and independent research program and contribute to the teaching activities of the Department.

Molecular Medicine is a basic science department committed to making discoveries that advance human and animal health and promote the development of novel therapies. It is part of a vibrant and interdisciplinary Life Sciences community on Cornell's main campus in Ithaca, New York that includes the Weill Center for Cell and Molecular Biology and the Center for Vertebrate Genomics. (Visit **http://www.cornell.edu/lifesciences/**).

Qualifications: Candidates should have a Ph.D., D.V.M., M.D, or equivalent degree, postdoctoral experience, a track record of excellence in research, and the potential to develop an outstanding, extramurally funded research program.

We are interested in candidates who can contribute to the diversity and excellence of our academic community through their research, teaching and/or service. Cornell also seeks to meet the needs of dual-career couples through a Dual Career program and is a member of the Upstate New York Higher Education Recruitment Consortium (Visit **http://www.upstatenyherc.org**).

Please submit a single Adobe PDF with cover letter, curriculum vitae, and a 2-3 page research plan to **MMsearch@cornell.edu**. In addition, applicants must arrange for three letters of recommendation to be sent to the same email address. The committee will begin considering applications December 1, and will continue until the position is filled.

Cornell University

Cornell University is an Affirmative Action/Equal Opportunity Employer and Educator. Women and minority candidates are strongly encouraged to apply.

Coastal Physical Oceanographer and Marine Biogeochemist

Tenure-track Assistant Professor Positions in Marine Sciences at UConn

UCONN

The Department of Marine Sciences at the University of Connecticut is seeking to fill two nine-month, tenure-track Assistant Professor positions to begin August, 2011:

Coastal Physical Oceanographer with interests focusing on regional scale dynamics and their effect on biogeochemical and ecological processes in the coastal ocean. **Minimum Qualifications:** Ph.D. in Oceanography, or closely related physical science; and experience in conducting and reporting significant research in coastal physical oceanography. Equivalent foreign degrees are acceptable.

Marine Biogeochemist with interests in pelagic microbial processes. Research focus may include global change, tracers of abiotic/biotic transformation processes, biochemical cycles, or proteomics/metabolomics. **Minimum Qualifications:** Ph.D. at time of appointment in oceanography, biogeosciences, chemistry, microbiology, or other relevant scientific disciplines; and strong communication skills. Equivalent foreign degrees are acceptable.

The successful candidates will be expected to enthusiastically engage in teaching at the undergraduate and graduate levels and develop programs fostering interdisciplinary research with faculty and students. These are nine-month, tenure-track positions located at the Avery Point campus. The complete position descriptions with more information on preferred qualifications are available at **http://marinesciences.uconn.edu/**.

To Apply: Applicants should apply online at **http://jobs.uconn.edu/** indicating the **Coastal Physical Oceanographer** (Search **#2011083**) or **Marine Biogeochemist** (Search **#2011199**). Documents required include: curriculum vitae, a letter of application, statement of research and teaching interests, and the names and contact information of three references. Review of applications will begin **November 30, 2010**. Applications will be reviewed until the position is filled.

The University of Connecticut is an EEO/AA Employer.

UW Genome Sciences

OPEN FACULTY POSITION

The Department of Genome Sciences at the University of Washington is continuing a major expansion under its chair, Dr. Robert Waterston. Research in the department encompasses both genetic and genomic analysis of humans and model organisms. The department also has a significant focus in technology development and in computational biology across all levels including sequence, expression, proteomics, network, and genetic analysis. The department invites applications in any of these areas for a full-time faculty position at the rank of **ASSISTANT PROFESSOR**, tenure-track. The position involves establishing an active research program as well as teaching duties. Applicants should hold a Ph.D. and/or M.D. degree. For full consideration complete applications must be received by **December 15, 2010**.

Candidates should **e-mail** their curriculum vitae and statement of research and teaching interests, and arrange to have three signed letters of reference sent to: **faculty-search@gs.washington.edu**.

For additional information that may be helpful in preparing an application, see the department's web site at **http://www.gs.washington.edu**.

The University of Washington is an affirmative action, equal opportunity employer. The University is building a culturally diverse faculty and staff and strongly encourages applications from women, minorities, individuals with disabilities and covered veterans. The University of Washington Faculty engage in teaching, research and service. The University of Washington, a recipient of the 2006 Alfred P. Sloan award for Faculty Career Flexibility,is committed to supporting the work-life balance of its faculty.

Tenure-Track Faculty Positions

The Institute of Biological Chemistry, Academia Sinica, Taiwan, is seeking highly qualified candidates to fill positions of Assistant Professor/Assistant Research Fellow (or higher) level. Candidates in all areas that would complement or strengthen the current topics in the Institute will be considered. Applicants should have a Ph.D. degree, relevant postdoctoral experience, and an outstanding record of research accomplishments. Successful candidates will receive a generous start up fund and annual intramural support, and will have full access to all the resources and graduate students at the Institute of Biological Chemistry, Academia Sinica (**http://www.ibc.sinica.edu.tw/**) and the Institute of Biochemical Sciences, National Taiwan University (**http://homepage.ntu.edu.tw/~ibs/index.htm**). Applicants should send their curriculum vitae, a description of past research accomplishments and future research interests (PDF files) and arrange to have three letters of reference sent to: **yujushih@gate.sinica.edu.tw**. All applications received before **Jan 31, 2011**, will be considered, but the search process will continue until the positions are filled.

Chief Scientist in Epigenetics
Permanent Position, RIKEN, Japan

RIKEN invites applications for the position of Chief Scientist (Laboratory Director) to lead a new laboratory working on Gene Function including Epigenetics. The laboratory will investigate epigenetic control of biological phenomena. The post is a permanent appointment, subject to RIKEN's mandatory retirement age of 60. The anticipated starting date is, in the earliest case, April 1, 2011.

Applicants should send a full curriculum vitae and photograph; a list of publications; one copy each of five key publications; a statement (about five pages A4 sized paper) explaining former research experience and proposals for research at RIKEN; and the names and addresses of three referees.

Closing date: 15 December 2010

Applicants should address all correspondence to: Dr. Shunsuke Ishii, Chief Scientist Search Committee Chair, RIKEN Advanced Science Institute, 3-1-1 Koyadai, Tsukuba, Ibaraki 305-0074, JAPAN

For more information, please visit:
http://www.riken.jp/engn/r-world/info/recruit/k101215_e_asi.html

RIKEN

UNIVERSITY OF WISCONSIN UWMILWAUKEE
College of Health Sciences

ASSISTANT/ASSOCIATE/FULL PROFESSOR

UW-Milwaukee is a premier research university serving approx. 30,000 students. The Department of Health Sciences invites applications for TWO full-time, 9-month tenure-track faculty positions. Successful candidates will be expected to establish a productive, collaborative extramurally funded research program. Positions involve teaching undergraduate and graduate students.

Molecular Pathology, Bioforensics, Molecular Biology
The successful candidate will have a background and a Ph.D. in molecular biology, molecular pathology and/or forensic sciences or related field. The appointment may begin as early as January 7, 2011.

Medical Microbiology
The successful candidate will have a background in medical microbiology or molecular diagnostics. A Ph.D. in microbiology, molecular biology, cell biology, or related fields is required. Board certification as MLS/MT (ASCP) is preferred. Position begins August 22, 2011.

Application Procedure: All applicants will need to apply online at **http://jobs.uwm.edu/postings/4192** for Molecular Pathology position and **http://jobs.uwm.edu/postings/4924** for Medical Microbiologist position. Submit electronically a curriculum vitae, cover letter, and contact information for 3 professional references (name, address, phone, e-mail). Review of applications will begin **November 1, 2010,** and continue until the position is filled. Women and minorities are encouraged to apply.

For UWM's Campus Security Report, which includes statistics about reported crimes and information about campus security policies, see www.cleryact.uwm.edu, or call the Office of Student Life at (414) 229-4632 to request a paper copy."

UWM is an AA/EEO Employer "Employment will require a criminal background check."

MAYO CLINIC

Heal the sick, advance the science, share the knowledge.

Cell/Molecular Biology Research Faculty Position in Prostate and Genitourinary Cancer

The Mayo Clinic and the Mayo Clinic Cancer Center in Rochester, MN, is seeking a junior to mid-level scientist in basic prostate cancer research to join the Biochemistry and Molecular Biology Department.

The ideal candidate would be an MD or PhD with NCI research funding and publications relevant to prostate and possibly other genitourinary cancers. Appointment will be at the assistant, associate or full professor level (depending upon experience). The selected faculty member will have membership in the Prostate Cancer Research Program of the Mayo Clinic's NCI-designated Cancer Center and the opportunity to interact with Mayo SPOREs in prostate, pancreas, breast, melanoma and lymphoma.

To learn more about Mayo Clinic and Rochester, MN, please visit **www.mayoclinic.org/physician-jobs**.

Interested parties should send letters of inquiry and CVs to:

Ms. Kristi Simmons
Search Committee Secretary
Mayo Clinic
200 First Street SW • Rochester, MN 55905
Email: simmons.kristi@mayo.edu

Mayo Foundation is an affirmative action and equal opportunity educator and employer. Post-offer/ pre-employment drug screening is required.

Faculty Position
Paleontology And Evolution

The Department of Organismic and Evolutionary Biology (OEB) at Harvard University invites applications for a faculty position in the field of paleontology, emphasizing an evolutionary perspective. The appointment may be made at either the untenured rank (Assistant Professor and Associate Professor) or at the tenured level. We seek an outstanding scientist who will establish an innovative research program and teach both undergraduate and graduate students. We are especially interested in individuals who conduct rigorous, field- and/or laboratory-based analyses of general problems in paleontology and evolution of animals, and who employ morphological, functional, developmental, molecular and/or phylogenetic approaches. In addition to a faculty appointment in OEB, the successful candidate will receive a curatorial appointment in the Museum of Comparative Zoology (MCZ) with oversight responsibilities for the museum's paleontology collections.

Please submit applications online at: **https://webapps.sciences.fas.harvard.edu/apply/oeb-paleo-2010/**. Required materials include a curriculum vitae; a statement of research and teaching interests; four representative publications; and the names, institutional affiliations, and e-mail addresses of three references. Letters of nomination from third parties are also welcome and should be sent by e-mail to **paleo_search@oeb.harvard.edu**. Review of applications and nominations will begin **November 10, 2010**, and conclude when the position is filled.

Further information about OEB and MCZ are available at **http://www.oeb.harvard.edu** and **http://www.mcz.harvard.edu**. Address questions about the position to **Professor Jonathan Losos, jlosos@oeb.harvard.edu** and about the application/nomination process to **Ms. Jeannette Everritt** in OEB, **jeverritt@oeb.harvard.edu**.

Harvard University is an Affirmative Action/Equal Opportunity Employer. Applications from women and minority candidates are strongly encouraged.

HERMAN B WELLS CENTER FOR PEDIATRIC RESEARCH
INDIANA UNIVERSITY
School of Medicine

Hematologic Malignancy and Stem Cell Biology Program
Assistant/Associate Professor

The Department of Pediatrics and the Herman B Wells Center for Pediatric Research is recruiting for faculty positions at the Assistant/Associate Professor level. The research focus for these positions will be on normal hematopoietic and leukemic stem cell biology with emphasis on translational research. Candidates will have a Ph.D., M.D. or M.D./Ph.D. and must have a strong research background and either current, or potential for, independent funding. Laboratory space will be in the Herman B Wells Center for Pediatric Research (**http://www.wellscenter.iupui.edu/**). New faculty will be provided with generous start-up packages and laboratory space. M.D. faculty will have protected time for research activities. New faculty will join an active and growing multi-disciplinary hematopoiesis research community with a strong collaborative atmosphere.

The search committee will begin evaluating applications as they are received and applications will continue to be reviewed until the positions are filled. Interested candidates are encouraged to submit curriculum vitae, summary of past accomplishments and future plans, and names and email addresses of three references to: **Reuben Kapur, Ph.D., Director, Program in Hematologic Malignancies and Stem Cell Biology, Wells Center for Pediatric Research, Departments of Pediatrics, Indiana University School of Medicine, 1044 W. Walnut Street, Room 425, Indianapolis, IN 46202, rkapur@iupui.edu**.

Indiana University is an EEO/AA educator, employer and contractor (M/F/D)

Laboratory Director
Schistosomiasis Laboratory
Biomedical Research Institute

The Schistosomiasis Laboratory of the Biomedical Research Institute (BRI) invites applications for a full-time position to direct a unique biological laboratory that provides life cycle stages of *Schistosoma* species to scientific investigators worldwide. This service supports numerous laboratories studying schistosomiasis and other diseases for which schistosomiasis in rodents serves as a useful model. Over the years this NIH-NIAID extramural-funded service has been a major driving force in the advancement of schistosomiasis research, and for research into numerous other diseases exhibiting similar pathologies. The candidate would ideally possess a Ph.D. or equivalent degree, and would be encouraged to establish an independent, externally funded research program. The candidate should have solid administrative and interpersonal skills, and a strong commitment to support a wide network of research scientists. Experience with small animal models of infectious disease is highly desirable. Although not a prerequisite, previous service on an IACUC would be a strength, and the successful candidate would be expected to participate in IACUC administrative duties. Salary will be commensurate with experience. BRI is a not-for-profit research institute located in Rockville, MD, within a few miles of the main NIH campus in Bethesda, MD.

Applications should include a cover letter, curriculum vitae with a research history, and the names and contact information of three references. Please submit application packets to: **Dr. Fred Lewis, Biomedical Research Institute, 12111 Parklawn Drive, Rockville, MD 20852**. Any inquiries can be addressed to **Dr. Lewis** at **flewis@afbr-bri.com**. Review of applications will begin on **November 15, 2010**. Applications will be accepted until the position is filled.

The Biomedical Research Institute is an Equal Opportunity Employer AA/EOE M/F/D/V.

Tenure/Tenure Track Investigator Position
Laboratory of Immunology

The Laboratory of Immunology (LI), Division of Intramural Research, National Institute of Allergy and Infectious Diseases, National Institutes of Health, invites applications for a tenure/tenure-track investigator position in immunology. Applicants should have a Ph.D., M.D., or equivalent degree; an outstanding record of postdoctoral accomplishment; and an interest in any area of biomedical research related to immunology.

Specifically, we seek a highly creative individual who will establish an independent, world-class research program that takes full advantage of the special opportunities afforded by the stable, long-term funding of the intramural research program at NIH. Applicants should be interested in developing and applying novel approaches to the study of problems of major biological and/or medical importance, which could include a significant clinical or translational effort in addition to bench research. The successful candidate would have access to the NIH Clinical Center, a state-of-the-art research hospital on the NIH campus in Bethesda, MD, and would have ample opportunity to participate in the activities of the Center for Human Immunology and other trans-NIH initiatives involving technology development, translational investigation, and multidisciplinary science.

Generous ongoing support for salary, technical personnel, postdoctoral fellows, equipment, and research supplies will be provided. Available cores or collaborative facilities include flow cytometry, advanced optical imaging, microarray generation and analysis, high throughput sequencing, computational biology, production of transgenic and gene-manipulated mice, biosafety level (BSL)-3 facilities, chemical genomics, and support for projects involving RNAi screening. In addition to an outstanding, international postdoctoral community, a superior pool of graduate and undergraduate students is available to the successful applicant.

NIAID's Laboratory of Immunology has a distinguished history of accomplishment in immunology. We strongly encourage application by outstanding investigators who can continue and enhance this record of achievement. Current LI investigators are Ronald Germain, Michael Lenardo, David Margulies, Stefan Muljo, William Paul, Ethan Shevach, and Tsan Xiao.

To apply, e-mail your curriculum vitae, bibliography, and an outline of a proposed research program (no more than two pages) in PDF format to Ms. Bao-Hanh Ngo at **LIT-TTSearch@niaid.nih.gov**. In addition, three letters of reference must be sent directly from the referee to Drs. Giorgio Trinchieri and Dan Kastner, Co-Chairs, NIAID Search Committee, c/o Ms. Bao-Hanh Ngo at **LIT-TTSearch@niaid.nih.gov** or 10 Center Drive, MSC 1356, Building 10, Room 4A22, Bethesda, MD 20892-1356. E-mail is preferred.

Applications will be reviewed starting **December 13, 2010**, and will be accepted until the position is filled. For further information about this position, contact Dr. William Paul at 301-496-5046 or **wpaul@niaid.nih.gov**.

A full package of benefits (including retirement and health, life, and long-term care insurance) is available. Women and minorities are especially encouraged to apply. U.S. citizenship is not required.

Further information on working at NIAID is available on our Web site at **www.niaid.nih.gov/careers/LIS**.

NIAID

National Institute of Allergy and Infectious Diseases

FACULTY POSITION IN BIOENGINEERING

The **California Institute of Technology** invites applications for a tenure-track faculty position in Bioengineering. Bioengineering research at Caltech focuses on the application of engineering principles to the design, analysis, construction, and manipulation of biological systems, and on the discovery and application of new engineering principles inspired by the properties of biological systems.

Applications are invited in any area of bioengineering research. Candidates with strong commitments to research and teaching excellence are encouraged to apply. We expect to make the appointment at the assistant professor level, but consideration will be given to exceptionally well-qualified applicants at the associate and full professor levels. Initial appointments at the assistant professor level are for four years, and are contingent upon completion of the Ph.D. degree.

Bioengineering at Caltech (**http://www.be.caltech.edu**) includes faculty from the Divisions of Engineering and Applied Science (**http://www.eas.caltech.edu)**, Chemistry and Chemical Engineering (**http://www.cce.caltech.edu)**, and Biology (**http://www.biology.caltech.edu)**.

APPLICATION INSTRUCTIONS

Applicants should electronically submit an application at **http://www.be.caltech.edu/search**, including curriculum vitae; a statement of research interests; a statement of teaching interests; and up to three representative publications. Applicants should arrange to have four reference letters uploaded.

Application review will commence immediately and continue until the position is filled.

CALIFORNIA INSTITUTE OF TECHNOLOGY
Division of Engineering and Applied Science
Caltech is an Equal-Opportunity/Affirmative-Action Employer.
Women, minorities, veterans, and disabled persons are encouraged to apply.

UC Irvine Environment Institute

Three Faculty Positions
Assistant Professor

The UC Irvine Environment Institute is recruiting three tenure-track positions at the level of Assistant Professor to begin July 2011. Recruitment of four additional faculty for 2012 is anticipated. Through the Institute, UCI seeks to build on its strengths in environmental research and develop broad, campus-wide collaborations that relate global change, energy, and sustainable resources to societal needs. This recruitment focuses on key anthropogenic systems and the forces driving global change today. Specifically, we seek hires in the areas of energy, land use, and global change, including related environmental sciences.

The new faculty will teach and conduct research in their primary departments within the School of Biological Sciences, School of Physical Sciences, or Henry Samueli School of Engineering. Candidate's research in science or engineering should fit within these Schools and have broad application to sustainability. In addition, these faculty will work as members of the Environment Institute to strengthen environmental research across UCI.

Applicants must have a Ph.D. plus post-doctoral experience in the recruited areas. Completed applications [cover letter, CV, statement of research, three publications, two reference letters from thesis and post-doctoral advisers (or equivalent), and contact information for two additional references] should be submitted through the online UCI recruitment system at **https://recruit.ap.uci.edu/apply#INST**. Candidates should also identify one or more departments within the three Schools listed above for their primary appointment. Review of completed applications will begin on **15 November 2010**, but the search will remain open until all positions are filled.

UCI is recruiting additional tenure-track faculty in the following related areas: comparative and evolutionary physiology; materials chemistry; geotechnical engineering; hydrometeorology; and Earth system science.

UCI is an equal opportunity employer committed to excellence through diversity and strongly encourages applications from all qualified applicants, including women and minorities. UCI is responsive to the needs of dual career couples, is dedicated to work-life balance through an array of family-friendly policies, and is the recipient of an NSF ADVANCE Award for gender equity.

UNIVERSITY *of* CALIFORNIA · IRVINE

UCSF University of California San Francisco

UCSF's Division of Pulmonary, Critical Care, Allergy and Sleep and the Cardiovascular Research Institute (CVRI) seek new faculty members to develop high impact and sustainable research programs to advance understanding of pulmonary biology, basic immunology and pulmonary and allergic diseases. Appointments may be at the Assistant, Associate or Full Professor level. Primary academic appointments in an appropriate basic science department or Medicine, membership in graduate programs, excellent space, ongoing partial salary support and startup funding will be provided. An advanced degree and substantial research background are required.

Applicants may apply to one of three parallel searches. Committees will refer applications across searches if appropriate. The 3 searches are:

Pulmonary Biology: Programs are sought in any area broadly related to pulmonary biology and disease, including, but not limited to Stem Cell Biology, Immunology, Cancer, Developmental Biology, Transplant Biology and Human Genetics. Programs may range from basic cell and molecular biology to clinical science and may use systems from cells to *Drosophila* to human. **Chair: Zena Werb**

Allergy/Immunology – Physician-Scientist: Seeking a board certified/eligible physician-scientist in allergy/immunology with a strong, sustainable research program broadly related to allergy/immunology. Programs may range from basic cell and molecular biology to clinical science and may use systems from cells to *Drosophila* to human **Chair: Art Weiss**

Pulmonary – Physician-Scientist: Seeking a board certified/eligible physician-scientist in pulmonary/critical care with a strong, sustainable research program broadly related to pulmonary biology and disease. Programs may range from basic cell and molecular biology to clinical science and may use systems from cells to *Drosophila* to human. **Chair: Dean Sheppard**

Please send CV, summary of current research (one page) and outline of future research (up to 2 pages) and arrange to send 3 letters of recommendation to **Christine Mok (Christine.mok@ucsf.edu**). Applications will be considered starting **October 1, 2010,** and accepted until **December 1, 2010**.

UCSF seeks candidates whose experience, teaching, research, or community service has prepared them to contribute to our commitment to diversity and excellence. UCSF is an Equal Opportunity/Affirmative Action Employer. The University undertakes affirmative action to assure equal employment opportunity for underutilized minorities and women, for persons with disabilities, and for covered veterans. All qualified applicants are encouraged to apply.

SALK INSTITUTE FOR BIOLOGICAL STUDIES

The Salk Institute for Biological Studies, a world class scientific environment located in La Jolla, CA, is inviting applications for an:

Assistant Professor

Nomis Center for Immunobiology and Microbial Pathogenesis

In this position, you will work in the areas of molecular and cellular immunology, microbial pathogenesis, and inflammation biology. Specific areas of interest include innate immunity, mucosal immunity, human genetics, and the influence of commensal bacteria on the immune system, health, and disease. The Salk Institute offers a highly interactive environment with leading programs in neuroscience, cancer, metabolism, and microbiology. The successful candidate will be expected to develop and maintain an independent research program and help establish new interdisciplinary programs aimed at investigating the role of inflammation in the onset and progression of human diseases.

The Salk Institute offers an excellent start-up package along with a competitive salary and benefits.

Qualified candidates are invited to submit their curriculum vitae, research statement, and also arrange to have three letters of recommendation sent directly from the referees to: **Chair, Nomis Center Search Committee, The Salk Institute for Biological Studies, 10010 North Torrey Pines Road, La Jolla, CA 92037, USA. Please refer to Job Code: A032.** Applications may also be sent electronically to: **Chair-NomisSearch@salk.edu.**

Applications with all required materials (curriculum vitae, research statement, and letters of recommendation) will be accepted until December 31, 2010.

The Salk Institute for Biological Studies is an Equal Opportunity Employer.

Nontraditional Careers:
Opportunities Away From the Bench
Webinar

Want to learn more about exciting and rewarding careers outside of academic/industrial research? View a roundtable discussion that looks at the various career options open to scientists across different sectors and strategies you can use to pursue a nonresearch career.

Now Available
On Demand
www.sciencecareers.org/webinar

Participating Experts:

Dr. Lori Conlan
Director of Postdoc Services,
Office of Intramural Training and Education
National Institutes of Health

Pearl Freier
President
Cambridge BioPartners

Dr. Marion Müller
Director, DFG Office North America
Deutsche Forschungsgemeinschaft
(German Research Foundation)

Richard Weibl
Director, Center for Careers in Science and Technology
American Association for the Advancement of Science

Produced by the
Science/AAAS Business Office.

Science Careers
From the journal *Science* AAAS

Oregon State OSU

Six New Faculty in the Life Sciences

Biochemistry & Biophysics / Microbiology / Zoology

Applications are invited for six full-time tenure-track Assistant Professor positions in the College of Science integrative life science disciplines of Biochemistry & Biophysics, Microbiology and Zoology. All appointees are expected to participate in graduate and undergraduate teaching and establish an extramurally funded research program; candidates enthusiastic about teaching and research collaboration are desired. Applicants must have a Ph.D. and (except ecosystem ecology and stress or aging biology positions) a minimum of 2 years relevant postdoctoral experience. These positions are associated with over 30 new positions across OSU that form the Provost's Faculty Investment Initiative, an exciting investment to strengthen OSU's research areas of excellence while increasing the ability of the University to respond to the needs and concerns of an increasingly diverse student body. At OSU we have an institution-wide commitment to diversity and multiculturalism, and we are intentional about providing a welcoming atmosphere and inclusive professional opportunities. ***OSU is an AA/EOE.***

Ecosystem Ecology *(posting 0006371)*

Enzymology/Protein Biochemistry & Biophysics *(posting 0006402)*

Environmental Microbiology *(posting 0006377)*

Prokaryotic Systems Biology *(posting 0006375)*

Stress or Aging Biology *(posting 0006370)*

Biochemistry of Aging (Asst/Assoc Professor) *(posting 0006383)*

For details of each position and to apply visit http://oregonstate.edu/jobs
Apply by 10 December 2010 for full consideration

VIB

Vesalius Research Center
VIB, K.U.Leuven
Director: Professor Dr Peter Carmeliet

LEUVEN

Senior Scientist position
Group leader: Prof Dr Peter Carmeliet

This position is immediately available in the group of Prof Carmeliet. The focus of the VRC is to unravel the molecular basis of neurovascular biological processes and diseases. VRC has recently started to study metabolism and its interaction with oxygen sensors (please visit the website for more info: **www.vrc-lab.be**).

We are seeking a highly motivated scientist who is willing to join a team of international researchers that investigates the interaction between metabolism and hypoxia. The successful candidate must have strong background in mass spectrometry for metabolite determination and identification. Expertise in proteomics techniques is a strong extra added value. The candidate is expected to independently establish all necessary techniques, introduce new technology, coordinate ongoing collaborations, and instruct other scientists. Experience as a postdoctoral researcher with a good publication record in the metabolomics field is preferred.

Postdoctoral Scientist - Cell Proliferation laboratory
Group leader: Professor Salvador Moncada

This position is available for 3 years to join the Cell proliferation laboratory, led by Prof Salvador Moncada. Primary research aim of the Cell Proliferation Laboratory is to understand the molecular basis of the link between cell proliferation and metabolism. The aim of this study is to investigate the possible changes that might occur during carcinogenesis (please visit: **www.vrc-lab.be**).

Successful candidate should be highly motivated and enthusiastic with the ambition to lead a small research group. Applicants must have a PhD in a relevant discipline and should be skilled in molecular and cellular biology methods. Interest and experience in biochemistry would be an advantage.

Applicants should have a strong publication record (including at least one paper as a first author) in peer-reviewed international journals, with an emphasis on quality rather than quantity of publications. Excellent communication skills in spoken and written English and capability to work in a team as well as independently. The position is available from November 2010, flexible start date.

Send CV, list of publications, summary of past research, contact info of 3 referees to **Peter.Carmeliet@vib-kuleuven.be** for Senior Scientist position and to **s.moncada@ud.ac.uk** for the Postdoctoral position. Interviews for top-ranked candidates will be held in Leuven, Campus Gasthuisberg O&N1, Herestraat 49 (B912), Belgium.

UTMB
The University of Texas Medical Branch

The Department of Obstetrics and Gynecology
Two Tenure Track Assistant/Associate Professors

The Department is expanding its Maternal-Fetal Pharmacology and Biodevelopment Laboratories to include innovative translational research projects and announces the availability of two tenure-track positions at the assistant/associate professor levels. The Department has an outstanding infrastructure of well-equipped laboratories and funded investigators, a division for the support of publications and grant applications, and a perinatal research division with nurses' support. Other research programs are in the areas of fetal origin of disease and reproductive endocrinology. The Department is a member of four NICHD collaborative research network grants, a Women's Reproductive Health Research (WRHR), and Building Interdisciplinary Research careers in Women's Health (BIRCWH).

Individuals interested in women's health research, particularly in the mechanisms underlying the treatment of drug dependence during pregnancy, gestational diabetes, drug delivery, preterm delivery, and the development of new diagnostic tools, are encouraged to apply. Opportunities are available for joint appointment with the Institute for Translational Sciences that supports translational teams, junior faculty training programs, and clinical/translational research. More information can be found at: **http://www.its.utmb.edu/**.

Assistant Professors: Ph.D., M.D. or equivalent with three or more years of postdoctoral training.

Associate Professors: Ph.D., M.D. or equivalent faculty with established and funded research projects in the above or related research areas.

Applicants should include a CV, a brief (two-page) description of their short-term and long-term research goals, and the names of three references with contact information to: **Mahmoud S. Ahmed, Professor and Chair of Search Committee, Department of OB/GYN, 301 University Blvd., Galveston, TX 77555-0587; E-mail: maahmed@utmb.edu**.

UTMB is an Equal Opportunity Affirmative Action Institution which proudly values diversity. Candidates of all backgrounds are encouraged to apply.

MIT Massachusetts Institute of Technology

Come work with us!

Neuroscientist

The Picower Institute for Learning and Memory at the Massachusetts Institute of Technology is seeking an outstanding neuroscientist for a tenure track position at the level of Assistant Professor.

We are interested in candidates studying brain function at the cellular, circuit, and systems levels using a multi-faceted approach combining different methodologies and levels of analysis. We are particularly seeking, though not exclusively, candidates whose research interest concerns mechanisms underlying experience-induced short or long term changes in the brain.

Academic appointments will be in the Department of Brain and Cognitive Sciences. Candidates must have a commitment to excellence in undergraduate and graduate education, and must demonstrate the ability to develop a significant and independent research program.

Applicants should submit a curriculum vitae, a summary of current and proposed research programs, an education plan, and arrange for three letters of recommendation. Applications are being accepted at Academic Jobs Online (https://academicjobsonline.org/ajo).

Search Contact: Prof. Elly Nedivi

Consideration of completed applications will begin immediately. Applications will be accepted for review until December 1, 2010.

MIT is an equal opportunity/ affirmative action employer, and we encourage applications from women and underrepresented minorities.

The Picower Institute
for learning and memory

http://web.mit.edu

POSITIONS OPEN

ASSISTANT PROFESSOR PHYSIOLOGICAL ECOLOGIST
Southern Illinois University Carbondale

The Department of Zoology at Southern Illinois University Carbondale (SIUC) invites applications for a tenure-track position in physiological ecology at the **Assistant Professor** level. We seek candidates who can complement our existing strengths in environmental biology by investigating physiological adaptability and responses to environmental change. The Department and University have exceptional capabilities for analyses of stable isotopes, fatty acids, and organic and inorganic contaminants; as well as excellent facilities and large academic programs in aquatic sciences, genetics, toxicology, and wildlife ecology. Interdisciplinary research is encouraged by the campus-wide Program in Ecology, and by links between Zoology and Microbiology, Physiology, and the SIU Medical School. The successful applicant will be expected to develop an externally funded research program, to mentor graduate students, and to teach undergraduate Zoology courses and a graduate course in their area of specialization. Minimum Qualifications: Applicants must hold a Ph.D. and postdoctoral experience is preferred.

Applicants should send their curriculum vitae, statement of teaching and research interests, copies of transcripts from all institutions attended, up to three representative reprints, and three letters of reference: **Physiological Ecologist Search Committee Chair, Department of Zoology, Mail Code 6501, Southern Illinois University Carbondale, 1125 Lincoln Drive, Carbondale, IL 62901 (fax: 1-618-453-2806).** Review of applications will begin 1 December 2010 and continue until the position is filled.

Southern Illinois University Carbondale is a large, research-oriented institution situated in a pleasant small-town setting southeast of St. Louis. The Department of Zoology has a full-time faculty of 24 with about 240 undergraduate majors and 90 MS and Ph.D. graduate students. For further information, visit our **website: http://www.zoology.siu.edu.**

SIUC is an Affirmative Action/Equal Opportunity Employer that strives to enhance its ability to develop a diverse faculty and staff, and to increase its potential to serve a diverse student population. All applications are encouraged and will receive consideration.

PROFESSOR of PRACTICE in Geographic Information Systems, Tulane University

The Department of Earth and Environmental Sciences seeks to fill a non-tenure-track, Professor of Practice position to teach courses in Geographic Information Systems (GIS), and to supervise the GIS computer lab. To be considered, the applicant must have experience using geologic, topographic, and geophysical raster and point cloud data sets. Expertise with ESRI products is required, including customization of GIS applications. We seek an individual possessing an enthusiastic dedication to teaching who is willing to make a long-term commitment to the department and the University. A Ph.D. is required at the time of appointment. The initial appointment will be for three years with the possibility of renewal after a performance review at the end of the second year. The deadline for applications is October 30, 2010, but the position will remain open until filled. Applications should include curriculum vitae, a statement of teaching interests and goals, and the names and contact information of at least three references, and should be sent to: **Dr. Stephen Nelson, Department of Earth & Environmental Sciences, Tulane University, 6823 Street Charles Avenue, New Orleans, LA 70118-5698. E-mail: snelson@tulane.edu** preferred. Further information about the department and University can be obtained at **website: http://tulane.edu/sse/eens.** *Tulane University is an Affirmative Action/Equal Opportunity Employer. Women and minorities are encouraged to apply.*

POSITIONS OPEN

BIOCHEMISTRY FACULTY POSITION
Kansas State University

The Department of Biochemistry at Kansas State University **(website: http://www.ksu.edu/bchem)** invites applications for a tenure-track position at the Assistant or Associate Professor level, to begin in August, 2011. Applicants should have a Ph.D. or equivalent degree and postdoctoral experience. Candidates at the Associate Professor level must have an established, extramurally-funded research program. Preference will be given to applicants with research interest and experience in areas that complement and enhance the existing programs, which include physical and structural biochemistry, cellular biochemistry, and biochemistry of insects and plants. The department seeks individuals who will sustain a strong, extramurally funded research program and excel in teaching a diverse population in the undergraduate and graduate programs in biochemistry. A competitive salary and start-up package will be provided for the successful candidate. For additional information about the department and the position, see **website: http://www.ksu.edu/bchem.** Applicants should submit a single PDF file that includes their curriculum vitae, statement of research and teaching interests, and selected reprints to **e-mail: bchsrch@ksu.edu**, and have three letters of reference sent to the same email address. Questions may be referred to: **Michael Kanost, Department Head, e-mail: kanost@ksu.edu**. Review of applications will begin on November 15, 2010 and continue until the position is filled. A background check is required for all new employees. *Kansas State University is an Equal Opportunity Employer and actively seeks diversity among its employees.*

FACULTY POSITIONS in Cardiovascular Research

The Heart and Vascular Center of Excellence at UMass Memorial Medical Center and the University of Massachusetts School of Medicine is seeking faculty candidates for SENIOR TENURED or JUNIOR TENURE-TRACK level positions in basic science or clinical investigation. These positions will involve the establishment or expansion of independently funded research programs that will benefit from a world-class infrastructure for basic and clinical investigation including core facilities in biostatistics, bioinformatics, clinical sampling, mouse phenotyping, zebrafish, imaging, and deep sequencing. Successful candidates will be allocated space in new, state-of-the-art clinical and basic research facilities. Positions will be highly competitive with regards to salary, start-up funds, and research space.

Please submit a cover letter, CV, and three references to either **John F. Keaney, Jr.** or **Nathan Lawson c/o: Debra Manseau, Cardiovascular Research, UMass Medical School, 381 Plantation Street, Biotech V, Suite 200, Worcester, MA, 01605** or by **e-mail:** to **Debra.Manseau@umassmed.edu**

University of Massachusetts and UMass Memorial Healthcare are Equal Opportunity Employers.

FACULTY POSITION in Inorganic or Organometallic Materials Chemistry. The Department of Chemistry at the University of Kansas is seeking exceptional candidates for a tenure-track position in Inorganic or Organometallic Materials Chemistry at the **ASSISTANT PROFESSOR** level available as early as August 18, 2011. A Ph.D. in chemistry or closely related field is expected by start date of appointment and postdoctoral experience is desirable. For a complete announcement and to apply online, go to **website: https://jobs.ku.edu** and search for position **00001867.** Additional information: send summary of two to three research proposals (two pages) and three letters of recommendations sent separately to: **Elaine Knight, e-mail: eknight@ku.edu, telephone: 785-864-5206.** Review of applications begins November 1, 2010, and continues as long as needed to identify a qualified pool. *Equal Opportunity/Affirmative Action.*

POSITIONS OPEN

ASSISTANT PROFESSOR

MIT's Department of Brain and Cognitive Sciences anticipates making a faculty appointment at the Assistant Professor level in cognitive science and cognitive neuroscience or computational cognition and neuroscience. We seek to hire a candidate whose research focuses on either 1) any area of cognitive science and/or human cognitive neuroscience, or 2) computational cognition or neuroscience – broadly on computational studies of intelligence. In addition to conducting research, faculty members at MIT teach undergraduate and graduate courses and supervise graduate and undergraduate participation in research.

Please note in cover letter if application is for cognitive or computational area. Please send a CV, a statement of research and teaching interests, and representative reprints. In addition, please arrange to have three letters of recommendation submitted. Please electronically submit complete applications and letters in pdf or Word format to the **Cognitive Search Committee c/o Judy Rauchwarger: e-mail: jrauch@mit.edu.** Information about the department can be found at **website: http://web.mit.edu/bcs/.**

December 1, 2010 is the deadline for submitting applications, but review of applications will begin as they are received.

MIT is an Affirmative Action Employer, and we encourage applications from women and underrepresented minorities.

POSITIONS OPEN

FACULTY POSITIONS
Department of Biochemistry and Molecular Biology
Saint Louis University
School of Medicine

Saint Louis University, a Catholic Jesuit institution dedicated to student learning, research, health care, and service, is seeking outstanding applicants for tenure-track faculty positions at the **ASSISTANT PROFESSOR** level in the Edward A. Doisy Department of Biochemistry and Molecular Biology **(website: http://biochem.slu.edu/).** The Department has an outstanding faculty, a long tradition of excellence in research and education and is housed in the state-of-the-art Doisy Research Center completed in 2007. We are interested in candidates with demonstrated ability to develop strong and independent research programs that would complement existing strengths in the Department. Research programs focusing on X-ray structural biology and molecular mechanisms of systems relevant to health and disease will be given high priority. A Ph.D. or M.D. degree, outstanding record of publications, evidence of current external funding, enthusiasm for teaching and mentoring research trainees are important criteria for selection.

Interested candidates should submit a cover letter, current curriculum vitae, relevant publications, future research plans, a detailed three-year budget, and addresses of three references to **website: http://jobs.slu.edu.**

Saint Louis University is an Affirmative Action, Equal Opportunity Employer, and encourages nominations and applications of women and minorities.

ASSISTANT PROFESSORS
Kansas State University
Cell, Molecular, Genetics or Developmental Biology

The Division of Biology of Kansas State University invites applications for three tenure-track Assistant Professor positions in the general areas of cell, molecular, developmental, genetics/genomics biology. We particularly encourage applications from individuals who are using model organisms (zebrafish, nematodes, etc.) in research areas that synergize with currently ongoing research foci in the Division **(website: http://www.ksu.edu/biology)**. The successful candidates will establish a vigorous, extramurally funded research program and contribute to graduate and undergraduate instruction to a diverse population. Excellent facilities exist at Kansas State. A Ph.D. or equivalent and post-doctoral training are required. More information, including application instructions, can be found at **website: http://www.ksu.edu/biology/position_openings/cellbiology.html**. Direct inquiries to: **Dr. Stephen K. Chapes, Search Committee Chair (e-mail: skcbiol@ksu.edu).** Review of applications will begin November 12, 2010 and continue until the positions are filled. *KSU is an Equal Opportunity Employer. Background checks are required for all employees.*

TENURE-TRACK FACULTY POSITIONS
in Neuropharmacology or Toxicology
School of Medicine and Biomedical Sciences
University at Buffalo
State University of New York

The Department of Pharmacology and Toxicology is continuing the second phase of an expansion and is recruiting candidates for Assistant, Associate or Full Professor with tenure-track 12-month fully state-funded appointments. Candidates should have a strong research focus in neuropharmacological or toxicological sciences including drug discovery, targeted therapeutic approaches to diseases, and/or environmental health science. Preferred research topics within these areas include: molecular recognition, signal transduction, neurodevelopment, drugs of abuse, behavior and circadian rhythms, molecular pharmacology or toxicology, pharmacogenomics/proteomics, and/or environmental pollutants and toxic agents.

Apply online at **website: https://www.ubjobs.buffalo.edu** (Postings 1000512 for toxicology and 1000568 for neuropharmacology).

UB is an Affirmative Action/Equal Opportunity Employer.

POSITIONS OPEN

FACULTY POSITIONS
in Chemistry and Biochemistry

The Department of Chemistry & Biochemistry at ARIZONA STATE UNIVERSITY invites applications for two tenure-track positions at the rank of assistant/associate professor in any energy-related area. At least one position will have an emphasis in inorganic chemistry. Topics of interest include, but are not limited to, bioenergy, catalysis, energy storage and conversion, nanochemistry, organic materials and polymer chemistry.

Duties include: establishing an externally funded research program of national/international recognition, teaching chemistry or biochemistry courses at the graduate and undergraduate levels, and participating on assigned governance and service committees in the Department of Chemistry and Biochemistry. Applicants must have a doctoral degree in chemistry, biochemistry or related field. Post-doctoral experience is desired.

Applicants must submit a cover letter, a curriculum vitae with a list of publications, a succinct outline of future research plans, and a statement of teaching philosophy and interests. These application materials must be submitted electronically in a single PDF document to **email: ChemSearch@asu.edu.** Applicants must also arrange for three letters of recommendation to be submitted to **email: ChemSearch@asu.edu.**

Review of applications will begin November 22, 2010, and will continue thereafter until the positions are filled. A background check is required for employment.

ASU is an equal opportunity/affirmative action employer and is committed to excellence through diversity. Women and minorities are encouraged to apply.

MARKETPLACE